

MATER. TEHNOL.	LETNIK VOLUME	47	ŠTEV. NO.	6	STR. P.	683–875	LJUBLJANA SLOVENIJA	NOV.–DEC. 2013
-------------------	------------------	----	--------------	---	------------	---------	------------------------	-------------------

VSEBINA – CONTENTS

IZVIRNI ZNANSTVENI ČLANKI – ORIGINAL SCIENTIFIC ARTICLES

Comparative study of the synthesis and photo-physical characteristics of a new blue-emitting nanocrystal for NUV-excited LEDs

Primerjalna študija sinteze in optično-fizikalnih značilnosti novih modro sevajočih nanokristalov za z NUV vzbujanih LED
H. Sameie, R. Salimi, A. A. Sarabi, A. A. Sabbagh Alvani, S. Nargesian, H. E. Mohammadloo, Y. Ebrahimi 685

Development of foundry cores based on inorganic salts

Razvoj livarskih jeder na podlagi anorganskih soli
P. Jelínek, F. Mikšovský, J. Beňo, E. Adámková 689

Effect of the abrasive grit size on the wear behavior of ceramic coatings during a micro-abrasion test

Vpliv velikosti brusnih zrn na vedenje keramičnih prevlek pri mikroabrazijskem preizkusu obrabe
M. Horik Korkut, Y. Küçük, A. C. Karaođlanli, A. Erdođan, Y. Er, M. S. Gök 695

Accelerated carbide spheroidisation and refinement (ASR) of the C45 steel during induction heating

Pospešena sferoidizacija in udrobnjenje karbidov (ASR) med indukcijskim segrevanjem jekla C45
D. Hauserova, J. Dlouhy, Z. Novy, J. Zrník 701

The effect of a styrene-acrylic copolymer synthesized in a high-pressure reactor on the improved corrosion protection of a two-component polyurethane coating

Vpliv stiren-akrilnega kopolimera, sintetiziranega v visokotlačnem reaktorju na izboljšanje korozijske zaščite dvokomponentnega poliuretanskega premaza
U. Šegedin, K. Burja, F. Malin, S. Skale, B. Znoj, B. Šket, P. Venturini 707

Processing poly(ether etherketone) on a 3D printer for thermoplastic modelling

Obdelava polyether etherketonea na 3D-tiskalniku za termoplastično modeliranje
B. Valentan, Ž. Kadivnik, T. Brajljeh, A. Anderson, I. Drstvenšek 715

Finite-element model of the indentation for YBCO-based superconductor thin films

Model končnih elementov za vtiskovanje tankih plasti superprevodnika YBCO
O. Culha, I. Turkmen, M. Toparli, E. Celik 723

Effect of viscosity on the production of alumina borate nanofibers via electrospinning

Vpliv viskoznosti na izdelavo aluminijevooksidnaboratnih nanovlaken z elektrospinningom
M. Ozdemir, E. Celik, U. Cocen 735

Effects of solidification parameters on the micro- and macrostructure of the X19CrMoVNbN11-1 steel

Vplivi parametrov strjevanja na makro in mikrostrukturo jekla X19CrMoVNbN11-1
M. Koležnik, A. Nagode, G. Klančnik, J. Medved, B. Janet, M. Bizjak, L. Kosec 739

Influence of cutting speed on intensity of the plastic deformation during hard cutting

Vpliv hitrosti rezanja na intenziteto plastične deformacije med odrezovanjem
M. Neslušán, I. Mrkvica, R. Čep, M. Čilliková 745

Effect of iron and cerium additions on rapidly solidified Al-TM-Ce alloys

Vpliv dodatkov železa in cerija na hitro strjene zlitine Al-TM-Ce
A. Michalcová, D. Vojtěch, G. Schumacher, P. Novák, E. Plišingrová 757

Shrinkage behavior of a self-compacting concrete

Vedenje samozgoščevalnega betona pri krčenju
N. Bouhamou, N. Belas, K. Bendani, A. Mebrouki 763

Failure mode of M130 martensitic steel resistance-spot welds

Način porušitve uporovnih točkastih varov pri martenzitem jeklu M130
M. Pouranvari, S. M. Mousavizadeh 771

Synthesizing a new type of mullite lining

Sinteza nove vrste obloge iz mulita
Z. Aćimović, A. Terzić, L. Andrić, L. Pavlović, M. Pavlović 777

Influence of processing factors on the tensile strength of 3D-printed models Vpliv procesnih dejavnikov na natezno trdnost tridimenzionalno tiskanih modelov T. Galeta, I. Kladarić, M. Karakašić	781
Non-singular method of fundamental solutions for the deformation of two-dimensional elastic bodies in contact Nesingularna metoda fundamentalnih rešitev za deformacijo dvo-dimenzionalnih stikajočih se elastičnih teles Q. Liu, B. Šarler	789
Removal of surface impurities from QCM substrates with the low-pressure oxygen-plasma treatment Odstranjevanje površinskih nečistoč s QCM-podlag z obdelavo v nizkotlačni kisikovi plazmi R. Zaplotnik, D. Kreuh, A. Vesel	795
Structural, optical and electrical studies on Si-doped polymer electrolytes Študij strukture, optične in električne lastnosti elektrolitov polimerov, dopiranih s Si A. Saxena, P. K. Singh, B. Bhattacharya	799
Electroless Ni-B-W coatings for improving hardness, wear and corrosion resistance Nanašanje Ni-B-W s cementacijskim galvaniziranjem za izboljšanje trdote, obrabe in odpornosti proti koroziji A. I. Aydeniz, A. Göksenli, G. Dil, F. Muhaffel, C. Calli, B. Yüksel	803
Physical and numerical modelling of a non-stationary steel flow through a subentry shroud with an inner metering nozzle Fizikalno in numerično modeliranje nestacionarnega toka jekla skozi potopljen izlizek z notranjo šobo K. Michalek, M. Tkadlečková, K. Gryc, J. Cupek, M. Macura	807
Research of thermal processes for the continuous casting of steel Raziskave termičnih dogajanj pri kontinuirnem ulivanju jekla M. Velicka, D. Dittel, R. Pyszko, M. Prihoda, M. Vaculik, P. Fojtik, J. Burda	815
Stationary-creep-rate equations for tempered martensite Enačbe za hitrost stacionarnega lezenja žarjenega martenzita F. Vodopivec, B. Žužek, D. A. Skobir Balantič, M. Jenko, M. Godec, D. Steiner Petrovič	819
Numerical calculations of stress-intensity factors for a WWER-1000 reactor pressure vessel under a pressurized thermal shock Numerični izračuni faktorja intenzitete napetosti v reaktorski tlačni posodi WWER-1000 pri toplotnem šoku pod tlakom S. V. Kobelsky	825
Dissolution of a copper wire during a hot-dipping process using a SnCu1 lead-free solder Raztapljanje bakrene žice med vročim omakanjem pri uporabi spajke brez svinca SnCu1 D. Steiner Petrovič, J. Medved, G. Klančnik	831
Structural characterization of platinum foil for neural stimulating electrodes using a four-point resistivity-measuring device Strukturne lastnosti platinske folije za elektrode pri stimulaciji živcev, ugotovljene z napravo za širitočkovno merjenje upornosti P. Pečlin, M. Bizjak, M. Pribošek, M. Godec, S. Ribarič, J. Rozman	837

STROKOVNI ČLANKI – PROFESSIONAL ARTICLES

Variation in magnetic properties of sol-gel-synthesized cobalt ferrites Spreminjanje magnetnih lastnosti kobaltonih feritov, sintetiziranih po sol-gel postopku A. Hunyek, C. Sirisathitkul	845
--	-----

KRATKE NOVICE – SHORT NOTES

Assessing the quality of corrosion education in the United Arab Emirates Presoja kvalitete izobraževanja na področju korozije v Združenih arabskih emiratih H. L. Lim, L. Al Tayeb Ait Tayeb, M. A. Othman	849
---	-----

DOGODKI – EVENTS

Šolski center Ravne na Koroškem končal projekta energetske sanacije in gradnje sodobnega izobraževalnega centra v skupni vrednosti približno tri milijone evrov	853
---	-----

COMPARATIVE STUDY OF THE SYNTHESIS AND PHOTO-PHYSICAL CHARACTERISTICS OF A NEW BLUE-EMITTING NANOCRYSTAL FOR NUV-EXCITED LEDS

PRIMERJALNA ŠTUDIJA SINTEZE IN OPTIČNO-FIZIKALNIH ZNAČILNOSTI NOVIH MODRO SEVAJOČIH NANOKRISTALOV ZA Z NUV VZBUJANJIH LED

Hassan Sameie^{1,2}, Reza Salimi^{1,2}, Ali Asghar Sarabi¹, Ali Asghar Sabbagh Alvani², Saleheh Nargesian³, Hossein Eivaz Mohammadloo^{1,2}, Yalda Ebrahimi^{1,2}

¹Amirkabir University of Technology, Faculty of Polymer Engineering & Color Tech., 424 Hafez Ave., 15875-4413 Tehran, Iran

²Amirkabir University of Technology, Color and Polymer Research Center (CPRC), 424 Hafez Ave., 15875-4413 Tehran, Iran

³University of Ottawa, Telfer School of Management, 55 Laurier Ave., East Ottawa, K1N 6N5 Ontario, Canada, h-sameie@aut.ac.ir

Prejem rokopisa – received: 2012-07-27; sprejem za objavo – accepted for publication: 2013-04-02

In this research, a new blue-emitting nanocrystalline phosphor, $\text{SrZn}_2\text{Si}_2\text{O}_7: \text{Eu}^{2+}$, utilizable in InGaN LEDs, was successfully synthesized via two routes: the sol-gel method (SG) and solid-state reaction (SS). The effects of the preparation processes on the crystallization, morphology and thermal properties were analyzed by appropriate techniques, such as thermogravimetric-differential thermal analysis (TG-DTA), X-ray diffraction (XRD) and scanning electron microscopy (SEM). The sample synthesized by the wet chemical method has a relatively regular morphology, a higher phase purity and a crystallite size of approximately 30 nm. Furthermore, luminescence spectrophotometry was performed for the investigation of the optical characteristics. The obtained phosphors emit blue light due to the $4f^65d^1(^2D) \rightarrow 4f^7(^8S_{7/2})$ transition of the Eu^{2+} ions, which act as luminescence centers in the host lattice. After the excitation in the near-UV region, the phosphors prepared by SG have a higher emission intensity with a color coordination of $x = 0.176$, $y = 0.193$.

Keywords: synthesis, nanocrystalline, luminescence, functional materials, photonic devices

V tej raziskavi je bil uspešno sintetiziran nov, modro sevajoč nanokristalni fosfor $\text{SrZn}_2\text{Si}_2\text{O}_7: \text{Eu}^{2+}$, uporaben v InGaN LED, po dveh metodah: po sol-gel-metodi (SG) in reakciji v trdnem (SS). Učinek postopka priprave na kristalizacijo, morfologijo in termične lastnosti je bil analiziran s primernimi tehnikami, kot je termogravimetrična diferenčna termična analiza (TG-DTA), rentgenska difrakcija (XRD) in vrstična elektronska mikroskopija (SEM). Vzorec, sintetiziran z mokro kemijsko metodo, ima relativno pravilno morfologijo, veliko čistost faze in velikost kristalov okrog 30 nm. Izvršena je bila tudi luminescenčna spektrofotometrija za preiskavo optičnih značilnosti. Dobljeni fosforji so emitirali modro svetlobo zaradi $4f^65d^1(^2D) \rightarrow 4f^7(^8S_{7/2})$ -prehoda Eu^{2+} ionov, ki učinkujejo kot centri luminescence v gostujoči rešetki. Po vzbujanju blizu področja UV so imeli fosforji, pripravljene po SG-metodi, višjo intenziteto emisije s koordinacijo barve $x = 0,176$, $y = 0,193$.

Ključne besede: sinteza, nanokristaliničnost, luminescenca, funkcijski materiali, fotonске naprave

1 INTRODUCTION

In recent years, light-emitting diodes (LEDs) have emerged as a prominent class of lighting devices and the study of RGB phosphors suitable for near-ultraviolet (NUV) excitation has been attracting more and more attention for fabricating white LEDs.^{1,2} LEDs have a great potential to replace conventional lighting sources, like incandescent and fluorescent lamps, due to their many favorable characteristics, such as a long lifetime and environment-friendly properties.^{3,4} The new developments in the field of optical materials are the search for ideal/suitable phosphors for the conversion of the NUV emission from InGaN chips into visible light. Among the different sorts of these materials, silicate phosphors have attracted researchers' attention because of the advantages of a stable crystal structure, stability to high irradiation powers, etc.^{5,6} In general, various preparation methods may greatly affect the crystallization, morphology, particle size and optical characteristics of phosphor materials.

Compared with samples obtained by the conventional SS route, the phosphor materials synthesized by the wet chemical method have advantages such as a low calcination temperature, good mixing of the starting materials and a higher uniformity of the particle size distribution.⁷⁻⁹ But from another point of view, the solid state as the most convenient method has industrial possibilities. In order to optimize the characteristics of $\text{SrZn}_2\text{Si}_2\text{O}_7: \text{Eu}^{2+}$, in this study, two experimental methods, SS and SG, were used to prepare the nanocrystalline phosphors and the effects of the preparation processes on the crystallization, morphologies, and optical properties were investigated.

2 EXPERIMENTAL METHOD

$\text{Sr}_{0.96}\text{Zn}_2\text{Si}_2\text{O}_7:0.04\text{Eu}^{2+}$ samples were synthesized using the SG and SS methods. TEOS and nitrate salts in SG and metal oxides and acid boric as a flux in the SS were used to prepare the precursors. Finally, the

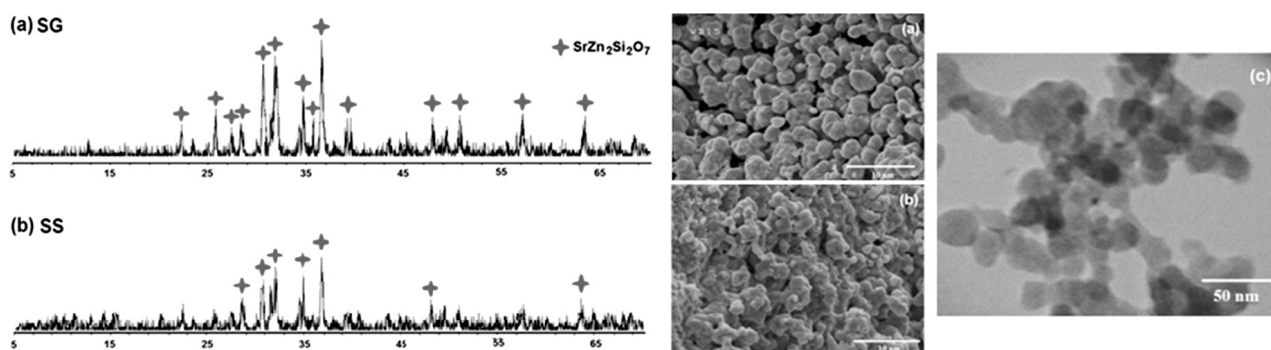


Figure 1: XRD patterns, SEM images and TEM micrograph of SrZn₂Si₂O₇: Eu²⁺ prepared via different methods
Slika 1: XRD-posnetka, SEM-posnetka in TEM-posnetek SrZn₂Si₂O₇: Eu²⁺, pripravljenega z različnimi metodami

precursors were calcined at 1100 °C for 1 h in a weak reductive atmosphere of flowing 5 % H₂-95 % N₂ gas. Also, in order to characterize the final phosphors, X-ray diffraction (XRD), scanning and transition electron microscopy (SEM/TEM), thermogravimetric-differential thermal analysis (TG-DTA), and fluorescence spectroscopy were used.

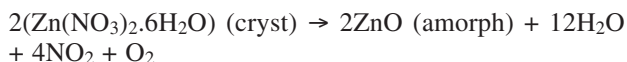
3 RESULTS AND DISCUSSION

The XRD patterns and the SEM micrographs of the samples synthesized with SG and SS are shown in **Figure 1**. The main phase can be indexed to the phase of SrZn₂Si₂O₇ for both samples (JCPDS 10-0051). From the diffraction intensity, it can be seen that the order of the crystallization and the microstructural regularity for the phosphor which were prepared via SG are higher than those of the SS due to the uniformity of the starting reactants, and thus this method is more favorable for the formation of superfine phosphors. Moreover, the TEM image depicts that the average size of the crystallites for the SG sample is about 30 nm.

The TG-DTA curves of the SrZn₂Si₂O₇ precursors were studied, as presented in **Figure 2**, to understand their pyrolysis behavior and crystallization process. The following chemical reactions could be inferred, during the synthesis of the two phosphors:^{10,11}

Sol-gel sample:

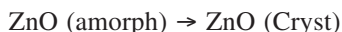
Reaction A:



Reaction B:



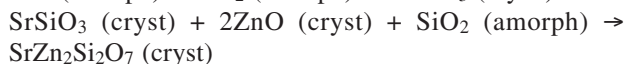
Reaction C:



Reaction D:



Reaction E:

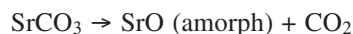


Solid state sample:

Reaction A:



Reaction B:



Reaction C:

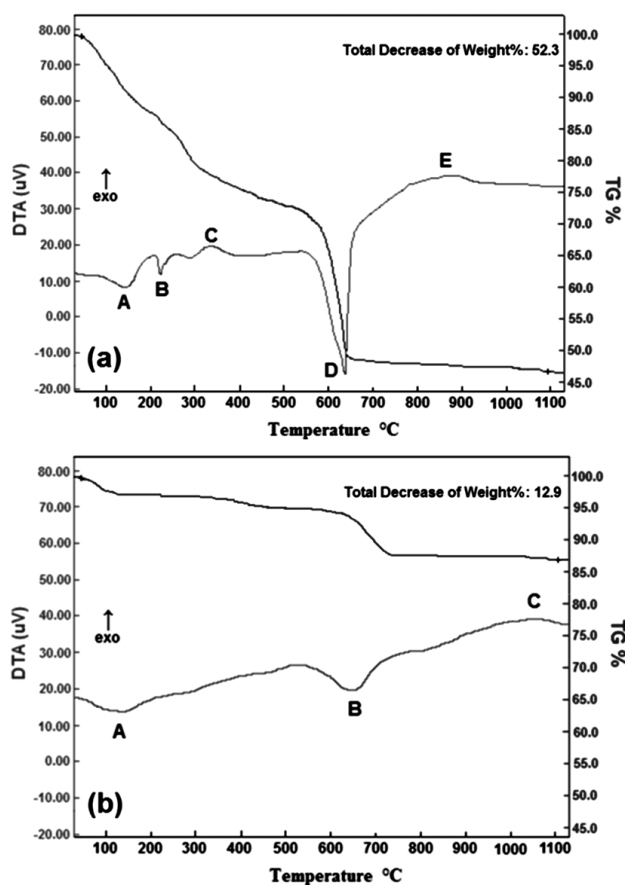
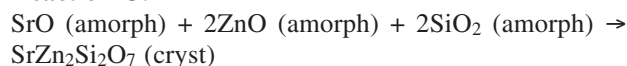


Figure 2: DTA and TG curves of SrZn₂Si₂O₇ gels from 25 °C up to 1150 °C for: a) SG and b) SS samples

Slika 2: DTA- in TG-krivulje gela SrZn₂Si₂O₇ od 25 °C do 1150 °C za: a) vzorce SG in b) vzorce SS

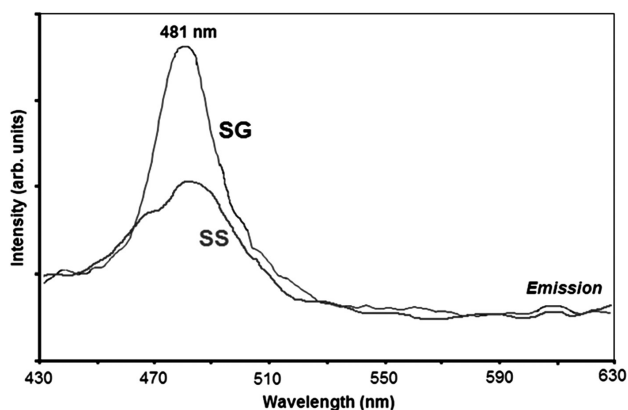


Figure 3: Emission spectra of $\text{SrZn}_2\text{Si}_2\text{O}_7: \text{Eu}^{2+}$ prepared via different methods

Slika 3: Emisijski spekter $\text{SrZn}_2\text{Si}_2\text{O}_7: \text{Eu}^{2+}$, pripravljen z različnimi metodama

The effects of the different synthesis methods on the optical properties were also investigated. **Figure 3** shows the emission spectra of the $\text{SrZn}_2\text{Si}_2\text{O}_7: \text{Eu}^{2+}$ phosphors prepared by SG and SS. Under near-UV excitation the phosphors emit an intense blue light, peaking at 481 nm, with similar profiles because of the same composition and the same crystalline lattice, while the intensity is different, which is consistent with the degree of crystallization of the phosphors. The emission peak is attributed to a typical $4f^65d^1(^2D) \rightarrow 4f^7(^8S_{7/2})$ transition of Eu^{2+} and for SG sample, the color coordination is ($x = 0.176$, $y = 0.193$). However, there is no special emission of Eu^{3+} in these spectra, which implies that Eu^{3+} ions have been reduced to Eu^{2+} completely. Double or triple Eu ions can be present in ionic solids. For the case of the triple charged, all the $5d$ and $6s$ orbitals are empty and the $4f$ is partially occupied. The optically active $4f$ electrons are shielded from the crystalline electric field by the outer $5s$ and $5p$ shells. The resulting effect is that the neighboring ligands have very little affect on the $4f$ electrons. But for the case of the divalent Eu ions, the

energy separation between the $4f^7$ and $4f^65d^1$ configurations will be large and these transitions are dipole-allowed, which are about 10^6 times stronger than the very frequently observed $4f \rightarrow 4f$ transitions in trivalent Eu ions.¹² Therefore, a reducing atmosphere helps to reduce Eu^{3+} to Eu^{2+} ions for better optical properties.

4 CONCLUSION

In summary, blue-emitting phosphor $\text{SrZn}_2\text{Si}_2\text{O}_7: \text{Eu}^{2+}$ was synthesized via two methods, SS and SG, for LED applications. The reducing atmosphere helped the Eu^{3+} ions to reduce to Eu^{2+} and the $4f^65d^1(^2D) \rightarrow 4f^7(^8S_{7/2})$ transition of Eu^{2+} caused the strong emission peak at about 480 nm for the sample prepared via the SG method. The results reveal that the sample synthesized by wet chemical method has a relatively regular morphology, a small particle size and a higher luminescence intensity.

5 REFERENCES

- X. Y. Sun, J. H. Zhang, X. Zhang, Y. S. Luo, X. J. Wang, J. Rare Earths, 26 (2008), 421
- F. Xiao, Y. N. Xue, Q. Y. Zhang, Physica B, 404 (2009), 3743
- K. Sakuma, N. Hirotsaki, R. Xie, J. Lumin., 126 (2007), 843
- S. Yao, D. Chen, J. Opt. Laser Technol., 40 (2008), 466
- W. H. Hsu, M. H. Sheng, M. S. Tsai, J. Alloys Compd., 467 (2009), 491
- J. S. Kim, P. E. Jeon, J. C. Choi, H. L. Park, Solid-state Commun., 133 (2005), 187
- M. Pang, X. Liu, J. Lin, J. Mater. Res., 20 (2005), 2676
- R. P. Rao, J. Electrochem. Soc., 143 (1996), 189
- R. Balakrishnaiah, D. Kim, S. S. Yi, K. Jang, H. S. Lee, J. H. Jeong, Mater. Letters, 63 (2009), 2063
- G. A. El-Shobaky, A. S. Ahmed, G. A. Fagal, M. Mokhtar, Thermochim Acta, 319 (1998), 67
- P. V. Ravindran, B. B. Kalekar, K. V. Rajagopalan, C. G. S. Pillai, P. K. Mathur, J. Nucl. Mater., 317 (2003), 109
- G. Blasse, B. C. Grabmaier, Luminescent materials, Springer Verlag, Berlin 1994

DEVELOPMENT OF FOUNDRY CORES BASED ON INORGANIC SALTS

RAZVOJ LIVARSKIH JEDER NA PODLAGI ANORGANSKIH SOLI

Petr Jelínek, František Mikšovský, Jaroslav Beňo, Eliška Adámková

VŠB-Technical University of Ostrava, Faculty of Metallurgy and Materials Engineering, Department of Metallurgy and Foundry, Ostrava, Czech Republic
jaroslav.beno@vsb.cz

Prejem rokopisa – received: 2012-08-30; sprejem za objavo – accepted for publication: 2013-03-20

The aim of this study is to describe the possibilities of using salt cores for gravity, low-pressure or high-pressure die-casting technology. Determinations of the primary, secondary and final residual strengths were carried out in order to evaluate the possibilities of the salt-core utilization. Furthermore, this contribution is focused on developing composite salts with better mechanical properties. The solubility of these cores and a possibility of their reclamation in a closed cycle with positive impacts on the environment were also studied.

Keywords: salt cores, inorganic salts, die casting, PUR Cold-Box, Warm-Box, core solubility and stability

Namen te študije je opisati možnosti uporabe slanih jeder pri gravitacijski, nizkotlačni in visokotlačni livarski tehnologiji. Izvršeno je bilo določanje primarnih, sekundarnih in končnih zaostalih napetosti, da bi ocenili uporabnost slanih jeder. Poleg tega je prispevek usmerjen na razvoj kompozitnih soli z boljšimi mehanskimi lastnostmi. Preučevana je bila tudi topnost jeder in možnosti njihove predelave v zaprti zanki s pozitivnim učinkom na okolje.

Ključne besede: slana jedra, anorganske soli, tlačno litje, PUR Cold-Box, Warm-Box, topnost jeder in stabilnost

1 INTRODUCTION

The first salt cores appeared in the foundry industry in the 1970s. An extensive expansion took place in the 1990s in the mass production of Diesel engine pistons. The cores of simple forms (rings) are made from cooking salt (NaCl) by high-pressure compacting and they serve for blank casting of the holes (channels) hardly accessible to mechanical cleaning. They are dissolved in water, which is a precondition for the use in a technologically closed production cycle. Pistons are made by gravity or low-pressure casting in dies. The strength characteristics of the compacted cooking salt meet the requirements regarding the primary strength (the cold strength) and hot strength (650–700 °C) of the cores heated before they are inserted in the mould, which is also necessary for improving the fluidity of Al-alloys. The main advantages of this technology are as follows:

- dimensional accuracy and smoothness of the castings without the use of protective coats;
- solubility of the cores in water and possible recyclability of the salts and water;
- environmentally friendly core production;
- sufficient storage ability of the cores under common climatic conditions.

When changing to more complex and shape-demanding cores with a possibility of an additional functioning, using an increased press and dynamics of the metal injected into the mould (the high-pressure casting), the research focuses, above all, on improving the mechanical properties, not only the primary strengths under high

temperatures, but also the residual (secondary) strengths after a thermal exposure, which have recently drawn a lot of attention. More efficient ways of a core production, different from the compacting processes, are searched for.^{1,2}

For the blank casting of simple holes the high-pressure casting technology uses metal cores, in addition to the sand ones, made with the PUR COLD-BOX technology or the Combicore system,³ and the aluminium channels filled with a salt mixture (cleaned with water). Though sand cores (PUR COLD-BOX) allow blank casting of the holes with highly intricate shapes, low strengths and the possibilities of penetrating the base sand grains in the alloy and, above all, a bad collapsibility after the casting, are their disadvantages. Especially with the new applications of die-casting technologies (e.g., the master squeeze) lowering the temperature of the injected alloy, the perfect thermal destruction of the core polyurethane binder is not followed by difficult cleaning.

2 PRESENT TRENDS IN THE SALT-CORE MANUFACTURE

2.1 Cast cores from molten salts

The salt melt is cast in core boxes and to prevent the moistening, the crystallized cores are stored in an oven (a minimum of 200 °C). A contraction and volume shrinkage occur during solidification. High density (minimum porosity) prevents the dissolution in the water and, therefore, the cast cores are difficult to remove. To

eliminate the shrinkage, a mixture of salts and sand is recommended. Then the melt (820 °C) is cast in a core box under pressure.

2.2 High-pressure compacting of salts

A mildly moistened salt is compacted under high pressure. The cores are then strengthened by way of a mechanical deformation of the grains (conglomeration) and a recrystallization along the grain boundaries. Compacting takes place either under low pressures (30.0–50.0 MPa) and at the heating temperatures of 500–750 °C or under high compacting pressures (136.0–362.8 MPa) and lower sintering temperatures (180–300 °C), allowing a stress release.

2.3 Shooting in core boxes using the binders

After the core shooting (6 bars), the mixture with inorganic binders (alkali silicates) is hardened either with the aid of CO₂ or with thermal dehydration (180–210 °C). In the case of organic binders (synthetic resins) the cores are hardened with the core-box heat (Warm-Box, 150–300 °C). A possibility of applying common processes and equipment to the production of sand cores is an advantage. A higher porosity of salt cores (25–35 %) enables even dissolution in water though the bending strength is 2–3 times lower than that of the compacted cores.

All the mentioned processes, using cooking salt (NaCl), show a relatively low strength and they do not meet the requirements for the cores for high-pressure castings. The research was, therefore, aimed at applying the high-pressure compacting and improving the strength characteristics of the cores (the bending strength) by studying the compacting conditions, the choice of inorganic salts and their different mixtures, the influence of the salt-crystal shapes, granulometry and, above all, the composite salts with additives, as well as the hydration and kinetics during dissolution of the cores in water.

3 INFLUENCING THE STRENGTHS OF THE SALT CORES COMPACTED UNDER HIGH PRESSURES

The main criterion was the bending strength measured with an adapted universal apparatus LRu-2e (MULTISERVIS MOREK, PL). We measured both primary strengths, the cold strength and the strength under high temperatures (650 °C), and the residual (secondary) cold strength after the thermal exposure (650 °C, 1 h). Primary strengths were evaluated after 48 h, after the compacting had been completed and the second phase of hardening – recrystallization of salt-grain boundaries – began (Figure 1).

The moisture content of the salts plays a role in the initial phases of the strengthening (a lower moisture provides for a higher primary strength) but after a longer

storing time the influence of different moisture contents is balanced (Figure 2).

The basic tests were done on the chemically pure salts of KCl and NaCl with the granulometry as follows: D10 = 72.6–73.4 μm, D50 = 188–189 μm, D90 = 367–370 μm, using a FRITSCH-ANALYSETTE 22 MICRO Tcplus – isopropanol medium.

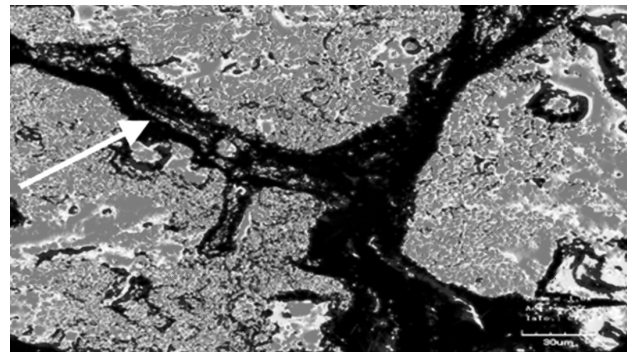


Figure 1: Grain boundaries after the KCl squeezing ($\rho = 1.85 \text{ g cm}^{-3}$, bending strength = 8.8 MPa)

Slika 1: Meje zrn po stiskanju KCl ($\rho = 1,85 \text{ g cm}^{-3}$, upogibna trdnost = 8,8 MPa)

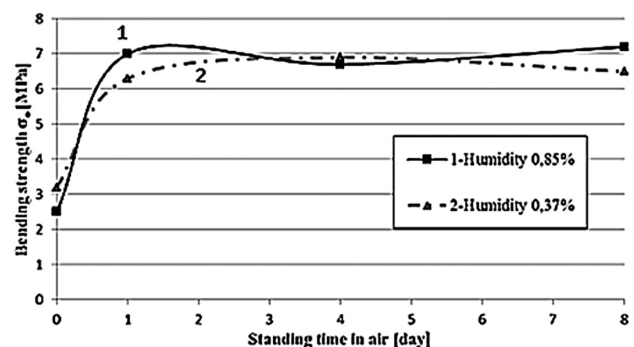


Figure 2: Course of the KCl compacting with different moisture contents after squeezing with a compression power of $100 \cdot 10^3 \text{ N}$ (23 °C, RV 65 %)

Slika 2: Potek kompaktiranja KCl z različno vsebnostjo vlage, po stiskanju s silo $100 \cdot 10^3 \text{ N}$ (23 °C, RV 65 %)

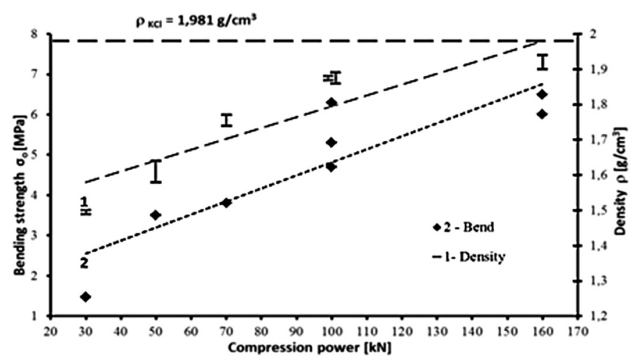


Figure 3: Influence of compression power on density and bending strength of KCl samples ($d_{50} = 190 \mu\text{m}$; humidity of 0.87 %)

Slika 3: Vpliv sile stiskanja na gostoto in upogibno trdnost vzorcev iz KCl ($d_{50} = 190 \mu\text{m}$; vlaga 0,87 %)

The influence of the compacting force ($30 \cdot 10^3$ – $160 \cdot 10^3$ N) on the bending strength and density of the cores were evaluated, too (**Figure 3**).

The bending strength grows with the compacting force up to the value of 6.5 MPa, with a simultaneous growth of density (**Table 1**). If the density of the crystalline KCl salt (1.981 g cm^{-3}) is taken as the base, then the so-called seeming porosity m can be determined as follows:

$$m = \frac{\rho_{\text{KCl}} - \rho_{\text{core}}}{\rho_{\text{KCl}}} \cdot 100\% \quad (1)$$

where:

m – porosity (%)

ρ_{KCl} – density of KCl (g cm^{-3})

ρ_{core} – density of the core (g cm^{-3})

Table 1: Comparison of the primary strengths of KCl after squeezing with different compression tensions

Tabela 1: Primerjava primarne trdnosti KCl po stiskanju z različnimi tlačnimi napetostmi

Compression power	$50 \cdot 10^3$ N		$100 \cdot 10^3$ N		$160 \cdot 10^3$ N	
Compression tension	28 MPa		56 MPa		87 MPa	
Salt	<i>BS</i>	<i>D</i>	<i>BS</i>	<i>D</i>	<i>BS</i>	<i>D</i>
KCl	4.65	1.68	5.53	1.90	6.5	1.94

Note: *BS* – bending strength (N mm^{-2}); *D* – density (g cm^{-3})

or the compacting force of $160 \cdot 10^3$ N $m = 2.06 \%$. The growth from $100 \cdot 10^3$ N up to $160 \cdot 10^3$ N does not significantly reflect on the primary strength nor on the density. A decrease in the seeming porosity from 4 % to 2 % is not significant either. The achieved strengths exceed multiple times the strength of the sand cores made with the PUR COLD-BOX technology.

4 HOT STRENGTH AND THE RESIDUAL STRENGTH

The chosen temperature ($650 \text{ }^\circ\text{C}$, 0.5 h and 1 h) corresponded to the temperatures of heating the cores when inserting them in the dies for gravity casting of the

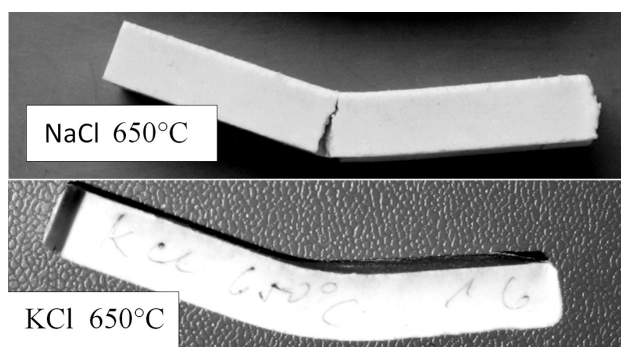


Figure 4: Plastic deformation of salt samples

Slika 4: Plastična deformacija slanih vzorcev

pistons. It is also the temperature that strengthens the cores for possible mechanical work. A comparison of the results of primary and residual strengths of the cores compacted with different forces is given in **Table 2**. The cores from NaCl, under the same compacting conditions, always had substantially lower primary strengths than the KCl cores (**Table 3**), even with the same densities.

Table 2: Comparison of primary strengths of KCl after squeezing with different compression tensions

Tabela 2: Primerjava primarne trdnosti KCl po stiskanju z različnimi tlačnimi napetostmi

Salt	<i>M</i>	<i>A</i>	<i>ST</i>	<i>CP</i>	<i>BS</i>	<i>D</i>
	%	h	h	10^3 N	MPa	g cm^{-3}
KCl	1.2	0.5	24	50	3.53	1.58–1.64
					3.44*	1.72
	0.87	1.0	72	100	5.41	1.71–1.75
					4.73*	1.71

Note: *M* – moisture; *A* – annealing at $650 \text{ }^\circ\text{C}$; *ST* – storage time; *BS* – bending strength,* – primary *BS*; *D* – density

Table 3: Comparison of the primary strengths of KCl and NaCl cores made at a constant compression power

Tabela 3: Primerjava primarne trdnosti KCl in NaCl s konstantno tlačno silo

Salt	<i>M</i>	<i>A</i>	<i>ST</i>	<i>CP</i>	<i>PBS</i>	<i>D</i>
	%	h	h	10^3 N	MPa	g cm^{-3}
KCl	0.87	1	72	100	6.77	1.86–1.88
NaCl	0.83	1	72	100	3.69	1.87–1.89

Note: *M* – moisture; *A* – annealing at $650 \text{ }^\circ\text{C}$; *ST* – storage time; *PBS* – primary bending strength; *D* – density

Different behaviour was especially evident during the evaluation of hot strengths. While the cores from KCl showed a plastic state at $650 \text{ }^\circ\text{C}$, cracks were formed in the cores from NaCl (**Figure 4**).

The reason for different behaviours of the cores from KCl and NaCl was not found in the physical or chemical properties of both salts (**Table 4**).

Table 4: General properties of used salts

Tabela 4: Splošne lastnosti uporabljenih soli

Properties of salts	KCl	NaCl	
Molar mass	g mol^{-1}	74.551	58.443
Melting point	$^\circ\text{C}$	770.3	801
Boiling point	$^\circ\text{C}$	1411	1413
Density	g cm^{-3}	1.981	2.163
Water solubility	$20 \text{ }^\circ\text{C}$, $\text{g}/100 \text{ ml}$	34.19	35.86
Crystal lattice edge	pm	$a = 693$	$a = 562.7$
Crystal structure	–	cubic	cubic

The principal difference is found between the crystal shapes of both salts. While KCl had a homogeneous granularity of a regular cubic form (**Figure 5**), NaCl typically consisted of oval crystals (**Figure 6**).

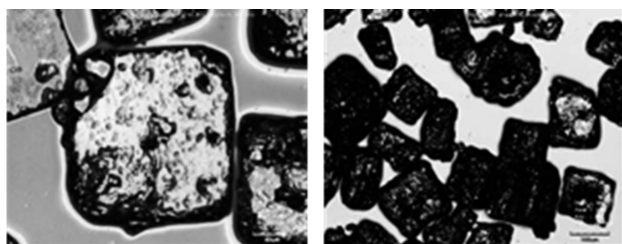


Figure 5: KCl crystals
Slika 5: Kristali KCl

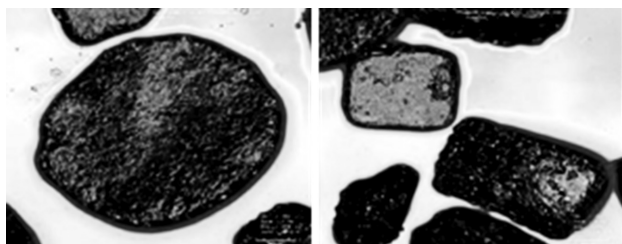


Figure 6: NaCl crystals
Slika 6: Kristali NaCl

Differences in the salt-grain shape were also confirmed with the measurement of the mean roundness related to the volume of the particles, for NaCl: SPHT3 = 0.906; for KCl: SPHT3 = 0.778. A similar dependence of the salt-core strengths on the crystal shape was confirmed by C. R. Loper.⁴

The integrity failure (the crack) in the NaCl sample runs through the salt crystals under the influence of a high grain equivalent (Figure 7). Different properties of both samples can also be identified with the aid of morphology of the fracture surfaces. The surface of KCl is compact without any pores or cracks (Figure 8).

5 COMPOSITE SALTS

Up to this time we worked with pure salts (KCl, NaCl) and the mixtures with other inorganic salts (K_2CO_3 , Na_2CO_3 , $MgSO_3$, Na_2SO_4). However, even with the highest compacting forces ($160 \cdot 10^3$ N) we could not obtain the cores with the mechanical properties that would meet the requirements for the applications of high-pressure casting.

For this reason we proceeded to develop composite salts. Very fine particles with defined granulometry of

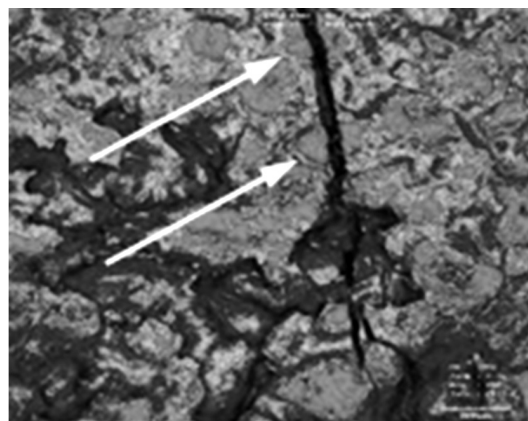


Figure 7: Crack in the NaCl structure
Slika 7: Razpoka v strukturi NaCl

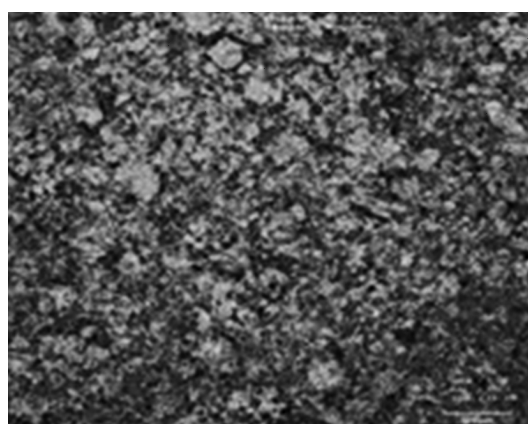


Figure 8: Compact structure of KCl
Slika 8: Zgoščena struktura KCl

different quartz- and non-quartz-based sands were dispersed in pure salts (KCl, NaCl), with the aim of failing the long dislocation lines present in the salt matrix. Three types of additives (marked as A, B, C) in the amounts of up to 30 % of the weight of a salt base were tested. Some partial results are summarized in Table 5.

The results show that with the aid of the composite salts and some additives (base sands) the core strengths can be considerably improved, especially the hot strength (650 °C) – the amounts of the A and B additives were up to 10 %. The composites with the NaCl matrix again show considerably lower strengths than those of KCl. The achieved residual bending strengths in the range of 8–9 MPa also make it possible to use the me-

Table 5: Strengths of composite salts
Tabela 5: Trdnost kompozitnih soli

KCl 100 · 10 ³ N	A/%			B/%			C/%			NaCl 100 · 10 ³ N	C/%		
	0	10	30	0	10	30	0	10	30		0	10	30
after 48 h (MPa)	7.53	7.93	3.72	7.63	8.11	1.93	6.47	7.21	6.79	after 48 h (MPa)	3.63	4.26	3.77
Hot strength 650 °C, 1 h (MPa)	>8.9	13.16	4.44	8.89	10.14	1.62	8.05	8.92	9.01	Hot strength 650 °C, 1h (MPa)	5.33	2.89	1.35
Residual strength 650 °C, 1 h (MPa)	8.49	8.66	3.91	6.84	9.94	6.02	7.88	7.78	8.06	Residual strength 650 °C, 1h (MPa)	2.55	6.80	1.15

chanical working of the cores, while the hot strengths of 10–13 MPa give hopes that these cores can be used for high-pressure castings.⁵

6 CONCLUSION

In the technology of salt-water soluble cores both new salt mixtures and their manufacturing processes meeting highly demanding conditions of high-pressure casting, especially of the automotive castings, are searched for. High primary strengths and the strengths under high temperatures (substantially higher than that of PUR COLD-BOX) give possibilities of treating the cores by mechanical working. It turns out that utilization under high pressure, especially when using composite salt mixtures, can be taken into account, too.

Shooting the salt cores with inorganic or organic binders in hot-core boxes (WARM-BOX) is a topic for the next research that could contribute to more extensive applications of wasteless foundry technology.

Acknowledgement

The research was done with the financial support of the Technological Agency of the Czech Republic within the Alfa Programme, TA 02011314.

7 REFERENCES

- ¹ P. Stingl, G. Schiller, Leichte und rückstandsfreie Entkernung, Gießerei Erfahrungsaustausch, (2009) 6, 4–8
- ² M. Dobosz et al., Development tendencies of moulding and core sands, China Foundry, 8 (2011) 4, 438–446
- ³ F. Heppes, Combicore, Giesserei, 98 (2011) 8, 69
- ⁴ C. R. Loper et al., The use of salt in Foundry Cores, AFS Transaction, 85–82 (1985), 545–560
- ⁵ P. Jelínek et al., Ovlivňování pevnostních charakteristik solných, ve vodě rozpustných jader, Slévárenství, 55 (2012) 3–4, 85–89

EFFECT OF THE ABRASIVE GRIT SIZE ON THE WEAR BEHAVIOR OF CERAMIC COATINGS DURING A MICRO-ABRASION TEST

VPLIV VELIKOSTI BRUSNIH ZRN NA VEDENJE KERAMIČNIH PREVLEK PRI MIKROABRAZIJSKEM PREIZKUSU OBRABE

Mehmet Horik Korkut¹, Yılmaz Küçük², Abdullah Cahit Karaoğlanlı³, Azmi Erdoğan³, Yusuf Er⁴, Mustafa Sabrı Gök³

¹Department of Metallurgy Education, Firat University, 23100 Elazığ, Turkey

²Department of Mechanical Engineering, Bartın University, 74100 Bartın, Turkey

³Department of Metallurgy and Materials Engineering, Bartın University, 74100 Bartın, Turkey

⁴Gazi Vocational High School, Section of Machine Technologies, 06500 Ankara, Turkey
aerdogan@bartin.edu.tr

Prejem rokopisa – received: 2012-08-31; sprejem za objavo – accepted for publication: 2013-03-25

Micro-abrasion tests are commonly used to perform the wear tests on hard coatings. In this study, AISI 1040 mild-steel specimens were coated with ceramic coatings including oxides with different hardness values. The free-ball micro-abrasion testing method was used to examine the wear behavior of the ceramic surfaces over different test durations. The coating-hardness measurements were carried out with a micro-hardness tester. In the experimental studies, the SiC abrasive particles with three different grain sizes (800, 1000 and 1200 mesh), were used to explore the effect of the abrasive particle size on the wear ratio of ceramic coatings. The abrasive effect of the SiC particles in the abrasive slurry was evaluated by examining the SEM micrographs of the coating surfaces. According to the test results, the sample surface coated with Cr₂O₃ exhibited a higher wear resistance than those covered with Al₂O₃ and its compositions with TiO₂. It can also be concluded from the results that an increase in the percentage of the TiO₂ powders in the Al₂O₃ mixture leads to a decrease in the wear resistance.

Keywords: micro-abrasion, ceramic coating, abrasive grain size

Za preizkušanje obrabe trdih prevlek se navadno uporablja mikroabrazijski preizkus. V tej študiji so bili vzorci mehkega jekla AISI 1040 prevlečeni s keramično prevleko iz različno trdih oksidov. Za ugotavljanje vedenja keramičnih površin pri obrabi z različnim trajanjem preizkusa je bila uporabljena metoda mikroabrazijskega preizkusa s tremi prostimi krogli. Trdota prevleke je bila izmerjena z merilnikom mikrotrodote. Pri eksperimentih so bili za ugotavljanje vpliva velikosti abrazijskih delcev na obrabo keramične prevleke uporabljeni abrazijski delci SiC s tremi različnimi velikostmi (zrnatost 800, 1000 in 1200). Abrazijski učinek SiC-delcev in abrazijskih odpadkov je bil ocenjen in preiskan s SEM-posnetki površine prevleke. Glede na rezultate imajo vzorci, prekriti s Cr₂O₃, večjo odpornost proti obrabi kot vzorci z Al₂O₃ in njihova kombinacija s TiO₂. Iz rezultatov se lahko tudi ugotovi, da povečanje deleža TiO₂ v mešanici z Al₂O₃ povzroči zmanjšanje odpornosti proti obrabi.

Ključne besede: mikroabrazija, keramična prevleka, velikost abrazijskih zrn

1 INTRODUCTION

Generally, the coatings used for improving the performance of industrial parts are available in various types, ranging from hard coatings with high abrasion resistance to soft, lubricating coatings and applications requiring low friction coefficients.¹

Ceramics stand out in the friction and abrasion applications in the industry on account of their high hardness, high chemical stabilities, high oxidation-resistance values, high temperature- and thermal-barrier features. However, the high costs involved in their manufacturing and their brittle characteristics limit the use of ceramics. For these reasons, ceramics are preferred for the formation of anti-abrasive layers, applied with thermal-spray methods rather than being used as bulk materials.² For years, various metallic and ceramic coatings have been applied on materials in order to form abrasion-resistant surface layers using the powders sized between 10–100 μm with thermal-spray methods.³ The essence of the atmospheric-plasma-spray (APS) method, which is a

thermal-spray-coating method, is to form a plasma jet for melting the powder material. Powder particles are injected by means of a protective gas and the powders derive their speed and temperature from the plasma jet via the thermal and kinematic transfer. The particulates form abrasion-resistant, rapidly stiffening and thin layers on the surface to be coated.⁴⁻⁷

The micro-scale abrasion test is implemented successfully in assessing the abrasive performances of various materials. This technique is applied on metallic and non-metallic bulk and coating materials along with various abrasive slurry media.⁸⁻¹¹ The abrasion crater obtained in this way is measured with optical or profilometric methods and thus the abrasion results are evaluated in terms of the volume and abrasion mechanisms.¹²⁻¹⁴ The ceramic coatings such as Cr₂O₃, Al₂O₃ and TiO₂ applied with the thermal-spray method were examined tribologically at high temperatures as well as at room temperature, in dry and lubricant sliding conditions.² However, there are not enough studies for an

abrasion analysis of the mentioned ceramic coatings by means of the micro-abrasion technique. For this reason, in this study, the abrasion behaviours of the Cr_2O_3 , Al_2O_3 , $\text{Al}_2\text{O}_3 + 13\% \text{TiO}_2$ and $\text{Al}_2\text{O}_3 + 40\% \text{TiO}_2$ coatings were examined using the micro-abrasion test.

2 MATERIALS AND METHOD

In this study, the AISI 1040 steel with a diameter of 20 mm and length of 50 mm was selected as the substrate material. Firstly, the surface was cleaned of the unwanted residues (oil, dust and residual metals) with a blasting process to achieve a certain roughness value. After this process, the powders with a composite rate of 80 % Cr and 20 % Ni and baked at 100 °C were applied to the substrate material so as to form an intermediate surface with a thickness of 30 μm . The aim of this process is to ensure that a stronger bond is established between the substrate surface material and the ceramic coating material. Finally, the ceramic-powder coatings were applied, in two stages, on the substrate surfaces using the plasma method. The coating thickness was about 150 μm and the process parameters used are shown in **Table 1**. In accordance with the mixture composition of the ceramic powders, different hardness values for the ceramic coatings were obtained (**Table 2**). The SEM micrographs regarding the Cr_2O_3 and Al_2O_3 coatings that include 40 % of TiO_2 are given in **Figures 1** and **2**, respectively.

Table 1: Atmospheric-plasma-spraying conditions

Tabela 1: Pogoji pri naprševanju v atmosferski plazmi

Arc flow rate	80–100 L min ⁻¹
Arc pressure	0.689 MPa
Auxiliary gas flow rate	5–15 L min ⁻¹
Auxiliary gas pressure	0.345 MPa
Spray rate	2.7–6.8 kg/h
Arc voltage	61–68 V
Arc current	400–600 A
Spray distance	70–100 mm

Table 2: Hardness values of the coatings

Tabela 2: Trdota prevlek

Coating material	Hardness (Hv)	Roughness ($R_a/\mu\text{m}$)
Cr_2O_3	960	0.353
Al_2O_3	820	0.326
$\text{Al}_2\text{O}_3 + 13\% \text{TiO}_2$	730	0.237
$\text{Al}_2\text{O}_3 + 40\% \text{TiO}_2$	630	0.250

The aim of the micro-abrasive wear test is to generate "the wear craters" on the specimen. So, one can calculate the wear volume (V), using the crater depth (h) and the crater diameter (b)^{15,16} after the wear tests. The volumetric mass-loss value can be calculated using both the crater radius and the crater height. The formulas required for the calculations are clearly specified in¹⁷.

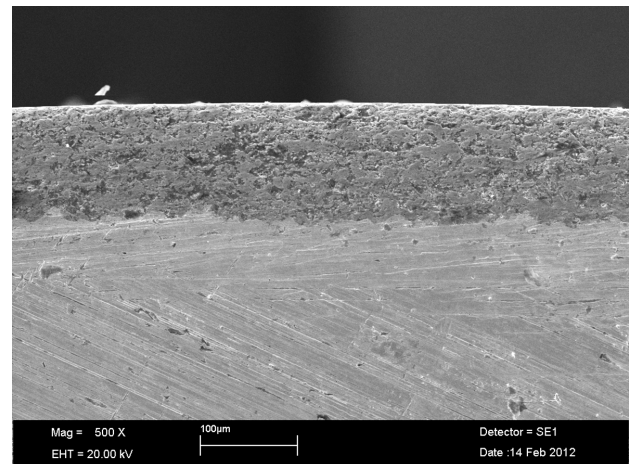


Figure 1: Cross-section of the Cr_2O_3 coating layer
Slika 1: Prečni prerez prevleke iz Cr_2O_3

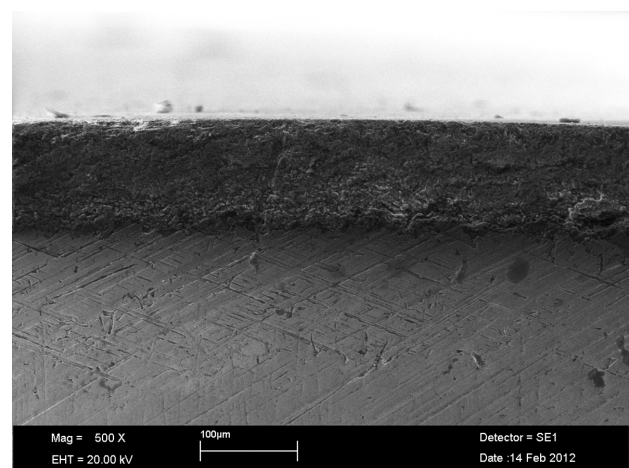


Figure 2: Cross-section of the $\text{Al}_2\text{O}_3 + 40\% \text{TiO}_2$ coating layer
Slika 2: Prečni prerez prevleke iz $\text{Al}_2\text{O}_3 + 40\% \text{TiO}_2$

After the coating process, the free-ball micro-abrasion wear test was applied to each sample. The free-ball micro-abrasion method is a simple test technique for determining the wear behavior of coatings and is explained in detail in some studies.^{15,18–20} The ball used in this test was made from the AISI 52100 steel and had a diameter of 25.4 mm. Silicon carbide (SiC) was used as the abrasive with three particle sizes (800, 1000 and 1200 mesh). The abrasive slurry that was created was composed of 25 % of SiC and 75 % of distilled water. Each test was repeated three times. During the tests, the abrasive slurry droplet was implemented as one drop per 20 seconds. To determine the experimental test combinations, the abrasive grit size, the test duration, the coating material and the spindle speed were selected as the test factors (**Table 3**). Each factor has three levels except for the coating material that has four levels. A total of forty-five test combinations were carried out in accordance with the factorial design. Conventional characterization techniques, such as scanning electron microscopy (SEM), micro hardness and X-ray diffraction, were

employed to study the microstructure of the coating zone.

Table 3: Factors and their levels

Tabela 3: Dejavniki in njihova veličina

Factor	Level 1	Level 2	Level 3	Level 4
Coating material	Cr ₂ O ₃	Al ₂ O ₃	Al ₂ O ₃ + 13 % TiO ₂	Al ₂ O ₃ + 40 % TiO ₂
Abrasive grit size (mesh)	800	1000	1200	
Test duration (min)	1	2	3	
Spindle speed (r/min)	115	160	230	

3 RESULTS AND DISCUSSION

After the micro-abrasion tests, the volumetric wear values were calculated and so, the influence of each test factor on the results could be determined using an ANOVA table (**Table 4**).

The wear loss values for all parameters are given in **Table 5**. The factors that have significant effects on the mass-loss value of the coatings were determined by analyzing the ANOVA table. Hence, from the ANOVA table, the significance of the factors, according to their effects on the mass-loss values, can be presented in a descending order such as the grit size, the test duration and the coating material. However, the spindle speed does not have a significant effect on the wear behavior, if the selected confidence interval is 95 %. This case can be attributed to the reduced effect of free-mass weight of steel ball with increasing the tangential velocity. Increasing the tangential velocity also leads to a decrease in abrasive effect by applying lower pressure to the surface of coating. The effects of the abrasive grit size and the coating-material factors on the mass loss are given in **Figure 3**.

The volumetric mass-loss values increased in all the samples as a function of the increasing abrasive particle size. Additionally, it was observed that the Cr₂O₃ coating exhibited the lowest degree of abrasion due to its high hardness values contrary to the expectation. This case can be explained by taking into account both the surface roughness and hardness values of coated samples (**Table**

Table 4: ANOVA table for the main factors

Tabela 4: Tabela ANOVA glavnih dejavnikov

Factor	Degree of freedom	Sum of squares	Mean square	F value	Prob>F
Model	9	4.084E-03	4.538E-04	9.24	<0.0001
Material	3	9.217E-04	3.072E-04	6.26	0.0016*
Spindle speed	2	3.012E-04	1.506E-04	3.07	0.0592
Duration	2	9.419E-04	4.710E-04	9.59	0.0005*
Grit size	2	2.031E-03	1.016E-03	20.69	<0.0001*
Residual	35	1.719E-03	4.911E-05		
Corrected total	44	5.802E-03			

*significant factor

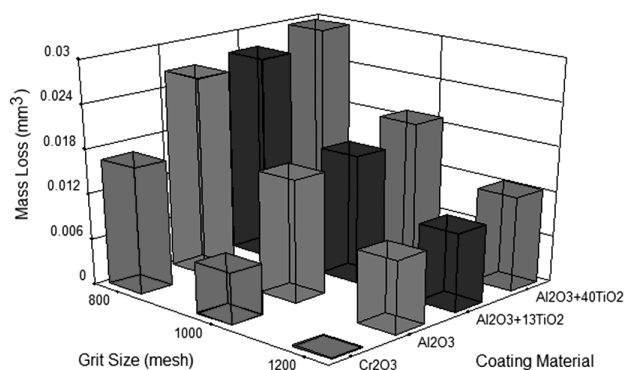


Figure 3: Effect of the abrasive grit size vs. the coating material on the mass loss

Slika 3: Vpliv velikosti zrn abrazijskega sredstva in materiala prevleke na izgubo mase

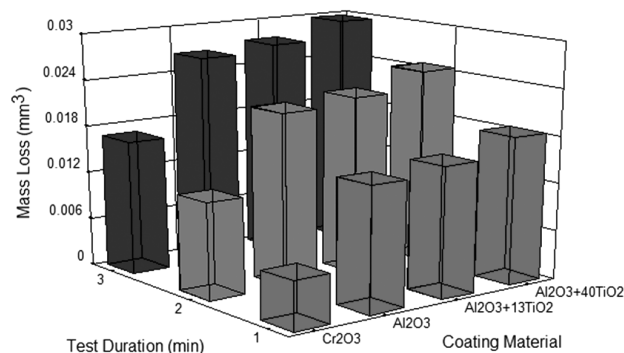


Figure 4: Effect of the abrasive grit size vs. the coating material on the mass loss

Slika 4: Vpliv velikosti zrn abrazijskega sredstva in materiala prevleke na izgubo mase

2), it was observed, contrary to the expectations, that the Cr₂O₃ coating exhibited the lowest degree of abrasion due to its high hardness values. As it is well-known, hardness is one of the most important parameters in increasing the resistance to abrasion. On the other hand, the surfaces with high roughness and hardness values need to be abraded more as they have low rates of toughness. However, the abrasive particles fed into the medium in the form of slurry soon filled in the rough surfaces, thus acting as a bed between the free ball and the material, preventing a rapid abrasion of a sample.

Table 5: Volume loss values for all parameters**Tabela 5:** Zmanjšanje volumna za vse parametre

Run	Material	Spindle speed /(r/min)	Duration /min	Grit size mesh	Volumetric mass loss (mm ³)
1	Cr2O3	160	3	1000	0.004794
2	Al2O3+13TiO2	230	3	1000	0.028231
3	Cr2O3	115	1	1000	0.003041
4	Al2O3	160	1	800	0.015952
5	Cr2O3	160	2	800	0.007424
6	Al2O3+40TiO2	160	1	1000	0.012665
7	Cr2O3	115	3	800	0.008543
8	Al2O3+13TiO2	160	2	1000	0.015395
9	Al2O3+13TiO2	115	2	800	0.019840
10	Al2O3+40TiO2	160	1	800	0.016524
11	Al2O3+13TiO2	230	1	1000	0.008543
12	Al2O3+40TiO2	115	1	1200	0.005107
13	Al2O3+13TiO2	115	1	1200	0.003621
14	Al2O3+40TiO2	230	1	1200	0.007531
15	Al2O3+40TiO2	115	3	1000	0.017919
16	Cr2O3	115	2	1200	0.003747
17	Al2O3+40TiO2	160	2	1200	0.005605
18	Al2O3+40TiO2	230	2	800	0.033143
19	Al2O3	115	2	1200	0.002218
20	Al2O3+13TiO2	160	1	1000	0.007748
21	Al2O3+40TiO2	115	1	800	0.009525
22	Al2O3	115	1	1000	0.010870
23	Al2O3+13TiO2	115	3	1000	0.015952
24	Al2O3	160	3	1200	0.001384
25	Al2O3	230	2	800	0.033470
26	Cr2O3	160	1	1200	0.003380
27	Al2O3+40TiO2	160	3	1000	0.017112
28	Cr2O3	230	1	800	0.007009
29	Al2O3+13TiO2	160	1	1200	0.005188
30	Cr2O3	230	2	1000	0.006231
31	Al2O3+13TiO2	160	3	800	0.039037
32	Al2O3+13TiO2	230	2	1200	0.008543
33	Al2O3	230	1	1200	0.002934
34	Al2O3+13TiO2	230	1	800	0.019840
35	Al2O3+13TiO2	115	3	1200	0.009915
36	Al2O3+40TiO2	230	3	1200	0.012197
37	Al2O3	115	3	800	0.032819
38	Al2O3	160	2	1000	0.018125
39	Al2O3	230	3	1000	0.017112
40	Al2O3+13TiO2	115	1	800	0.009784
41	Cr2O3	230	3	1200	0.004281
42	Al2O3+40TiO2	230	3	800	0.059443
43	Al2O3+13TiO2	115	2	1000	0.010729
44	Al2O3+40TiO2	230	1	1000	0.012508
45	Al2O3+40TiO2	115	2	1000	0.015765

The increase in the mass losses as a function of the increasing grit size can be explained as follows: An increase in the size of the abrasive grit causes an increase in the kinetic energy and the contact area of the grit as a function of speed; thereby, the abrasive capacity is increased in a directly proportional way. It is observed that the factor with the second biggest importance is the test duration. An increase in the rate of fresh abrasers along with the extended duration, in accordance with the abrasive slurry dropping frequency (one drop per 20 s),

caused a further loss in the mass (**Figure 4**). Furthermore, the abrasive grits came into contact with a wider area of the sample surface, along with the sliding distance that increased in direct proportion with the test duration.

Thirdly, taking the coating-material factor into account, Cr₂O₃ demonstrated the highest abrasion resistance when compared to the hardness values. Additionally, the hardness value was reduced, along with the

increase in the TiO₂ percentage in the Al₂O₃ content, resulting in an increase in the abrasion amount.

4 CONCLUSIONS

In this study, the wear behaviors of different types of ceramic coatings were evaluated via the micro-abrasion tests. The conclusions can be summarized as follows: Among the specimens, the ceramic coating including Cr₂O₃ has the highest value of hardness. The other coating-hardness quantities, according to their order of magnitude, are pure Al₂O₃, Al₂O₃ + 13 % TiO₂ and Al₂O₃ + 40 % TiO₂.

The most influential factor for the mass loss was the abrasive grit size. The test duration and the coating material were the other effective factors. An increase in the abrasive grit size led to certain differences in the abrasive surface topography. The influence of the plastic deformation of the sample surface with a mesh grit size of 800 is greater than that of 1 200 mesh.

It was observed that the abrasive mechanism changed with the change in the coating composition. The plastic deformation on the surfaces of the Cr₂O₃ and Al₂O₃ coatings was seen to be more prominent, whereas the increase in the rate of TiO₂ in Al₂O₃ brought about a decrease in the hardness, resulting in a reduced plastic-deformation severity and a smoother surface topography. The spindle speed has not much effect on the value of mass loss due to reducing effect of tangential velocity on the pressure applied on surface of coating by the steel ball. The micro-abrasion technique is a method that can be used for comparative assessments, examining the abrasive behaviours of ceramic coatings.

5 REFERENCES

- ¹ P. Cosemans, X. Zhu, J. P. Celis, M. Van Stappen, Development of low friction wear-resistant coatings, *Surface and Coatings Technology*, 174–175 (2003), 416–420
- ² J. E. Fernandez, Y. Wang, R. Tucho, M. A. Martin-Luengo, R. Gancedo, A. Rincon, Friction and wear behaviour of plasma-sprayed Cr₂O₃ coatings against steel in a wide range of sliding velocities and normal loads, *Tribology International*, 29 (1996) 4, 333–343
- ³ J. F. Li, H. Liao, X. Y. Wang, B. Normand, V. Ji, C. X. Ding, C. Coddet, Improvement in wear resistance of plasma sprayed yttria stabilized zirconia coating using nanostructured powder, *Tribology International*, 37 (2004), 77–84
- ⁴ M. Bounazef, S. Guessasma, G. Montavon, C. Coddet, Effect of APS process parameters on wear behaviour of alumina–titania coatings, *Materials Letters*, 58 (2004), 2451–2455
- ⁵ S. Guessasma, M. Bounazef, P. Nardin, T. Sahraoui, Wear behavior of alumina–titania coatings: analysis of process and parameters, *Ceramics International*, 32 (2006), 13–19
- ⁶ S. Guessasma, C. Coddet, Microstructure of APS alumina titania coatings analysed using artificial neural network, *Acta Materialia*, 52 (2004), 5157–5164
- ⁷ Y. Kucuk, Investigation of abrasiveness property of blast furnace slag on ceramic coatings via the abrasive slurry wear method, *Tribology Transactions*, 55 (2012) 6, 762–771
- ⁸ F. Fernandes, A. Ramalho, A. Loureiro, A. Cavaleiro, Mapping the micro-abrasion resistance of a Ni-based coating deposited by PTA on gray cast iron, *Wear*, 292–293 (2012), 151–158
- ⁹ K. Bose, R. J. K. Wood, Optimum tests conditions for attaining uniform rolling abrasion in ball cratering tests on hard coatings, *Wear*, 258 (2005), 322–332
- ¹⁰ A. J. Gant, M. G. Gee, A review of micro-scale abrasion testing, *Journal of Physics D: Applied Physics*, 44 (2011), 073001
- ¹¹ P. H. Shipway, J. J. Hogg, Wear of bulk ceramics in micro-scale abrasion-The role of abrasive shape and hardness and its relevance to testing of ceramic coatings, *Wear*, 263 (2007), 887–895
- ¹² M. J. Ibáñez, J. Gilabert, M. Vicent, P. Gómez, D. Munoz, Determination of the wear resistance of traditional ceramic materials by means of micro-abrasion technique, *Wear*, 267 (2009), 2048–2054
- ¹³ A. Günen, M. Sabri Gök, A. Erdoğan, B. Kurt, N. Orhan, Investigation of micro-abrasion wear behavior of boronized stainless steel with nanoboron powders, *Tribology Transactions*, 56 (2013) 3, 400–409
- ¹⁴ M. F. C. Andrade, R. P. Martinho, F. J. G. Silva, R. J. D. Alexandre, A. P. M. Baptista, Influence of the abrasive particles size in the micro-abrasion wear tests of TiAlSiN thin coatings, *Wear*, 267 (2009), 12–18
- ¹⁵ R. C. Cozza, D. K. Tanaka, R. M. Souza, Friction coefficient and abrasive wear modes in ball-cratering tests conducted at constant normal force and constant pressure – Preliminary results, *Wear*, 267 (2009), 61–70
- ¹⁶ D. A. Kelly, I. M. Hutchings, A new method for measurement of particle abrasivity, *Wear*, 250 (2001), 76–80
- ¹⁷ K. L. Rutherford, I. M. Hutchings, Theory and application of a micro-scale abrasive wear test, *Journal of Testing and Evaluation*, 25 (1997) 2, 250–260
- ¹⁸ W. M. da Silva, Effect of pressing pressure and iron powder size on the microabrasion of steam-oxidized sintered iron, M.Sc. Dissertation, Federal University of Uberlândia, Uberlândia - MG, Brazil, 2003, 98 (in Portuguese)
- ¹⁹ W. M. da Silva, R. Binder, J. D. B. de Mello, Abrasive wear of steam-treated sintered iron, *Wear*, 258 (2005), 166–177
- ²⁰ R. C. Cozza, J. D. B. de Mello, D. K. Tanaka, R. M. Souza, Relationship between test severity and wear mode transition in micro-abrasive wear tests, *Wear*, 263 (2007), 111–116

ACCELERATED CARBIDE SPHEROIDISATION AND REFINEMENT (ASR) OF THE C45 STEEL DURING INDUCTION HEATING

POSPEŠENA SFEROIDIZACIJA IN UDROBNENJE KARBIDOV (ASR) MED INDUKCIJSKIM SEGREVANJEM JEKLA C45

Daniela Hauserova, Jaromir Dlouhy, Zbysek Novy, Jozef Zrnik

COMTES FHT, Prumyslova 995, 334 41 Dobruška, Czech Republic
daniela.hauserova@comtesfht.cz

Prejem rokopisa – received: 2012-09-14; sprejem za objavo – accepted for publication: 2013-04-08

The present research focused on improving the mechanical properties of the C45 structural carbon steel. The microstructure of this material can be transformed, with the accelerated carbide spheroidisation and refinement (ASR) process, to increase the proof stress and ultimate tensile strength, as well as plasticity and toughness. In this study, the heat-treatment cycle was carried out using induction heating, which offers high heating rates. The process consists of rapid heating of the feedstock to the austenitizing temperature, a short hold, cooling down and rapid cycling at around the transformation temperature A_{c1} . Within a short interval of time, of the order of no more than a few minutes, this cycle produces a microstructure of fine ferrite grains with globular carbides. The present paper describes the impact of ASR process parameters on the mechanical properties and microstructure of the C45 steel.

Keywords: induction heating, grain refinement, carbide spheroidisation

Ta raziskava je bila usmerjena v izboljšanje mehanskih lastnosti konstrukcijskega ogljičnega jekla C45. Mikrostruktura tega materiala se lahko spremeni s postopkom pospešene sferoidizacije in udrobnjenja karbidov (ASR), kar poviša mejo plastičnosti, natezno trdnost, kot tudi plastičnost in žilavost. V tej študiji je bil izveden cikel toplotne obdelave z indukcijskim segrevanjem, ki omogoča velike hitrosti segrevanja. Postopek sestavlja hitro segrevanje ogrevanca na temperaturo avstenitizacije, kratko zadržanje, ohlajanje in hitro cikliranje okrog temperature transformacije A_{c1} . V časovnem intervalu – ne več kot nekaj minut – to cikliranje povzroči nastanek mikrostrukture iz drobnih feritnih zrn z globularnimi karbidi. Članek opisuje vpliv procesnih parametrov ASR na mehanske lastnosti in mikrostrukturo jekla C45.

Ključne besede: indukcijsko segrevanje, udrobnjenje zrn, sferoidizacija karbida

1 INTRODUCTION

Grain refinement in steels is a traditional process for enhancing their strength. It is often used in plain carbon steels where the appropriate treatment increases the yield strength and ultimate strength without additional alloying or hardening, thus saving costs.¹ In addition to the grain size, carbide morphology is important with regard to toughness. Where high toughness is required, globular carbides are the right choice, whereas lamellar pearlite is not a suitable type of microstructure. When obtaining the optimum combination of strength and toughness, the ideal microstructure consists of fine ferrite grains and globular carbides.

ASR (Accelerated Spheroidisation and Refinement) is a process producing fine grains and globular carbides throughout the workpiece in a very short time: of the order of no more than a few minutes.² This paper describes the results of an optimization of the ASR process using induction heating. This heating method allows the workpiece temperature to be changed very rapidly in contrast with conventional annealing in a furnace.³

2 EXPERIMENTAL WORK

The experimental material was hot rolled and normalized C45 structural steel. The chemical composition of the steel is listed in **Table 1**. The initial microstructure consisted of pearlite and ferrite with areas of lamellar pearlite (**Figures 1a** and **b**). The ferrite grain size was about 20 μm .

Heat treatment was carried out using a medium-frequency converter. The number of coils of the inductor was selected in such a way as to provide as homogeneous an electromagnetic field as possible in the coil centre, leading to a uniform temperature field. The heating was controlled by a PLC unit and the temperature was measured by means of a pyrometer and thermocouples (**Figure 2**). The heat-treated specimens were 15-mm-diameter bars with a length of 400 mm.

Table 1: Chemical composition of the C45 steel in mass fractions (w/%)

Tabela 1: Kemijska sestava jekla C45 v masnih deležih (w/%)

C	Mn	Si	P	S	Cr	Ni	Mo
0.47	0.70	0.23	0.026	0.017	0.07	0.02	0.007

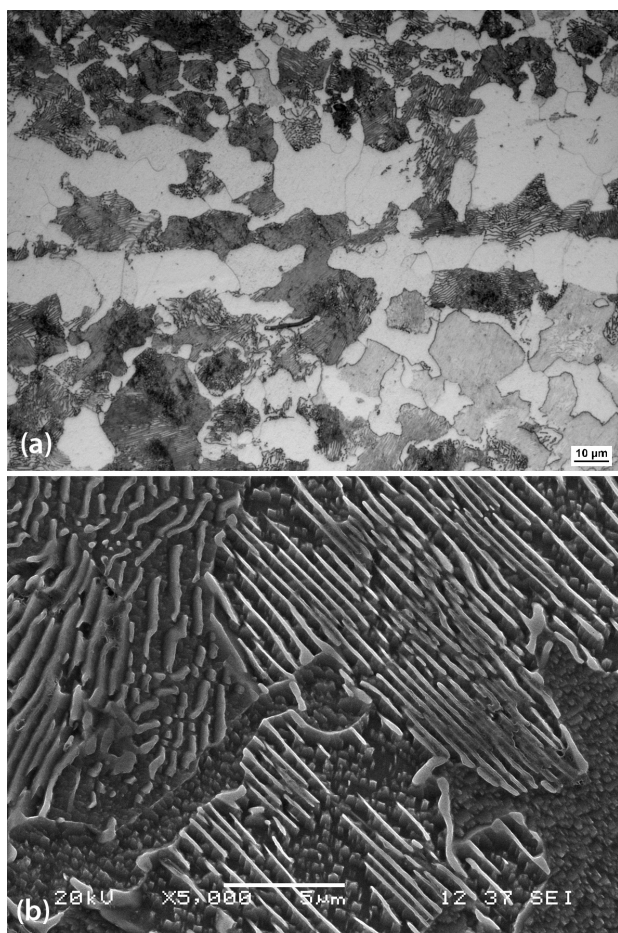


Figure 1: a) Optical micrograph of the initial microstructure, b) scanning electron micrograph of the initial microstructure

Slika 1: a) Svetlobni posnetek začetne mikrostrukture, b) SEM-posnetek začetne mikrostrukture

For the purpose of converting lamellar carbides to a globular morphology, schedules were designed with the temperature cycling at around or slightly above A_{c1} (see **Table 2**). The A_{c1} temperatures for both heating rates were determined from the temperature-time records of

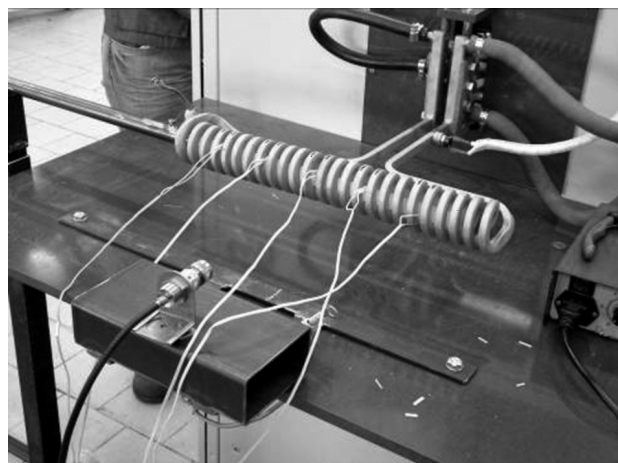


Figure 2: Induction heating of a sample
Slika 2: Indukcijsko segrevanje vzorca

induction heating. A_{c1} for the heating rate of 80 °C/s was 762 °C and for 20 °C/s it was 747 °C. All the schedules comprised rapid induction heating, subsequent rapid temperature cycling and air cooling. Each of schedules 1, 2 and 3 had four temperature cycles. The maximum and minimum cycle temperatures varied. The difference between the maximum and minimum cycle temperatures was 60 °C. In schedule 1, the maximum cycle temperature was 740 °C; in schedule 2, it was 760 °C and in schedule 3, it was 780 °C. These schedules took 200 s, starting with heating and ending with cooling the specimen to 550 °C.

Table 2: List of schedules

Tabela 2: Seznam zaporedja ukrepov

Schedule	Heating rate (°C/s)	Austenitizing (°C)	T_h /°C	T_l /°C	Number of cycles
1	80	–	740	680	4
2	80	–	760	700	4
3	80	–	780	720	4
4	80	840/25 s	–	–	–
5	80	840/25 s	740	670	4
6	80	840/25 s	780	720	4
7	20	–	760	700	4
8	20	–	780	720	4
9	20	840/25 s	780	720	4

Schedule 4 was designed for a microstructure refinement. It comprised austenitizing and the subsequent air cooling, i.e., essentially, a normalizing process. The combined normalizing and carbide spheroidising were intended to create fine ferrite grains with globular carbides (schedules 5 and 6). The austenitizing temperature was 840 °C. Schedule 5 included austenitizing at 840 °C, cooling in air to 600 °C, heating to 740 °C and additional three cycles at around this temperature. Schedule 6 was only different in the cycling temperature that was 780 °C. An overview of the schedules is given in **Table 1**. Schedule 4 took 250 s, while schedules 5 and 6 took about 300 s between the start of heating and cooling to the temperature of 550 °C.

Schedules 7, 8 and 9 were proposed with the aim of finding the influence of the heating rate on the material properties and microstructure. The heating rate was reduced from 80 °C/s to 20 °C/s. Apart from the heating rates, the pairs of schedules 7 and 2, schedules 8 and 3, and schedules 9 and 6 were identical.

3 RESULTS AND DISCUSSION

3.1 Metallography

The temperatures achieved with schedules 1 and 2 were not sufficient for an extensive austenitization of the microstructure. When compared with the initial microstructure, the grain size remained almost unchanged; part of the cementite lamellae in pearlite transformed to rod-like particles.

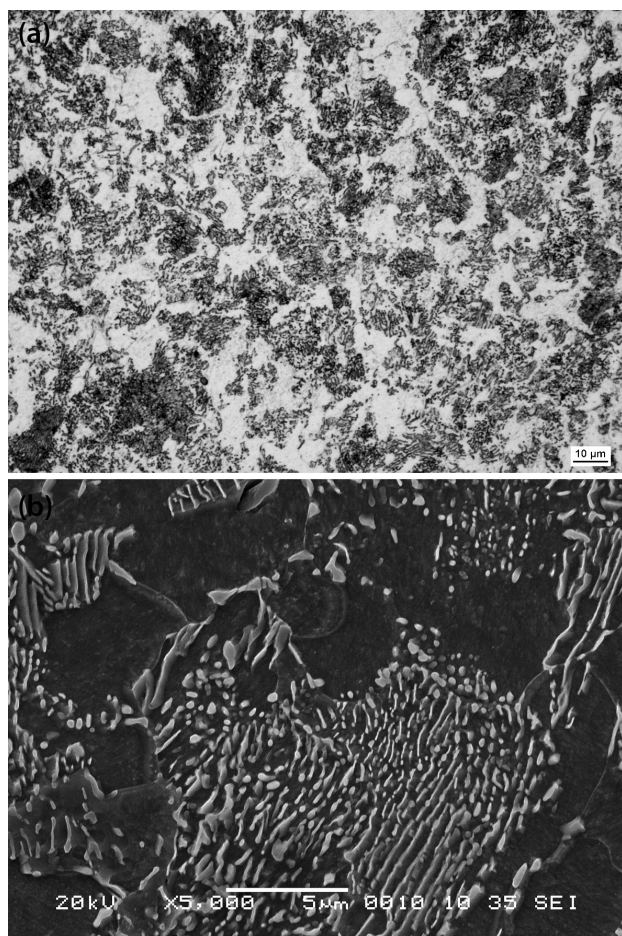


Figure 3: a) Optical micrograph after schedule 3, b) scanning electron micrograph after schedule 3

Slika 3: a) Svetlobni posnetek mikrostrukture po ukrepu 3, b) SEM-posnetek mikrostrukture po ukrepu 3

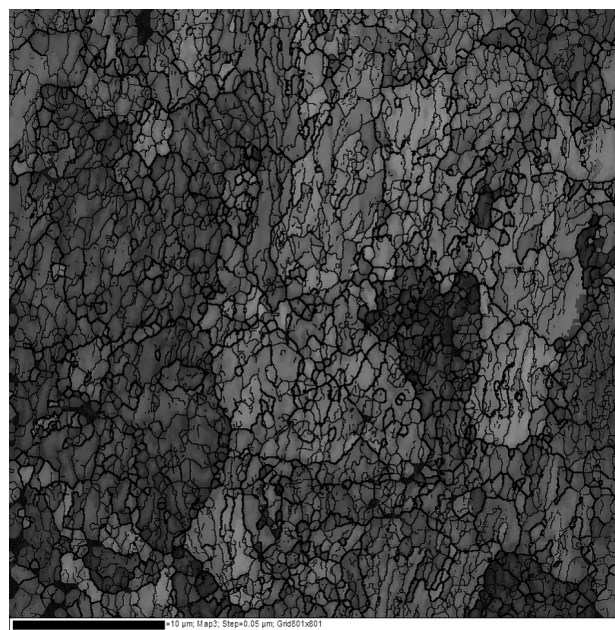


Figure 4: EBSD map with grain boundaries after schedule 5

Slika 4: EBSD-posnetek zrn z mejami zrn po ukrepu 5

The temperature record for schedule 3 showed a temperature hold during cooling, indicating a pearlitic transformation. Temperature cycling, therefore, led to a partial austenitization accompanied by cementite dissolution. Cementite lamellae underwent a partial fragmentation (Figures 3a and b). The micrographs on these figures show a partial spheroidisation of cementite lamellae and a certain expansion of cementite into the ferritic regions.

Schedule 4 led to an almost complete microstructure austenitization. The resulting microstructure consists of ferrite and pearlite. Part of the pearlitic cementite is lamellar and part is spheroidised. Lamellar cementite was probably newly formed. Globular cementite appears to be the original spheroidised cementite that did not dissolve during the schedule. Cooling in air resulted in a rapid eutectoid transformation and the undissolved cementite lamellae acted as a nucleation agent.⁴ It was mainly this schedule that produced considerably refined ferrite grains: from 20 μm to less than 10 μm.

Schedules 5 and 6 were designed as a combination of normalisation and the temperature cycling at around critical temperature A_{c1} . The initial stage of the sche-

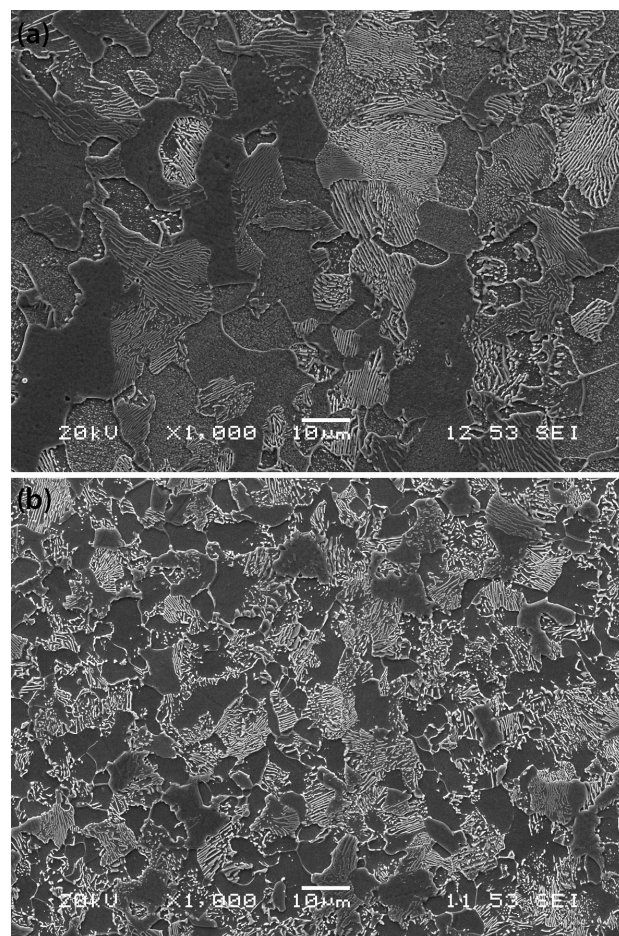


Figure 5: a) Scanning electron micrograph of the initial state, b) scanning electron micrograph after schedule 9

Slika 5: a) SEM-posnetek začetne mikrostrukture, b) SEM-posnetek mikrostrukture po ukrepu 9

dules was intended to refine the grains, whereas the cycles at a lower temperature were to spheroidize the carbides. The microstructures after schedules 5 and 6 were very similar. These schedules led to a grain refinement in the steel producing new carbide regions between the new finer grains, as did schedule 4. The cycling at around A_{c1} fragmented and partially spheroidised the cementite lamellae. The EBSD map (**Figure 4**) shows a substructure of the ferrite grains both in pearlite and ferrite regions. The thick lines represent high-angle boundaries ($>15^\circ$) and the thin lines represent low-angle boundaries (from 2° to 15°).

In the schedules with lower heating rates, the temperature of 760°C (schedule 7) was sufficient for a partial austenitization and a certain expansion of the cementite into ferritic regions to take place. It was due to the fact that, at lower heating rates, transformation start temperatures become lower. A partial austenitization at 760°C is evidenced by the temperature record as well. The temperature records for all the schedules with lower heating rates (schedules 7, 8 and 9) showed a temperature plateau on the cooling curve, indicating a pearlitic transformation. Temperature cycling, thus, leads to a partial austenitization accompanied by cementite dissolution. The cementite lamellae underwent a partial fragmentation and the structure underwent a grain refinement. **Figures 5a** and **b** illustrate a comparison between the scanning electron micrographs of the initial state and the heat-treated sample 9. The heat-treated specimen underwent a grain refinement and a partial carbide spheroidisation (ASR).

3.2 Mechanical Properties

Tension tests were performed on the specimens with the diameter of 8 mm and length of 50 mm. The specimens used for impact testing were of the miniature Charpy type, with the size of $3\text{ mm} \times 4\text{ mm} \times 27\text{ mm}$ and a 1 mm deep V-notch. Hardness values were measured on the Vickers HV30 scale.

In **Table 3** you can see the results of proof stress (PS), ultimate tensile strength (UTS), elongation (A_5), area reduction (RA), impact toughness (KCV) and Vickers hardness (HV). The results for the initial state were: $PS = 309\text{ MPa}$, $UTS = 642\text{ MPa}$, elongation $A_5 = 27\%$, $RA = 47\%$, impact toughness $KCV = 37\text{ J/cm}^2$ and hardness reached 179 HV.

For schedules 1, 2 and 3, the proof stress increased with the growing temperature of the cycles. Schedules 1 and 2 led to a significant increase in the toughness that could have been caused by a recovery of ferrite grains. Schedule 3 did not cause a significant increase in the notch toughness, probably due to a formation of new fine lamellar pearlite.

The specimens treated according to schedule 4 showed a higher proof stress, a slightly higher ultimate strength and a higher toughness. This was due to the

Table 3: Mechanical properties

Tabela 3: Mehanske lastnosti

Schedule	PS/ MPa	UTS/ MPa	$A_5/\%$	RA/%	KCV/ (J cm^{-2})	HV
OS	309	642	27	47	37	179
1	381	645	29	48	99	165
2	387	645	30	49	93	167
3	390	633	32	57	41	169
4	417	653	30	56	52	174
5	431	660	29	55	58	178
6	426	643	32	61	38	174
7	356	613	32	60	61	169
8	403	635	31	58	58	178
9	423	638	32	60	62	180

grain refinement. Schedule 5 led to a similar enhancement of the mechanical properties as schedule 4 but resulting in the highest proof stress and in a higher toughness. The specimens of schedule 6 did not have a higher toughness than the initial material. This might be attributed to the formation of a large amount of new lamellar pearlite during the final cycling at around 780°C and 720°C .

A trend in the proof-stress values was apparent in the specimens treated with the schedules involving the heating rate of 20°C/s or higher heating rates. The proof stress rose upon cycling at around a higher temperature, i.e., 780°C . The specimens that were austenitized and subjected to cycling at around 780°C exhibited an even higher proof stress: 423 MPa. Their ultimate strength was slightly lower or equal to that of the initial material. However, elongation as well as impact toughness increased for all three specimens. The highest impact-toughness and hardness values were found in the specimens for schedule 9. In this case, the impact toughness is higher than that of the specimen treated with the schedule with the highest heating rate. This might be attributed to the lower amount of new cementite lamellae. Despite that the difference in the mechanical properties of the specimens heated at higher and lower rates was not substantial. Hence, no significant impact of the heating rate on the mechanical properties of the material was found.

4 CONCLUSION

Grain refinement and partial carbide spheroidisation were achieved in the AISI C45 steel using induction heating. The temperature cycling at around the A_{c1} temperature was responsible for the change in the cementite morphology. Ferritic grain size was reduced by the austenitization and the following cooling in air. These changes in the microstructure were reflected in an increase in the proof stress, ultimate tensile strength and impact toughness, whereas the elongation value remained unchanged. The proof stress was increased by 120 MPa, the ultimate tensile strength by 20 MPa and

the impact toughness by 20 J/cm^2 in comparison with the initial state. The schedule that led to this improvement in the mechanical properties took about 300 s and consisted of the normalizing and subsequent cycling at around the A_{c1} transformation temperature.

Acknowledgment

The results presented in this paper were obtained within the project West-Bohemian Centre of Materials and Metallurgy CZ.1.05/2.1.00/03.0077, co-funded by the European Regional Development Fund.

5 REFERENCES

- ¹ L. Kraus, S. Nemecek, J. Kasl, Mechanical properties of cast Mn steel after intercritical heat treatment and microalloying, *Transferability of fracture mechanical characteristics*, 78 (2002), 15–32
- ² B. Masek, H. Jirkova, L. Kucerova, Rapid Spheroidization and Grain Refinement Caused by Thermomechanical Treatment for Plain Structural Steel, *Materials Science Forum*, 706–709 (2012), 2770–2775
- ³ A. Kamygabi-Gol, M. Seikh-Amiri, Spheroidising Kinetics and Optimization of Heat Treatment Parameters in CK60 Steel Using Taguchi Robust Design, *Journal of Iron and Steel*, 17 (2010), 45–52
- ⁴ P. R. Howell, The Pearlite Reaction in Steels: Mechanisms and Crystallography, *Materials Characterization*, 40 (1998), 227–260

THE EFFECT OF A STYRENE-ACRYLIC COPOLYMER SYNTHESIZED IN A HIGH-PRESSURE REACTOR ON THE IMPROVED CORROSION PROTECTION OF A TWO-COMPONENT POLYURETHANE COATING

VPLIV STIREN-AKRILNEGA KOPOLIMERA, SINTETIZIRANEGA V VISOKOTLAČNEM REAKTORJU NA IZBOLJŠANJE KOROZIJSKE ZAŠČITE DVOKOMPONENTNEGA POLIURETANSKEGA PREMAZA

Urban Šegedin¹, Klemen Burja², Franci Malin¹, Saša Skale¹, Bogdan Znoj¹, Boris Šket³, Peter Venturini¹

¹Central R&D of Helios Group, Helios Domžale, d. d., Količevo 2, 1230 Domžale, Slovenia

²Centre of Excellence for Polymeric Materials and Technologies, Tehnološki park 24, 1000 Ljubljana, Slovenia

³Faculty of Chemistry and Chemical Technology, University of Ljubljana, Aškerčeva 5, 1000 Ljubljana, Slovenia
urban.segedin@helios.si

Prejem rokopisa – received: 2012-09-28; sprejem za objavo – accepted for publication: 2013-04-02

In the present research the synthesis of a high-solids styrene-acrylic copolymer in a high-pressure reactor is described and a comparison of its properties with those of a copolymer synthesized at atmospheric pressure are given. The described procedure enables the synthesis of styrene-acrylic copolymers with a higher solids content under elevated pressure in a significantly shorter time, when compared to the process conducted at atmospheric pressure. The elevated pressure and higher temperature of the synthesis result in a copolymer with a lower average molecular mass and a narrower molecular mass distribution as well as a lower viscosity of the solution with an equal dry weight. Synthesized copolymers were used for the preparation of the two-component polyurethane coatings for corrosion protection. Cross-linked films were formed with a hexamethylene diisocyanate homopolymer. With electrochemical impedance spectroscopy measurements a higher level of cross-linking and a lower porosity of the two-component polyurethane coating based on styrene-acrylic copolymer synthesized in a high-pressure reactor have been determined. This implies a better anti-corrosion protection of the metal substrates.

Keywords: styrene-acrylic copolymer, high-pressure synthesis, 2K-PUR coatings, electrochemical impedance spectroscopy

V raziskavi je opisan postopek sinteze stiren-akrilnega kopolimera s povečano vsebnostjo suhe snovi pri povišanem tlaku, kar vodi do skrajšanja časa sinteze v primerjavi s postopkom pri atmosferskem tlaku. Podana je primerjava lastnosti kopolimera, sintetiziranega pri povišanem tlaku, in kopolimera, sintetiziranega pri atmosferskem tlaku. Sinteza pri povišanem tlaku in višji temperaturi vodi do manjše povprečne molekulske mase, ožje porazdelitve molekulskih mas ter do nižje viskoznosti raztopine kopolimera pri enaki suhi snovi. Sintetizirana produkta sta bila uporabljena za pripravo dvokomponentnih poliuretanskih premazov za protikorozijsko zaščito. Z uporabo homopolimera heksametilen diizocianata so bili pripravljene zamreženi premazi. Z elektrokemijsko impedančno spektroskopijo je bilo ugotovljeno, da je stopnja zamreženosti premaza s stiren-akrilnim kopolimerom, sintetiziranim pri povišanem tlaku, višja, poroznost pa nižja. To kaže na boljšo protikorozijsko zaščito kovinskih podlag.

Ključne besede: stiren-akrilni kopolimer, sinteza pri visokem tlaku, 2K-PUR premazi, elektrokemijska impedančna spektroskopija

1 INTRODUCTION

Styrene acrylic copolymers (SACs) are widely used in the coatings industry as one of the main components of coating formulations. SACs are part of one-component acrylic as well as two-component polyurethane coatings (2K-PUR). In the latter the SACs represent component A (polyol) that reacts with component B (polyisocyanate) to form polyurethane.¹ The main reaction occurs between the hydroxyl groups of the polyol and the isocyanate groups of the polyisocyanate to give urethanes. Other reactions, leading to the formation of allophanate, amine, urea, biuret and amide linkages¹⁻⁶ are shown in **Figure 1**. The amount of hydroxyl functional (meth)acrylic monomers in the SAC formulation determines the degree of cross-linking, the porosity

and the hardness of the cross-linked 2K-PUR films. When formulating the SAC, at least one hydroxyl functional (meth)acrylic monomer is used. The rest of the monomers are used to control the glass-transition temperature (T_g) and the viscosity or to give additional functionality to the SAC. Styrene is commonly used in formulations for the adjustment of T_g , hardness and the rate of physical drying. In some cases, special monomers like monoglycidyl modified esters, ethylene, propylene and alphaolefins with 7–20 carbon atoms are used to achieve higher solids and lower viscosities for the SAC solutions.²⁻¹⁰

Syntheses are usually performed at the reflux temperature of the organic solvent or the solvent mixture. The possibility of conducting reactions at elevated pressure is

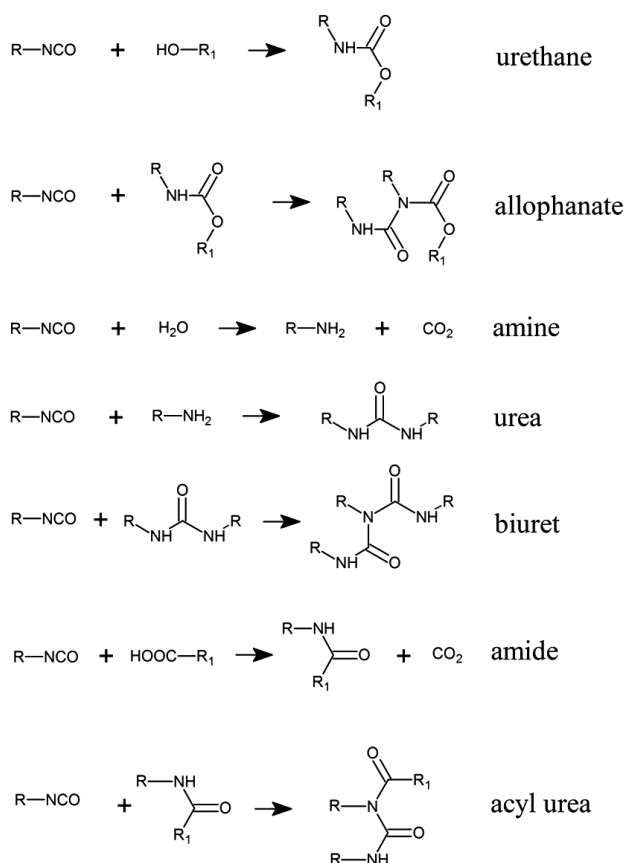


Figure 1: Formation of urethane group and other reactions present during the cross-linking of SAC and polyisocyanate^{1,3}

Slika 1: Nastanek uretanske vezi ter druge reakcije pri zamreževanju SAC in poliizocianata^{1,3}

mentioned in literature, but the syntheses are limited to special, highly volatile or gaseous monomers and no comparison with atmospheric-pressure synthesis has been reported.^{8,9,11,12}

The effects of the process parameters on the properties of SAC are also well known.¹³ The increase of the initiator concentration in the reaction mixture results in a lower average molecular mass (M_w) and faster polymerization rates. The increase in the temperature increases the polymerization rate as well. Higher reaction temperatures reduce the M_w , the molecular-mass distribution (M_w/M_n) and the viscosity.¹³

Solutions of SAC in organic solvents are being replaced by high-solids SACs (HS SACs) as a result of European legislation on volatile organic compounds (VOCs) in coatings (Directive 2004/42/CE). One way is to synthesize the SACs with a lower and less-dispersed M_w . This can be achieved by increasing the initiator concentration, slower dosing, raising the reaction temperature and using a chain-transfer reagent. In most cases the synthesis is performed in the excess solvent and distillation is needed to reach the desired dry weight. In some cases the solvent is distilled off and replaced with a more suitable solvent, and as a result lower solution viscosities are obtained.^{1,2,8-13}

Electrochemical impedance spectroscopy (EIS) is a powerful tool, not only to monitor the degradation of coatings, but also a rapid non-destructive method to assess the quality of protective performance prior to the development of corrosion.¹⁴⁻¹⁶ In the early stages of the coating degradation the coating's capacitance, the Warburg coefficient and the pore resistance are present. The measurements are fitted with equivalent circuits (transmission line model), which describe the charge-transfer mechanisms through the coatings (**Figure 2**). The coating capacitance (C_c) represents the water uptake in the coatings and corresponds to the charge separation on the phase boundaries between the coating and the steel substrate enables ion diffusion through the film matrix. This mechanism of charge transfer is represented by the Warburg coefficient (σ_c). Classical ion conduction through pores filled with an electrolyte solution is represented by the pore resistance (R_{po}).^{14,15,17-27} EIS measurements are usually conducted in the frequency range from 10^{-2} Hz to 10^5 Hz. The results are presented as Bode and Nyquist diagrams. The high quality of 2K-PUR coatings is represented with phase values of over 80° over a wide range of frequencies and the impedance values are mainly determined by the coating's capacitance. The pure capacitor has impedance values over $10^{10} \Omega \text{ cm}^2$, displaying superb barrier properties. With the development of pores phase and absolute impedance values decrease at lower frequencies. Typical impedance values in this case are around $10^7-10^8 \Omega \text{ cm}^2$. The impedance values of the coatings displaying entire loss of corrosion protection are around $10^4 \Omega \text{ cm}^2$.^{16,27}

The aim of the present work is to give a comparison of the polymerization processes at atmospheric and elevated pressure. Random copolymers were synthesized via free-radical polymerization in a semi-batch process. A comparison of the properties of both end-products is presented as well. It is shown that besides a shorter reaction time the quality of cross-linked 2K-PUR films of

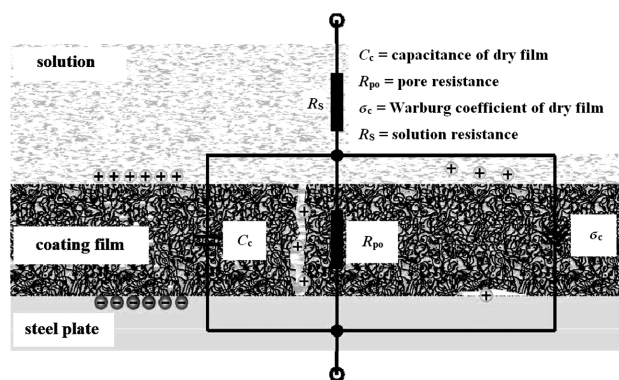


Figure 2: Charge-transfer mechanisms through the coating film during EIS measurements for the porous film prior to the development of corrosion¹⁷

Slika 2: Mehanizmi prenosa naboja preko premaza pri EIS-meritvah za plast z razvitimi porami pred nastankom korozije¹⁷

SAC synthesized in a high-pressure reactor is also improved.

2 EXPERIMENTAL

2.1 Materials

Acrylic acid (AA, Clariant), butyl acrylate (BA, BASF), 2-hydroxypropyl methacrylate (HPMA, Prochema) and styrene (S, Enichem) monomers as well as the heat-sensitive free-radical initiator t-butyl perbenzoate (t-BPB, $t_{1/2} = 10$ h, $T = 104$ °C, Dow) were used for the syntheses of the SACs. Methoxypropyl acetate (MPA, BASF) served as an organic solvent. Hexamethylene diisocyanate homopolymer (HDI homopolymer; Desmodur N75 (D-N75, Bayer)) was used for the preparation of the 2K-PUR coatings.

2.2 Preparation of a monomer mixture for the syntheses of SACs

For the purpose of the present study two styrene-acrylic copolymers suitable for the preparation of the 2K-PUR coatings were synthesized. Both were prepared from the same monomer mixture containing AA, BA, HPMA and S. All the monomers were industrial grade with hydroquinone monomethyl ether (MEHQ) as a stabilizer and were used as delivered without purification. The initiator (t-BPB) was added and the mixture was stirred under mild shear conditions. The composition of the final mixture prepared for dosing is given in **Table 1**.

Table 1: Monomer mixture prepared for syntheses of SACs (mass fraction: $w/\%$; mol fraction: $x/\%$)

Tabela 1: Mešanica monomera, pripravljena za sintezi SAC (masni delež: $w/\%$; molski delež: $x/\%$)

	$w/\%$	$x/\%$
AA	0.8	1.31
BA	30.7	28.36
S	45.5	51.72
HPMA	21.7	17.82
t-BPB	1.3	0.79
Σ	100.0	100.00

2.3 Syntheses of SACs

Both syntheses were carried out in a semi-batch mode on a reaction calorimeter RC1e™ (Mettler Toledo) with iControl software for monitoring and controlling the process parameters.

2.3.1 The synthesis of SAC 1

SAC 1 was synthesized in a 2-L triple-wall glass reactor AP01-2-RTC with temperature sensors, calibration heater, a 4-bladed glass pitch blade stirrer, glass condenser, N₂ purge and a ReactIR 45 m Probe A with an MCT Detector using HappGenzel apodization, a DiComp (diamond) probe connected via a K6 Conduit

(16 mm probe) with a sampling area of 4000 cm⁻¹ to 650 cm⁻¹ at 8 cm⁻¹ wavelength resolution and a sampling interval of 30 s during the synthesis. Online data from FTIR (Fourier Transform Infrared Spectroscopy) measurements was collected and analyzed with iC IR software (Mettler Toledo) in real time. The reactor was filled with 400 g of MPA and heated to 135 °C at atmospheric pressure (below the boiling point of MPA at atmospheric pressure, 145 °C) with a stirring rate of 350 r/min. When the working temperature was reached, 900 g of monomer mixture with an initiator was continuously dosed into the reactor for 3 h using a Prominent Beta/4 solenoid diaphragm metering pump. After the dosing was finished the reaction mixture was kept at the working temperature for an additional 2.5 h.

2.3.2 The synthesis of SAC 2

SAC 2 was synthesized in a 1.8 L stainless-steel high-pressure reactor HP60 at a temperature of 175 °C and elevated pressure. The reactor was equipped with temperature sensors, a pressure sensor, a calibration heater, a stainless-steel anchor stirrer, a N₂ purge and an online FTIR measuring system (as described in the synthesis of SAC 1). The tightly closed reactor was filled with 300 g of MPA and 78 g of monomer mixture with an initiator and heated to 175 °C at 280 kPa of absolute pressure with a stirring rate of 200 r/min. When the working temperature was reached, 668 g of monomer mixture with an initiator was continuously dosed into the reactor for 90 min using a Prominent Beta/4 pump. After the dosing was finished the absolute pressure reached 550 kPa and the reaction mixture was kept at the working temperature for an additional 20 min, after which 15 g of the mass fraction 10 % t-BPB in MPA was dosed in 15 min for residual monomer depletion. After an additional 20 min heating at the working temperature and 570 kPa of absolute pressure the reaction mixture was cooled down and the pressure released.

2.4 Characterization of SACs

The chemical and physical properties of the products were evaluated through standard test methods. Acid-value (AV) measurements were carried out in compliance with the standard EN-ISO-2114, hydroxyl value (OH, EN-ISO-4629), dry weight of copolymer solution in MPA (DW, ISO-3251) and viscosity (η , EN-ISO-3219). The viscosity measurements were performed at 23 °C on a rotational viscometer (Haake Viscotester 550) with a coaxial cylinder sensor system.

2.4.1 Nuclear magnetic resonance (NMR) measurements

The composition of both copolymers and coatings was evaluated via ¹H and ¹³C NMR measurements. 1D ¹H and ¹³C NMR spectra of the SACs, D-N75 and 2K-PURs were recorded at 25 °C on a Unity Inova 300 MHz NMR spectrometer (Agilent Technologies). The ¹H

and ^{13}C chemical shifts were referred to the residual signal of DMSO-d₆ at $\delta = 2.50 \cdot 10^{-6}$ for ^1H and $\delta = 39.50 \cdot 10^{-6}$ for ^{13}C .

2.4.2 Rheological properties

The rheological properties of the SAC solutions (as synthesized and diluted to the mass fraction 50 %) were assessed using a Physica MCR301 rheometer (Anton Paar GmbH). A cone-plate geometry sensor system ($R = 25$ mm, $gap = 0.207$ mm) was used to perform rotational tests where the samples were exposed to increasing shear rates (0.1 s^{-1} to 670 s^{-1}) in the first run and to decreasing shear rates (670 s^{-1} to 0.1 s^{-1}) in the second. In both cases, 29 measuring points on a logarithmic scale were taken.

2.4.3 DSC evaluations

The T_g of dried SACs was determined by differential scanning calorimetry (DSC) on a DSC 1 STAR^e System calorimeter (Mettler Toledo). The SAC samples were heated twice at 20 K/min in the temperature range from $-50 \text{ }^\circ\text{C}$ to $200 \text{ }^\circ\text{C}$ with a nitrogen purge of 20 mL/min . The second heating run was used for the T_g determination. For each sample at least three distinct measurements were performed. Average values were then calculated and given as a result.

2.4.4 Gas chromatography – mass spectroscopy measurements

The amount of residual monomers in the SACs was determined with coupled gas chromatography – mass spectroscopy (GC-MS). A 6890N GC Network System with a HP-5 column with polysiloxane-based column packing (30 m in length, I. D. 0.32 mm , film $0.25 \text{ }\mu\text{m}$) and 5973 Network Mass Selective Detector (Agilent Technologies) were used. The sample solution concentration in methylenechloride was 0.1 g g^{-1} and heptane was added as an internal standard. Helium was used as an inert carrier gas with a constant flow rate of 0.7 mL min^{-1} . Standard monomer solutions with known concentrations were used for the quantitative analyses. The area under each peak was used to determine the quantity of the specific compound.

2.4.5 Size-exclusion chromatography

M_w and M_w/M_n were measured using size-exclusion chromatography (SEC) on a Waters 2690 chromatograph with a Waters 410 refractive-index detector (Waters S.A.S.). Tetrahydrofuran (THF) was used as an eluent with a flow rate of 0.7 mL min^{-1} . Three $7.8 \times 300 \text{ mm}$ single pore-sized columns with a styrene divinylbenzene copolymer column packing and a particle size of $5 \text{ }\mu\text{m}$ were used in a sequence - Styragel HR 0.5 column with an effective molecular mass range of $0\text{--}10^3$, Styragel HR 4E ($50\text{--}10^5$) and Styragel HR 5E ($2 \cdot 10^3\text{--}4 \cdot 10^6$). A sample solution concentration in THF was 2 mg mL^{-1} . Before the analysis the samples were filtered through a $0.45 \text{ }\mu\text{m}$ PTFE filter and a $100 \text{ }\mu\text{L}$ of prepared sample

was injected onto the column. As a result, the average molecular masses relative to polystyrene standards are given.

2.5 Preparation of cross-linked 2K-PUR coating films

Cross-linked 2K-PUR coating films were prepared with a HDI-homopolymer (D-N75). Diluted SAC (50 %) and D-N75 were mixed with a propeller stirrer (dry weight mass ratio $3.2 : 1$) at 1500 r/min for 15 min , applied on $20 \text{ cm} \times 7.5 \text{ cm}$ steel plates with an applicator and left to dry for 48 h . The dry film thickness of each 2K-PUR film was measured using the Elcometer 456 with the F1 magnetic induction probe (Elcometer Ltd.). For each film at least 20 measurements were performed, in compliance with the standard ISO 2178.

2.6 Electrochemical impedance spectroscopy

The electrochemical properties of the cross-linked coating films were measured via EIS at $20 \text{ }^\circ\text{C}$. The measuring (Tait) cell for the EIS contained a working electrode (coated sample plate) with a 34.21 cm^2 area, immersed in a NaCl solution 0.1M , a hastelloy counter electrode and a standard calomel reference electrode (SCE). The potential difference between the working and the counter electrode versus SCE was -0.6 V and the amplitude of the signal was 30 mV . The measurements were performed with a Parstat 2273 Advanced Electrochemical System (Advanced Measurement Technology Inc.) and the data analyzed using the Electrochemistry Power Suite and PowerSINE software (Princeton Applied Research). The value of the frequency was in the range from 65536 Hz to 0.1 Hz .

3 RESULTS AND DISCUSSION

3.1 Syntheses of the SACs

Both syntheses described above were previously optimized in terms of dosing rate, initiator concentration and working temperature to give products suitable for the application of 2K-PUR coatings (evaluated by the amount of residual monomers in the final product, **Table 2**). The synthesis of SAC 1 was carried out at $135 \text{ }^\circ\text{C}$ to ensure constant conditions. The temperature for the synthesis of SAC 2 was carefully selected at $175 \text{ }^\circ\text{C}$. According to the literature data, the coloration of the product progresses with temperature. In some cases $180 \text{ }^\circ\text{C}$ can already be too high¹³. The pressure in the synthesis of the SAC 2 was raised due to the evaporation of the solvent and the monomers as well as inflow of a fresh monomer mixture. This caused the elevation of the boiling point of the reaction mixture. Previous syntheses (not shown) indicated that an additional initiator is needed to reach a sufficient monomer conversion – a lower final residual monomer content (**Table 2**). Performing the synthesis at $175 \text{ }^\circ\text{C}$ significantly reduces the

reaction times in comparison to a synthesis at 135 °C (2 h 25 min versus 5 h 30 min). Higher reaction temperatures led to a lower M_w and a narrower M_w/M_n ¹³. This reduces the viscosity of the system and allows for the preparation of high-solids SACs (in our case SAC 2, **Table 2**).

Table 2: Properties of synthesized SACs

Tabela 2: Lastnosti sintetiziranih SAC

	SAC 1	SAC 2
DW [w/%]	62.4	71.3
η /(mPa s) (23 °C, 0.1 s ⁻¹)	8200	15500
M_w	23000	9000
M_w/M_n *	2.6	2.3
T_g /°C**	32 ± 2	23 ± 2
AV [mg KOH / g dry copolymer]	9.3	9.3
OH [mg KOH / g dry copolymer]	110	110
Residual monomers [w/%]	0.5	0.4

* ratio between mass average (M_w) and number average molecular mass (M_n)

** $T_g, Fox = 33.3$ °C

Figure 3 shows a comparison of both syntheses through thermal conversion. The reaction calorimeter measured the heat released due to the polymerization (q_r) in real time. From this data the thermal conversion was calculated as the ratio between the heat release until a certain time (t_r) and the total heat release from the reaction (t_{tot} stands for the total reaction time):

$$X_{th} = \frac{\int_0^{t_r} q_r(t) dt}{\int_0^{t_{tot}} q_r(t) dt} \quad (1)$$

It should be stressed that a 100 % thermal conversion does not imply total monomer consumption. For a better

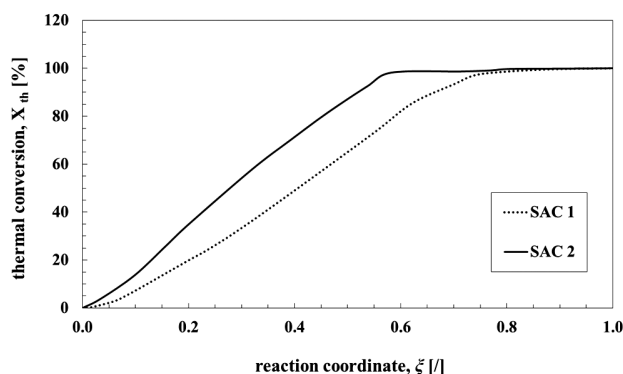


Figure 3: Thermal conversion for polymerizations of SACs

Slika 3: Termična konverzija pri polimerizacijah SAC

comparison the x -axis in **Figure 3** is not absolute time, but rather the reaction coordinate (ξ), defined as the progress of syntheses ($\xi = 0$ meaning start of dosing, $\xi = 1$ meaning the end of synthesis – the beginning of cooling the reaction mixture down). **Figure 3** shows that in the synthesis of SAC 2, a 98.2 % thermal conversion was reached after the dosing was completed (at $\xi = 0.56$), whereas in the synthesis of SAC 1 only a 74.4 % thermal conversion was achieved (at $\xi = 0.58$). In terms of heat removal, only 1.8 % of all the reaction heat needed to be removed after the dosing in the synthesis of SAC 2. On the other hand, in the synthesis of SAC 1, 25.6 % of all the reaction heat needed to be removed after the dosing was completed. In terms of heat release controlled by dosing, the synthesis in a high-pressure reactor turns out to be safer than the synthesis at a temperature below the boiling point of the solvent.

3.2 Characterization of the SACs

The described syntheses performed on the RC1eTM reaction calorimeter were made in parallel. There were no discrepancies between the parallels in terms of

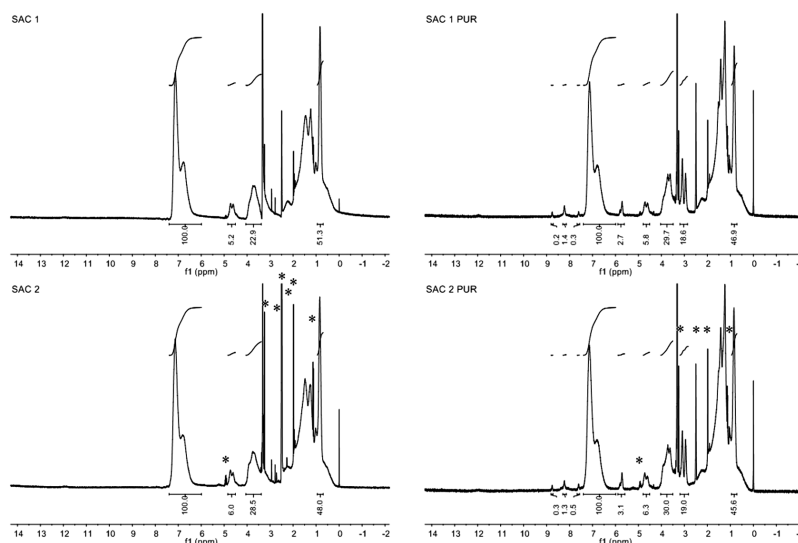


Figure 4: Comparison of ¹H NMR spectra of SACs and 2K-PURs; * denotes signals of solvents MPA and DMSO at $2.5 \cdot 10^{-6}$

Slika 4: Primerjava ¹H-spektrov SAC in 2K-PUR; * označuje signale topil MPA in DMSO pri $2,5 \cdot 10^{-6}$

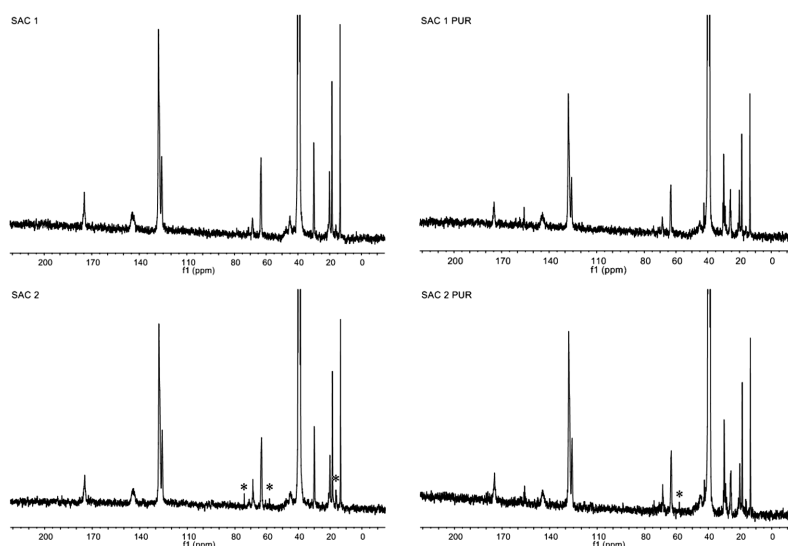


Figure 5: Comparison of ^{13}C NMR spectra of SACs and 2K-PURs; * denotes signals of solvent MPA
Slika 5: Primerjava ^{13}C -spektrov SAC in 2K-PUR; * označuje signale topila MPA

process parameters due to the excellent process control. Therefore, the syntheses were highly reproducible. This resulted in matching properties of the products such as M_w , M_w/M_n , residual monomers and viscosity. The results are not shown due to the negligible differences.

Furthermore, analyses of the acid and hydroxyl values (**Table 2**) confirmed the same functionality of both SACs. Since the on-line FTIR data provided insufficient information on the SACs' composition, NMR measurements were performed. The ^1H and ^{13}C NMR spectra of the dry SACs and 2K-PURs show no significant differences in functionality. As can be seen in **Figure 4** there are no peaks in the $5\text{--}6 \cdot 10^{-6}$ range of the ^1H NMR spectra of the SACs that are assigned to the protons around the double bonds of the (meth)acrylic monomers. Also, there is no peak at $112 \cdot 10^{-6}$ in the ^{13}C NMR spectra of the SACs assigned to vinyl $=\text{CH}_2$ of styrene (**Figure 5**). This supports the GC-MS measurements of the residual monomers and implies that the monomer mixture was sufficiently converted to the copolymer.

The HDI homopolymer ^1H NMR spectrum (**Figure 6**) shows peaks at $8.3 \cdot 10^{-6}$ ($-\text{NH}-\text{CO}-$, biuret H), $3\text{--}3.5 \cdot 10^{-6}$ ($-\text{CH}_2-\text{N}=\text{}$, HDI) and $1\text{--}2 \cdot 10^{-6}$ ($-\text{CH}_2-$, HDI). The typical peaks in the ^{13}C NMR spectrum are at $155 \cdot 10^{-6}$ ($-\text{NH}-\text{CO}-\text{N}$, biuret), $121 \cdot 10^{-6}$ ($-\text{NCO}$, isocyanate) and $25\text{--}45 \cdot 10^{-6}$ ($-\text{CH}_2-$, HDI). This confirms the structure of the HDI homopolymer (D-N75). The HDI monomers react with water to form trimers with a biuret linkage. These trimers further react to form the HDI-homopolymer.

In the preparation of the 2K-PURs the depletion of the $-\text{NCO}$ group in the ^{13}C NMR spectra can be seen (**Figure 5**, SAC 1 PUR and SAC 2 PUR), whereas the peaks at 8.3 (^1H NMR) and $155 \cdot 10^{-6}$ (^{13}C NMR) assigned to the biuret remain visible. The urethane

groups are overlapping with the styrene aromatic ring ($7 \cdot 10^{-6}$ and $7\text{--}7.8 \cdot 10^{-6}$ in ^1H NMR spectra, **Figure 4**). Small amounts of urea produced by side reactions can be seen from the ^1H NMR spectra at $5.7 \cdot 10^{-6}$ ^{28–31}. The

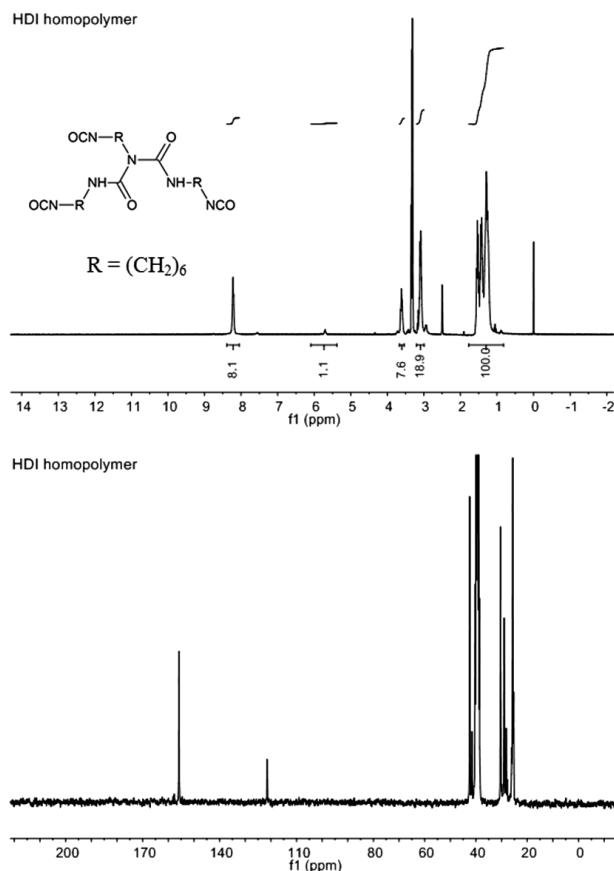


Figure 6: ^1H and ^{13}C NMR spectra of HDI homopolymer with trimer structure

Slika 6: ^1H - in ^{13}C NMR-spektra HDI homopolimera s strukturo trimera

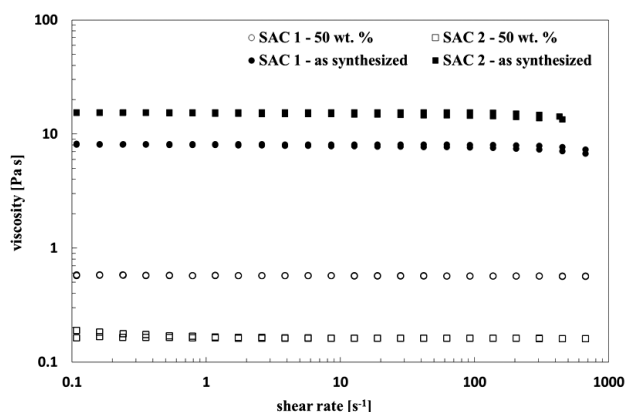


Figure 7: Flow curves of original (closed symbol) and diluted SACs (open symbol)

Slika 7: Tokovne krivulje osnovnih (črne oznake) in razredčenih SAC (bele oznake)

NMR results show the similar composition of both SACs and of both 2K-PUR films.

As **Table 2** shows, a high solids SAC was synthesized (DW of SAC 2 > 70 %). A higher temperature in the synthesis of the SAC 2 led to a lower M_w (9000 versus 23000) and a narrower M_w/M_n (2.3 versus 2.6). The shorter copolymer chains result in a decrease of the SAC 2 T_g in comparison to the SAC 1 (23 °C versus 32

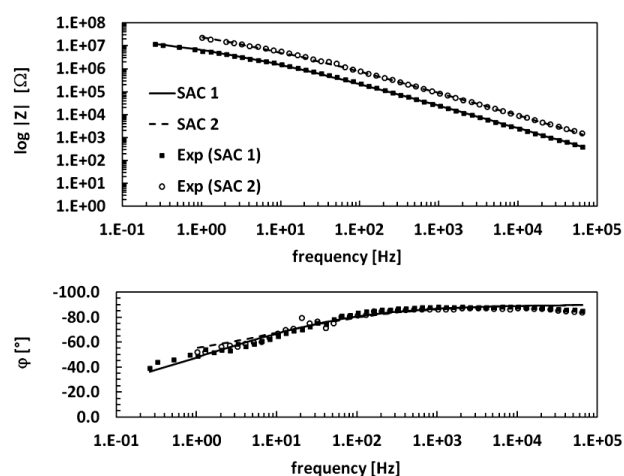


Figure 8: Bode diagrams for cross-linked 2K-PUR films; lines represent the fitting model

Slika 8: Bodejeva diagrama za zamrežene 2K-PUR premaze; črte prikazujejo prilaganje modela

Table 3: Electrochemical properties of cross-linked 2K-PUR films
Tabela 3: Elektrokemijske lastnosti zamreženih 2K-PUR premazov

	SAC 1	SAC 2
$d_c/\mu\text{m}$	75 ± 3	65 ± 3
$\sigma_c/(\Omega^{-1} \text{ rad}^{-1/2} \text{ s}^{1/2} \text{ cm}^2)$	4.2×10^{-8}	1.3×10^{-8}
$R_{po}/(\Omega \text{ cm}^{-2})$	3.7×10^7	ND
$C_c/(\text{F cm}^{-2})$	6.1×10^{-9}	1.7×10^{-9}

d_c = thickness of cross-linked 2K-PUR film
 σ_c = Warburg coefficient of film
 R_{po} = pore resistance
 C_c = capacitance of cross-linked 2K-PUR film

°C), which complies with the literature data¹³. Both SACs have a T_g lower than that predicted by the Fox equation (33 °C). The viscosity of the SAC 2 is higher due to the higher solids content (15500 mPa s versus 8200 mPa s, **Table 2**, **Figure 7**). After the dilution of both SACs with additional solvent to 50 % the effect of shorter copolymer chains can be observed as lower viscosity values (160 mPa s versus 570 mPa s, **Figure 7**). Both products were suitable for the preparation of 2K-PUR coatings.

The results of the EIS measurements and the evaluations for cross-linked 2K-PUR films of SAC 1 and SAC 2 are shown in **Figure 8** (Bode diagrams) and **Figure 9** (Nyquist diagram) and the fitting model parameters are given in **Table 3**. The experimental data were fitted by equivalent circuits – the transmission-line model^{16,19,27} – indicating a better quality of cross-linked 2K-PUR film prepared with the SAC 2. The transmission-line model for the SAC 2 film has no pore resistance ($R_{po} > 10^9 \Omega \text{ cm}^{-2}$, **Figure 9**), indicating that no pores are developed. The lower Warburg coefficient (σ_c) of the SAC 2 represents a better cross-linking of the shorter SAC chains and a lower coating capacitance (C_c) represents a lower water uptake of the cross-linked 2K-PUR film prepared with the SAC 2 in comparison to the one prepared with SAC 1.^{12,16,17,27} The impedance values shown in the Bode and Nyquist diagrams (**Figures 8 and 9**) for cross-linked 2K-PUR films prepared with the SAC 1 and SAC 2 in combination with comparable film thicknesses (**Table 3**) of both films directly indicate the better quality of the SAC 2.^{16,17,27} The impedance values at low frequencies are above $10^7 \Omega$ for both films and the improved quality of the 2K-PUR film prepared with the SAC 2 can be seen. The generally accepted absolute value of the impedance for the

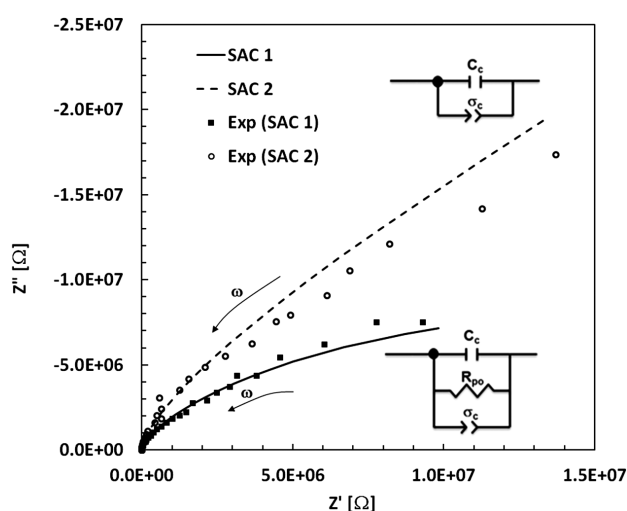


Figure 9: Nyquist diagram for cross-linked 2K-PUR films (SAC 1 and SAC 2) with equivalent circuits used for fitting model (R_S not shown); ω arrow denotes the increase in angular frequency

Slika 9: Nyquistov diagram zamreženih 2K-PUR premazov (SAC 1 in SAC 2) z odgovarjajočima nadomestnima tokokrogoma (R_S ni prikazan); ω puščica kaže v smeri naraščanja kotne frekvence

protective coatings is at least $10^6 \Omega$.³² This means that both SACs are suitable for the preparation of 2K-PUR coatings.

4 CONCLUSIONS

Synthesis in a high-pressure reactor under high temperature and elevated pressure proved to be a better alternative to the synthesis of high-solids SACs in a solution of an organic solvent at atmospheric pressure. The proposed direct synthesis leads to a product with no need of subsequent solvent removal by distillation and compliant with the European legislation on volatile organic compounds in coatings. Apart from the significant cutoff in the reaction times a much higher thermal conversion is reached while the monomer mixture is still being dosed when compared to the synthesis below the reflux temperature of the solvent. The cross-linked 2K-PUR coating prepared with the SAC 2 shows better anti-corrosion properties in comparison to the SAC 1, making it suitable for the protection of metal substrates.

Acknowledgements

Operation was part financed by the European Union, European Social Fund. Operation implemented in the framework of the Operational Program for Human Resources Development for the Period 2007-2013, Priority axis 1: Promoting entrepreneurship and adaptability, Main type of activity 1.1.: Experts and researchers for competitive enterprises.

The authors acknowledge the support from CE PoliMaT (financially supported by the Ministry of Education, Science, Culture and Sport of the Republic of Slovenia through the contract No. 3211-10-000057 (Centre of Excellence for Polymer Materials and Technologies)) where the syntheses on RC1eTM were performed.

5 REFERENCES

- ¹ D. K. Chattopadhyay, K. V. S. N. Raju, *Progress in Polymer Science*, 32 (2007), 352–418
- ² U. Poth, R. Schwalm, M. Schwartz, *Acrylic Resins*, Vincentz Network, Hannover 2011
- ³ J. Huybrechts, P. Bruylants, A. Vaes, A. De Marre, *Progress in Organic Coatings*, 38 (2000), 67–77
- ⁴ D. E. Fiori, *Progress in Organic Coatings*, 32 (1997), 65–71
- ⁵ Z. W. Wicks Jr., D. A. Wicks, J. W. Rosthauser, *Progress in Organic Coatings*, 44 (2002), 161–183
- ⁶ M. Melchioris, M. Sonntag, C. Kobusch, E. Jürgens, *Progress in Organic Coatings*, 40 (2000), 99–109
- ⁷ A. Kumar, R. K. Gupta, *Fundamentals of polymer engineering*, second edition, Marcell Dekker Inc., New York 2003
- ⁸ A. I. Yezrielev, M. G. Romanelli, W. E. Welman, *Improved high solids acrylic based coatings*, EPA 0 225 809 A2, 1987
- ⁹ G. W. Meyer, J. E. M. Fletcher, *High solids acrylic resin*, WO 02/066527, 2002
- ¹⁰ W. J. Blank, *High solids polymer resin coating composition containing amino resin cross-linking agent*, GB 2 112 398 A, 1982
- ¹¹ C. J. Bouboulis, *Superior solvent blends for synthesis of acrylic resins for high solids coatings*, EP 0 099 647 B1, 1983
- ¹² M. Manea, *High Solid Binders*, Vincentz Network, Hannover 2008
- ¹³ M. Slinxcs, N. Henry, A. Krebs, G. Uytterhoeven, *Progress in Organic Coatings*, 38 (2000), 163–173
- ¹⁴ J. N. Murray, *Progress in Organic Coatings*, 31 (1997), 375–391
- ¹⁵ S. Skale, V. Doleček, M. Slemnik, *Progress in Organic Coatings*, 62 (2008), 387–392
- ¹⁶ Y. Zhu, J. Xiong, Y. Tang, Y. Zuo, *Progress in Organic Coatings*, 69 (2010), 7–11
- ¹⁷ S. Skale, *Evaluation of Epoxy Coatings Surface Protection with Electrochemical Impedance Spectroscopy*, Doctoral Dissertation, University of Maribor, Faculty of Chemistry and Chemical Engineering, Maribor, 2009
- ¹⁸ M. G. Fontana, *Corrosion Engineering*, 3rd Ed., McGraw-Hill Book Company, New York 1986
- ¹⁹ S. Skale, V. Doleček, M. Slemnik, *Corrosion Science*, 49 (2007), 1045–1055
- ²⁰ D. D. Macdonald, *Techniques for Characterization of Electrodes and Electrochemical Processes*, John Wiley & Sons, Inc., New York 1991, Ch. 11
- ²¹ F. Mansfeld, *Journal of Applied Electrochemistry*, 25 (1995), 187–202
- ²² M. Kendig, J. Scully, *Corrosion*, 46 (1990), 22–29
- ²³ A. S. Castela, A. M. Simoes, *Corrosion Science*, 45 (2003), 1631–1646
- ²⁴ B. Liu, Y. Li, H. Lin, C. N. Cao, *Corrosion*, 59 (2003), 817–820
- ²⁵ M. Stratmann, *Corrosion*, 61 (2005), 1115–1124
- ²⁶ T. Skoulikidis, A. Ragoussis, *Corrosion*, 48 (1992), 666–670
- ²⁷ R. Posner, K. Wapner, S. Amthor, K. J. Roschmann, G. Grundmeier, *Corrosion Science*, 52 (2010), 37–44
- ²⁸ B. S. Selukar, S. P. Parwe, K. K. Mohite, B. Garnaik, *Advanced Materials Letters*, 3 (2012), 161–171
- ²⁹ E. Žagar, M. Žigon, *Polymer*, 40 (1999), 2727–2735
- ³⁰ E. Žagar, M. Žigon, *Polymer*, 41 (2000), 3513–3521
- ³¹ Y. Kaya, M. Kamaci, *Polimery*, 56 (2011), 721–733
- ³² J. R. Vilche, E. C. Bucharsky, *Corrosion Science*, 44 (2002), 1287–1309

PROCESSING POLY(ETHER ETHERKETONE) ON A 3D PRINTER FOR THERMOPLASTIC MODELLING

OBDELAVA POLYETHER ETHERKETONEA NA 3D-TISKALNIKU ZA TERMOPLASTIČNO MODELIRANJE

Bogdan Valentan¹, Žiga Kadivnik², Tomaž Brajljih², Andy Anderson³, Igor Drstvenšek^{1,2}

¹Ortotip, d. o. o., Ulica Škofa Maksimiljana Držečnika 6, 2000 Maribor, Slovenia

²University of Maribor, Faculty of Mechanical Engineering, Smetanova ulica 17, 2000 Maribor, Slovenia

³Invio Ltd., Technology Centre-Hillhouse International, Thornton Cleveleys, Lancashire FY5 4QD, United Kingdom
valentan@gmail.com

Prejem rokopisa – received: 2012-10-12; sprejem za objavo – accepted for publication: 2013-03-25

PEEK, poly(ether etherketone), is one of the high-quality industrial polymers. It is widely used in extremely demanding areas like automotive, aircraft and space industries. Because of the fact that it is bio-compatible, PEEK is also used for medical implants that are usually made by milling a block of the material. The article presents the results of an investigation of processing PEEK on a 3D printer for thermoplastic modelling. The used procedure is one of the additive manufacturing procedures and, as such, it builds a product by adding material layer by layer to get the finished product. Commercially available machines are unable to achieve the required melting and environment temperatures, so a new machine was developed. The machine was designed and built at the company Ortotip d.o.o. and it is able to produce the parts of up to 130 mm × 130 mm × 150 mm. After the initial testing, test specimens, according to standards EN ISO 527-2: 2012 and EN ISO 178: 2011, were produced and tested at the facilities of the PEEK manufacturer Invbio (from the UK). The article presents the steps taken when developing the PEEK modelling machine, the test methods to verify the mechanical properties of manufactured products and the results of the material testing. The machine was developed to produce medical implants (specific maxillofacial prosthesis), but with additional testing (that will help to improve the mechanical properties of produced parts) practically all bone-replacement implants can be made.

Keywords: PEEK, 3D printer, implant, medical application, thermoplastic, FDM, biocompatible, additive technology

PEEK, polyether etherketon, je eden izmed visoko kvalitetnih industrijskih polimerov. Uporablja se na zahtevnih področjih, kot so avtomobilska, letalska in vesoljska industrija. Zaradi dejstva, da je biokompatibilen, je uporaben tudi za medicinske vsadke, ki so navadno narejeni s frezanjem iz bloka materiala. Članek predstavlja izsledke raziskave oblikovanja PEEK s 3D-tiskalnikom za termoplastično modeliranje. Uporabljen postopek spada med tako imenovane dodajalne tehnologije in kot tak gradi izdelek po slojih. Komercialno dostopni stroji ne zmorejo doseči zahtevanih procesnih in okoljskih temperatur, zato je bila razvita nova naprava. Ta je bila oblikovana in izdelana v podjetju Ortotip, d. o. o., in je primerna za izdelke do velikosti 130 mm × 130 mm × 150 mm. Po uvodnih preizkusih so bile izdelane preizkusne epruvete v skladu s standardoma EN ISO 527-2: 2012 in EN ISO 178: 2011 in preizkušene od proizvajalca PEEK-materiala Invbio (iz VB). Predstavljeni so ključni koraki pri razvoju naprave za direktno izdelavo modelov, preizkusne metode za verifikacijo mehanskih lastnosti izdelanih kosov in rezultati meritev. Naprava je bila razvita za izdelavo medicinskih vsadkov (posebno lobanjske vsadke), vendar bo ob dodatnih preizkusih (za izboljšanje mehanskih lastnosti izdelanih kosov) primerna za vse vrste medicinskih vsadkov.

Ključne besede: PEEK, 3D-tiskalnik, vsadek, medicinska aplikacija, termoplast, FDM, biokompatibilnost, dodajalne tehnologije

1 INTRODUCTION

Today the majority of long-lasting human-body implants are made from three materials. The first is the bone cement, to technicians more known as poly(methyl methacrylate) – PMMA. Its great advantage is that it can be processed during the operation since it can be made of two components (liquid and powder) that are mixed together and directly processed (by hand or with some basic tools) in a short time (the curing time can be as short as 2 min). The production of the implants made from solid PMMA is used only in special cases like the lens for trabeculum. The second material is titanium (actually one of the titanium alloys) that is processed with a conventional machining process (usually the CNC milling or turning) or with one of the additive manufacturing procedures like SLM (selective laser melting),¹ MLSS (metal-laser-sintering system)² or EBM (electron-beam melting).³ After a long-term use titanium shows some problems,⁴ but it is irreplaceable when

excellent mechanical properties are needed. The material that promises the most is PEEK – poly(ether etherketone). The implants from PEEK⁵⁻⁷ are usually made with the conventional machining process or the method, presented in 2010, of direct manufacturing with an SLS (selective laser sintering) machine.⁸ Since PEEK is thermoplastic it can be formed also with the other procedures that are widely used for other thermoplastics.⁹ The challenges are the specific requirements relating to a higher viscosity (**Figure 1**) that need to be taken into consideration, so the idea of developing a dedicated device (a 3D printer for thermoplastic modelling) was born.

2 BASIC PRINCIPLES OF THE 3D PRINTER FOR THERMOPLASTIC MODELLING

The 3D printer for thermoplastic modelling is basically an FDM (fused-deposition modelling) machine. As

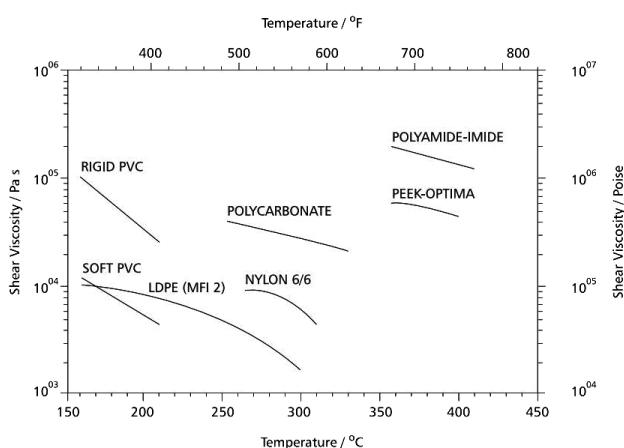


Figure 1: Shear viscosity versus the temperature for some common, industrial, engineering thermoplastics, comparable to PEEK Optima® LT1⁹

Slika 1: Viskoznost v odvisnosti od temperature za nekaj termoplastov v široki uporabi v primerjavi z PEEK Optima® LT1⁹

any additive manufacturing procedure (also known as the rapid prototyping)^{10–14} it starts with a 3D CAD model that is usually exported as an STL file from a CAD (engineering or dedicated medical) program. The STL file is then sliced by the computer software into horizontal layers that are as high as the layer in the machine. The rod-shaped filament is supplied to the machine through a nozzle. The nozzle is computer controlled in the X, Y plane and, in one layer, it forms a raster of the item in the respective layer. The material is liquefied in the nozzle and it hardens quickly when applied to the layer at a lower temperature. The entire system must be preheated to a higher surrounding temperature. After the layer is finished, the working bed in the Z direction is lowered by the thickness of one layer and the new layer is extruded. When the geometry of a part is more complex¹⁵ (overhangs), a support structure must be added.

3 MACHINE DESIGN

The machine design was based on the 3D printer Ciciprinter¹⁶ presented in 2011 and was made with the CAD program Solid Works. In the prototypes the open-source control electronics¹⁷ and the software made for RepRap printers¹⁸ were used, with a simple adaptation, to achieve the desired application. The basic principle of thermoplastic modelling stays the same, but there are completely different requirements for industrial or medical machines, comparable with the distinction between home-used or educational tools. For medical equipment, standard ISO 13485¹⁹ is valid and for electronic circuits, several other guidelines (like 89/392/EEC, 73/23/EEC and 89/336/EEC) need to be taken into consideration. PEEK, like most of the widely used thermoplastic materials (ABS, HDPE, LDPE, etc.), is not easy to process and in order to get the best results,

the manufacturer's instructions⁹ must be followed. The basic material properties were studied and discussed with the material supplier to get the data of the processing parameters for a small-nozzle extrusion.

At this point the decision was made to develop a PEEK printer that uses a rod-shaped material rather than a more classical approach with the grains and an extrusion screw because of the required screw length, a need for an expensive regulation equipment (pressure measurements and electronic valves) and a requirement for cleaning after the completion of each batch (which, in the case of a unique or small-series production, means practically every day).⁹

For the testing purposes the first machine with a heating chamber was produced (**Figure 2**). The heaters with a combined power of 1000 W were used to preheat the working plate to around 240–300 °C. The first problem was the implementation of a mobile platform inside the chamber that required a mechanism for an accurate movement in the Z direction with a minimum loss of heat. The soft isolation and the central holder for the platform were eventually used. The second problem was how to assure the movement in the XY direction of the nozzle and prevent the heat loss at the top of the chamber. The known industrial solution with protective bellows would be an elegant solution, but the working

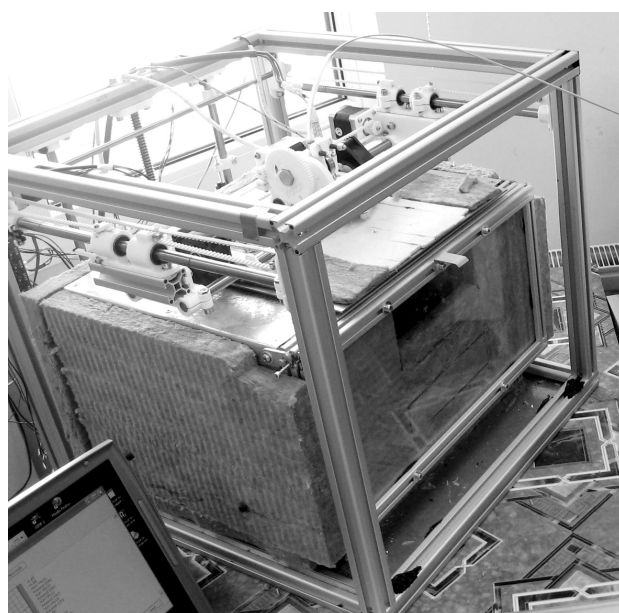


Figure 2: First laboratory PEEK machine. On the top there is an extruder mechanism with the 1 : 5 thrust ratio from the small NEMA 17 step motor to the specially shaped stainless-steel thrust screw. The PEEK rod diameter of 2.2 mm (± 0.1 mm) was routed from the nearby roll. The maximum chamber temperature was only around 300 °C because of the 1000 W heat source and a poorly applied insulation.

Slika 2: Prva preizkusna naprava za predelavo PEEK-a. Na vrhu je mehanizem za podajanje materiala z razmerjem 1 : 5 in pogonskim koračnim motorjem NEMA 17. Pogon je izveden preko nazobčanega pogonskega vijaka iz nerjavnega jekla. PEEK-žica, premera 2,2 mm ($\pm 0,1$ mm), je bila speljana iz koluta v bližini. Zaradi grelnikov 1000 W in slabe izvedbe izolacije je bila najvišja dosežena temperatura komore samo okrog 300 °C.

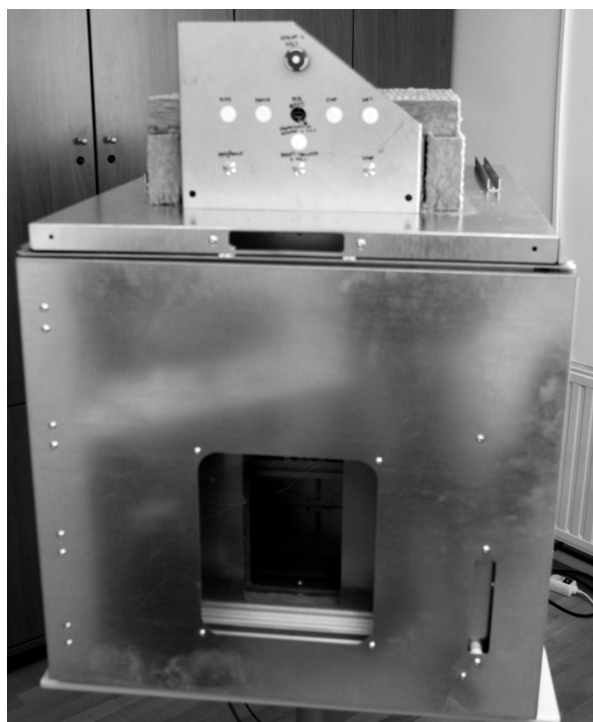


Figure 3: PEEK2 machine with a better insulation, more powerful heaters, a preheated chamber for the material and a new and improved electric controller

Slika 3: PEEK2-naprava z izboljšano izolacijo, močnejšimi grelniki, komoro za predgretje materiala in novim, izboljšanim električnim krmiljem

temperature was simply too high, so a movable insulated panel was used. The design of the hot-end part, together with the extrusion nozzle, required another special solution. The hot end is the part where the melting process takes place, so it needs to be insulated from the hot-end holder to prevent the heat transfer through the leading pipe that could cause the material melting in the leading pipe and the subsequent blockage of the material at the next start. Some tests were made with ceramic or composite materials,^{20–22} but, at the end, the nozzle was thermally separated from the holder with a thermal barrier made on the leading pipe in the shape of narrowing/ thinning walls.

The second machine (**Figure 3**) was designed with all the updates that had been developed in practice after the previous tests. The working chamber was insulated with a thicker insulation and was more carefully closed so that the heat losses were, subsequently, lower than before. The building chamber was increased to allow a more equal air heating and a bit larger building volume, especially in the Z direction. With the use of more powerful heaters, the preheating time needed to reach the working temperature (now set at 280 °C to 300 °C) was shortened from more than one hour to 20 min. The extrusion tests also showed a need for a new hot-end design, so the hot end with a bayonet mechanism for a fast and simple exchange was made.

4 MATERIAL PROPERTIES

The PEEK supplier Invibio prepared two different PEEK Optima® materials – LT3 and LT1. The properties of both materials,²³ for the case of injection moulding, can be found in **Table 1** and the shear viscosity versus the shear stress at different temperatures is presented in **Figure 4**. When used in the injection-moulding process, LT3 has slightly higher mechanical properties and a lower viscosity and as such it should be ideal for our application.

Table 1: Mechanical properties of the PEEK Optima® LT1 and LT3 materials processed with injection moulding²³

Tabela 1: Mehanske lastnosti PEEK Optima® LT1 in LT3 materialov, izdelanih z brizganjem v forme²³

Property	Units	LT1	LT3
Melt viscosity	(kN s)/m ²	0.44	0.16
Density	g cm ⁻³	1.3	1.3
Tensile strength (Yield)	MPa	100	108
Tensile elongation (Break)	%	40	25
Flexural strength	MPa	165	170
Water absorption (24h)	%	0.5	0.5
Melt temperature	°C	340	340
Mould shrinkage	%	1.2	1.3

5 PRELIMINARY TESTS

The first tests were made with PEEK LT3 on a simple extrusion device. Those tests just confirmed the possibilities of processing PEEK in the desired way (extrusion through a small nozzle). **Figure 5** presents the results of the first extrusion test that, due to a short delivery time, was made with an industrial PEEK form another manufacturer.²⁴ The first extrusion was successful, so during the next steps the first PEEK 3D printer (shown previously on **Figure 3**) was constructed.

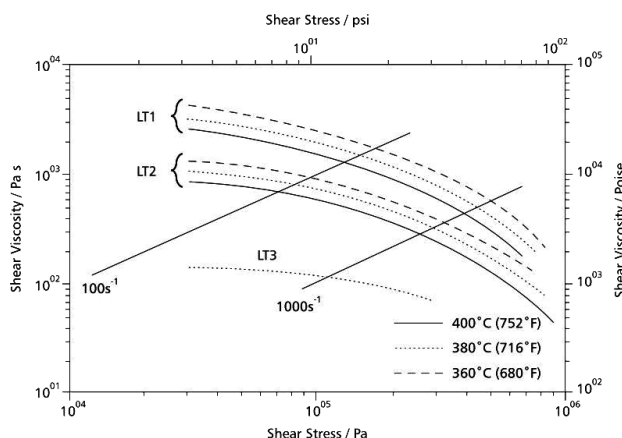


Figure 4: Shear viscosity versus shear stress at different temperatures shows that PEEK Optima® LT3 has a significantly lower viscosity when compared to LT1 or LT2⁹

Slika 4: Viskoznost v odvisnosti od strižne napetosti in temperature kaže na nižjo viskoznost PEEK Optima® LT3 v primerjavi z LT1 ali LT2⁹

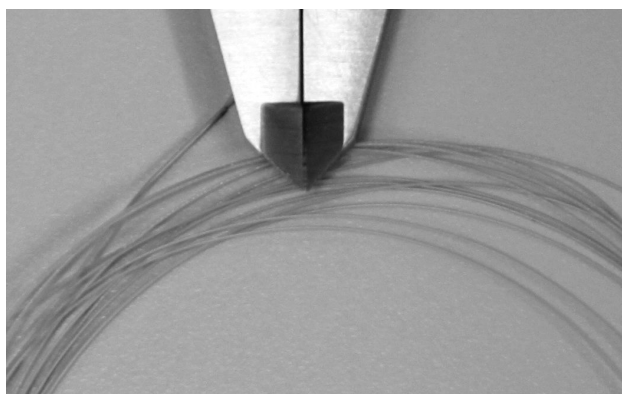


Figure 5: First extrusion tests showed that an extrusion of PEEK through a small-diameter nozzle is possible

Slika 5: Prvo poizkusno ekstrudiranje je pokazalo, da je ekstrudiranje PEEK-a skozi šobo majhnega premera mogoče

After the approval of the possibility of using the extrusion principle, the first PEEK processing machine was made and the first parts were produced. After several



Figure 6: Degradation of PEEK inside the nozzle as a result of several heating cycles. The left figure shows the inside of the nozzle after being used for 15 cycles (15 working days). The right figure shows small particles that are caused by the material degradation inside the nozzle and are eventually deposited onto the product.

Slika 6: Razgradnja PEEK-a v šobi kot rezultat večkratnega segrevanja. Leva slika prikazuje notranjost šobe po 15 ciklih (15 delovnih dneh). Na desni sliki so vidni majhni črni delci, ki so se pojavili v izdelku kot posledica razgrajenega materiala, ki je iz notranjosti šobe prehajal v izdelek.

Table 2: Test settings of the TA Instruments Q2000 differential scanning calorimeter

Tabela 2: Nastavitve TA-naprave Q2000 za diferenčno vrstično kalorimetrijo

Parameter	Value
Number of cycles	5
Sampling interval	0.20 s/pt
Equilibrate temperature	30.00 °C
Ramp 1	20.00 °C/min to 400.00 °C
Isothermal	2.00 min
Mark end of cycle	0
Ramp 2	20.00 °C/min to 30.00 °C
Isothermal	5.00 min
Mark end of cycle	0
Ramp 3	20.00 °C/min to 400.00 °C
Mark end of cycle	0

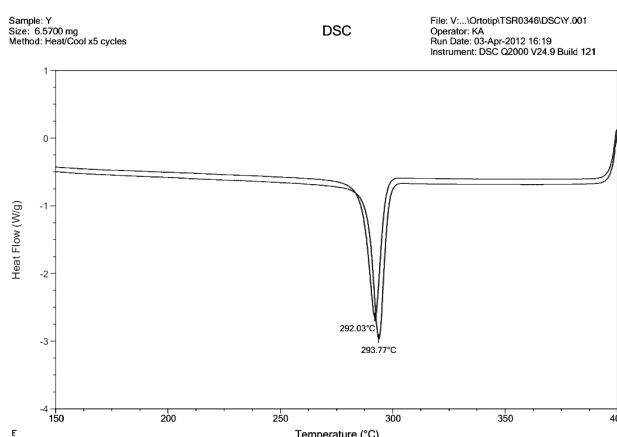


Figure 7: Results of the differential scanning calorimeter. Set-A traces show the first and the fifth crystallisation cycles.

Slika 7: Rezultati diferenčnega vrstičnega kolorimetra. Sledi seta A prikazujeta prvi in peti cikel kristalizacije.

production cycles some problems with the material thermal decomposition inside the extrusion nozzle appeared (**Figure 6**).

To verify the cause of a degraded polymer, additional tests were made. The presence of a degraded polymer was performed using a TA Instruments Q2000 differential scanning calorimeter with the settings presented in **Table 2**.

The results (**Figure 7**) of a multi-cycle DSC analysis did not indicate the presence of a degraded polymer. The difference between the first and the last recrystallization cycles was approximately 1.7 °C. If a degraded polymer had been present, the value (difference) would have been significantly larger, at least 5 °C to 10 °C. It is, therefore, likely that the bubbles are due to the presence of the moisture in the polymer when the sample specimens were made.

To get the best possible results, the material was dried again (according to the manufacturer,⁹ the LT3 material should be dried for at least 3 h at 150 °C or 12 h at 120 °C) and a new, clean extruder was used for the sample production.

6 PROCESSING DATA AND TEST PROCEDURES

According to the standards EN ISO 527-2: 2012 plastics – determination of tensile properties and EN ISO 178: 2011 plastics – determination of flexural properties, several sets of test specimens were made (**Figure 8**). Optical microscopy was performed using an Olympus SZX7 optical microscope and the Spot imaging software. The tensile-strength testing was performed on an Instron 3367 tensometer using the InVibio laboratory test method INV-LAB-TM12 revision 2. SEM was performed on a Hitachi TM3000 scanning electron microscope.

The SEM analyses of the gaps and voids (**Figure 9**) showed a presence of moisture even after the raw material was dried according to the material manufacturer's

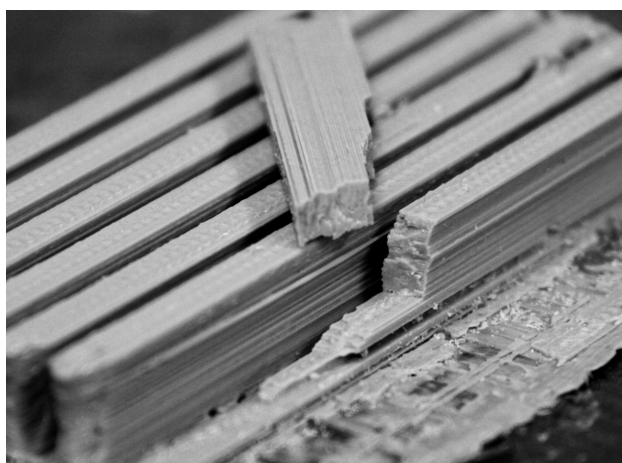


Figure 8: PEEK test specimens made on the PEEK plate. A nicely fulfilled structure is seen and so are the layers in the Z direction.

Slika 8: PEEK-preizkusni vzorci, izdelani na delovni plošči iz PEEK-a. Vidi se lepo izpopolnjena notranja struktura in sloji v Z-smeri.

data. The problem is that it takes several hours to produce a set of samples, so the material gains the moisture back from the surrounding air. The results lead us to improve the design of the PEEK printer and include a drying chamber, so that the material can be in dry condition all the time.

The results of the tensile stress showed that the tensile strength of the parts made with the presented technology (thermoplastic modelling or FDM) is significantly lower (**Figure 10**) than the results for the parts made with injection moulding (**Table 1**). However, the tensile strength is still high enough for designated applications (higher than for the implants made of PMMA).

To test the impact of heat treatment (present due to a long production time) on the product, the test specimens were produced and left in the chamber at a high tempera-

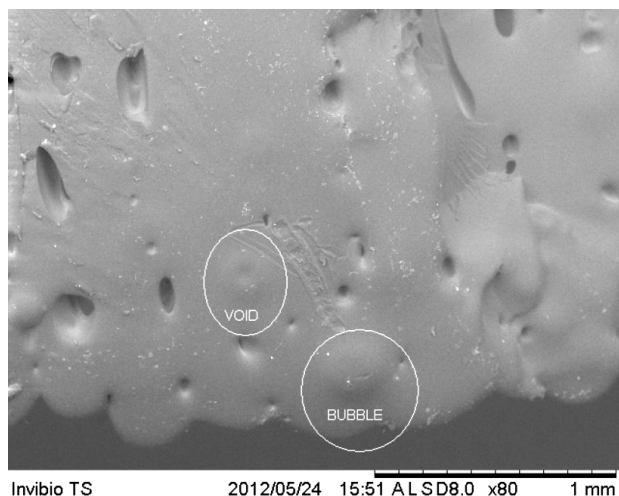


Figure 9: Gaps and bubbles in the model are a result of the moisture in the material

Slika 9: Vrzeli in mehurčki v izdelku so posledica vlage v materialu

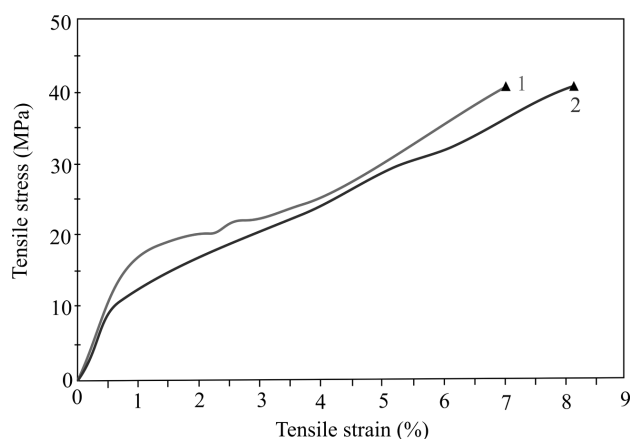


Figure 10: Typical response of a PEEK specimen. After trimming the second PEEK printer, the average tensile stress of approximately 60 MPa can be achieved for the large parts that are taken out of the production chamber immediately after the end of the production.

Slika 10: Značilen diagram preizkušanja mehanskih lastnosti. Po nastavitvi parametrov na drugem PEEK-tiskalniku je mogoče doseči natezno trdnost okrog 60 MPa, če so deli odstranjeni iz delovne komore takoj po končani izdelavi.

ture for additional 12 h. The results (**Figure 11**) showed it has a negative impact on the mechanical properties that should be avoided, so the parts should be taken out of the chamber immediately after the production.

The last test presents the problem of a non-uniform raw material that was delivered (**Figure 12**). These test specimens showed that a change in the rod diameter from 2.3 mm to 2 mm (in the case of the first delivered charge, resulting in a material deficit in volume of 30 %) can cause a drop in mechanical properties of up to 50 % (**Figure 13**).

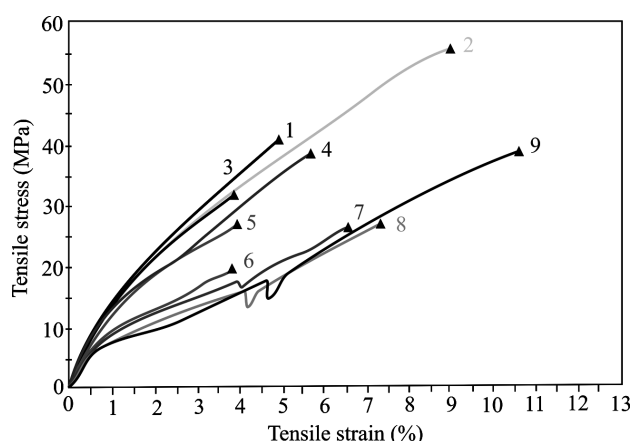


Figure 11: Response of the test specimens after being left in a heated environment for 12 h. Mechanical properties of the products under the obligatory high temperature are deteriorating with time. The colour change from light brown to dark brown was also detected. Specimens 2 and 9 have unusually high values, so they are excluded from the average-value calculations.

Slika 11: Diagram preizkusnih vzorcev, zadržanih na visoki temperaturi okoli 12 h. Mehanske lastnosti izdelkov se zaradi vpliva visokih temperatur hitro slabšajo. Opaziti je tudi spremembo v barvi izdelkov, od svetlo rjave na temno rjavo. Vzorca 2 in 9 imata nenavadno visoke vrednosti, zato pri izračunih srednje vrednosti nista bila upoštevana.

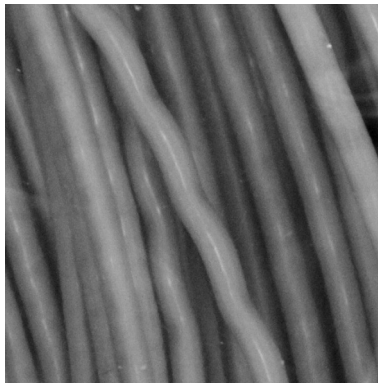


Figure 12: Non-uniform raw rod varying from 2 mm to 2.3 mm in diameter presents a big problem, since it leads to a lack of the material inside the produced part and, subsequently, to a drop in the mechanical properties.

Slika 12: Neenakomeren prerez osnovnega materiala, ki variira med 2 mm in 2,3 mm, je velik problem, saj povzroči pomanjkanje materiala v izdelku in posledično slabše mehanske lastnosti.

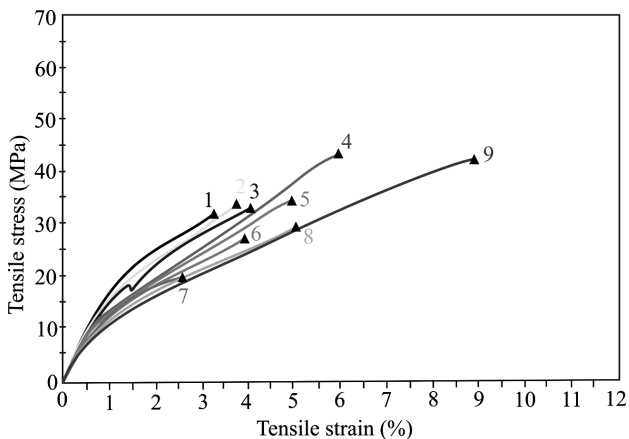


Figure 13: Drop in the mechanical properties as a result of the change in the diameter of the rod from 2.3 mm to 2 mm

Slika 13: Poslabšanje mehanskih lastnosti kot posledica spremembe premera žice iz 2,3 mm na 2 mm



Figure 14: Thin-wall tornado (the wall thickness of only 0.55 mm) produced from LT3 PEEK

Slika 14: Tankostenski tornado (debelina stene samo 0,55 mm), izdelan iz materiala PEEK LT3

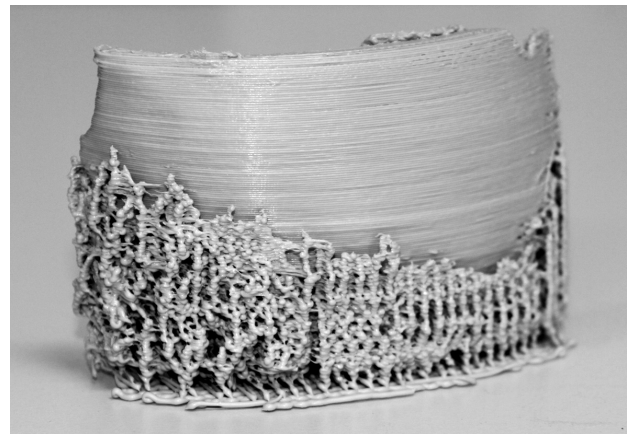


Figure 15: Part of a real-shape implant (a skull implant) made with the support material in the vertical position

Slika 15: Del lobanjskega vsadka, izdelanega z dodatnimi podporami v pokončnem položaju

7 PRODUCTS

For additional tests and calibration three basic shapes were used: a cube to get the right amount of the extruded material, a cylinder to check the X and Y movement synchronisation and a test specimen according to the standards (ISO) for mechanical properties. The goal of the 3D printer is to produce more complex shapes, so real-life products (also in the shapes of implants) were also produced. **Figure 14** presents one of the first successfully produced bigger parts (a height of 100 mm) with a really small wall thickness, due to poor mechanical properties later replaced by the LT3 PEEK Optima® material. **Figure 15** shows one of the latest parts in the shape of a real-size (a width of approx. 120 mm) skull implant with a support structure. The implant was made in the vertical position since we found that in this position smoother products can be made.

8 CONCLUSION

The article presents only a small amount of the research done in the project to make a 3D printer capable of directly producing PEEK parts. In the process of developing the appropriate device, several other products were made. The PEEK printer is currently in its final prototype phase, it is functional but to produce a part, additional knowledge on the part orientation, machine tricks and G-code generation is still needed. Because of the bio-compatibility requirement, the whole hot end (the part where PEEK changes the aggregate state from solid to liquid) is exchangeable and must be exchanged after a part has been produced. The hot end is then renewed at the manufacturer's facility.

Future development is planned to improve the mechanical properties, so some more tests with appropriate building temperatures and speeds need to be done. The next step is also to replace the control electronics with

robust, accurate and reliable home-made electronics developed specially for this application (so additional parameters will be monitored and, if needed, more powerful motors can be used).

Acknowledgement

This work has been partly financed from the European Union – European Social Funds.

9 REFERENCES

- ¹ Producer of Selective Laser Melting machines [cited 2012-10-10]. Available from World Wide Web: <http://www.realizer.com/en/>
- ² Producer of metal laser sintering systems [cited 2012-10-10]. Available from World Wide Web: <http://www.eos.info/>
- ³ Producer of the EBM[®] machines that are builds parts layer-by-layer from metal powder using a powerful electron beam [cited 2012-10-10]. Available from World Wide Web: <http://www.arcam.com/>
- ⁴ M. Joseph, Titanium Implants Can Cause Cancer [cited 2012-10-10]. Available from World Wide Web: http://www.anaturalcure.com/mambo/index2.php?option=com_content&do_pdf=1&id=482
- ⁵ P. Scolozzi, A. Martinez, B. Jaques, Complex Orbito-fronto-temporal reconstruction using computer designed PEEK implant, *The journal of craniofacial surgery*, 18 (2007) 1, 224–227
- ⁶ M. M. Kim, D. O. K. Boahene, P. J. Byrne, Use of customized Polyetheretherketone (PEEK) implants in the reconstruction of complex maxillofacial defect, *Arch. facial. plast. surg.*, 11 (2009) 1, 53–57
- ⁷ M. M. Hanosano, N. Goel, F. DeMonte, Calvarial reconstruction with Polyetheretherketone implants, *Annals of plastic surgery*, 62 (2009) 6, 653–655
- ⁸ M. Schmidt, D. Pohle, T. Rechtenwald, Selective Laser Sintering of PEEK, *CIRP Annals – Manufacturing Technology*, 56 (2007) 1, 205–208
- ⁹ PEEK Optima[®], Unfilled PEEK-OPTIMA Polymer Processing Guide [cited 2012-10-10]. Available from World Wide Web: <http://www.invibio.com/resource-library/guidelines-preview.php?id=19>
- ¹⁰ I. Drstvenšek, Slojevite dodajalne tehnologije, In: K. Kuzman, (ed.), *Moderno proizvodno inženirstvo, priručnik*, Grafis trade, Grosuplje 2010, 777–812
- ¹¹ I. Drstvenšek, T. Brajljeh, B. Valentan, Hitra izdelava prototipov, In: J. Balič, I. Veža, F. Čuš (eds.), *Napredne proizvodne tehnologije, Univerza v Mariboru, Fakulteta za strojništvo, Sveučilište u Splitu, Fakultet elektrotehnike, Maribor, Split 2007*, 98–120
- ¹² A. Pilipovic, P. Raos, M. Sercer, Experimental analysis of properties of materials for rapid prototyping, *International journal of advanced manufacturing technology*, 40 (2009) 1–2, 105–115
- ¹³ T. Brajljeh, B. Valentan, J. Balič, I. Drstvenšek, Speed and accuracy evaluation of additive manufacturing machines, *Rapid prototyping j.*, 17 (2010) 1, 64–75
- ¹⁴ K. Lokesh, P. K. Jain, Selection of rapid prototyping technology, *Advances in Production Engineering & Management*, 5 (2010) 2, 75–84
- ¹⁵ B. Valentan, T. Brajljeh, I. Drstvenšek, J. Balič, Development of a part-complexity evaluation model for application in additive fabrication technologies, *Stroj. vestn.*, 57 (2011) 10, 709–718
- ¹⁶ Web page of 3D printer producer Ortotip, d. o. o. [cited 2012-10-10]. Available from World Wide Web: <http://www.ortotip.com/soustvar-jalech.html>
- ¹⁷ Generation 6 Electronic - web page with resources for GEN 6 electronic [cited 2012-10-10]. Available from World Wide Web: http://reprap.org/wiki/Generation_6_Electronics
- ¹⁸ Web page of RepRap printers [cited 2012-10-10]. Available from World Wide Web: <http://www.reprap.org/wiki/RepRap>
- ¹⁹ ISO 13485:2003 standard [cited 2012-10-10]. Available from World Wide Web: http://www.iso.org/iso/catalogue_detail?csnumber=36786
- ²⁰ A. Maglica, K. Krnel, M. Ambrožič, Ceramic composites based on silicon nitride, *Mater. Tehnol.*, 43 (2009) 3, 165–169
- ²¹ T. Kroupa, R. Zemčík, J. Klepáček, The temperature dependence of the parameters of non-linear stress-strain relations for carbon-epoxy composites, *Mater. Tehnol.*, 43 (2009) 2, 69–72
- ²² I. N. Orbulov, K. Májlinger, Microstructure of metal-matrix composites reinforced by ceramic microballoons, *Mater. Tehnol.*, 46 (2012) 4, 375–382
- ²³ PEEK-OPTIMA Typical Material Properties [cited 2012-10-10]. Available from World Wide Web: <http://www.invibio.com/resource-library/brochures-preview.php?id=30>
- ²⁴ Properties of Quadrplastics Ketron PEEK 1000 [cited 2012-10-10]. Available from World Wide Web: http://www.quadrantplastics.com/fileadmin/quadrant/documents/QEPP/EU/Product_Data_Sheets_PDF/AEP/KetronPEEK_1000_E_PDS_0907.pdf

FINITE-ELEMENT MODEL OF THE INDENTATION FOR YBCO-BASED SUPERCONDUCTOR THIN FILMS

MODEL KONČNIH ELEMENTOV ZA VTISKOVANJE TANKIH PLASTI SUPERPREVODNIKA YBCO

Osman Culha¹, Ilyas Turkmen¹, Mustafa Toparli², Erdal Celik²

¹Celal Bayar University, Department of Materials Engineering, Muradiye Campus, Manisa, Turkey

²Dokuz Eylul University, Department of Metallurgical and Materials Engineering, Tinaztepe Campus, Buca, Izmir, Turkey
osman.culha@cbu.edu.tr

Prejem rokopisa – received: 2012-10-16; sprejem za objavo – accepted for publication: 2013-03-25

Superconducting films with poor mechanical properties are useless even if they possess good transport and flux-pinning properties. Since additive particles as pinning centers are important changes in a microstructure, their effect on the micromechanical properties such as Young's modulus and hardness have to be investigated with respect to the additional-particle type and quantity, using experimental and numerical methods. In this study, films were dip-coated onto (001) SrTiO₃ (STO) single-crystal substrates with metalorganic deposition using the trifluoroacetate (TFA-MOD) technique. The phase analysis and the microstructure of the superconducting thin films were determined with an X-ray diffractometer (XRD) and a scanning electron microscope (SEM). The mechanical-property variations of the pure YBCO and the YBCO thin films with Mn (reacting as BaMnO₃) were experimentally obtained with nanoindentation techniques. Thus, the BaMnO₃ nanoparticle effects on the structural and mechanical properties of the films were observed. According to the nanoindentation results, the Young's modulus and indentation hardness of the films decreased from 88.54 GPa to 76.47 GPa and from 12.51 GPa to 3.88 GPa, respectively, depending on the additive particles. In addition, the finite-element modeling (FEM) of the indentation was applied to estimate the failure stress/stress distribution relation at the contact region between the indenter and the surface of a YBCO-based thin film, obtaining the same force/penetration depth curve as with the indentation experiment. According to these main aims of FEM, the mesh-design effect, material properties and the boundary condition of the axisymmetric model were chosen and optimized to obtain the mechanical results of the instrumented indentation.

Keywords: superconducting films, mechanical properties, nanoindentation, finite-element modelling, stress distribution

Superprevodne tanke plasti s slabimi mehanskimi lastnostmi so neuporabne, čeprav imajo dobre transportne lastnosti in zmožnost zadrževanja toka. Ker so dodani delci kot mesta zadrževanja pomembna sprememba v mikrostrukturi, je treba z eksperimentalnimi in numeričnimi metodami raziskati njihov vpliv na mikromehanske lastnosti, kot sta Youngov modul in trdota, v odvisnosti od vrste in količine dodanih delcev. V tej študiji so bile mono- kristalne tanke plasti (001) SrTiO₃ (STO) s potapljanjem obložene s kovinsko-organskim nanosom z uporabo tehnike s trifluoroacetatom (TFA-MOD). Fazna analiza in mikrostruktura superprevodnih tankih plasti sta bili določeni z rentgenskim difraktometrom (XRD) oziroma z vrstičnim elektronskim mikroskopom (SEM). Spreminjanje mehanskih lastnosti čistega YBCO in tankih plasti YBCO z Mn (reagira kot BaMnO₃) je bilo eksperimentalno določeno z nanovtiskovanjem. Opaženi so bili učinki nanodelcev BaMnO₃ na strukturne in mehanske lastnosti plasti. Na podlagi rezultatov nanovtiskovanja sta se Youngov modul in trdota plasti zmanjšala iz 88,54 GPa na 76,47 GPa oziroma iz 12,51 GPa na 3,88 GPa, odvisno od dodanih delcev. Dodatno je bilo uporabljeno tudi modeliranje vtiskovanja s končnimi elementi (FEM) za določanje porušitvene razporeditve napetosti v področju stika vtisnega telesa in površine tanke plasti na osnovi YBCO, da bi dobili krivulje sila – globina vtiskovanja pri preizkusu vtiskovanja. Skladno s ciljem FEM-modela, je bil izbran učinek oblike mreže, lastnosti materiala in robni pogoji za osnosimetrični model in izvršeno je bilo optimiranje glede na dosežene rezultate pri mehanskem instrumentiranem vtiskovanju.

Gljučne besede: superprevodne tanke plasti, mehanske lastnosti, nanovtiskovanje, modeliranje s končnimi elementi, razporeditev napetosti

1 INTRODUCTION

Since the discovery of high- T_c superconductors, numerous researchers focused on their electric properties. The production effect and the critical-current density (J_c) dependence on the external magnetic field and on the temperature in high- T_c superconductor (HTS) YBCO films have been widely investigated.¹⁻⁷ The results demonstrate a high potential for an application of YBCO films in power devices such as fault current limiters (FCL) and motors. J_c depends on the vortex-pinning capability of a film, the optimization of which is currently achieved by controlling the microstructure and the defect distribution (BaMeO₃ as a nanorod and dot) in a film. However, increasing the pinning-center density

up to the value, at which the distance between the nearest centers reaches the coherence length will severely deteriorate the mechanical properties of the films. Thus, it may occur that for many of the HTS thin-film applications requiring a high critical-current density, the limiting factor will no longer be the critical-current density magnitude but the mechanical strength against the body forces caused by flux pinning. The mechanical strength makes a crucial contribution to the stability and credibility of any device based on this form of materials.⁸ In addition, the mechanical properties are also very important for the final industrial application.

In the literature, there have been several reports on their hardness, bending strength and internal friction. A precise knowledge of the elastic and deformation beha-

viour is a prerequisite for a successful production and operation of such devices. However, very little information on the elastic-to-plastic transition is available in the literature.^{9–11} On the other hand, nanoindentation has been used routinely in the mechanical characterization of thin films and thin-surface layers in recent years.¹² The technique applies a programmed function of an increasing and decreasing load to the surface of interest with an indenter of a well-defined shape, continuously measuring the indenter displacement (**Figure 1**). The advantage of this method is that the mechanical information, such as the elastic modulus, can be obtained through an analysis of the load-displacement behavior using only the coating of the material to be tested on a substrate made from a different material. This makes it an ideal tool. The technique has been used to assess the elastic and plastic properties of coatings on a range of substrates, but there are limitations in measuring the properties of much thinner coatings, particularly when elastic properties are required.^{13,14} For the coatings with a thickness of a few hundred nanometers, it has been suggested that extrapolating the properties determined for a range of peak loads or indenter displacements to zero load/depth can be used to determine the coating-only properties. With high-quality sharp indenters it is possible to assess coatings down to the thickness of 100 nm using this method.¹⁵

The indentation-system frame stiffness and the diamond tip shape were carefully calibrated with a fused-silica test sample, using the standard Oliver and Pharr method (1992), before and after the measurements with no change for either of them. Nano-indentation load (P) vs. displacement (h) curves were then recorded for each indent and only the ones showing evidence of a plastic deformation (i.e., the loading and unloading curves are different) were used in the analysis of Young's modulus using the above methods.^{15–18} In addition, most of the previous studies about the depth-sensing nano-indentation technique demonstrate that: to extract the mechanical properties of the coatings or films from the indentation test, we should limit the indentation depth to less than 10–20 % of the film thickness.^{19,20} As we know, during the nanoindentation experiments, especially when the indentation depth is about 100–1000 nm, size-scale-dependent indentation effects become important. These possible size-scale-dependent effects on the hardness have been modeled using higher-order theories^{21–23} and these effects can also be related to the bluntness of the nominally sharp indenters.^{24,25} For the cases when the tip bluntness is on the same order as the indentation depth, Borodich and Keer²⁴ proposed fundamental relations for depth of indentation, size of contact region, load, hardness, and contact area for various boundary conditions. If the indentation is sufficiently deep (typically deeper than 1 μm), then the scale-dependent effects become small and negligible. Therefore, the limitation of the indentation depth to less than 10–20 % of the film thickness

for the films with the thickness measured in micrometers is not a good rule. However, when the indentation depth is deeper than 1 μm , the deformation of the substrate has an effect on extracting the mechanical properties of the film from the indentation test for very thin films. Saha and Nix²⁶ examined the effects of the substrate on determining the hardness and elastic modulus of thin films with nanoindentation. They found that the effect of the substrate hardness on the film hardness was negligible in the case of soft films and the substrate hardness affected the measured film hardness in the case of a hard film on a soft substrate.

Compared to hardness, the nanoindentation measurement of the elastic modulus of thin films was more strongly affected by the substrate. Recently, with respect to an elastic-plastic film applied to an elastic substrate system, some researchers^{23,27,28} have proposed the techniques that allow us to extract a film's elastic-plastic properties, taking into account the influence of the elastic substrate from a conical indentation test using the finite-element method (FEM). In this study, elastic properties and the limits (E and σ_f) of YBCO-based films with/without BaMnO_3 defects as pinning centers were designated with the finite-element method (FEM) and nanohardness experiments according to the theory of indentation. Furthermore, failure (σ_f), contact-deformation characteristics, stress distribution near the contacts of the films depending on the amount of formed BaMnO_3 particles were obtained using an algorithm with FEM and a comparison between the experimental and simulation results of the nanoindentation.

2 EXPERIMENTAL PROCEDURE

Initially, (100) STO single-crystalline substrates with dimension of 10 mm \times 10 mm \times 0.75 mm were rinsed in acetone using a standard ultrasonic cleaner. After that, the solutions were deposited on the substrates using a dip-coating process with a withdrawal speed of 0.3 cm/s in a vacuum atmosphere. The deposited gel films were converted to an epitaxial pure YBCO and a YBCO film with BaMnO_3 nanoparticles through a combination of calcining and heat-treatment procedures. After that, the structural development of the produced thin films was investigated with the X-ray diffraction (XRD-Rigaku D/MAX-2200/PC) patterns that were recorded using the Co K_α irradiation (the wavelength, $\lambda = 0.178897$ nm), with the scanning range between $2\theta = 10^\circ$ and 90° . The surface topographies and additional-particle effects on the microstructure of the films were examined with a high-resolution scanning electron microscope SEM (JEOL JSM 6060). The hardness and Young's modulus of the produced thin films were measured under the peak load of 300 μN three times with the CSM Berkovich nanoindentation tester (the loading-unloading test mode) to determine the additional-particle effects on the mechanical properties.

3 INDENTATION MODELING OF YBCO-BASED THIN FILMS

A simulation of YBCO-based thin-film indentation analysis exposed very important mechanical properties such as the maximum (fracture-fracture) strength that influenced the mechanical stability of the coated superconductor under service conditions. The elastic modulus and hardness of YBCO-based thin films could be determined from the instrumented indentation with the loading-unloading curves. However, the maximum stress, the stress-strain relationship, the substrate and the thickness effect on the characteristic loading-unloading curves could not be obtained from the experimental results. At this time, researchers used a simulation and finite-element modeling with the developed algorithms. Normally, until the 2000 s, a finite-element analysis of an indentation problem was applied to bulk ceramic and metallic-based materials. However, after the development of thin-film technologies and materials had increased, the determination of mechanical properties of films and coatings became more focused. For instance, thin-film-based technologies provide for a higher performance, a

higher density and a smaller overall size of a micro-system package. Although thin films are increasingly used for the sake of performance, functionality and size, it is important to understand the mechanical behavior of thin films to address the reliability concerns.

The indentation analysis of YBCO-based thin films was started with a design of an axisymmetric model. A diamond conical surface with a half-apex angle of 70.3° was used to model the widely used Berkovich indenter. In addition, the thicknesses of YBCO-based thin films and substrates were 300 nm and 5000 nm, respectively, and the ratio of the film thickness to the substrate was

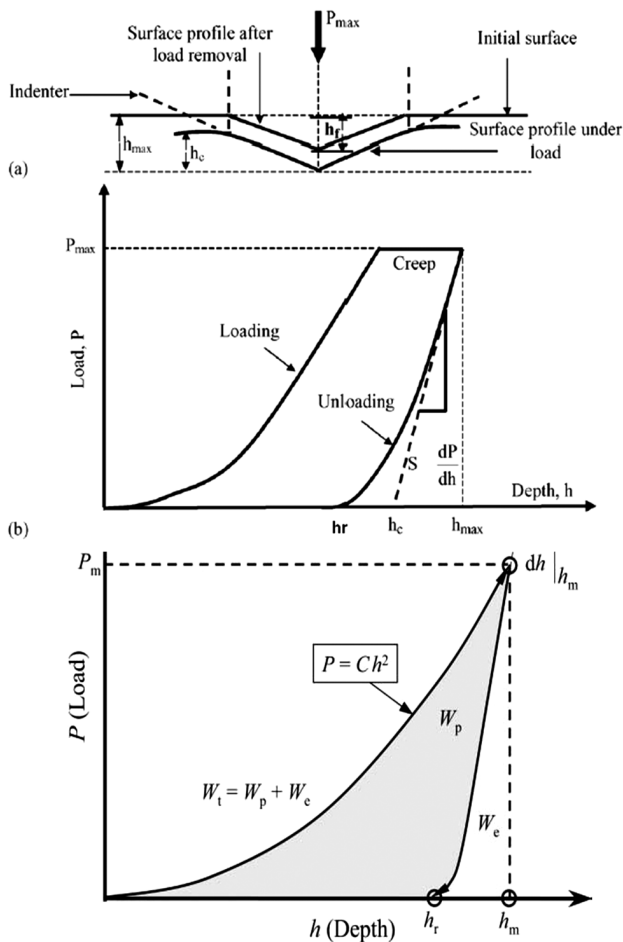


Figure 1: Characteristic indentation curve and representation of the parameters

Slika 1: Značilna krivulja vtiskovanja in predstavljeni parametri

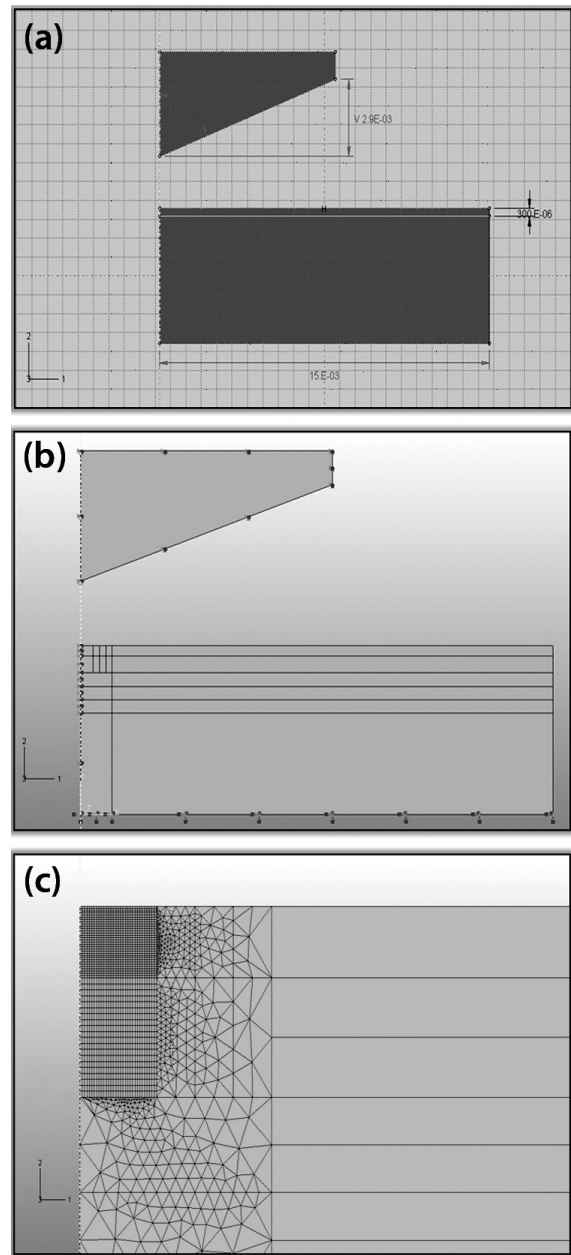


Figure 2: Finite-element model of YBCO-based thin films on an STO single-crystal substrate

Slika 2: Model končnih elementov tanke plasti na osnovi YBCO na monokristalni podlagi STO

6 % in this model. The substrate dimensions (both width and height) are taken to be at least 16 times larger than those of the film, so as to simulate a semi-infinite substrate (**Figure 2a**). On the other hand, four different material inputs were loaded to the model as a pure YBCO thin film, a YBCO thin film with 0.05 g Mn, a YBCO thin film with 0.10 g Mn and a YBCO thin film with 0.15 g Mn (BaMnO_3). The input data of the material properties of the axisymmetric thin-film model with a substrate and an equivalent cone are listed in **Tables 1** and **2**. Elastic modules were experimentally determined from the indentation unloading curves for four different YBCO-based thin-film models. So, the determined elastic modules were loaded with Poisson's ratio as the material elastic properties in the finite-element simulation. While fixing the elastic properties presented in **Table 2** for each sample, the maximum stresses (failures) of YBCO-based thin films were changed to determine the same penetration force/depth curve with the experimental indentation analysis.

The properties of the contact region between the indenter and the surface of a thin film/ substrate system could be designed in the assembly and interaction modulus of the Abaqus package program. The contact areas of YBCO-based thin films were divided into partitions. As known from the indentation-analysis theory, a fine-mesh design could be applied to the mesh part so as to create the partitions near the contact region. The contact regions of YBCO-based thin films were calculated as the dimensions of 300 nm \times 400 nm (thickness \times length). After this area determination (depending on the indentation depth), the whole model began to partition from the contact region to the substrate with dimensions of 500 nm and 400 nm, respectively (**Figure 2b**). This partitioned model can be used for different element-type

and region determinations for a fine-mesh design of a contact area. At the same time, interaction properties for the indenter and the film surface are established as the finite-sliding formulation and surface-to-surface constraint-enforcement method. The contact property of the entire model was assumed to be tangential, being frictionless between the indenter and the surface of a film.

As the main aim of the study was to obtain the stress distributions and force-depth curves of YBCO thin films, the mesh design of the entire model became important, especially when a problematic region included a contact between two separated surfaces. As we already know, the instrumented indentation analysis was carried out with a diamond indenter that penetrated the surface of a thin film at the nanoscale, deforming the contact region, not the whole surface, plastically under the applied load. The importance of a divided surface near a contact region required very correct and sensitive results for simulated loading-unloading curves of YBCO-based thin films. For that reason, the elements were the finest in the central contact area and became coarser outwards for the entire model and a magnified view of the contact region can be seen in **Figure 2**. According to **Figure 2c**, the contact region was meshed as a structured CAX4R element type, A-4 node bilinear axisymmetric quadrilateral, reduced integration and hourglass control with 2, 4, 8, 16, 32 and 40 numbers for a determination of the indentation depth and load dependency on the mesh-element number. In this model, as presented in **Figure 2c**, the contact-region size of YBCO-based thin films was 300 nm \times 400 nm. When the element number increased from 2 to 40, the element size was decreased from approximately 200 nm to 10 nm. The smallest element size and the total element number were 10 nm and 3764, respectively, which enabled an accurate determination of the real-impression size.

Table 1: Indentation-experiment results for YBCO-based superconducting thin films

Tabela 1: Rezultati eksperimentalnega vtiskovanja v superprevodno plast na osnovi YBCO

Material	Force (μN)	Max. depth (nm)	Res. depth (nm)	Film thickness (nm)	Hardness (HV)	Indentation hardness (GPa)	Young's modulus (GPa)
Pure YBCO thin film	300	40.24 ± 6.4	30.12 ± 7.8	292 ± 9	695 ± 28	12.51 ± 4.8	88.54 ± 3.1
YBCO thin film with 0.05 g Mn		42.32 ± 9.4	32.11 ± 8.7	297 ± 5	525 ± 16	8.21 ± 1.2	83.41 ± 1.8
YBCO thin film with 0.10 g Mn		42.45 ± 5.9	33.53 ± 4.4	294 ± 6	495 ± 21	5.75 ± 1.1	79.11 ± 1.9
YBCO thin film with 0.15 g Mn		47.04 ± 6.1	37.48 ± 5.7	305 ± 8	454 ± 18	3.88 ± 0.8	76.47 ± 1.3

Table 2: Material properties of the entire model

Tabela 2: Lastnosti materiala za celoten model

Material type	Elastic modulus (GPa)	Poisson ratio (ν)	Maximum stress (GPa)	Ratio of maximum stress to elastic modulus
Pure YBCO thin film	88.54	0.261	7.50–9.50	0.0847–0.1073
YBCO thin film with 0.05 g Mn	83.41		6.50–9.00	0.0779–0.1079
YBCO thin film with 0.10 g Mn	79.11		5.00–6.75	0.0632–0.0853
YBCO thin film with 0.15 g Mn	76.47		2.75–4.25	0.0360–0.0556
STO substrate	278	0.238	–	–
Equivalent cone	1040	0.07	–	–

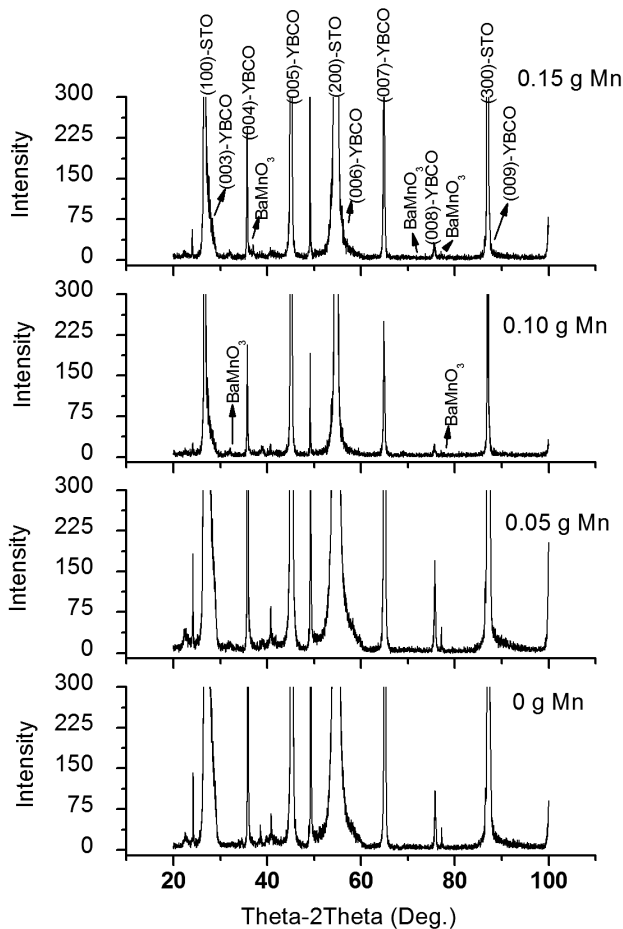


Figure 3: Phase analysis of YBCO-based superconductor thin films with additional particles

Slika 3: Fazna analiza superprevodne tanke plasti na osnovi YBCO z dodanimi delci

4 RESULTS AND DISCUSSION

4.1 Characterization of YBCO-based thin films

Details of the phase analysis of YBCO-based thin films are shown in **Figure 3** relating to the pure YBCO, and the YBCO with 0.05 g, 0.10 g and 0.15 g of BaMnO_3 nanoparticles on the STO single-crystal substrate. XRD patterns illustrate that YBCO films have (001) and parallel plane reflections for the pure YBCO thin film. The major diffraction peaks corresponding to the (001) parallel plane was developed. In addition, no second phases such as $\text{Y}_2\text{Cu}_2\text{O}_5$, BaF_2 and CuO were found, and only the pure YBCO phase was formed. Apart from that, BaMnO_3 perovskite peaks with a low intensity were determined on account of the Mn doping effect. On the other hand, the surface analysis of YBCO-based thin films indicated that structural defects could react as nanodots or nanoparticles (due to the Mn addition) along the c -axis of a YBCO film as presented in **Figure 4**. Since Mn reacts with Ba and a BaMnO_3 perovskite structure forms in the YBCO film during the heat-treatment process, the microstructures of superconducting thin films were changed as expected.

4.2 Instrumented indentation results of YBCO-based thin films

Since the general purpose is to determine the mechanical properties such as the Young's modulus and hardness of the pure YBCO thin film and the YBCO thin films with a Mn addition (Mn reacts as BaMnO_3), an instrumented nanoindentation test was used. At this time, the importance of the applied load became apparent. The indentation response of YBCO-based thin films on the

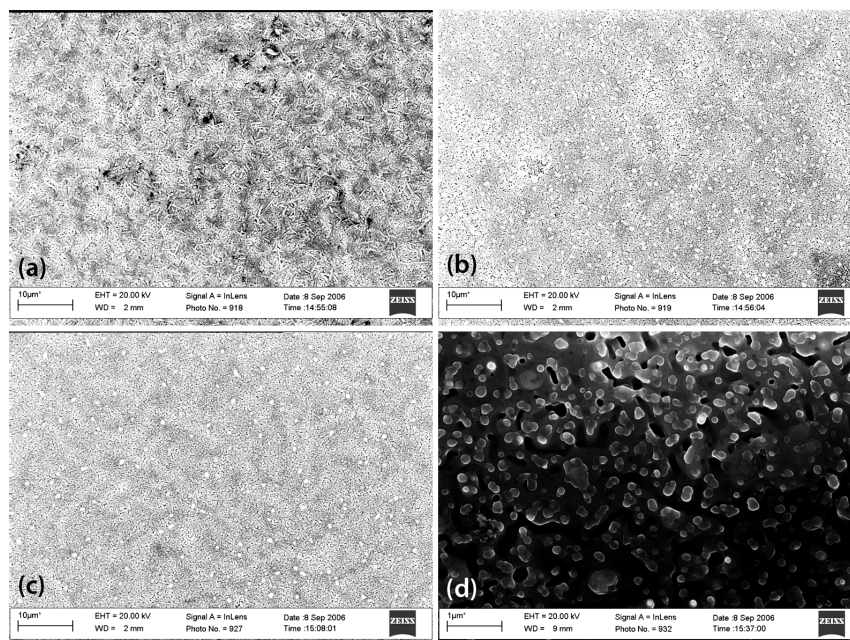


Figure 4: Surface analysis of YBCO-based superconductor thin films with additional particles

Slika 4: Analiza površine superprevodne tanke plasti na osnovi YBCO z dodanimi delci

STO substrate is a complex function of the elastic and plastic properties of both the film and the substrate and it is crucial to understand how the intrinsic mechanical properties of the film can be determined from the overall mechanical response of the film/substrate system. As the values of the elastic modulus and hardness, determined from indentations, do not depend on the value of h (indentation depth) and, therefore, on the value of the maximum load, the indentation depth should not exceed 10–20 % of the film thickness, otherwise the results will be affected by the properties of the substrate. Another parameter that can influence the indentation test is the surface roughness. It has a very active role in the indentation experiment at the nanoscale. If the surface roughness is bigger than the maximum indentation depth for the applied load, the curve has a very scattered loading and unloading part. According to the surface analysis, the surface roughness of the pure YBCO thin film is (21 ± 5) nm.

As presented in **Table 1**, the ratio of the indentation depth to the film thicknesses is applicable for the instrumented indentation with the 300 μ N applied load. The smoothing procedure was applied to all of the instrumented indentation results of the samples. The loading-unloading (load-displacement) curves of YBCO thin films under the 300 μ N applied peak load are shown in **Figure 5**, at the nanometer scale, three times and the total test time was 60 s. The maximum and residual indentation depths of the YBCO thin film were increased from (40.24 ± 6.4) nm to (47.04 ± 6.1) nm and from (30.12 ± 7.8) nm to (37.48 ± 5.7) nm, respectively, by increasing the Mn content in the structure (**Table 1**). The ratios of the indentation depth to the film thickness of the YBCO thin film, the YBCO with 0.05 g Mn, the YBCO with

0.10 g Mn and the YBCO with 0.15 g Mn were 13.78 %, 14.14 %, 14.43 % and 15.04 %, respectively. Furthermore, the elastic modulus and instrumented hardness of YBCO thin films were decreased from (88.54 ± 3.1) GPa to (76.47 ± 1.3) GPa and from (12.51 ± 5.1) GPa to (3.88 ± 0.8) GPa under the 300 μ N applied load as listed in **Table 1**. The loading and unloading parts of the curves have some fluctuations due to the surface roughness and porosity of YBCO-based thin films. For that reason the standard deviations were added to all the indentation-test characteristics, such as the maximum indentation depth, the residual depth, the elastic modulus and the instrumented hardness of the films.

According to the results, the indentation hardness of the films decreased with the increasing Mn content in the film structure. Depending on the Mn content, the maximum indentation depth, the residual depth and the indentation hardness were changed scientifically. Since the Mn content increased in the microstructures of YBCO-based films, the intensity of BaMnO_3 phases in the X-ray analysis increased. Furthermore, the SEM analysis showed that the BaMnO_3 phase structure dispersed and agglomerated in the YBCO thin-film structure. So, the characteristic indentation curves of YBCO-based thin films changed depending on the Mn content and the BaMnO_3 phase structure. As expected, BaMnO_3 reacted as a defect, becoming the pinning center in the structure. When the defect concentration increased due to the increased Mn content, the stability of the structure and interatomic bonding mechanism changed to particle-doped YBCO-based thin films. Although the lattice parameter was very close to YBCO, the BaMnO_3 based structure in YBCO thin films caused some distortion (the residual stress) and irregularities. Although the indenta-

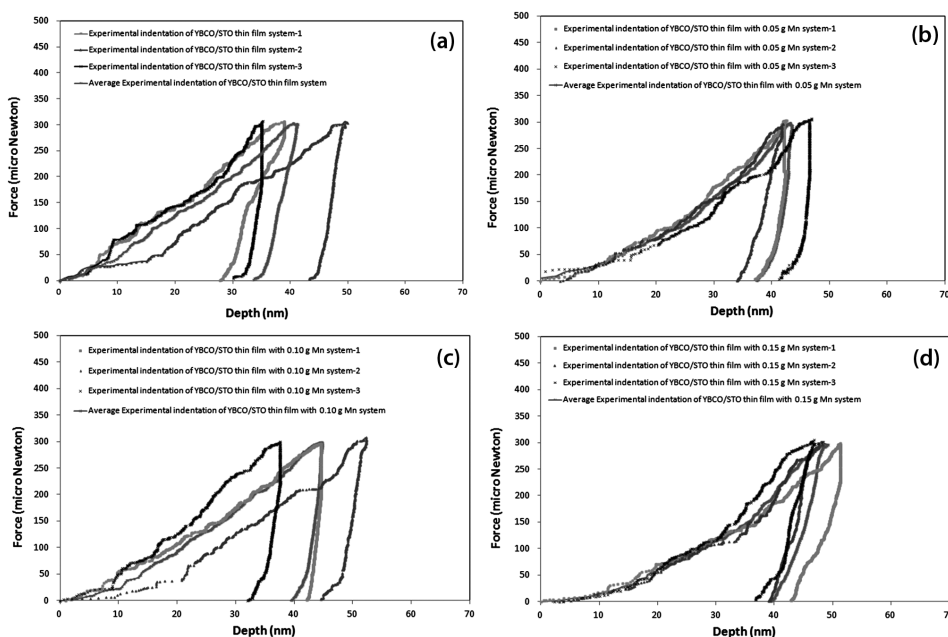


Figure 5: Indentation curves of YBCO-based thin films on the STO single-crystal substrate
Slika 5: Krivulje vtiskovanja tanke plasti na osnovi YBCO na monokristalni podlagi STO

tion load was fixed at 300 μN , the indentation hardness was decreased as if the indentation size effect had influenced the mechanical properties. Since the hardness is accepted as an inherent material property, it should not vary with the indentation load and size but can change with different phase formations. A decrease in the hardness due to the increasing BaMnO_3 content in the YBCO thin-film structure caused differences in the indentation depth. According to this explanation, it can be concluded that the pure YBCO thin film is harder and more brittle than the BaMnO_3 films. As presented in **Figure 6**, the indentation hardness of YBCO-based thin films decreased from 12.51 GPa to 3.88 GPa depending on the Mn content in the structure. The elastic-modulus variation of YBCO-based thin films is also demonstrated in **Figure 6**. Although hardness was very sensitive to the maximum indentation depth and thickness ratio of the samples, changing from 12.51 GPa to 3.88 GPa, the elastic modulus of YBCO-based thin films did not show any sharp decrease. However, as listed in **Table 1**, the elastic modulus of the pure YBCO, the YBCO with 0.05 g Mn, the YBCO with 0.10 g Mn and the YBCO with 0.15 g Mn was 88.54 GPa, 83.41 GPa, 79.11 GPa and 76.47 GPa, respectively. However, the references about the mechanical properties of this material, particularly the yield strength and the stress-strain curve, are scarce.

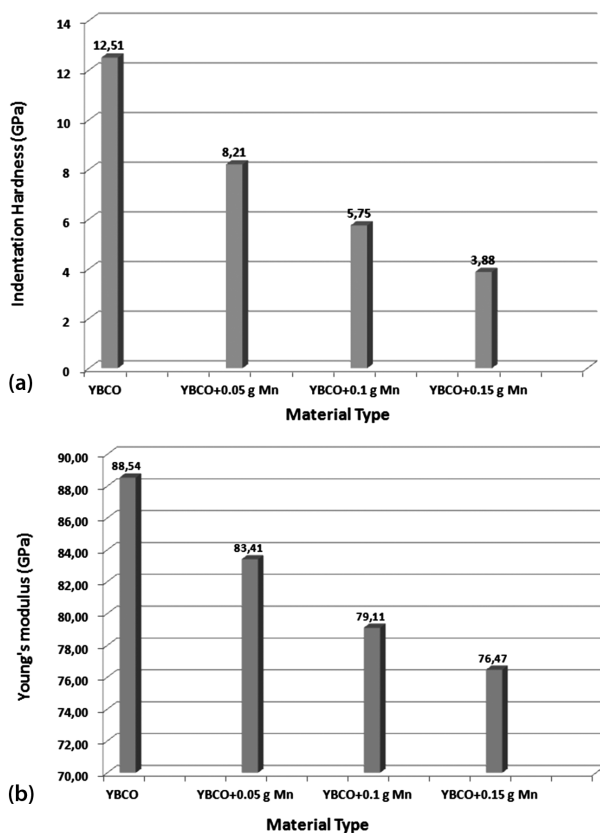


Figure 6: Indentation-hardness and elastic-modulus variations of YBCO-based thin films

Slika 6: Spreminjanje trdote in modula elastičnosti tanke plasti na osnovi YBCO

The mechanical properties (the hardness, the Young's modulus and the fracture toughness) of YBCO samples were examined with the techniques such as ultrasound²⁹ X-ray diffraction³⁰ and nanoindentation.³¹ The reported values of the Young's modulus for Y-123 are within the range of $E = 40\text{--}200$ GPa. This large scatter may be due to the residual porosity and poor contact between the grains.³² Other authors,³³ also using nanoindentation, reported a value of $E = 171\text{--}181$ GPa for the YBCO samples textured with the Bridgman technique, which is in agreement with Johansen, who applied between 30 mN and 100 mN. Nanohardness values in the range of 7.8–8.0 GPa at the maximum loads of 30 mN were recently reported by Lim and Chaudhri³⁴ for a bulk, single-crystal YBCO. Roa et al.³³ found a hardness value of (8.9 ± 0.1) GPa using nanoindentation on the YBCO samples textured with the Bridgman technique.^{32–37}

4.3 FEM results of indentation

The depth-sensing instrumented nanoindentation technique provided a continuous record of the variation in the indentation load and the penetration depth into the specimens. This technique has attracted considerable attention in recent years due to its high resolution at a low-load scale with respect to determining the elastic modulus and hardness of thin films. The importance of the mechanical stability of superconductor thin films with/without additional particles under service condition was exposed during the experimental work and finite-element modeling.

Additional particles behave as defect centers increasing the superconducting properties under a given temperature as explained above. While increasing superconducting properties with additional particles, in this study they are Mn (BaMnO_3) particles, the elastic modulus and the hardness of thin films decreased from 88.54 GPa to 76.47 GPa, 12.51 GPa and 3.88 GPa. However, the variations in the plastic properties of YBCO-based thin films with additional particles could not be determined with the instrumented indentation test. For that reason, the finite-element modeling of YBCO-based thin films with and without BaMnO_3 particles was carried out using the Abaqus 6.10-1 package program, taking into account the experimentally determined elastic properties of the films.

According to the depth analysis, indentation with a different element number and size for FEM, 40 elements with the element size of 10 nm, was chosen, due to its sensitivity at the nanometer scale, for the simulated loading and unloading curves of the pure YBCO thin film and the YBCO thin films with 0.05 g, 0.10 g and 0.15 g Mn. **Figure 7** shows that the simulated maximum and residual indentation depth variations for the four different YBCO-based thin films depend on the maximum stress rises under the 300 μN indentation load. According to the FEM indentation analysis, the maximum depth values decreased from 40.74 nm to 39.58 nm, 43.13 nm to 41.36 nm, 44.89 nm to 42.84 nm and

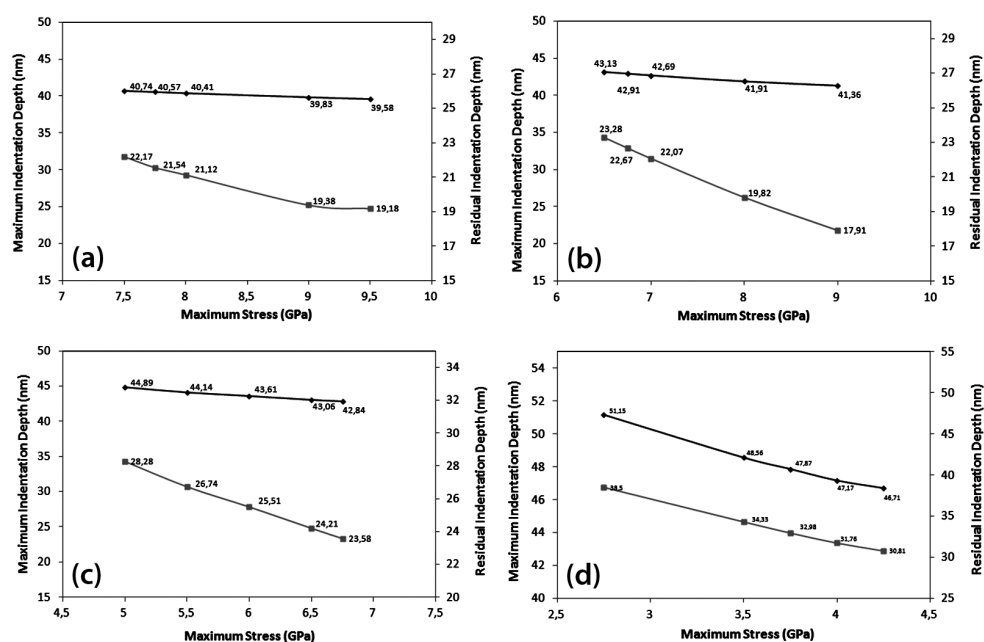


Figure 7: Depth analysis of the FEM model for YBCO-based thin film
Slika 7: Analiza globine s FEM-modelom pri tanki plasti na osnovi YBCO

51.15 nm to 46.71 nm due to an increase in the maximum stress value from 2.75 GPa to 9 GPa, respectively, for the material input data of the pure YBCO thin film and the films with Mn additions. On the other hand, the residual indentation depth of thin films decreased from 22.17 nm to 19.18 nm, 23.28 nm to 17.91 nm, 28.28 nm to 23.58 nm and 38.50 nm to 30.81 nm under the conditions of the same indentation-analysis input data (**Figures 7a, b, c and d**). However, the increases in the Mn content in the structures of YBCO-based thin films caused significant variations in mechanical properties. When the indentation results for the pure YBCO-based thin film and the film with the addition of 0.15 g Mn are compared under the same simulation conditions, it is found that the maximum and residual depths were increased from 40.74 nm to 51.15 nm and from 19.18 nm to 30.81 nm (**Figure 7**), respectively. It means that the ductility or the plastic-deformation properties of YBCO-based thin films increased due to the increased Mn content in the thin-film structure or the BaMnO₃ formation during the production procedure of the instrumented indentation.

Depending on the experimental set-up used to perform the indentation, the loading and unloading characteristics of the $P-h$ curve, and thus the material properties estimated from the analysis of the $P-h$ curves, could be obtained at varying levels of accuracy. Thus, the sensitivity of the estimated elasto-plastic properties to the variations in the input parameters obtained from the $P-h$ curves is an important issue. In the FEM study, the structural model of the instrumented indentation test was performed as an axisymmetric and, therefore, two-dimensional model. The indentation process is complex,

so simplifications and assumptions have to be made to achieve a low numerical cost but, of course, sufficient accuracy. For the time being, the problem is idealized: it was assumed that the surface of the specimen was ideally smooth, whereas in reality a certain roughness may be present as well, e.g., thin films of four different YBCOs. The indenter is an equivalent cone and, furthermore, isothermal conditions are adopted. The model set-up is described below. First, the appropriate boundary conditions were selected and the contact to be modeled was defined. All the simulations were carried out under the load-controlled conditions. Two reasons can be given for this: First, a real-indentation experiment is hard to execute under displacement-controlled conditions, i.e., up to the maximum displacement. Second, regarding the numerical cost and accuracy, neither displacement-controlled nor load-controlled experiments show an important advantage. A force-depth ($P-h$) curve is a straightforward characterization of indentation results that can be precisely obtained with the instrumented indentation equipment. As described above, the surfaces of YBCO-based thin films were ideally smooth. However, the instrumented indentation results are affected by the surface roughness of materials. Both loading and unloading parts of indentation curves can have more scattered data depending on the ratio of the indentation depth and roughness to the film thickness. **Figure 8a** presents both indentation and simulation results of pure YBCO-based thin films under the same condition of instrumented indentation. The same maximum penetration depth was obtained by setting E at 88.54 GPa and the maximum stress at 8.00 GPa for the experimental and simulation analyses (**Table 2**) for the pure YBCO thin film. The surface-roughness effect on the indentation

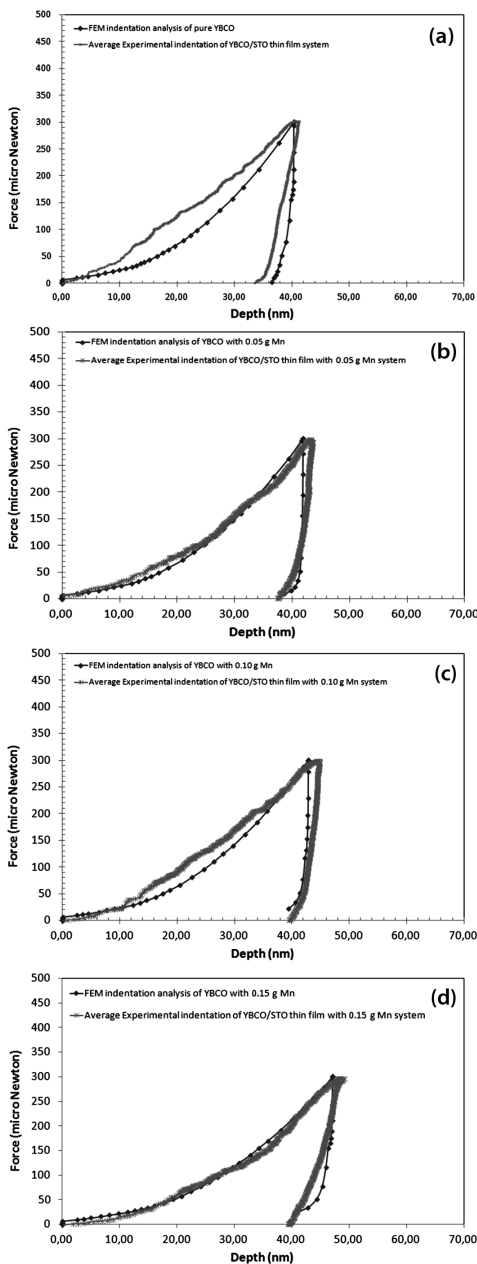


Figure 8: Comparison of experimental and simulation indentation curves

Slika 8: Primerjava eksperimentalnih in simuliranih krivulj vtiskovanja

simulation could not be seen due to the choice of an ideally smooth surface. According to the experimental indentation results, h_{\max} and h_r were (40.24 ± 6.4) nm and (30.12 ± 7.8) nm, respectively, for the $300 \mu\text{N}$ applied load. Similarly, the finite-element modeling of the pure YBCO-based thin-film indentation had the maximum and the residual indentation depths of 40.41 nm and 32.27 nm. Good agreement was found between the maximum indentation depth and the loading curves of pure YBCO-based thin films, having an error of 0.4 %. In addition, when the average experimental-indentation

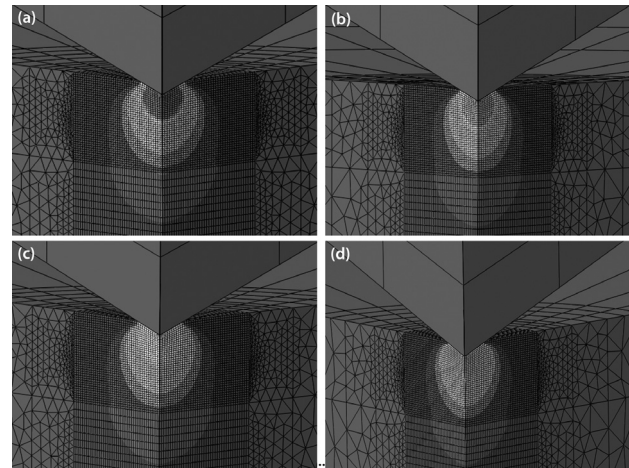


Figure 9: Stress-strain distributions on the contact regions between the indenter and the surfaces of the films

Slika 9: Razporeditev napetost – raztezek na področju kontakta med vtisnim telesom in površino tanke plasti

loading/unloading was considered, this error value was graphically obtained as 7 %, as presented in **Figure 8a**. This may be due to the differences in the maximum strength or due to the use of a constitutive model of both YBCO-based thin films, like the elastic/perfect plastic one without any strain-hardening exponent. On the other hand, **Figures 8b, c and d** show instrumented (the average for three different regions) and simulation indentation results for the YBCO-based thin films with 0.05, 0.10 and 0.15 g Mn under the $300 \mu\text{N}$ applied load. The experimentally determined maximum and residual indentation depths for YBCO-based thin films were (42.31 ± 9.4) nm and (32.11 ± 8.7) nm, (42.45 ± 5.9) nm and (33.53 ± 4.4) nm, and (47.04 ± 6.1) nm and (37.48 ± 5.7) nm, respectively. According to the FEM indentation results, the maximum and residual indentation depths for the YBCO-based thin film with Mn were 42.69 nm and 38.61 nm, 42.84 nm and 39.42 nm, and 47.17 nm and 40.43 nm, in line with the material input data from **Table 2**. When the average curves of the indentation were considered, the loading parts of the curves were much closer to the numerically determined ones.

With respect to the pure YBCO thin-film indentation results, the unloading part of the curves was separated as it was modeled without a strain hardening exponent. The strain hardening exponent of ceramics and, especially, oxide thin films was close to zero. As expected, ceramics- and oxide-based materials did not plastically deform and harden with deformation like the metals. Additionally, they showed brittle failures at the maximum stress. The main aim of the FEM study of indentation was to obtain the same experimental and numeric loading/unloading curves for YBCO-based thin films, while the elastic and plastic properties of the model were iterated according to **Table 2**. Depending on the material-property variation listed in **Table 2** for the FEM model, the maximum stress of YBCO-based films was

changed from 2.75 GPa to 9.50 GPa for different Mn additions. When the Mn content in the structure increased from 0 g to 0.15 g, allowing a BaMnO₃ formation, the maximum stress of the films decreased from 8.00 GPa to 4.00 GPa.

Stress distributions near the contact region of the indented material and the indenter give very important information about the simulation of the experimental indentation. The effects of the maximum depth, the residual depth and the film thickness on the substrate-film system under the applied load could be observed when the field-output request of the indentation analysis was undertaken depending on the steps of the simulations. **Figure 9** shows the Von Mises equivalent stress distributions for the pure YBCO-based thin film and the YBCO with 0.05 g, 0.10 g and 0.15 g Mn under the 300 μ N applied load at the contact regions. According to the analysis of the indentation, firstly, the indenter approached and made a contact with the surface. Secondly, the indenter was penetrating the surface until a load of 300 μ N was reached. As seen in **Figure 9**, the stress distribution shows yielded elements near the contact region for the indenter and the surface. It is understood that if an increase in the stress formation approaches the set maximum stress during the loading step, the plastically deformed part of the contact region can be analyzed easily when the unloading step of the simulation has finished. The maximum stresses for the pure YBCO and the ones with additional Mn were applied to the FEM model, described in **Table 2** as 7.50–9.50 GPa, 6.50–9.00 GPa, 5.00–6.75 GPa and 2.75–4.25 GPa, respectively. The same penetration force/depth curves were obtained with the instrumented indentation and simulation for the above films when the maximum stresses were loaded into the Abaqus 6.10-1 program in the following order: 8.00 GPa, 7.00 GPa, 6.75 GPa and 4.00 GPa.

5 CONCLUSION

In this study, finite-element modeling (FEM) of the indentation was applied to estimate the failure stress/stress distribution relation at the contact region between an indenter and a surface of YBCO-based thin films on an STO single-crystal substrate, and obtain the same force/penetration depth curve with an indentation experiment to determine the additional-particle effects on both structural and mechanical properties. So, the following results were obtained:

- XRD patterns show that YBCO films have (001) and parallel plane reflections for both the pure YBCO and the YBCO with a BaMnO₃ thin film.
- SEM micrographs indicate structural defects comprised of the nanodots or nanoparticles of BaMnO₃ along the *c*-axis of a YBCO film. These properties result in an enhanced pinning over the pure YBCO film.

- The calculated Young's modulus of YBCO-based thin films with/without BaMnO₃ decreased down to the range of 88.54–76.41 GPa, with the increased Mn content in the microstructure. In addition, the indentation-hardness values of the films were decreased from 12.51 GPa to 3.88 GPa depending on the Mn content.
- The finite-element-analysis results showed that the maximum, or failure, stress of YBCO-based thin films decreased due to the increased Mn content in the microstructure. The yield stresses of the pure YBCO thin film, the YBCO thin film with 0.05 g Mn, the YBCO thin film with 0.10 g Mn and the YBCO thin film with 0.15 g Mn were found to be 8.00 GPa, 7.00 GPa, 6.75 GPa and 4.00 GPa, respectively, by comparing the experimental work and numerical load-penetration-depth analysis under the applied load of 300 μ N.

6 REFERENCES

- ¹ G. Blatter, M. V. Feigelman, V. B. Geshkenbein, A. I. Larkin, V. M. Vinokur, Vortices in high-temperature superconductors, *Rev. Modern Phys.*, 66 (1994), 1125
- ² C. S. Pande, Microstructural aspects of high and low T_c Superconductor, *Mater. Phys. Mech.*, 2 (2000), 1
- ³ E. Sheriff, R. Prozorov, Y. Yeshurun, A. Shaulov, G. Koren, C. Chabaud-Villard, Magnetization and flux creep in thin YBa₂Cu₃O_{7-x} films of various thickness, *J. Appl. Phys.*, 82 (1997), 4417
- ⁴ T. Araki, I. Hirabayashi, Review of a chemical approach to YBa₂Cu₃O_{7-x} coated superconductors-metalorganic deposition using trifluoroacetates, *Superconducting Science and Technology*, 16 (2003), 71–94
- ⁵ T. Araki, T. Kato, T. Muroga, T. Niwa, T. Yuasa, H. Kurosaki et al., Carbon Expelling scheme and required conditions for obtaining high-Jc YBa₂Cu₃O_{7-x} film by metalorganic deposition using trifluoroacetates, *IEEE Transactions on Applied Superconductivity*, 13 (2003) 2, 2803–2808
- ⁶ E. Celik, E. Avci, Y. S. Hascicek, Growth Characteristic of ZrO₂ Insulation Coatings on Ag/AgMg Sheathed Bi-2212 Superconducting Tapes, *Mat. Sci. Eng. B*, 110 (2004), 213–220
- ⁷ X. M. Cui, B. W. Tao, J. Xiong, X. Z. Liu, J. Zhu, Y. R. Li, Effect of annealing time on the structure and properties of YBCO films by the TFA-MOD method, *Physica C*, 432 (2005), 147–152
- ⁸ A. Verdyan, Y. M. Soifer, J. Azoulay, E. Rabkin, M. Kazakevich, Nanohardness and Crack Resistance of HTS YBCO Thin Films, *Transaction and applied superconductivity*, 15 (2005) 2, 3585–3588
- ⁹ J. J. Roa, E. Jiménez-Piqué, X. G. Capdevila, M. Segarra, Nanoindentation with spherical tips of single crystals of YBCO textured by the Bridgman technique: Determination of indentation stress-strain curves, *Journal of the European Ceramic Society*, 30 (2010), 1477–1482
- ¹⁰ N. Güçlü, U. Kölemen, O. Uzun, S. Çelebi, Work of indentation approach for investigation of mechanical properties of YBCO bulk superconductor at cryogenic temperatures, *Physica C*, 433 (2005), 115–122
- ¹¹ O. Uzun, U. Kölemen, S. Çelebi, N. Güçlü, Modulus and hardness evaluation of polycrystalline superconductors by dynamic microindentation technique, *Journal of the European Ceramic Society*, 25 (2005), 969–977
- ¹² S. J. Bull, Nanoindentation of coatings, *Journal of Physics D: Applied Physics*, 38 (2005), 393–413

- ¹³ A. M. Korsunsky et al., On the hardness of coated systems, *Surface & Coatings Technology*, 99 (1998), 171–183
- ¹⁴ J. Chen, S. J. Bull, A critical examination of the relationship between plastic deformation zone size and Young's modulus to hardness ratio in indentation testing, *Journal of Materials Research*, 21 (2006), 2617–2627
- ¹⁵ J. Chen, S. J. Bull, On the factors affecting the critical indenter penetration for measurement of coating hardness, *Vacuum*, 83 (2009), 911–920
- ¹⁶ W. C. Oliver, G. M. Pharr, An Improved Technique for Determining Hardness and Elastic Modulus Using Load and Displacement Sensing Indentation Experiments, *J. Mater. Res.*, 7 (1992) 6, 1564–1583
- ¹⁷ A. E. Giannakopoulos, S. Suresh, Determination of elastoplastic properties by instrumented sharp indentation, *Scripta Materialia*, 40 (1999) 10, 1191–1198
- ¹⁸ F. Sen, E. Celik, M. Toparli, Transient thermal stress analysis of CeO₂ thin films on Ni substrates using finite element methods for YBCO coated conductor, *Materials and Design*, 28 (2007), 708–712
- ¹⁹ C. Gamonpilas, E. P. Busso, On the effect of substrate properties on the indentation behaviour of coated systems, *Materials Science and Engineering A*, 380 (2004) 1–2, 52–61
- ²⁰ N. Panich, Y. Sun, Effect of penetration depth on indentation response of soft coatings on hard substrates: a finite element analysis, *Surface and Coatings Technology*, 182 (2004) 2–3, 342–350
- ²¹ W. W. Gerberich, J. C. Nelson, E. T. Lilleodden, P. Anderson, J. T. Wyrobek, Indentation induced dislocation nucleation: the initial yield point, *Acta Materialia*, 44 (1996) 9, 3585–3598
- ²² N. A. Fleck, J. W. Hutchinson, A phenomenological theory for strain gradient effects in plasticity, *Journal of the Mechanics and Physics of Solids*, 41 (1993) 12, 1825–1857
- ²³ D. J. Ma, K. W. Xu, J. W. He, J. Lu, Evaluation of the mechanical properties of thin metal films, *Surface and Coatings Technology*, 116–119 (1999), 128–132
- ²⁴ F. M. Borodich, L. M. Keer, C. S. Korach, Analytical study of fundamental nanoindentation test relations for indenters of nonideal shapes, *Nanotechnology*, 14 (2003) 7, 803–808
- ²⁵ V. M. Kindrachuk, B. A. Galanov, V. V. Kartuzovl, S. N. Dub, On elastic nanoindentation of coated half-spaces by point indenters of non-ideal shapes, *Nanotechnology*, 17 (2006) 4, 1104–1111
- ²⁶ R. Saha, W. D. Nix, Effects of the substrate on the determination of thin film mechanical properties by nanoindentation, *Acta Materialia*, 50 (2002) 1, 23–38
- ²⁷ M. H. Zhao, N. Ogasawara, N. Chiba, X. Chen, A new approach to measure the elastic-plastic properties of bulk materials using spherical indentation, *Acta Materialia*, 54 (2006) 1, 23–32
- ²⁸ X. Chen, J. J. Vlassak, Numerical study on the measurement of thin film mechanical properties by means of nanoindentation, *J. Mater. Res.*, 16 (2001), 2974
- ²⁹ F. Sandiumenge, T. Puig, J. Rabier, J. Plain, X. Obradors, Optimization of flux pinning in bulk melt textured 1–2–3 superconductors; Bringing dislocations under control, *Adv. Mater.*, 12 (2000), 375
- ³⁰ S. Block, G. J. Piermarini, R. G. Munro, W. Wong-Ng, The bulk modulus and Young's modulus of the superconductor Ba₂Cu₃YO₇, *Adv. Ceram. Mater.*, 2 (1987), 601
- ³¹ T. H. Johansen, Flux-pinning-induced stress and magnetostriction in bulk superconductors, *Supercond. Sci. Technol.*, 13 (2000), 12
- ³² H. M. Ledbetter, M. W. Austin, S. A. Kim, M. Lei, Elastic constants and Debye temperature of polycrystalline yttrium barium copper oxide (YBa₂Cu₃O_{7-x}), *J. Mater. Res.*, 2 (1987), 786
- ³³ J. J. Roa, X. G. Capdevila, M. Martinez, F. Espiell, M. Segarra, Nanohardness and Young's modulus of YBCO samples textured by the Bridgman technique, *Nanotechnology*, 18 (2007), 385
- ³⁴ Y. Y. Lim, M. M. Chaudhri, Nanohardness mapping of the curved surface of spherical macroindentations in fully annealed polycrystalline oxygen-free copper, *Phys. Status. Solid. A: Appl. Res.*, 194 (2002), 19–29
- ³⁵ W. A. Ortiz, R. Zadorosny, W. A. C. Passos, P. C. de Camargo, C. M. Lepienski, Vortex matter in a thin film of YBCO with columnar indentations-very small and moderate field regimes, *Physica C: Superconductivity*, 437–438 (2006), 254–257
- ³⁶ F. Yu, K. W. White, R. Meng, Mechanical characterization of top-seeded melt-textured YBa₂Cu₃O_{7-δ} single crystal, *Physica C: Superconductivity*, 276 (1997) 3–4, 295–308
- ³⁷ Y. M. Soifer, A. Verdyan, I. Lapsker, J. Azoulay, AFM investigations of the morphology features and local mechanical properties of HTS YBCO thin films, *Physica C: Superconductivity*, 408–410 (2004), 846–847

EFFECT OF VISCOSITY ON THE PRODUCTION OF ALUMINA BORATE NANOFIBERS VIA ELECTROSPINNING

VPLIV VISKOZNOSTI NA IZDELAVO ALUMINIJEVOOKSIDNOBORATNIH NANOVLAKEN Z ELEKTROSPININGOM

Mehtap Ozdemir^{1,2}, Erdal Celik¹, Umit Cocen¹

¹Dokuz Eylul University, Faculty of Engineering, Dept. of Metallurgical and Materials Engineering, 35160, Buca, Izmir, Turkey

²Gediz University, Faculty of Engineering, Dept. of Electrical and Electronics Engineering, 35665, Seyrek, Izmir, Turkey
mehtap.koklu@gediz.edu.tr

Prejem rokopisa – received: 2012-11-06; sprejem za objavo – accepted for publication: 2013-04-02

Alumina borate ($\text{Al}_{18}\text{B}_4\text{O}_{33}$) nanofibers have been successfully fabricated with the electrospinning method using a solution that contains polyvinyl alcohol (PVA) and aluminium acetate stabilized with boric acid. The effect of the viscosity on the production of alumina borate nanofibers was investigated and the optimum parameters were determined to obtain the best fibers. DTA/TG analyses were performed to determine the heat-treatment regime. The morphology of the fibers was evaluated by SEM analyses, the phase structure of the fibers was obtained using XRD and the chemical bonding structure was determined by FTIR. On the whole, the results indicated that the viscosity of a solution is an important parameter for producing a homogeneous and thin fiber, while the calcination temperature has a significant effect on the phase structure of the fibers.

Keywords: nanomaterials, nanofiber, electrospinning, $\text{Al}_{18}\text{B}_4\text{O}_{33}$

Aluminijevoooksidnoboratna ($\text{Al}_{18}\text{B}_4\text{O}_{33}$) nanovlakna so bila uspešno izdelana z elektrospining metodo z uporabo raztopine, ki vsebuje polivinil alkohol (PVA) in aluminijev acetat, stabiliziran z borovo kislino. Preiskovan je bil vpliv viskoznosti na izdelavo aluminijevoooksidnoboratnih nanovlaken in določeni so bili optimalni parametri za pridobivanje najboljših vlaken. Za določitev režima toplotne obdelave so bile izvršene DTA/TG-analize. Morfologija vlaken je bila ocenjena s SEM-analizo, fazna struktura vlaken je bila dobljena z rentgensko difrakcijo (XRD), strukture kemijskih vezav pa so bile ugotovljene s FTIR. Rezultati so pokazali, da je viskoznost raztopine pomemben parameter za proizvodnjo homogenih in tankih vlaken, medtem ko ima temperatura kalcinacije pomemben vpliv na strukturo faz vlaken.

Ključne besede: nanomateriali, nanovlakna, elektrospining, $\text{Al}_{18}\text{B}_4\text{O}_{33}$

1 INTRODUCTION

One-dimensional materials, such as nanowires, nanorods, nanowhiskers and nanofibers, have stimulated great interest due to their importance in basic scientific research and their potential in technological applications. They are expected to play an important role as both interconnector and functional components in the fabrication of nanoscale devices. Many unique properties have already been proposed or demonstrated for this class of materials, such as a high elastic modulus and tensile strength, chemical inertness, excellent resistance to oxidation/corrosion, a low thermal expansion coefficient, a high thermal conductivity, a good stability at high temperature and low-cost production.¹⁻⁵ Of these properties, aluminium borate is a famous material as it can be used in a variety of applications, such as high-temperature structural components, nonlinear optical and tribological materials, electronic ceramics and reinforced composite materials.^{2,6}

Due to the superior properties of alumina borates, nanostructures such as filaments, powders, fibers, whiskers and wires, they have been synthesized using various techniques. These are vapor-solid reaction,⁷ powder

technology,⁸ the electrospinning technique,^{3,9} the flux method with microwaves,¹⁰ calcination techniques.^{1,6,11-14} Dai et al.³ and Tuttle et al.⁹ have produced approximately alumina borate nanofibers 550 nm using the electrospinning technique. Because it is difficult to fabricate the extremely fine nanofibers using electrospinning, we have investigated the effect of viscosity on the process to produce thin nanofibers.

Electrospinning is the most preferred technique to produce nanofibers with a diameter ranging from 20 nm to 1000 nm. The diameter of the fibers depends on the process parameters, such as the viscosity of the solution, the applied electric field, the distance between the collector and the needle, and the feeding rate of the solution.¹⁵ The viscosity of the solution and its electrical properties determine the extent of the elongation of the solution that affects the diameter of the resultant electrospun fibers.¹⁶ Moreover, the viscosity of the solution is very important for its spinability. When the viscosity is too high, pumping of the solution through the syringe needle becomes difficult, which may result in drying of the solution at the tip of the needle before the electrospinning initiates. Additionally, the applied electric field affects the morphology of the fibers that are obtained. Generally, a

higher voltage leads to greater stretching of the solution due to the greater coulombic forces in the jet as well as the stronger electric field. These have the effect of reducing the fiber diameter.¹⁶ On the other hand, the distance between the tip and the collector plate must be high for thin fibers. The feed rate determines the amount of solution available for electrospinning. When the feed rate is increased, the fiber diameter increases.¹⁶

In this study we attempt to form alumina borate nanofibers and investigate the effect of viscosity during the electrospinning process on the nanofiber morphology and spinability, and the effect of temperature on the phase structure.

2 EXPERIMENTAL

PVA solutions were prepared in different concentrations in mass fractions, i.e., 6 %, 8 %, and 10 %, by dissolving the PVA in 80 °C distilled water and cooling down to room temperature while stirring for 24 h. Next, 1 g of aluminium acetate stabilized with boric acid ($\text{CH}_3\text{CO}_2\text{Al}(\text{OH})_2 \cdot 1/3\text{H}_3\text{BO}_3$) was added to the PVA solution and the stirring was continued until a transparent and homogeneous solution was obtained. The viscosities of solutions were determined by CVO 100 Digital Rheometer (Bohlin Instrument).

In order to produce the nanofibers, transparent solutions were immediately loaded into a plastic syringe. A 22-gauge stainless-steel needle was used as a nozzle. The emitting electrode from a power supply was attached to the needle. The grounding electrode from the same power supply was attached to a piece of 316L stainless steel, which was used as the collector plate and was placed approximately 10 cm below the tip of the needle. A high voltage ranging between 20 kV and 30 kV was applied across the needle and a non-woven mat of fine fibers were fabricated. The alumina borate/PVA fibers were heat treated at 800–1200 °C for 2 h in air using an electrical tube furnace to obtain the alumina borate fibers.

The prepared solution used in the electrospinning was dried at 100 °C for 1 h and the obtained powder was subjected to thermogravimetric differential thermal analysis (DTA/TG) (Shimadzu DTG-60H) to define the reaction type of the intermediate temperature products and to use a suitable process regime. The chemical bonding structures of the fibers before and after the heat treatment were determined with Fourier Transform Infrared Spectroscopy (FTIR) (Perkin Elmer Spectrum BX). The X-ray diffraction (XRD) measurements were performed for the crystal-phase identification (Rigaku D/Max-2200/PC) with $\text{CuK}\alpha$ radiation. The morphology and the average fiber diameter of the nanofibers were characterized using a scanning electron microscope (JSM-6060 JEOL).

3 RESULTS AND DISCUSSION

The solution viscosity plays a major role in producing a uniform nanofiber. For a low viscosity it is common to find beads along the fibers. As the viscosity increases, a gradual change in the shape of the fibers takes place until smooth fibers are obtained.¹⁶ For spinability the viscosity must be neither very high nor very low. The viscosity of the prepared solutions at various concentrations are determined in the range 0.17–2.34 Pa s (**Figure 1**). In the **Figure 1** it is clear that as the concentration of the solution increases, the viscosity of the solution increases. Furthermore, the viscosity does not change with time, indicating the stability of the solution, which is an important property for obtaining uniform fibers. While the viscosity of the solution prepared by dissolving 6 % PVA is very low for spinability, it is very high for the solution prepared by dissolving 10 % PVA. However, the viscosity of the solution prepared by dissolving 8 % PVA is convenient for spinability.

Figure 2 shows SEM images of heat-treated $\text{Al}_{18}\text{B}_4\text{O}_{33}$ nanofibers that were prepared with solutions that have different concentrations. It is clear that the fibers that were obtained from the 6 % PVA solutions are very thin, but the amount of them is very small. On the other hand, the diameter of the fibers produced from the 10 % PVA solution is very large. These results were consistent with the viscosity analyses. As a result, the solution prepared with 8 % PVA was determined to be the optimum solution and used in the following process.

The DTA/TG analysis of the prepared alumina-borate/PVA solution is shown in **Figure 3**. The DTA curve shows endothermic peaks between 100 °C and 300 °C that indicates the loss of citric acid, which gets stabilized with boric acid in the aluminium acetate. Degradation of the PVA occurs between 300 °C and 600 °C in four steps. A broad endothermic peak in the range 900 °C to

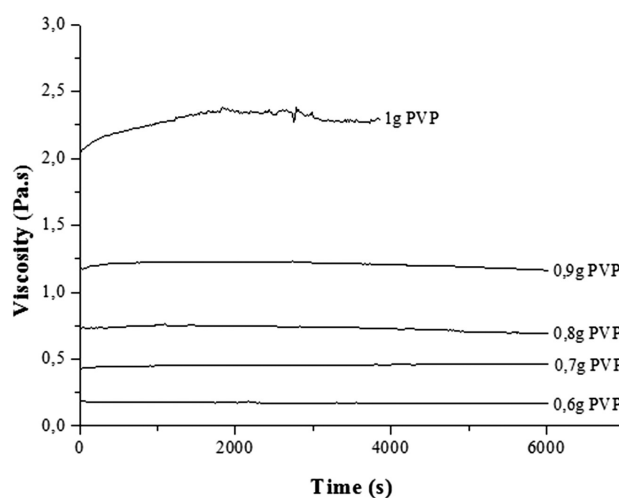


Figure 1: Viscosity of the solutions prepared with mass fractions 6 %, 8 % and 10 % PVA solutions

Slika 1: Viskoznost raztopine, pripravljene z masnimi deleži 6 %, 8 % in 10 % PVA

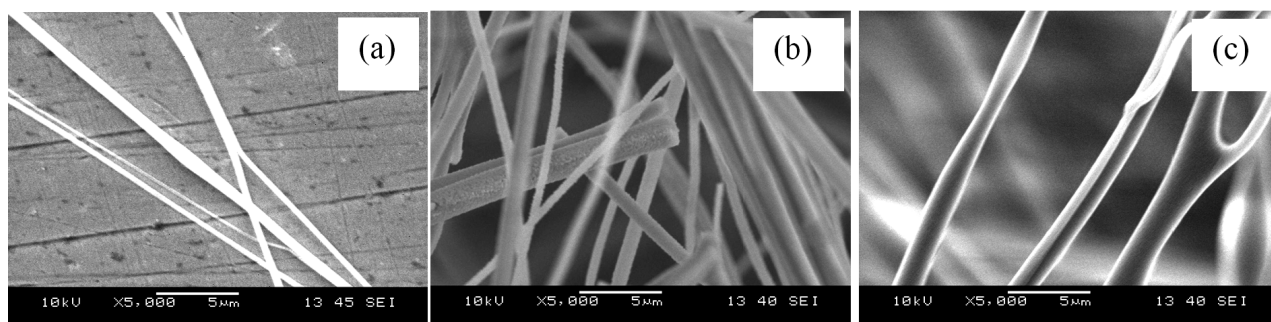


Figure 2: SEM images of nanofibers prepared at: a) 6 %, b) 8 % and c) 10 % concentrations

Slika 2: SEM-posnetki nanovlaken, pripravljenih s koncentracijo: a) 6 %, b) 8 % in c) 10 %

1200 °C indicates the crystallization of the $\text{Al}_{18}\text{B}_4\text{O}_{33}$. According to the studied TG curve, the weight loss of the alumina-borate/PVA solution was determined to be approximately 63 % and it was followed by the removal of the PVA from the sol structure.

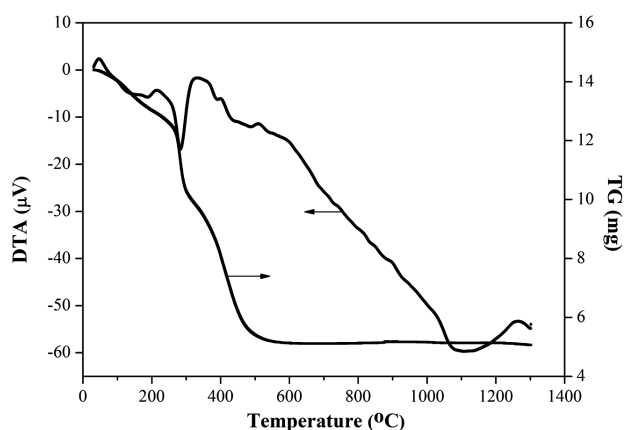


Figure 3: DTA/TG analyses of the prepared solutions prepared with the mass fraction 8 % PVA solution

Slika 3: DTA/TG-analiza pripravljene raztopine, pripravljene z masnim deležem PVA raztopine 8 %

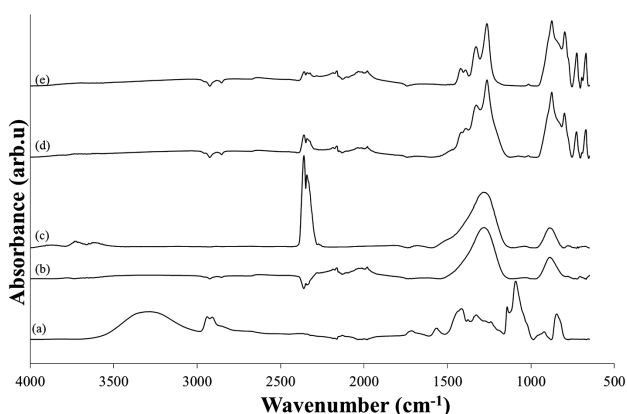


Figure 4: FTIR spectra of: a) PVA, b) alumina-borate/PVA composite fibers and alumina borate fibers heat treated at: c) 800 °C, d) 1000 °C and e) 1200 °C

Slika 4: FTIR-spektri: a) PVA, b) aluminijevoosidni borat/PVA kompozitna vlakna in aluminijevoosidnaboratna vlakna, toplotno obdelana pri: c) 800 °C, d) 1000 °C in e) 1200 °C

Figure 4 shows the FTIR absorption peaks of the PVA, the alumina-borate/PVA composite fibers and the alumina borate fibers heat treated at 800 °C, 1000 °C and 1200 °C. A broad peak at about 3400 cm^{-1} corresponds to the H-OH stretch. The peaks between 1300 cm^{-1} and 1700 cm^{-1} correspond to the characteristic PVA peaks in **Figure 4a**.³ When the PVA is mixed with Al acetate that is stabilized with boric acid the absorption peaks show a change (**Figure 4b**). This indicates that there is an interaction between them. After a heat treatment at 800 °C, there are no PVA peaks because of the degradation of the polymer (**Figure 4c**). When the calcination temperature is increased to 1000 °C and 1200 °C (**Figures 4d** and **4e**), a class of peaks appeared at 650–950 cm^{-1} and 1200–1500 cm^{-1} . These peaks can be attributed to the formation of crystalline alumina borate.³ Furthermore, all the FTIR graphs show a sharp peak at about 2400 cm^{-1} , which corresponds to the CO_2 peaks that appear because of the ambient atmosphere during the analyses.

Figure 5 presents a typical XRD pattern of the products before and after the heat treatment at different temperatures and the pure PVA powder. The characteristic peak of the PVA at $2\theta = 20^\circ$ is shown in **Figures 5a** and **5b**. When the alumina borate/PVA composite fibers

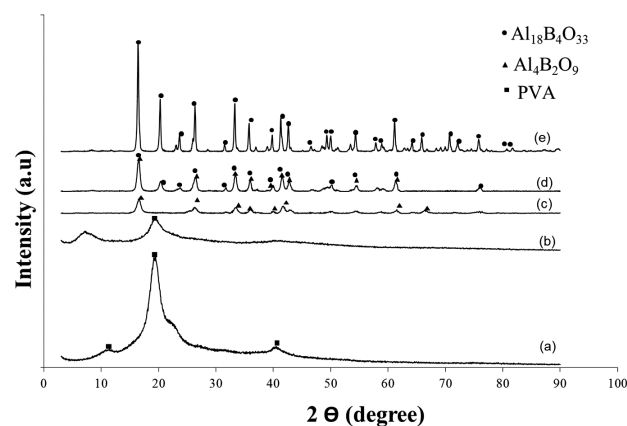


Figure 5: XRD pattern of: a) PVA, b) alumina-borate/PVA composite fibers and alumina borate fibers heat treated at: c) 800 °C, d) 1000 °C, e) 1200 °C

Slika 5: XRD-posnetek: a) PVA, b) aluminijevoosidni borat/PVA kompozitna vlakna in aluminijevoosidnaboratna vlakna, toplotno obdelana pri: c) 800 °C, d) 1000 °C, e) 1200 °C

were heat treated at 800 °C, this peak disappeared and the crystalline $\text{Al}_4\text{B}_2\text{O}_9$ peaks occurred. The peak positions and the relative intensities match well with those of the fiber $\text{Al}_4\text{B}_2\text{O}_9$ (JCPDS 00-047-0319). Nevertheless, as the intensity of the peaks increased with the increase in the calcination temperature from 800 °C to 1000 °C, the crystalline $\text{Al}_{18}\text{B}_4\text{O}_{33}$ formed. At a calcination temperature of 1200 °C, all the XRD peaks belong to crystalline $\text{Al}_{18}\text{B}_4\text{O}_{33}$, which matches with JCPDS 00-053-1233 and 00-032-0003.

4 CONCLUSION

In summary, this study was structured to use the electrospinning technique to produce alumina borate/PVA composite nanofibers. In addition, the effect of viscosity on the spinability and the morphology of the alumina borate/PVA nanofibers were investigated. After a heat treatment at 1200 °C, alumina borate ($\text{Al}_{18}\text{B}_4\text{O}_{33}$) fibers were produced.

On the whole, we found that the viscosity of the prepared solution affects the fiber morphology. The increase in the viscosity depends on the increase of the concentration of the solution, while the spinability of the solution adopts an opposing relation with the dense solution, which leads to clogging of the needle tip. As a conclusion, the viscosity of the PVA polymer solution has a very important effect on the diameters of the nanofibers. In addition, the phase structure of the aluminium borate depends on the calcination temperature.

Acknowledgment

This work was supported by BOREN (National Boron Research Institute) and TUBITAK (Scientific and Technical Research Council of Turkey) project number

105M363. Also, Mehtap Ozdemir acknowledges support from TUBITAK in the framework of the National Scholarship Programmes for PhD Students.

5 REFERENCES

- ¹ J. Wang, G. Ning, X. Yang, Z. Gan, H. Liu, Y. Lin, *Materials Letters*, 62 (2008), 1208–1211
- ² H. Song, J. Luo, M. Zhou, E. Elssfah, J. Zhang, J. Lin, S. Liu, Y. Huang, X. Ding, J. Gao, C. Tang, *Crystal Growth & Design*, 7 (2007), 576
- ³ H. Dai, J. Gong, H. Kim, D. Lee, *Nanotechnology*, 13 (2002), 674–677
- ⁴ E. Elssfah, C. Tang, *J. Phys. Chem. C*, 111 (2007), 8176–8179
- ⁵ C. C. Tang, E. M. Elssfah, J. Zhang, D. F. Chen, *Nanotechnology*, 17 (2006), 2362–2367
- ⁶ J. Wang, J. Sha, Q. Yang, Y. Wang, D. Yang, *Materials Research Bulletin*, 40 (2005), 1551–1557
- ⁷ F. Rohmund, R. E. Smalley, *Journal of Materials Science Letters*, 19 (2000), 921–923
- ⁸ J. M. Mota, M. A. Martinez, F. Velasco, A. J. Criado, *Ceramics International*, 30 (2004), 301–306
- ⁹ R. W. Tuttle, A. Chowdury, E. T. Bender, R. D. Ramsier, J. L. Rapp, M. P. Espe, *Applied Surface Science*, 254 (2008), 4925–4929
- ¹⁰ S. W. Kim, S. G. Lee, J. K. Kim, J. Y. Kwon, H. C. Park, *Journal of Materials Science*, 39 (2004), 1445–1447
- ¹¹ L. M. Peng, X. K. Li, H. Li, J. H. Wang, M. Gong, *Ceramics International*, 32 (2006), 365–368
- ¹² H. S. Song, E. M. Elssfah, J. Zhang, J. Lin, J. J. Luo, S. J. Liu, Y. Huang, X. X. Ding, J. M. Gao, S. R. Qi, C. Tang, *J. Phys. Chem. B*, 110 (2006), 5966–5969
- ¹³ E. M. Elssfah, H. S. Song, C. C. Tang, J. Zhang, X. X. Ding, S. R. Qi, *Materials Chemistry and Physics*, 101 (2007), 499–504
- ¹⁴ E. M. Elssfah, C. C. Tang, J. Zhang, H. S. Song, X. X. Ding, S. R. Qi, *Materials Research Bulletin*, 42 (2007), 482–486
- ¹⁵ D. Li, Y. Xia, *Adv. Mater.*, 14 (2004), 1151–1170
- ¹⁶ S. Ramakrishna, K. Fujihara, W. E. Teo, T. C. Lim, Z. Ma, *An Introduction to Electrospinning and Nanofibers*, World Scientific Publishing Company, United States of America 2005, 69

EFFECTS OF SOLIDIFICATION PARAMETERS ON THE MICRO- AND MACROSTRUCTURE OF THE X19CrMoVNbN11-1 STEEL

VPLIVI PARAMETROV STRJEVANJA NA MAKRO IN MIKROSTRUKTURO JEKLA X19CrMoVNbN11-1

Mitja Kolečnik¹, Aleš Nagode², Grega Klančnik², Jože Medved², Bernarda Janet¹,
Milan Bizjak², Ladislav Kosec²

¹Metal Ravne, d. o. o., Koroška cesta 14, 2390 Ravne na Koroškem, Slovenia

²Faculty of Natural Sciences and Engineering, University of Ljubljana, Aškerčeva cesta 12, 1000 Ljubljana, Slovenia
mitja.koleznik@metalravne.com

Prejem rokopisa – received: 2012-11-27; sprejem za objavo – accepted for publication: 2013-04-15

Differential scanning calorimetry (DSC) of the X19CrMoVNbN11-1 steel was used for determining phase-transformation temperatures. To study the effect of the cooling rate on the shape and chemical composition of primary precipitates with SEM and EDXS, an investigation was made on DSC samples. With a decreasing cooling rate precipitates became shorter and thicker and with a higher cooling rate the contents of Nb and V increased.

The effects of solidification parameters on micro-segregations were investigated on the re-melted steel solidified at different parameters (experimental ingots). The microstructure was examined using SEM and EDXS. A higher volume fraction of segregation is present in the more rapidly cooled steel. In positive segregations the largest increase of the Cr content and a minor increase in the concentrations of Mo and V were observed. The effect of melt superheating on the columnar and equiaxed crystallization zone shares was also investigated. At higher melt temperatures a higher fraction of columnar crystals was present.

Keywords: solidification parameters, transformation temperatures, precipitate shape, segregation, melt superheating, crystallization zones

Za določitev temperatur faznih pretvorb v jeklu X19CrMoVNbN11-1 smo izvedli diferenčno vrstično kalorimetrijo (DSC). Pri vzorcih smo z vrstičnim elektronskim mikroskopom (SEM) in energijsko disperzijsko spektroskopijo rentgenskih žarkov (EDXS) preiskovali vpliv različnih hitrosti ohlajanja na obliko in kemijsko sestavo primarnih karbonitridov. Z manjšo hitrostjo ohlajanja so bili izločki krajši in debelejši. Vsebnost Nb in V v izločkih pa je naraščala z večjo hitrostjo ohlajanja.

Izdelani so bili eksperimentalni ingoti, ki so bili strjeni v različnih razmerah. Preiskovali smo vpliv razmer pri strjevanju na razsežnost izcejanja, ki smo ga ugotavljali z vrstičnim elektronskim mikroskopom in EDXS-analizo. Obseg izcejanja je bil večji pri jeklu z večjo hitrostjo ohlajanja. V pozitivnih izcejah se je najbolj povečala koncentracija Cr, v manjšem obsegu pa se je povečala tudi koncentracija Mo in V. Preiskali smo tudi vpliv pregretja taline na delež kristalizacijskih področij s stebrastimi in enakoosnimi zrnji. Z višjo temperaturo pregretja taline se je povečal delež stebrastih kristalnih zrn.

Ključne besede: vpliv parametrov strjevanja, temperature premen, oblika izločkov, izcejanje, pregretje taline, kristalizacijska področja

1 INTRODUCTION

The vital parts (like the components for steam and gas turbines, steam pipes, boilers, etc.) for thermal power plants must fulfil very high quality standards. The most widely used creep-resistant steels in power plants are martensitic steels with 9 % to 12 % Cr. They have the best combination of physical and elastic properties, a high creep strength, a high resistance against thermal fatigue and a high steam-oxidation resistance.¹⁻⁵ To ensure the adequate properties the minimum structure homogeneity right from the start of a manufacturing process is necessary.

During solidification in industrial conditions, non-equilibrium conditions prevail resulting in chemical inhomogeneities on the macro- and micro-scale (macro- and micro-segregations).⁶⁻⁸ Micro- or crystal segregations represent a change in the concentration of alloying elements across a grain cross-section with low melting

elements on the grain boundaries. The smallest concentration of alloying elements is expected to be found in the core of dendrites. Since the mobility of atoms in the solid phase is rather small and the diffusion times are short, chemical inhomogeneities remain to room temperature. The intensity of segregations and the microstructural evolution in an as-cast sample depends on the solidification rate. Casting parameters also affect the volume fraction of individual crystallization zones in solidified ingots. The anisotropy of columnar zones can decrease the ductility of steel during a plastic deformation.⁹⁻¹¹

2 EXPERIMENTAL WORK

The alloy used in this study was the creep-resistance steel X19CrMoVNbN11-1 with a typical chemical composition shown in **Table 1**. Differential scanning calorimetry was used for determining the characteristic

Table 1: Typical chemical composition of the X19CrMoVNbN11-1 steel in mass fractions, w/%

Tabela 1: Tipična kemijska sestava jekla X19CrMoVNbN11-1 v masnih deležih, w/%

C	Si	Mn	Cr	Mo	Ni	V	Nb	N	B
0.19	0.30	0.55	10.75	0.75	0.5	0.20	0.33	0.08	max. 0.0015

temperatures of solidification, using a Netzsch STA 449 C Jupiter. In **Table 2** the parameters of DSC analyses are given. DSC analyses were performed in a protective atmosphere of volume fraction 99.999 % N₂ and, as a reference, an empty corundum crucible was used. DSC specimens were also used to determine the effects of solidification parameters on the microstructure. Thermodynamic calculations were performed using the ThermoCalc program with an internal thermodynamic database, TCFE7.

Table 2: Parameters of an DSC analysis

Tabela 2: Parametri DSC-analize

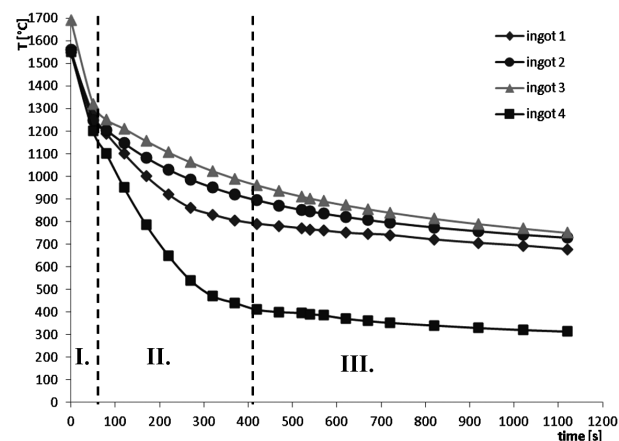
sample	T _{max} /°C	v _{heating} / (K min ⁻¹)	v _{cooling} / (K min ⁻¹)
S1	1550	1	1
S25	1550	25	25
S6P	1600	6	6
S6	1550	6	6

Table 3: Casting parameters of experimental ingots

Tabela 3: Parametri litja eksperimentalnih ingotov

No.	m _{load} /kg	T _{mold} /°C	T _{casting} /°C	Mold isolation
1	11	318	1547	no
2	10.97	280	1560	yes
3	11.02	330	1690	yes
4	8.75	30	1550	no

The experimental ingots of the X19CrMoVNbN11-1 creep-resistant steel were prepared by melting the steel in an inductive vacuum furnace. The steel was solidified under different cooling conditions. To achieve different cooling rates of the castings, different preheated moulds


Figure 1: Cooling rates of ingots

Slika 1: Hitrost ohlajanja posameznega ingota

were used. The casting parameters are shown in **Table 3** and the cooling rates of the ingots are shown in **Figure 1**.

The samples for the investigation of the macro- and microstructure were cut from the ingots without heat treatment. For the metallographic examination of the macrostructure, the steel plates were grinded and etched in a hot 50 % HCl solution at 50 °C. The samples for the microstructural investigation were grinded, polished and etched with the Villela etchant.

The metallographic investigation of the steel was carried out on a scanning electron microscope (SEM), JEOL JSM-5610 with an energy-dispersive x-ray spectrometer (EDXS), GRESHAM Scientific Instruments, model SIRIUS 1YSUTW. The results are given as a quantitative spot (EDXS spectrum) and qualitative EDXS line profile and as mapping analyses.

2.1 Thermodynamic model for M(C, N)

In the CALPHAD approach each phase should be described with a proper thermodynamic model. In this paper emphasis is placed only on the thermodynamic modelling of M(C, N). M stands for the metals mixing on the first sublattice, sublattice #1. M_{a1}(C, N)_{a2} is modelled with two sublattice models with the second sublattice representing the interstitial atoms of C and N. Va stands for vacancy. The carbonitrides present in steels can be modelled with a combination of Fe, Nb, Ti and others on the first sublattice, and C, N and Va on the second one; an example is given for (Fe, Nb, Ti)_{a1}(C, N, Va)_{a2}. The Gibbs free energy, G_m, of such a formula for one formula unit is described with the following equation:¹²

$$G_m = y_{Fe}y_c^0G_{Fe:C} + y_{Nb}y_c^0G_{Nb:C} + y_{Ti}y_c^0G_{Ti:C} + y_{Fe}y_N^0G_{Fe:N} + y_{Nb}y_N^0G_{Nb:N} + y_{Ti}y_N^0G_{Ti:N} + y_{Fe}y_{Va}^0G_{Fe:Va} + y_{Nb}y_{Va}^0G_{Nb:Va} + y_{Ti}y_{Va}^0G_{Ti:Va} + a_1RT(y_{Fe} \ln y_{Fe} + y_{Nb} \ln y_{Nb} + y_{Ti} \ln y_{Ti}) + a_2RT(y_C \ln y_C + y_N \ln y_N + y_{Va} \ln y_{Va}) + EG_m$$

where y_i represents the site fractions of component i on the first or second sublattice (I or II). G_{ij}⁰ is the Gibbs free energy where only i and j are occupying the sublattices. G_m^E represents the excess Gibbs energy. In addition, the term for magnetic contribution can also be added. For a more complex formula with more elements on the first sublattice the Gibbs energy is described below; here a₁ or a₂ represent the site occupancy:

$$G_m = \sum_i \sum_j y_i y_j^0 G_{ij} + RT \left(a_1 \sum_i y_i \ln(y_i) + a_2 \sum_j y_j \ln(y_j) \right) + EG_m$$

In this study the modelling was done using the following formula for carbonitride with an fcc structure:



where in sublattice #1 the major constituents are Nb, Cr, V and in sublattice #2 the major constituents are C and N, with Va as a minor constituent.

3 RESULTS AND DISCUSSION

Differential scanning calorimetry was used for determining transformation temperatures. The increasing heating rate influenced the phase transformation at higher temperatures and with the increasing cooling rate these transformations were moved to lower temperatures.

Table 4 shows the A_{r1} temperatures of the solidification curves.

Table 4: Phase-transformation temperatures

Tabela 4: Temperature faznih premen

sample	S1	S6	S25	S6P
$T_{\max}/^{\circ}\text{C}$	1550	1550	1550	1600
v_s/v_o	1/1	6/6	25/25	6/6
$A_{r1}/^{\circ}\text{C}$	812	823	835	821
$T_{\text{liquidus}}/^{\circ}\text{C}$	1497	1510	1462	1495
$T_{\text{solidus}}/^{\circ}\text{C}$	1492	1493	1443	1480

The metallographic investigation of DSC samples revealed that the cooling rate has a great effect on the shape and chemical composition of the precipitates. Combining the Thermo-Calc software and EDXS analysis, the precipitates were identified as Nb(C, N) with low contents of V and Mo. At the highest cooling rate of 25 K min^{-1} , the precipitates were needle shaped with a diameter of approximately $0.5 \mu\text{m}$ and a length of up to $35 \mu\text{m}$ with a faceted surface. At a lower cooling rate, the precipitates were shorter and thicker, and their surface was less faceted. At the cooling rate of 6 K min^{-1} , the diameter of the precipitates was approximately $1 \mu\text{m}$ and the length was approximately $15 \mu\text{m}$. The precipitates formed at different cooling rates are shown in **Figures 2**

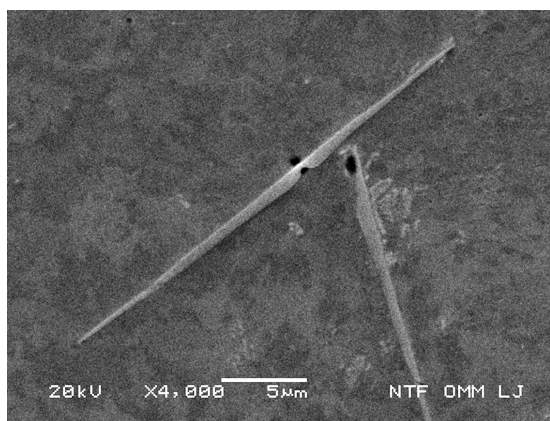


Figure 2: Shape of precipitates at 25 K min^{-1}

Slika 2: Oblika izločkov pri hitrosti ohlajanja 25 K min^{-1}

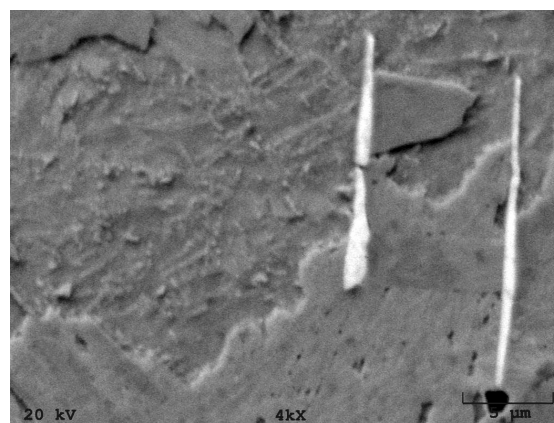


Figure 3: Shape of precipitates at 6 K min^{-1}

Slika 3: Oblika izločkov pri hitrosti ohlajanja 6 K min^{-1}

and **3**. A micro-chemical analysis of the precipitates indicated that at higher cooling rates the contents of Nb and V increased. **Figure 4** shows the concentration ratio of Nb and V $w(\text{Nb})/w(\text{V})$ in the precipitates as a function of the cooling rate. At higher cooling rates the $w(\text{Nb})/w(\text{V})$ ratio was increased indicating that, at a higher cooling rate, the content of Nb in the precipitates increased faster than the content of V.

A comparison of the macro- and microstructures of the experimental ingots was made. In all the ingots three distinct crystallization zones were found. In the central region there was a zone of fine, randomly oriented, equiaxed grains and, in the outer region, a zone of columnar grains was observed. On the ingot surfaces, a zone of very fine equiaxed grains (chill crystals) was observed. The degree of melt superheating has the strongest influence on the shares of the columnar and equiaxed zones in the experimental ingots (in our case the temperatures of melt superheating and the casting temperatures from **Table 3** are equal). The smallest share of the columnar zone was found in ingot 1 with the melt heated to the lowest temperature (1547°C). The highest share of the columnar zone was found in ingot 3 with the overheating of up to 1690°C . **Table 5** shows the shares

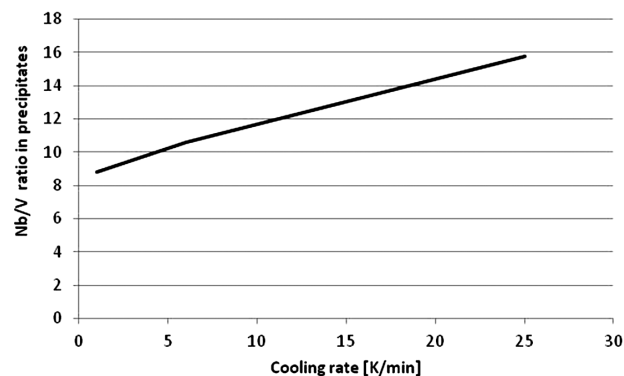


Figure 4: Concentration ratio of Nb and V in precipitates as a function of the cooling rate

Slika 4: Razmerje koncentracije Nb in V v izločkih v odvisnosti od hitrosti ohlajanja

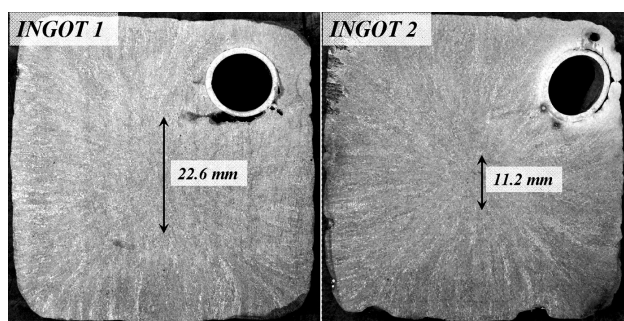


Figure 5: Equiaxed and columnar zones in ingots 2 and 3

Slika 5: Primerjava deleža področij s stebrastimi in enakoosnimi zrnji v ingotih 2 in 3

of the columnar zones ($w_{trans}/\%$) in each ingot. In Figure 5 a comparison of the macrostructures of ingots 2 and 3 can be observed together with the corresponding diameters of the equiaxed zones. At a higher degree of melt superheating more heterogeneous nuclei dissolve. The smaller is the concentration of heterogeneous nuclei in a melt, the higher the degree of supercooling that is needed for the solidification to start. A higher degree of supercooling increased the share of the columnar zone in a solidified ingot.

Table 5: Share of the columnar zone in ingots

Tabela 5: Delež področja stebrastih zrn v posameznem ingotu

	ingot 1	ingot 2	ingot 3	ingot 4
$T_{casting}/^{\circ}C$	1547	1560	1690	1550
$w_{trans}/\%$	88.9	90.7	95.5	89.9

The cooling curves of experimental ingots are shown in Figure 1. It can be seen that every curve shows three distinct regions. Region I with the highest slope represents a very intense cooling of the ingots immediately after casting when the melt comes into contact with the wall of the colder metallic mold. However, the steepest slope shows ingot 3 with the highest casting temperature. In region II the cooling rates slow down due to the generated crystallisation heat. In this region the cooling rates depend on the casting parameters (the mold temperature and the mold isolation) (Table 3). In this region, the highest drop in the temperature is observed for ingot 4 with the coldest mold (not preheated) and without isolation. In region III with the stationary cooling having the lowest cooling rates, a small difference in the slopes of the cooling curves are found except for ingot 4 with an unpreheated mold and without isolation. In all the investigated ingots crystal segregations were observed with the segregation intensity (the volume fraction) depending on solidification parameters. The most intense segregation was found in ingot 4, cast in a cold mold (the highest cooling rate). The least intense segregation was found in ingot 2, cooled with the lowest rate. In the region with the maximum and minimum contents of alloying elements, a micro-chemical analysis was carried out. In Figure 6 the EDXS micro-chemical analysis of

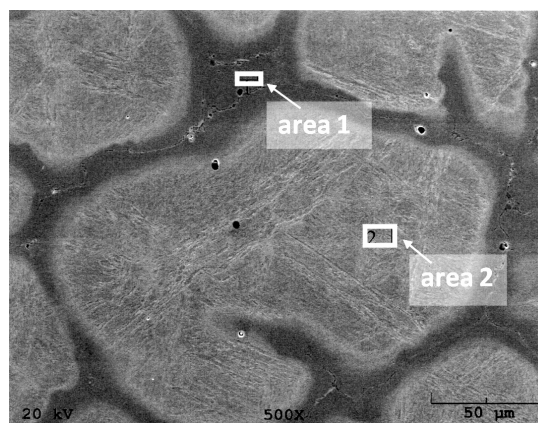


Figure 6: EDXS analysis of the microstructure of ingot 4. Chemical compositions of areas 1 and 2 are in Table 6. The darker area – higher contents of alloying elements.

Slika 6: Mikrokemijska analiza (EDXS) ingota 4. Kemijska sestava področja 1 in področja 2 je podana v tabeli 6. Temnejša območja – povečana koncentracija zlitinskih elementov.

Table 6: Chemical composition (EDXS analysis) of segregations in mass fractions, w/%; see also Figure 6

Tabela 6: Kemijska sestava (EDXS-analiza) izcej v masnih deležih, w/%; glej sliko 6

	Fe	Si	Cr	Mn	Mo	Ni	V	Nb
Area 1	84.45	0.29	13.10	0.32	0.66	0.62	0.29	0.27
Area 2	89.24	0.26	9.03	0.36	0.42	0.48	0.18	0.03

ingot 4 is presented and the chemical composition of the selected areas is given in Table 6. Differences in the chemical composition affect the intensity of etching. Darker areas on Figure 6 are positive segregations with higher chromium contents. The concavity of positive segregations indicates that they were solidified last with the formation of one carbide eutectic with the lowest melting point (Figure 7). The largest variation between the alloying elements was measured for the concentration of Cr. The difference between the maximum and minimum Cr contents was much more explicit for the rapidly cooled ingot. For ingot 2 the difference in the concentration of Cr was approximately 2.5 % and for

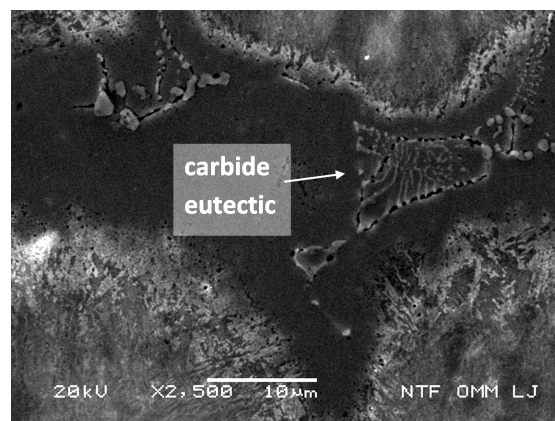


Figure 7: Positive segregations with carbide eutectic

Slika 7: Pozitivne izceje s karbidnim evtetikom

ingot 4 the difference was approximately 4 % (mass fractions). The segregation of Cr in each ingot was characterised with the segregation index I_s (1) and segregation rate I_{sg} (2):

$$I_s = \frac{C_{\max}}{C_{\min}} \quad (1)$$

$$I_{sg} = \frac{C_{\max} - C_{\min}}{C_0} \quad (2)$$

where C_{\max} is the maximum, and C_{\min} is the minimum content, while C_0 is the average content of Cr in each ingot. The results are shown in **Table 7**. The concentrations of V and Mo were also increased in positive segregations.

Table 7: Mass index and level of the Cr segregation in ingots

Tabela 7: Masni indeks ter stopnja izcejanja Cr za posamezen ingot

	$C_{\max}/\%$	$C_{\min}/\%$	$C_0/\%$	I_s	$I_{sg}/\%$
ingot 1	11.12	9.47	9.98	1.17	16.54
ingot 2	12.88	10.41	10.24	1.24	24.44
ingot 3	11.83	10.10	10.10	1.17	17.12
ingot 4	13.10	9.03	10.02	1.45	40.63

The change in the concentration of the alloying elements in the dendrite cross-section was determined with the qualitative EDXS line analysis of ingot 4 in **Figure 8**. The line intersects one positive segregation in two areas (between 20–40 μm and between 56–68 μm along with the carbide at approximately 62). There is a significant increase in the concentrations of Cr and Mn and a minor increase in the concentrations of V in the

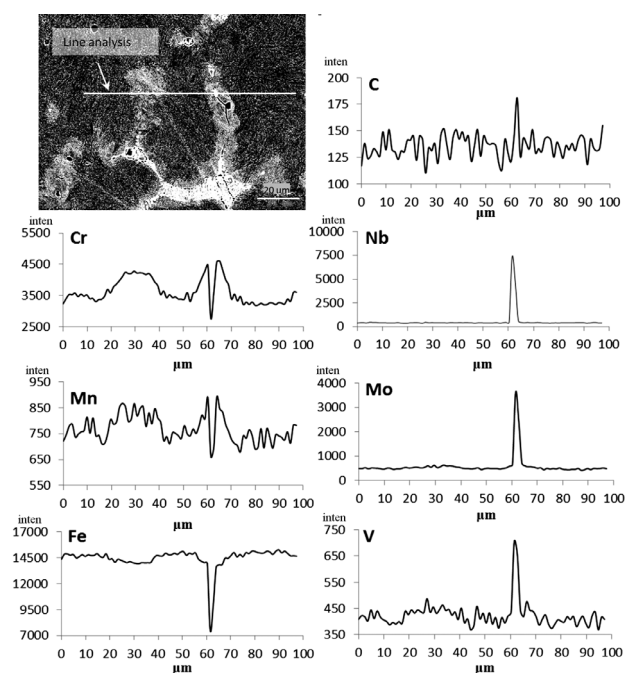


Figure 8: Qualitative EDXS line analysis of ingot 4

Slika 8: Kvalitativna črtna EDXS-analiza ingota 4

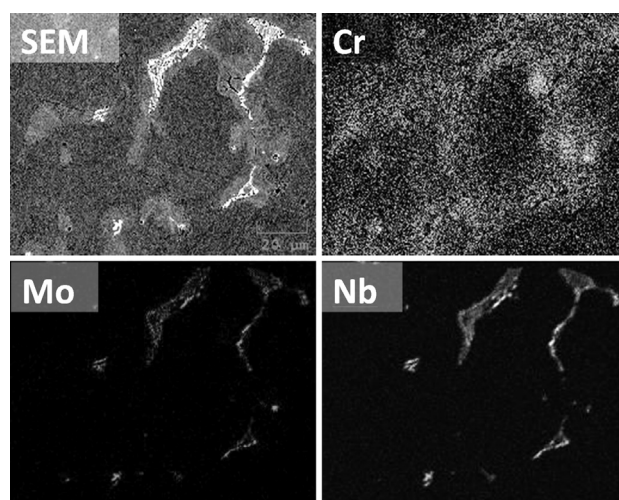


Figure 9: Qualitative EDXS mapping analysis of the segregations with carbide eutectic

Slika 9: Kvalitativna ploskovna EDXS-analiza izcej s karbidnim evtetikom

areas of positive segregation. At the carbide intersection, a large increase in the carbide-forming elements, like Nb, Mo and V, is present. In the microstructure in **Figure 8** carbide eutectic is also presented. In **Figure 9** a qualitative mapping analysis of carbide eutectic is shown, indicating increased contents of Mo, Nb and V like for the carbide in the line analysis from **Figure 8**.

4 CONCLUSIONS

To determine the influence of solidification parameters, the macro- and microstructure as well as the chemical homogeneity of the creep-resistant steel of grade X19CrMoVNbN11-1 were investigated.

- The heating and cooling rates affect the solidification interval. By increasing the heating rate, the solidification interval is shifted to a higher temperature, while with a higher cooling rate the solidification interval is shifted to a lower temperature.
- The cooling rate affects the shape and chemical composition of precipitates. At the higher cooling rates the precipitate shapes were long faceted needles, and at a lower cooling rate the precipitates were shorter and thicker. They were identified as the Nb(C, N)-type precipitates.
- At the higher cooling rates the contents of Nb and V were higher.
- The degree of melt overheating influenced the respective proportions of columnar and equiaxed zones. With higher melt superheating the share of the columnar zones increases.
- At a higher cooling rate the intensity of segregation and the intensity of positive segregations of Cr were greater.
- In the investigated steel the last solidified melt had a eutectic composition.

5 REFERENCES

- ¹ A. Nagode, L. Kosec, B. Ule, G. Kosec, Review of creep resistant alloys for power plant applications, *Metalurgija*, 50 (2011) 1, 45–48
- ² F. Vodopivec, D. A. Skobir, M. Jenko, B. Žužek, M. Godec, Nucleation and growth of $M_{23}C_6$ particles in high-chromium creep resistant steel, *Mater. Tehnol.*, 46 (2012) 6, 633–636
- ³ D. Rojas Jara, 9–12 % Cr heat resistant steels: Alloy design, TEM characterisation of microstructure evolution and creep response at 650 °C, Fakultät für Maschinenbau der Ruhr, Universität Bochum, 2011
- ⁴ R. L. Klueh, R. H. Donald, High-Chromium Ferritic and Martensitic Steels for Nuclear Applications, ASTM International, (2001), 5–27
- ⁵ F. Abe, T. Kern, R. Viswanathan, Creep-resistant steels, Woodhead Pub. Ltd, Cambridge, England 2008
- ⁶ W. Kurz, D. J. Fisher, Fundamentals of solidification, Trans Tech Publications Ltd, Aedermannsdorf 1986
- ⁷ University of Cambridge, Casting: Microstructure and segregation in castings [online]. 2004, [cited 2012-07-26]. Available from World Wide Web: <http://www.doitpoms.ac.uk/tlplib/casting/microsegregation.php>
- ⁸ S. Spaić, Fizikalna metalurgija: zgradba kovinskih materialov, strjevanje kovinskih zlitin, Naravoslovnotehniška fakulteta, Univerza v Ljubljani, Ljubljana 2002
- ⁹ M. Durand-Charre, Microstructure of Steels and Cast Irons, Springer, Paris 2003
- ¹⁰ J. W. Elmer, S. M. Allen, T. W. Eagar, Microstructural development during solidification of stainless steel alloys, *Metallurgical transactions*, 20 (1989), 2117–2131
- ¹¹ H. Biloni, W. J. Boettinger, Solidification, In: R. W. Chan, P. Haasen (eds.), *Physical Metallurgy*, Elsevier Science BV, Amsterdam 1996, 670–842
- ¹² B. J. Lee, Thermodynamic Assessment of the Fe-Nb-Ti-C-N System, *Metallurgical and Materials Transactions A*, 32 (2001), 2423–2439

INFLUENCE OF CUTTING SPEED ON INTENSITY OF THE PLASTIC DEFORMATION DURING HARD CUTTING

VPLIV HITROSTI REZANJA NA INTENZITETO PLASTIČNE DEFORMACIJE MED ODREZOVANJEM

Miroslav Neslušan¹, Ivan Mrkvica², Robert Čep², Mária Čilliková¹

¹University of Žilina, Faculty of Mechanical Engineering, Žilina, Slovakia

²VŠB-Technical University of Ostrava, Ostrava, Czech Republic
miroslav.neslusan@fstroj.utc.sk, robert.cep@vsb.cz

Prejem rokopisa – received: 2013-01-29; sprejem za objavo – accepted for publication: 2013-03-27

The paper deals with an analysis of deformation processes and the aspects related to a chip formation such as the chip thickness, the chip ratio, the shear angle and the chip segmentation during turning the hardened steel 100Cr6. This paper investigates the influence of the cutting speed through a metallographic analysis, a calculation of significant aspects of deformation processes and the resulting experimental study. This experimental study is based on an application of acoustic emission. The results of this study indicate that the cutting speed significantly affects the parameters such as the chip ratio, deformation angle or the speeds in the cutting zone. On the other hand, the experimental study allows an analysis of the specific characters of deformation processes and their real intensity.

Keywords: turning, hardened steel, chip segmentation, acoustic emission

Članek obravnava analizo deformacijskih procesov in vidike pri nastanku odrezka, kot so debelina odrezka, odvzem, rezalni kot in segmentacija odrezkov med struženjem kaljenega jekla 100Cr6. V članku je obravnavan vpliv hitrosti odrezovanja z metalografsko analizo, izračun pomembnih vidikov deformacijskih procesov in temu sledeča eksperimentalna študija. Le-ta temelji na uporabi akustične emisije. Rezultati te študije kažejo pomemben vpliv hitrosti rezanja na parametre, kot so odvzem, deformacije in hitrosti v coni rezanja. Po drugi strani eksperimentalna študija omogoča analizo posebnosti deformacijskih procesov in njihove realne intenzivnosti.

Ključne besede: struženje, kaljeno jeklo, segmentacija ostružkov, akustična emisija

1 INTRODUCTION

With the development of super-hard cutting materials such as ceramics, CBN, PCBN and PCD, etc., the technology of hard turning has attracted considerable interest from several leading manufacturers. In order to specify the potential of this new production technology, several issues of hard turning such as cutting mechanism, tool wear, machined surface integrity, etc., have been recently investigated.^{1,2} One of the significant observations during hard turning, which is different from machining ductile materials, is that consistently cyclic, segmented chips are produced, essentially without any deformation at the shear plane.³⁻⁵

In metal cutting, the principal chip morphologies classified by Komanduri and Brown,⁶ are continuous, serrated chips. In machining, hard and difficult-to-machine materials tend to localize the heat generated due to the strain localization in a narrow band called an adiabatic shear band represented in **Figures 1** and **2**. Adiabatic shear banding investigated by Recht³ is used to describe a localization phenomenon that occurs in the high-strain-rate plastic-deformation processes such as cutting. This phenomenon can be explained in the following way: during a deformation the rate of heat generation is determined by the strain rate, and the heat-

dissipation rate is controlled by the heat conductivity of the material. When the heat-generation rate is larger than the heat-dissipation rate, the temperature increases and the softening associated with such temperature increases as well, exceeding the strain hardening and the catastrophic propagation of the shear occurs. Thermoplastic instability is a significant phenomenon in the segmented chip formation. The thermoplastic instability is caused by a decrease in the flow stress due to the thermal softening associated with an increase in the strain, offsetting

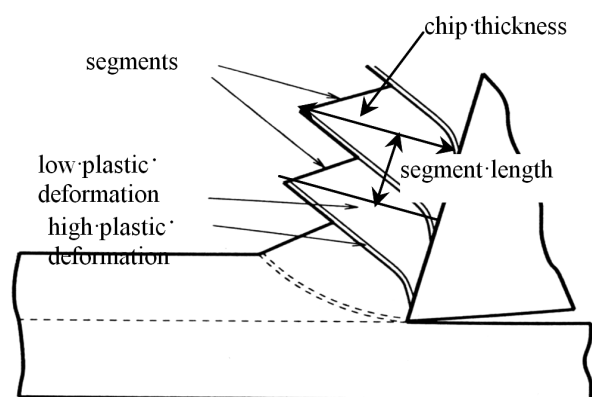


Figure 1: Illustration of a chip formation during hard turning
Slika 1: Prikaz nastanka odrezka pri struženju

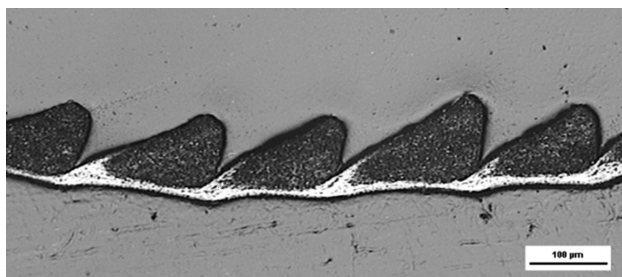


Figure 2: Chips after turning the 100Cr6 (hardened, 62 HRC), SEM, $v_c = 100 \text{ m min}^{-1}$, $f = 0.21 \text{ mm}$

Slika 2: Odrezki po struženju 100Cr6 (kaljeno, 62 HRC), SEM, $v_c = 100 \text{ m min}^{-1}$, $f = 0,21 \text{ mm}$

the strain hardening.⁴ The materials sensitive to a formation of a shear-localized chip can be characterized with poor thermal properties (titanium alloys, maraging steels) and a limited ductility (hardened steels).⁵

A proper understanding of the material-removal mechanisms taking place during hard cutting is essential for a process evaluation. An analysis of the work area is necessary to describe the chip generation in hardened materials. Depending on the cutting parameters and workpiece material properties, cutting may either lead to continuous or discontinuous chip formation.^{2,4,7} Continuous chips are formed during turning conventional soft steels (**Figure 3** – a decrease in the flow stress due to the thermal softening associated with an increase in the strain is less than the associated strain hardening⁴), while hard turning can lead to a formation of segmented chips. **Figures 1** and **2** illustrate a segmented chip during turning the hardened steel 100Cr6. **Figure 2** shows that the plastic deformation inside the segment is low and the material in this area stays nearly untouched. Deformation processes are concentrated in the shear zone, tool-chip contact and tool-workpiece contact. On the other hand, the formation of a continuous chip leads to a more homogenous dissipation of deformation processes across the whole chip (**Figure 3**).

It was found that the total energies entering the cutting processes of conventional and hard turning (derived from the cutting speed and tangential component of the cutting force) are nearly the same.^{8,9} The difference can

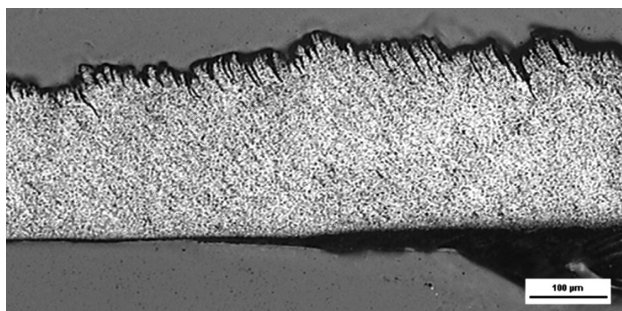


Figure 3: Chips after turning the 100Cr6 (annealed), SEM, $v_c = 100 \text{ m min}^{-1}$, $f = 0.21 \text{ mm}$

Slika 3: Odrezki po struženju 100Cr6 (žarjeno), SEM, $v_c = 100 \text{ m min}^{-1}$, $f = 0,21 \text{ mm}$

be found in the specific character related to the dissipation of this energy. An evaluation of the real intensity of deformation processes should be carried out with respect to the specific character of the chip formation. Intensity of deformation processes can be evaluated from the macroscopic point of view through metallographic observations. This conventional approach allows a calculation of the conventional parameters based on the measurements of chip thickness, undeformed chip thickness and derived parameters (deformation angle, chip speed, chip deformation and others). In this way, the average intensity of deformation processes in the cutting zone (across the whole chip) can be investigated.^{5,8}

An investigation of the real intensity of deformation processes related to the specific cutting zones is quite difficult and can be realized through acoustic emission (AE). The AE non-destructive technique is based on a detection and conversion of these high-frequency elastic waves to electrical signals. The major AE sources^{10,11} in a metal-cutting process are:

- deformation and fracture of work materials in the shear zone, tool-chip and tool-workpiece contacts;
- deformation and fracture of the cutting tool;
- collision, entangling and breakage of chips.

The main advantage of using AE to monitor a machining operation is that the frequency range of an AE signal is much higher than that of the machine vibrations and environmental noises, and does not interfere with the cutting operation.¹⁰ Due to its sensitivity to various contact areas and deformation regions during cutting, the AE signal is the basic tool for process monitoring.

Figures 2 and **3** show that the characters of deformation processes during the conventional soft and hard turnings differ. And so, the aim of this paper is to perform an analysis of the deformation processes in the cutting zone through the conventional metallographic observations and with the AE signal. Moreover, the differences between the conventional soft turning and hard turning should be investigated.

2 METALLOGRAPHIC OBSERVATIONS

The general aim of taking metallographic chip samples was to analyze the significant parameters of deformation processes in the cutting zone during hard turning and investigate the segmentation frequency in the chip (and comparing it with the frequency analysis from the accelerometer). The same analysis (except for the segmentation frequency) was carried out for soft steel with a view to comparing deformation processes in the cutting zone with respect to different properties of the machined material. The experimental setup and cutting conditions are listed in **Table 1**. **Figure 4** shows the chips, on which periodic cracks can be observed. These series of segments are measured all over the chip, and from more than 20 values the mean values are calculated. In the extensive cutting tests, the segmentation length and chip

thickness were statistically established. The parameters such as the chip ratio, the chip deformation, the chip speed, the shear speed, or the deformation angle were calculated. Moreover, the segmentation frequency could be evaluated. To obtain the segmentation frequency, the segmentation length had to be measured with a metallographic microscope and, knowing the cutting speed, the shear plane speed or the chip speed, and the frequency could be calculated.

Table 1: Experimental conditions during hard turning

Tabela 1: Eksperimentalni pogoji pri struženju

Cutting tool:	TiC reinforced Al ₂ O ₃ ceramic inserts DNGA150408 (TiN coating), rake angle $\gamma_n = -7^\circ$
Work material:	100Cr6 (hardened, 62 HRC and annealed, 27 HRC), external diameter of 56 mm, internal diameter of 40 mm, 125 mm long
Cutting condition:	$v_c = 25\text{--}250 \text{ m min}^{-1}$, $f = 0.09 \text{ mm}$, $a_p = 0.25 \text{ mm}$ (constant), dry cutting
Machine tool:	CNC Lathe Hurco TM8

The chip thickness was measured with a light microscope

Intensity of a plastic deformation in the cutting zone can be expressed in terms of various parameters. Except for the chip ratio, there are parameters such as the degree of segmentation (G) or chip deformation (γ_{sh}) and other derived parameters such as the chip and shear speeds.

The measurement of the chip thickness was carried out with an optical microscope and through the measurement of the etched chips shown on **Figure 4**.

The measurement of the chip thickness (h_c) allows us to calculate the chip ratio (equation (1)) and the other related parameters such as the shear angle Φ_1 , the chip speed (v_{ch}), the shear speed (v_{sh}) and the chip deformation (γ_{sh}):

$$K = \frac{h_c}{h} \quad (1)$$

where h is the undeformed-chip thickness and h_c is the chip thickness. The deformation angle can be calculated through equation (2):

$$\text{tg } \Phi_1 = \frac{\cos \gamma_n}{K - \sin \gamma_n} \quad (2)$$

The chip speed and shear speed can be derived from the cutting speed and shear angle (equations (3) and (4)):

$$v_{ch} = v_c \frac{\sin \Phi_1}{\cos(\Phi_1 - \gamma_n)} \quad (3)$$

A chip deformation can be expressed in a similar way, through equation (5):

$$v_{sh} = v_c \frac{\cos \gamma_n}{\cos(\Phi_1 - \gamma_n)} \quad (4)$$

$$\gamma_{sh} = \frac{\cos \gamma_n}{\cos(\Phi_1 - \gamma_n) \cdot \sin \Phi_1} \quad (5)$$

A degree of segmentation is calculated through equation (6) and illustrated in **Figures 4** and **5**:

$$G = \frac{h_c - h_0}{h_c} \quad (6)$$

Figure 6 illustrates that the chip thickness during turning hardened steel is much lower than that during turning annealed steel. The metallographic observations verify the previous investigations performed under similar conditions.^{12–14} The formation of the segments during turning hardened steel causes an elongation and a decrease in the chip thickness. As a result of the formation of thin and long chips, the chip ratio is smaller than 1, contrary to the turning of annealed steel (thick and short continuous chips causing the chip ratio to be

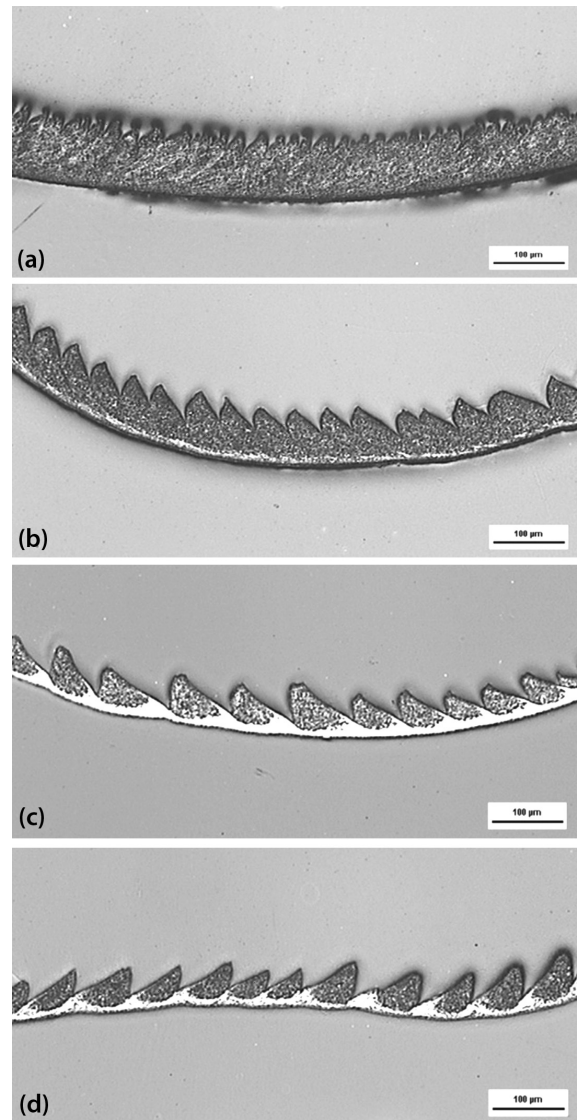


Figure 4: Chips after hard turning: a) $v_c = 25 \text{ m min}^{-1}$, $f = 0.09 \text{ mm}$, b) $v_c = 50 \text{ m min}^{-1}$, $f = 0.09 \text{ mm}$, c) $v_c = 100 \text{ m min}^{-1}$, $f = 0.09 \text{ mm}$, d) $v_c = 200 \text{ m min}^{-1}$, $f = 0.09 \text{ mm}$

Slika 4: Odrezki po struženju: a) $v_c = 25 \text{ m min}^{-1}$, $f = 0,09 \text{ mm}$, b) $v_c = 50 \text{ m min}^{-1}$, $f = 0,09 \text{ mm}$, c) $v_c = 100 \text{ m min}^{-1}$, $f = 0,09 \text{ mm}$, d) $v_c = 200 \text{ m min}^{-1}$, $f = 0,09 \text{ mm}$

more than 1, **Figure 7**). The average intensity of plastic deformation expressed with the chip ratio is much lower during hard turning than during the turning of soft steel.

The low intensity of plastic deformation must be attributed, first of all, to the material inside the segment. The plastic deformation inside the segment is low and the material in this area stays untouched. Although the plastic deformation in the localized areas of the segmented chip is extremely high (white areas), the total deformation of the segmented chip is much lower than for a continuous chip (during turning the annealed steel), as seen on **Figure 8**. On the other hand, the intensity of plastic deformation significantly changes with the cutting speed in the case of hard turning. The segmented chip becomes more continuous with a decreasing cutting speed. This aspect is verified with the degree of segmen-

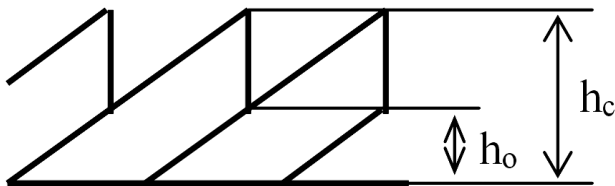


Figure 5: Illustration for a calculation of chip segmentation
Slika 5: Prikaz segmentacije odrezkov za izračun

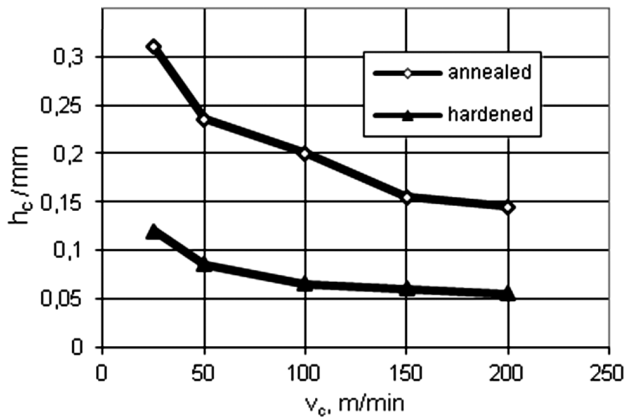


Figure 6: Influence of cutting speed on chip thickness
Slika 6: Vpliv hitrosti rezanja na debelino odrezka

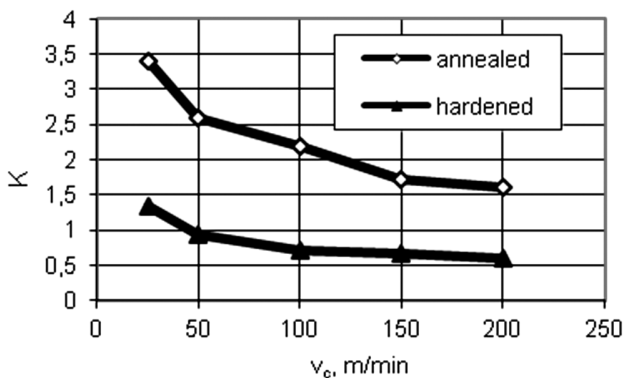


Figure 7: Influence of cutting speed on chip ratio
Slika 7: Vpliv hitrosti rezanja na razmerje odrezkov

tation illustrated in **Figure 9**. The continuous chip can be expressed as a segmented chip with the zero degree of segmentation. **Figure 9** illustrates that the degree of segmentation strongly decreases with a decreasing cutting speed. The specific character of the chip formation is related to the high shear angle, higher than the shear angle for turning annealed steel (**Figure 10**). The chip thickness, the chip ratio and the chip deformation increase with a decreasing cutting speed because the average intensity of plastic deformation increases (the chip becomes more and more continuous).

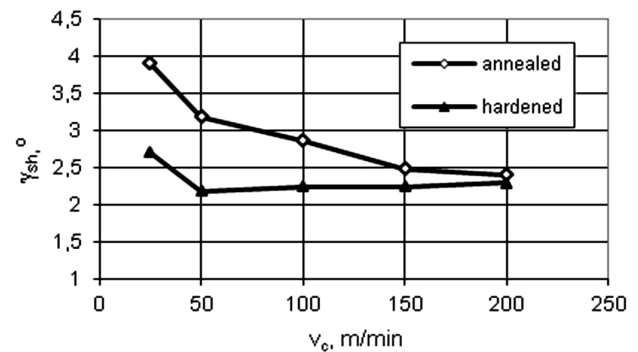


Figure 8: Influence of cutting speed on chip deformation
Slika 8: Vpliv hitrosti rezanja na deformacijo odrezkov

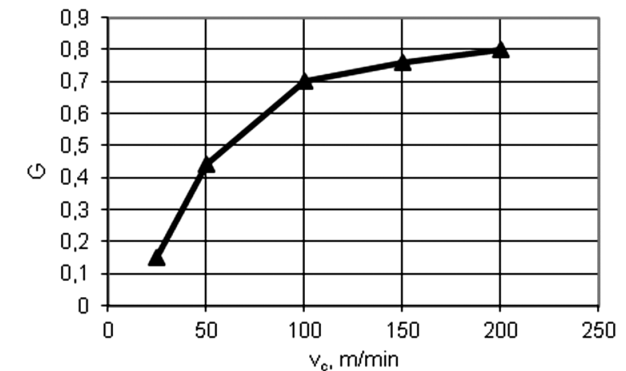


Figure 9: Influence of cutting speed on degree of segmentation
Slika 9: Vpliv hitrosti rezanja na stopnjo segmentacije

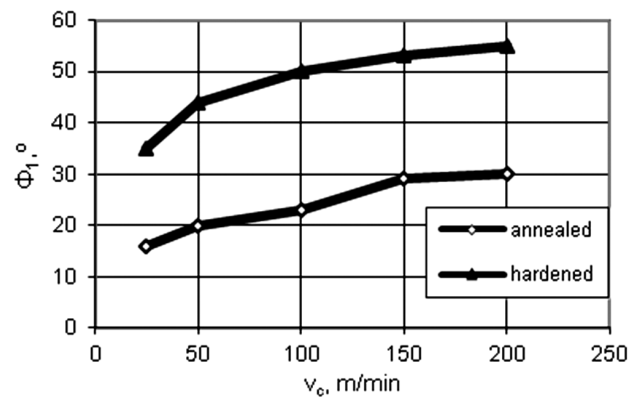


Figure 10: Influence of cutting speed on shear angle
Slika 10: Vpliv hitrosti rezanja na strižni kot

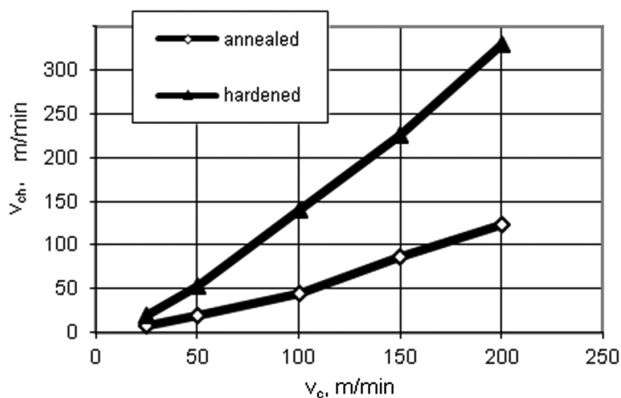


Figure 11: Influence of cutting speed on chip speed

Slika 11: Vpliv hitrosti rezanja na hitrost odrezka

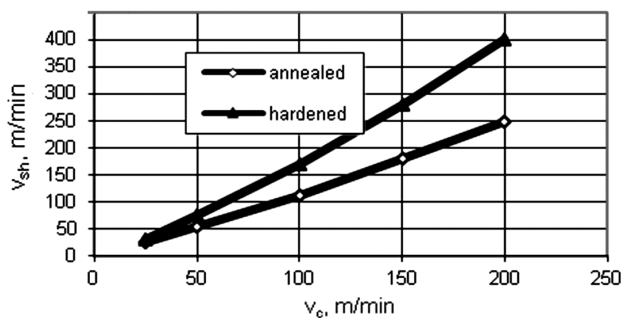


Figure 12: Influence of cutting speed on shear speed

Slika 12: Vpliv hitrosti rezanja na hitrost striženja

As a result of the formation of the thin and long chips (in the case of turning hardened steel) the shear speed and the chip speed are much higher than in the case of turning annealed steel (Figures 11 and 12). This aspect is attributed to the balance in the cutting zone between the incoming and outgoing volumes of the material. The increase in the chip ratio is strongly associated with a decrease in the chip speed.

It can be easily observed that the specific process of a chip segmentation leads to the thinning of the plastically deformed region as the chip moves up the tool face.^{12,13} The significance of the thinning of the plastically deformed region as the chip moves up the tool face is that this gives rise to a chip ratio less than one. This is usually the case when hard steel is turned with a negative rake tool. An important consequence is that the chip speed will be greater than the cutting speed and the shear angle will be greater than 45° .

3 EXPERIMENTAL RESULTS

The term segmented chip is often used to describe all of the cyclic types. This is unfortunate since these types of chips are distinctly different. For example, the cycle frequency for a wavy chip is typically about 100 Hz, while the one for a segmented chip is by 2 to 4 orders of magnitude greater.¹³⁻¹⁵ Dynamic forces that fluctuate at a frequency over 10 kHz are difficult to measure.

A conventional piezoelectric dynamometer limits the frequency response to about 3.5 kHz. However, an estimation of the relative changes in the force components and the frequency of force fluctuation may be obtained by using wire-resistance strain gauges¹⁵ or accelerometers. A conventional accelerometer limits the frequency response to about 20 kHz (special accelerometers limit the frequency response to about 50 kHz).

On the other hand, acoustic-emission techniques allow us to investigate the processes that fluctuate at a frequency over several MHz. AE signals can be classified into two types,¹⁶ as either continuous-type AE signals or burst-type AE signals. Continuous signals are associated with the shearing in the primary zone and the wear on the tool flank, while the burst type signals are observed during a crack growth in a material, tool, material fracture or chip breakage.

Apart from the conventional process monitoring, AE can be applied to an analysis of a chip form and a chip flow. The specific character of an AE signal can be observed under the specific cutting conditions related to a specific chip formation. Hard turning represents the case of a specific character of deformation processes mixed with a fracture of a machined material. There is a strong relaxation character of the related AE signal during hard turning. Uehara¹⁷ reported on remarkable patterns of the AE related to the segmented-chip formation. The AE signals accompanying the formation of a segmented chip exhibit remarkable patterns; the tool side signal shows a periodic bursting. The amplitude of AE varies correspondingly to the periodic change of the cutting force.

The elastic waves arising from different locations in the cutting zone can be detected through an AE system.^{10,17} The friction between the tool and the workpiece in the primary shear zone generates a continuous AE signal (during a formation of a continuous chip), providing comprehensive information on the cutting process. On the other hand, the chip formation during machining hardened steel allows us to work out the conditions for crack initiation and propagation. The surfaces that need to be machined are not perfectly smooth but rough and composed of microscopic ridges, cracks, voids, etc. Machining hardened materials using high compressive stress creates a subsurface material flow leading to the formation of cracks in the free surface. Strong elastic waves related to the crack formation during the segmented-chip formation can be detected through the AE systems, being inherent to the AE signals and related to the deformation processes in the cutting zone. The character of the AE signals during hard turning is complicated because mixed types of AE signals are generated in different zones. The aim of this experimental study is to analyze these aspects.

The experimental setup is shown in Figures 13 and 14. Commercial piezoelectric AE sensors (D9241A – the frequency range of 20 kHz to 180 kHz, WD – the frequency range of 100 kHz to 1000 kHz) by Physical

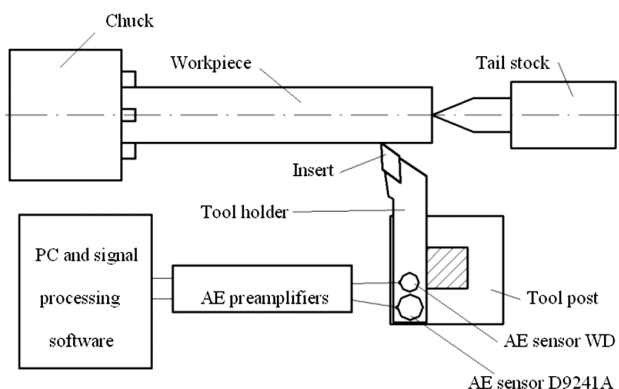


Figure 13: Schematic of experimental setup
 Slika 13: Shematski prikaz eksperimentalnega sestava

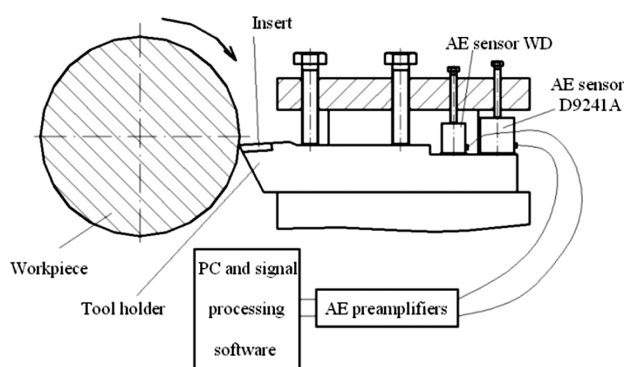


Figure 14: Detail of sensor placement
 Slika 14: Detajl namestitve senzorjev

Acoustics Corporation (PSC) were mounted on the top of the tool holder. To maintain a good propagation of the signals from the tool holder to the sensor, a semi-solid, high-vacuum grease was used. During the experiment, the AE signals were amplified, high passed at 20 kHz, low passed at 1000 kHz, and then sent through a pre-amplifier, at a gain of 40 dB, to the signal-processing software package. All the cutting tests were performed on a CNC lathe. The signals were real-time sampled, amplified, digitized and then fed to the signal processing unit. The AE signals were post-processed using AEwin.

3.1 Frequency analysis

When analyzing AE signals during hard turning, the segmentation frequency must be taken into consideration in relation to the frequency response of the applied AE sensors. Two sensors with different frequency ranges were applied. While the D9241A AE sensor allows us to analyze low frequencies (from 20 kHz), the low frequency limit of the WD AE sensor is 100 kHz.

The mean cycle frequency of the chip segmentation can be determined by dividing the speed of the chip v_{ch} by the mean spacing of the points of the maximum chip thickness p_c (the segment length in Figure 1) using equation 7:¹³

$$\text{segmentation frequency} = \frac{v_{ch}}{p_c} \quad (7)$$

To obtain the segmentation frequency, the segmentation length had to be measured with the metallographic microscope. Figure 4 illustrates that the segment length is not constant; it varies and so the segmentation frequency is not established as an exact value, but should be determined within a certain interval. As shown on Figure 15, the calculated segmentation frequencies lie in the frequency range of 10 kHz to 85 kHz. The verification of these frequencies can be performed through an application of the D9241A AE sensor, as the calculated frequencies are in the frequency range (or close to the low frequency limit at the low cutting speed) of this sensor.

An AE analysis could be limited under specific conditions because it could be difficult to find a relation between a physical process and the character of the AE signals. Because of this, many parameters of the AE signals implemented into the software package, such as the amplitude, the number of hits and counts, the signal strength, the energy, the average frequency and others could be analyzed. These parameters are derived from an AE wave with relation to the threshold value and they do not have to reflect the dynamic character of the process in real time. For example, Figure 15 illustrates that the segmentation frequency increases with the cutting speed. Figure 16 shows the relaxing and periodic character of the signal at different cutting speeds.

The time period between two consecutive amplitudes of an AE signal should reflect the segmentation frequency and should change in relation to different frequencies under different cutting conditions. Figure 16 illustrates that the time period between two consecutive pulses of an AE signal does not change and stays nearly constant. This is associated with the AE waveform transformation. The transformation of an AE waveform is compounded by the sensor response. When a resonant sensor is excited by a broadband transient pulse, it rings like a bell at

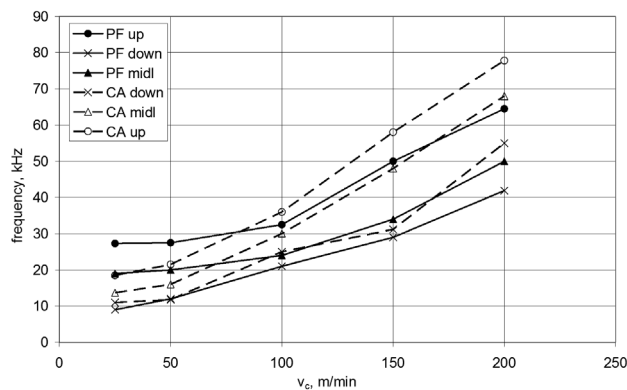


Figure 15: Influence of cutting speed on the peak frequency (PF) of the D9241A sensor and calculated segmentation frequency (CA)
 Slika 15: Vpliv hitrosti rezanja na maksimalno frekvenco (PF) senzorja D9241A in izračunana frekvenca segmentacije (CA)

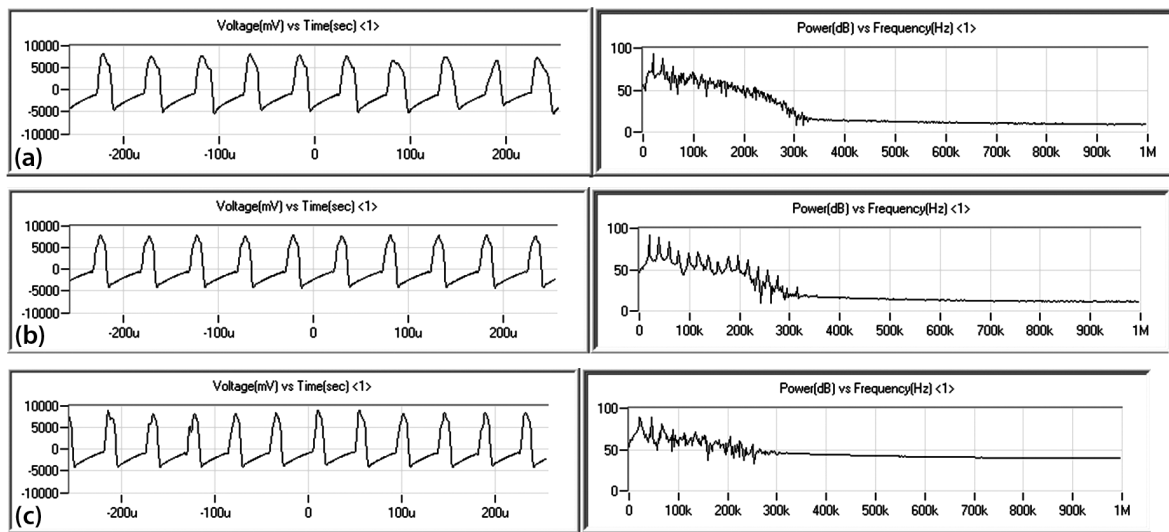


Figure 16: Signal of AE and its FFT spectrum for the 9241A sensor, hard turning: a) $v_c = 25 \text{ m min}^{-1}$, b) $v_c = 100 \text{ m min}^{-1}$, c) $v_c = 200 \text{ m min}^{-1}$
Slika 16: Signal AE in njegov FFT-spekter za senzor 9241A, struženje: a) $v_c = 25 \text{ m min}^{-1}$, b) $v_c = 100 \text{ m min}^{-1}$, c) $v_c = 200 \text{ m min}^{-1}$

its own frequency of oscillation. Therefore, the electrical signal at the sensor output is the product of this ringing, thus compounding the effects of multiple paths and multiple wave modes, with which the wave travels from the source to the sensor. The transformation of the AE waveform leads to a mismatch between the real dynamics of the signal and the derived AE parameters.

For example, the average frequency of the AE signal is determined as the average frequency over the entire AE hit and is derived from the AE-signal duration and the number of the counts (a count is a signal excursion over the AE threshold). This derived parameter (during this experiment) is in the range of 21 kHz to 24 kHz (for the D9241A sensor) and does not match the calculated values of the segmentation frequency in **Figure 16**. On the other hand, the applied AE system has the capability of calculating and processing the frequency-derived AE features in real time. Up to six frequency-based features can be processed by the AE system. Each of these features requires that a real time FFT is performed on the received AE-hit waveform. Except for four partial power frequency features, including the AE frequency features, they include frequency centroid and peak frequency (PF). The investigations into the centroid and peak frequency show that only the peak frequency (illustrated in **Figure 15**) matches the calculated values. The peak frequency is defined as a point in the power spectrum, at which the peak magnitude occurs. A real-time FFT (fast Fourier transformation) is performed on the waveform associated with the AE hit. The frequency that contains the largest magnitude is reported. Like the calculated values, the peak frequencies do not represent the exact values, but the AE Win software also processes this feature as an interval. **Figure 16** shows a good correlation between the peak frequencies and the calculated frequencies as an evidence of the AE system's capability

of truly reflecting the specific processes in the cutting zone during hard turning.

3.2 Intensity of deformation processes

It should be established that the AE sensors' responses depend on the frequency range of the applied sensor and the cutting speed. **Figures 16** and **17** illustrate the AE signals for different cutting speeds and the related FFT spectrums. It can be easily observed that the course of an AE signal (for the low-frequency sensor D9241A) reflects the relaxation character of the chip formation. The relaxation course of the signal is related to the relaxation process of the stress ahead of the cutting edge and the crack propagation in the shear region. According to the theory of the crack propagation and segment formation, the change in the amplitude of AE indicates a change in the sliding velocity during the tool-chip interface. Many pulse-like signals are observed, corresponding to the periodic fluctuation (the relaxation character) of the cutting process. The signal level of the AE between these pulses is quite small. During the segmented chip formation, the chip slides over the rake face with a varying speed corresponding to the period of the fracture in the shear plane.

Figure 16 shows the periodic peaks in the FFT spectrum. This character of the FFT spectrum confirms the dominant periodic character of the recorded signal and an ability of the D9241A AE sensor (the frequency range of 20 kHz to 180 kHz) to detect the periodic process typical for a segmented-chip formation. The segmentation frequencies of the investigated cutting speeds lie in the frequency range of the D9241A AE sensor (or close to the low-frequency limit). On the other hand, **Figure 17** illustrates that these peaks are missing during the formation of a continuous chip. Moreover, the excited amplitudes in the FFT spectrum during hard turning are

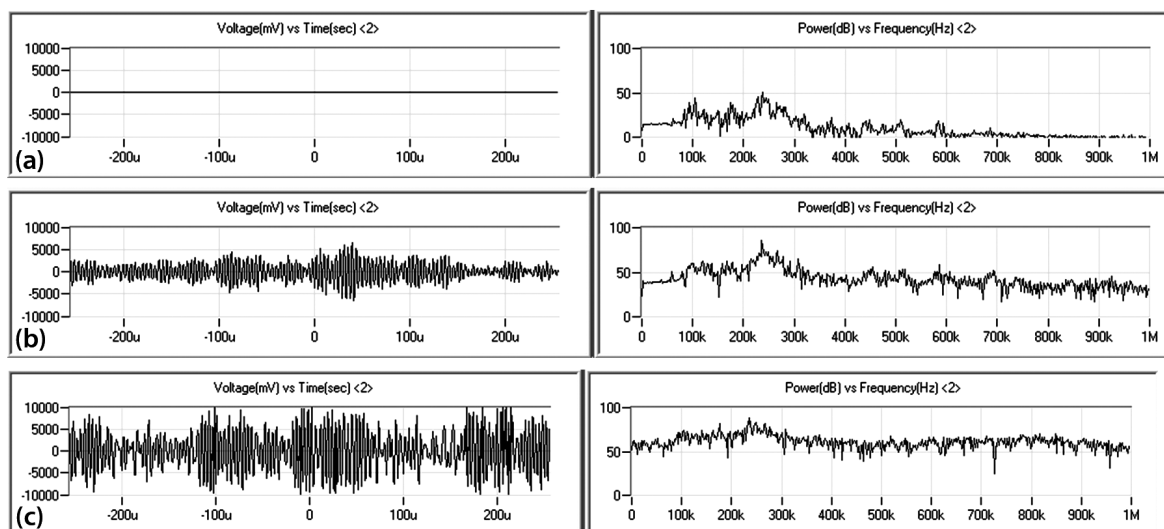


Figure 17: Signal of AE and its FFT spectrum for the WD sensor, hard turning
 Slika 17: Signal AE in njegov FFT-spekter za WD-senzor, struženje

significantly higher (above 50 dB, up to the 200 kHz frequency) in comparison with those occurring during the formation of continuous chips. It should be stated that the amplitudes of the AE signals, together with the amplitudes in the FFT spectrums, are nearly on the same level for all the cutting speeds. This indicates that the low-frequency AE sensor D9241A can be applied when making dynamic analyses (frequency responses) of hard turning, but this sensor is not sensitive to the variation of the deformation-process intensity in the cutting zone.

Considering the AE WD sensor (the frequency range of 100 kHz to 1000 kHz), all the segmentation frequencies lie outside the frequency range of this sensor and the periodic character of the AE signal is missing. The FFT spectrum of the AE signal for the WD sensor is

without the periodic peaks in this spectrum (Figure 17) as well as FFT spectrum in the case of turning annealing steel (Figure 18).

It was reported in the previous sections that AE signals can be classified into two types as either continuous-type AE signals or burst-type AE signals. Continuous signals are associated with the shearing in the primary zone, in the tool-chip and tool-workpiece contacts (Figure 19). These processes can be investigated and detected with the WD AE sensor, because the signals related to the chip segmentation (the crack propagation) are out of the segmentation-frequency range. Figure 17 shows that the amplitude of the AE signal for the WD sensor increases with the cutting speed. This aspect is associated with the increasing intensity of the friction

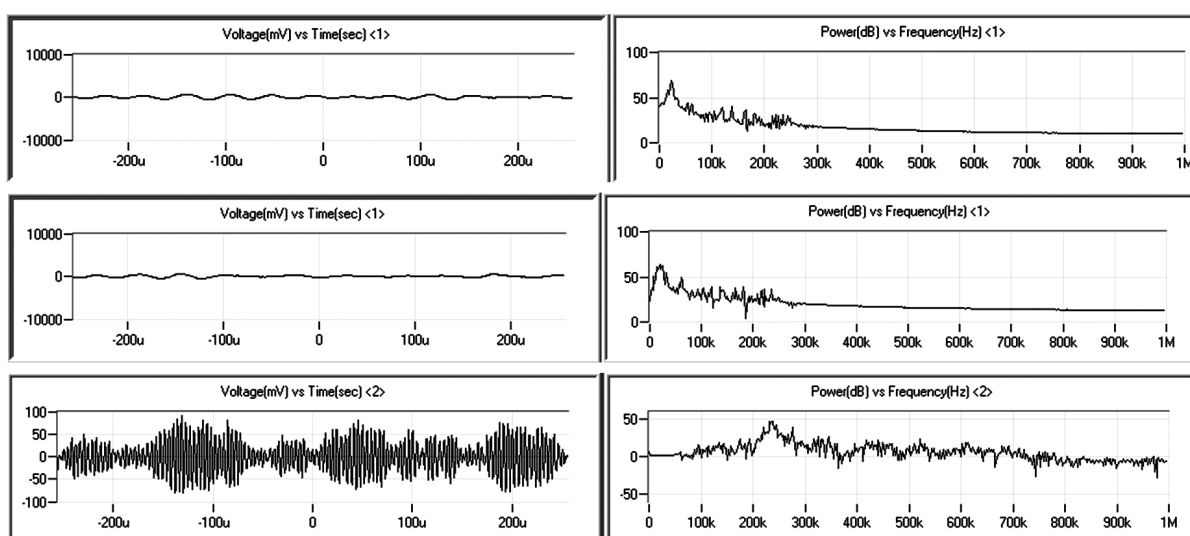


Figure 18: Signal of AE and its FFT spectrum, turning of annealed steel: a) $v_c = 25 \text{ m min}^{-1}$, 9241A sensor, b) $v_c = 100 \text{ m min}^{-1}$, 9241A sensor, c) $v_c = 200 \text{ m min}^{-1}$, WD sensor

Slika 18: Signal AE in njegov FFT-spekter, struženje žarjenega jekla: a) $v_c = 25 \text{ m min}^{-1}$, 9241A senzor, b) $v_c = 100 \text{ m min}^{-1}$, 9241A senzor, c) $v_c = 200 \text{ m min}^{-1}$, WD senzor

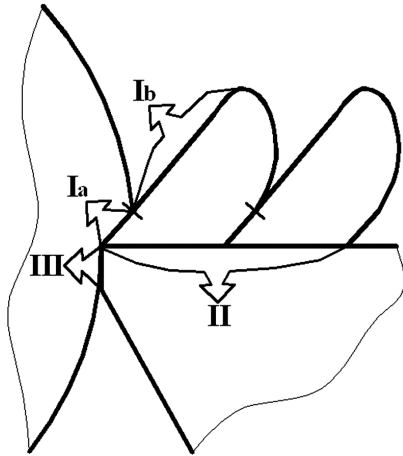


Figure 19: Cutting zone for hard cutting: Ia) microcracked and plastically deformed shear zone, Ib) cracked region, II) tool-chip contact, III) tool-workpiece contact

Slika 19: Cona odrezovanja pri rezanju: Ia) plastično deformirano strižno področje z mikrorazpokami, Ib) razpokano področje, II) stik orodje-odredek, III) stik orodje-obdelovanec

processes in the cutting zone in relation to the increasing chip and shear speeds. Moreover, the amplitudes of the related frequencies in the FFT spectrum are excited above 50 dB, across the whole frequency range and at the cutting speed of 200 m min⁻¹, while the amplitudes in the frequency spectrum at the cutting speed of 25 m min⁻¹ are lower (Figure 17).

An application of the D9241A sensor is limited for these analyses. The burst-type AE signal (related to the crack propagation) superposes with the signal from the tool-chip and tool-workpiece interface and so it causes the difficulties in the investigation of the processes in these regions. The segmentation frequencies lie in the frequency range of the D9241A sensor. These frequencies are associated with the crack formation and its propagation in the shear zone. The signal associated with a crack formation and its prolongation in the shear zone is very strong (the amplitude of the AE signals for all the cutting speeds is on the maximum level of 100 dB) generating a massive low-frequency noise. This noise negatively influences the detection of the friction process

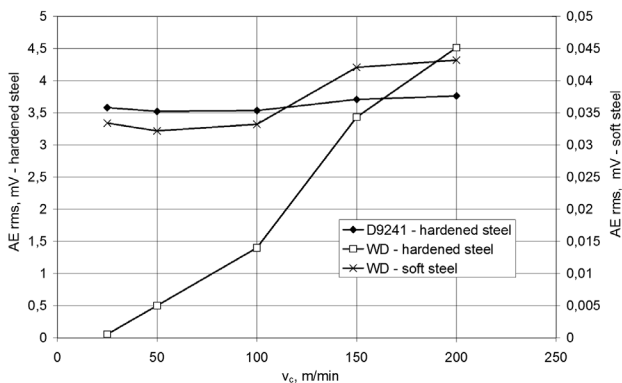


Figure 20: Influence of cutting speed on RMS values of AE
Slika 20: Vpliv hitrosti rezanja na RMS-vrednosti AE

in the shear zone, the tool-chip and tool-workpiece contacts (Figure 19). The AE signals recorded by the D9241A sensor are not sensitive to the friction processes in the cutting zone. Figures 20, 21 and 22 show that the RMS value, the signal strength and the absolute energy of the AE signal do not vary significantly with the increasing cutting speed. (The signal strength is defined as the integral of the rectified voltage signal over the duration of the AE waveform packet. The absolute energy is a true energy measure of the AE hit.)

On the other hand, the frequency range of the WD sensor lies above the segmentation frequencies and so the low-frequency limit of 100 kHz of the WD sensor represents a high-pass filter. The RMS values, the strength and the absolute energy of the AE signal increase with the increasing cutting speed (Figures 20, 21 and 22). This aspect is associated with an increasing intensity of the deformation processes in the cutting zone. These processes are dissipated to the narrow white areas in the shear zone (the white area is caused by the plastic deformation in this zone, contrary to the crack formation in the area without an occurrence of a structure transformation) as well as to the tool-chip and tool-workpiece contacts. The increase of the values in Figures 20, 21 and 22 cannot be attributed to the tool wear because all the tests were carried out in the normal phase of the tool wear (its VB being from 0.1 mm to

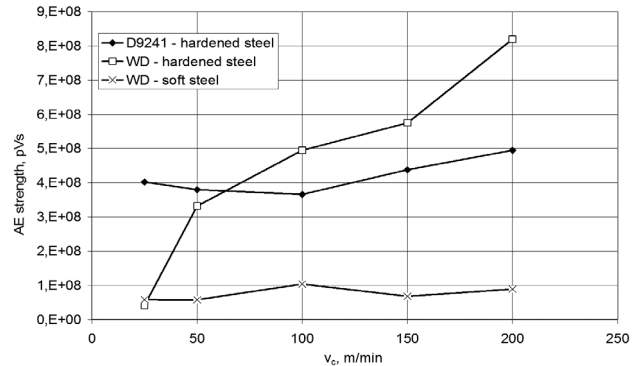


Figure 21: Influence of cutting speed on AE signal strength
Slika 21: Vpliv hitrosti rezanja na moč AE-signalov

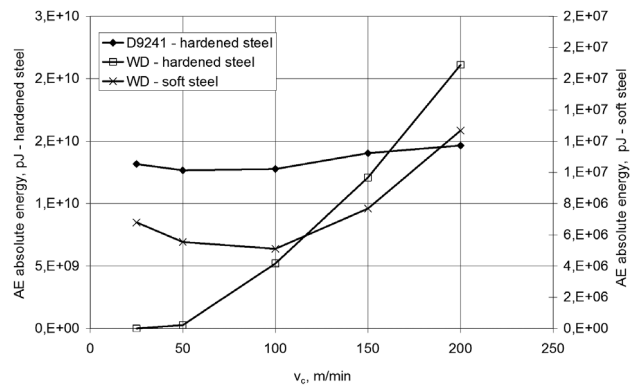


Figure 22: Influence of cutting speed on absolute energy of AE
Slika 22: Vpliv hitrosti rezanja na absolutno energijo AE

0.12 mm). The increasing intensity of deformation processes is attributed to the following aspects:

the increasing chip segmentation with the increasing cutting speed; a more intensive thinning of the micro-cracked region (the plastically deformed shear zone) as the chip moves up the face of the tool;

- the increasing non-homogeneity in the stress and temperature distribution in the cutting zone with the increasing cutting speed, together with the increasing chip and shear speeds;
- the temperature in the cutting zone increases with the increased cutting speed⁸ (forming suitable conditions for the processes of plastic deformation and the related structure transformation and reducing the zones of an undeformed chip).

The sensitivity of the AE signals concerning the intensity of the real-deformation processes in the cutting zone can be illustrated through a comparison of the AE signal and FFT spectrums during conventional (annealed steel) turning and hard turning. The analytic approach shows that the chip deformation and chip ratio are higher for the conventional continuous chips (**Figures 7 and 8**), but the amplitude of the AE signals and the excited amplitudes of the FFT spectrums in **Figure 18** are significantly lower. While the amplitudes of the AE signal during hard turning oscillate between ± 10000 mV, the formation of a continuous chip leads to an oscillation on the scale of ± 100 mV. Moreover, the excited amplitudes of the FFT spectrum in **Figure 18** are close to zero (except for the resonance frequency represented by the maximum amplitude in the spectrum), while, in contrast, those amplitudes excited above 50 dB cover the whole frequency spectrum during hard turning (**Figure 17**). Some other derived parameters such as the RMS value of the AE signal, the signal strength and the absolute energy are closely associated with the emission signals, correlating with the amplitude range of the responded emission waves. **Figures 20, 21 and 22** illustrate that all the values are significantly lower during the formation of conventional chips.

The metallographic and experimental studies give contradictory results because of their different methodologies. For example, the values of the chip ratio or the chip deformation for the hard-turning process in **Figures 7 and 8** decrease with the increasing cutting speed. This indicates a decreasing intensity of deformation processes in the cutting zone. However, **Figures 17, 18, 21 and 22** show that the absolute energy, the signal strength and the amplitudes of the AE signals increase with the increasing cutting speeds.

The conventional analytical approach does not facilitate an evaluation of the real intensity of deformation processes in the specific zones of the cutting process. This approach takes the whole chip into the consideration. The calculated values do not reflect the non-homogeneity of deformation processes during hard cutting, but provide information about the average value across the whole chip. On the other hand, the experi-

mental study (based on AE) can identify the real intensity of this specific process.

4 CONCLUSIONS

The findings of this study show that the AE signals can be used to monitor the dynamic character and intensity of plastic deformation in the cutting zone during hard turning in the following ways:

- metallographic analyses and the related calculations allow an analysis of the real intensity of deformation processes during the formation of conventional continuous chips, but this approach is less sensitive to the identification of the specific-character chip formation during hard turning;
- experimental analysis of the chip formation during hard turning should be investigated with respect to the specific dynamic character of the cutting process and the related frequencies;
- burst type of the AE signal is associated with a crack propagation in the shear zone because of the relaxing character of the chip formation and the related segmentation frequencies;
- analysis of the chip segmentation requires a match of the segmentation frequency and the frequency range of the applied AE sensor;
- continuous type of the AE signals is associated with the plastic deformation in the cutting zone related to the plastic deformation in the shear zone, the tool-chip and tool-workpiece sliding contacts;
- continuous type of the AE signal is more sensitive to the real intensity of deformation processes during hard turning, contrary to the metallographic analyses and the calculated parameters.

The dynamic character of a cutting process in hard turning and the specific character of a chip formation significantly affect the parameters such as the shear and chip speeds, the friction processes in the cutting zone, the related heat generation and high temperatures in this zone. These parameters have an impact on the surface quality represented by the residual stresses, surface hardness, structural changes and other attributes. And so, the studies about the dynamic character of the hard-turning process should be carried out.

Acknowledgement

This paper was supported by the Students Grant Competition of VSB-TU Ostrava, "SP2012/68 Effective machining of progressive materials and integrity surface evaluation", and also by the VEGA agency.

5 REFERENCES

- ¹ G. Bartarya, S. K. Choudhury, State of the art in hard turning, International Journal of Machine Tools and Manufacture, 53 (2012) 1, 1–14

- ² D. Kramar, J. Kopač, High Pressure Cooling in the Machining of Hard-to-Machine Materials, *Journal of Mechanical Engineering*, 55 (2009) 11, 685–694
- ³ R. F. Recht, Catastrophic Thermoplastic Shear, *Trans ASME*, 86 (1964), 189–193
- ⁴ K. Nakayama, M. Arai, T. Kanda, Machining Characteristics of Hardened Steels, *CIRP Annals*, 37 (1988) 1, 89–92
- ⁵ M. A. Elbestawi, A. K. Srivastava, T. I. El-Wardany, A Model for Chip Formation during Machining of Hardened Steel, *CIRP Annals*, 45 (1996) 1, 71–76
- ⁶ R. Komanduri, R. H. Brown, On the Mechanics of Chip Segmentation in Machining, *J. of Eng. for Ind. Trans. ASME*, 103 (1981), 33–51
- ⁷ G. Poulachon, A. Moisan, I. S. Jawahir, On Modeling the Influence of Thermo – Mechanical Behavior in Chip Formation during Hard Turning of 100Cr6 Bearing Steel, *CIRP Annals*, 50 (2001), 31–36
- ⁸ M. Neslušan, Turning of Hardened Steels, 1st ed., Edis Žilina, Žilina 2009, 245
- ⁹ M. Neslušan, R. Čep, B. Barišič, Chip formation analysis during hard turning, *Strojarstvo*, 50 (2008), 337–347
- ¹⁰ D. A. Dornfeld, Acoustic emission in monitoring and analysis in manufacturing, *Proceedings of AE Monitoring, Anal. Manuf.*, 14 (1984), 124
- ¹¹ D. A. Dornfeld, Manufacturing process monitoring and analysis using acoustic emission, *Journal of Acoustic Emission*, 4 (1985), 123–126
- ¹² G. Poulachon, A. Moisan, Contribution to the Study of the Cutting Mechanism during High Speed Machining of Hardened Steel, *CIRP Annals*, 47 (1998), 73–76
- ¹³ M. C. Shaw, A. Vyas, The Mechanism of Chip Formation with Hard Turning Steel, *CIRP Annals*, 47 (1998) 1, 77–82
- ¹⁴ M. C. Shaw, A. Vyas, Mechanics of Saw-Tooth Chip Formation in Metal Cutting, *ASME Journal of Manufacturing Science and Engineering*, 121 (1999), 163–172
- ¹⁵ B. Lindenberg, B. Lindstroem, Measurement of the Segmentation Frequency in the Chip Formation Process, *CIRP Annals*, 32 (1983) 1, 17–20
- ¹⁶ I. Inasaki, Application of acoustic emission sensor for monitoring machining processes, *Ultrasonics*, 36 (1998), 273–281
- ¹⁷ K. Uehara, Identification of Chip Formation Mechanism through Acoustic Emission Measurements, *CIRP Annals*, 33 (1974), 71–74

EFFECT OF IRON AND CERIUM ADDITIONS ON RAPIDLY SOLIDIFIED Al-TM-Ce ALLOYS

VPLIV DODATKOV ŽELEZA IN CERIJA NA HITRO STRJENE ZLITINE Al-TM-Ce

Alena Michalcová¹, Dalibor Vojtěch¹, Gerhard Schumacher², Pavel Novák¹, Eva Plížingrová³

¹Institute of Chemical Technology, Department of Metals and Corrosion Engineering, Technická 5, 166 28 Prague, Czech Republic

²Helmholtz-Zentrum Berlin für Materialien und Energie GmbH, Hahn-Meitner-Platz 1, 14109 Berlin, Germany

³Institute of Inorganic Chemistry AS CR, v.v.i., Husinec-Rez 1001, 258 68 Rez, Czech Republic
alena.michalcova@vscht.cz

Prejem rokopisa – received: 2013-02-23; sprejem za objavo – accepted for publication: 2013-03-25

The influence of the additions of the mass fractions 3 % of Fe and 1 % of Ce to an AlCr₄Ti_{0.4} alloy is described in this paper. The iron addition modifies the phase composition of the material leading to the formation of the Al₁₃Fe₄ crystalline and Al₈₀(Cr,Fe)₂₀ quasicrystalline phases. It also causes a grain refinement that was proved with transmission electron microscopy and X-ray diffraction. The microhardness of the Fe-alloyed material is changed by about a factor of two in comparison to the material without Fe. On the other hand, the Fe addition has no influence on the thermal stability of the alloy. The effect of 1 % of Ce on the AlCr₄Ti_{0.4} alloy hardly affects the microhardness but increases the thermal stability during long-term annealing at 400 °C.

Keywords: rapid solidification, aluminium, quasicrystals

V prispevku je opisan vpliv dodatka z masnim deležem 3 % železa in 1 % cerija zlitini AlCr₄Ti_{0.4}. Dodatek železa spremeni sestavo faz v materialu in povzroči nastanek Al₁₃Fe₄ kristalne in Al₈₀(Cr,Fe)₂₀ kvazikristalne faze. Povzroči tudi zmanjšanje zrn, kar je bilo dokazano s presežno elektronsko mikroskopijo in z rentgensko difrakcijo. Mikrotrdota z Fe legiranega materiala se spremeni za faktor dve glede na material brez Fe. Po drugi strani pa dodatek Fe ne vpliva na termično stabilnost zlitine. Učinek 1 % Ce v AlCr₄Ti_{0.4} neznatno vpliva na mikrotrdoto, vendar pa poveča termično stabilnost med dolgotrajnim žarjenjem pri 400 °C.

Ključne besede: hitro strjevanje, aluminij, kvazikristali

1 INTRODUCTION

Rapidly solidified (RS) aluminium alloys are promising materials for structural applications. Their main advantage is the superior strain-to-weight ratio. The best mechanical properties and thermal stability are achieved in an aluminium rare-earth transition-metal (RE-TM) alloy system with aluminium contents higher than 80 %.^{1,2} These alloys are usually prepared under the maximum available cooling rates that, together with the appropriate chemical compositions, lead to a formation of amorphous or partially amorphous alloys.¹ Such metastable materials are very interesting from the investigation point of view, but their potential for the applications at elevated temperatures is limited. The amorphous phase decomposes under the heat treatment, forming intermetallic phases in the fcc-Al matrix.³ Depending on the heat-treatment regime, annealed materials can exhibit higher hardness and other mechanical properties such as the yield strength and the ultimate tensile strength.¹ The production of such materials is highly demanding with respect to processing and it would be considerably complicated to manufacture them in industrial conditions. This paper is focused on an investigation of the rapidly solidified alloys, prepared with the cooling rates achievable in industry.

The influences of single alloying elements on extremely rapidly solidified aluminium alloys are described in detail.^{1,4} The authors usually focus on the effect of each element on the glass-forming ability (GFA), which qualifies the tendency of an alloy to form a glassy structure. Three empirical rules for a GFA determination were established:

1. The higher the number of elements in a system, the higher is GFA.
2. GFA is also high due to a negative mixing enthalpy of the components in a system.
3. A GFA increase is generally observed together with great differences in the atomic ratios of the elements.¹

The definition of the GFA described for glassy alloys can be generalized as the ability to form a metastable phase (MPFA), indicating the tendency of a system to form not only the glassy state, but, generally, to form any metastable phase, e.g., amorphous and quasicrystalline phases and supersaturated solid-solution phases.

In the case of amorphous alloys, the functions of all the REs are approximately the same with respect to the increasing GFA.⁵ The influences of single TMs on Al-based alloys cannot be simplified only in terms of GFA, because they vary significantly⁵ on the basis of the interatomic interactions. The Al-based alloys containing Fe are very exceptional. It was reported that there is a strong

interaction between the Al and Fe atoms in the amorphous Al-RE-Fe alloys⁶ and even in the alloy melts.⁷ It was found, in the amorphous Al-Ce-Fe alloys, that the Ce atoms are basically randomly distributed and that the Fe atoms are surrounded by many Al atoms.⁶ This is in agreement with the idea that the icosahedral Al-Fe clusters are present already in the melts.^{2,7} It is generally supposed that the melt clusters are formed by the elements with the lowest negative mixing enthalpies. Interestingly, the behavior of the Al-Ce-Fe alloys is in disagreement with this rule because the mixing enthalpy of Al-Fe is -11 kJ/mol⁸ and the mixing enthalpy of Al-Ce is -38 kJ/mol.⁹ It was also shown that an Fe addition changes the crystallization mechanism of an Al86Mm4Ni10 alloy (Mm means mischmetal – an alloy of Ce, La, Nd and Pr), increasing its thermal stability.⁶

Ce precipitates from the Al-TM based amorphous alloys in the form of an Al₄Ce phase.^{7,10} This phase is formed due to a decomposition of the Al₉₂Ce₈ metastable phase¹¹ and is one of the main strengthening phases. It was also reported¹² that REs can be present in four different phases in the Al-RE alloys or Al-TM-RE alloys rich in REs. This possibility of nucleating various phases can represent a "confusion principle" for an alloy. On the other hand, when Fe is added to an alloy, a formation of intermetallic phases is preferred.¹² The question is in which form Ce will be present in the crystalline RS alloys and whether it will significantly influence the alloys.

In this paper, the influence of a mass fraction 3 % Fe addition on the structure, hardness and thermal stability of the nanocrystalline AlCr₄Ti_{0.4}Ce₁ alloy will be shown. This influence will also be compared to the influence of a 1 % Ce addition to the AlCr₄Fe₃Ti_{0.4} alloy.

2 EXPERIMENT

The alloys with the compositions given in **Table 1** were studied in this paper. Ingots of the alloys were prepared by melting the appropriate amounts of master alloys and pure metals (AlCr₁₁, AlTi₄, Al, Fe and Ce) in a vacuum induction furnace. Consequently, RS ribbons were prepared by melt spinning. The cooling wheel diameter of the melt-spinning equipment was 14 cm. The cooling wheel velocity was 1800 r/min, corresponding to the circumferential speeds of 28 m/s. Melt-spinning procedures were performed in air. The rapidly solidified alloys were produced in the form of thin foils with a

Table 1: Chemical compositions of the studied alloys in mass fractions (w/%) determined with an XRF analysis

Tabela 1: Kemijska sestava preiskovanih zlitin v masnih deležih (w/%), določenih z XRF-analizo

Alloy	Al	Cr	Ti	Fe	Ce
AlCr ₂	97.24	2.13	0.38	0.25	0
AlCr ₄ Ce ₁	93.96	3.84	0.40	0.96	0.84
AlCr ₄ Fe ₃	91.70	4.16	0.63	3.51	0
AlCr ₅ Fe ₃ Ce ₁	90.33	4.93	0.29	3.43	1.02

thickness of approximately 50 μm and a width of 4–5 mm. The chemical composition was determined with X-ray fluorescence spectroscopy (XRF) using a spectrometer ARL 9400 XP for Ce, and with atomic absorption spectroscopy (AAS) using GBC 932plus for the other elements.

The microstructure of the cross-sectioned ribbons was examined using a scanning electron microscope (SEM) Hitachi S 4700 (30 kV) and a light microscope Neophot 2 in the immersion mode. The samples were etched in a solution of 0.5 % HF for 20 s. The phase composition of the materials was determined with X-ray diffraction (XRD) (PAN analytical X'Pert PRO + High Score Plus, Cu anode). All diffraction measurements were performed on the wheel side of the RS ribbons. The grain size was estimated from XRD diffraction patterns as the size of the coherently diffracting domain using the Scherrer formula (1),¹³ attributing the peak width expansion only to the influence of the average grain size:

$$\text{Crystallite size (average)} = \frac{K\lambda}{B \cos \theta} \quad (1)$$

In equation (1) λ describes the wavelength of the incident X-rays, K is the constant that varies with the method of taking the line width ($0.89 < K < 1$) and B describes the structural broadening, given by the difference in the integral profile width between the standard and the unknown samples:¹³

$$B = B_{\text{obs.}} - B_{\text{std.}} \quad (2)$$

The peak at the 2Θ position of about 78° corresponding to the diffraction on the Al (311) plane was used for the estimation. The Rietveld structure refinement was performed with the program Topas 4. The samples were examined using a transmission electron microscope (TEM) Jeol 3010 (an accelerating voltage of 300 kV, LaB₆). Thin foils for TEM were prepared by grinding the free sides of the RS ribbons until the final thickness reached approximately 50 μm, and by subsequently electropolishing the mixture of C₂H₅OH:HNO₃ with the ratio of 3:1 at 10 V and -20°C . The structural investigation was completed with the EDS (Oxford Instruments) measurements. The Vickers hardness HV 0.02 was also measured on the cross-sectioned ribbons. The load of 20 g was chosen to be the optimum one for measuring the average hardness of the ribbons. The indenter always pointed to the middle of the ribbons.

A long-term annealing of the alloys was carried out in an electric resistance furnace. Selected samples were annealed at 400°C to determine the thermal stability of the materials. After the long-term annealing (25, 50, 75 and 100) h, the room-temperature hardness HV 0.02 was measured.

3 RESULTS AND DISCUSSION

All the RS ribbons showed structural gradients in the cross-sections, as illustrated in **Figures 1** and **2**. The cooling wheel sides of the ribbons, shown at the bottom

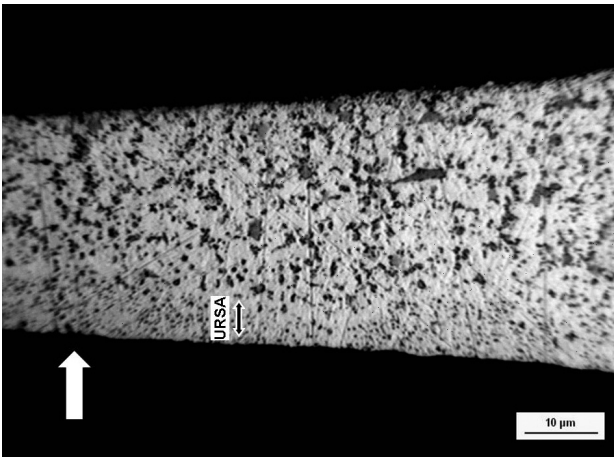


Figure 1: LM micrograph of a cross-section of a rapidly solidified ribbon of the AlCr4Ce1 alloy

Slika 1: Posnetek prereza hitro strjenega traku zlitine AlCr4Ce1

of **Figures 1 and 2** and marked with arrows, exhibit a very fine microstructure, called an ultra-rapidly-solidified area (URSA). The thickness of URSA depends on two main factors: 1) experimental parameters and 2) alloy properties. Experimental parameters include the cooling wheel speed, the atmosphere of the experiment and the geometry of the experimental device. These characteristics were identical during the preparation of all the rapidly solidified alloys. Therefore, all the differences among the rapidly solidified ribbons can be assumed to result from the chemical compositions of the alloys.

Figure 1 shows the structure of a cross-sectioned ribbon of the AlCr4Ce1 alloy. In comparison with the AlCr5Fe3Ce1 alloy, documented in **Figure 2**, its URSA is thinner and the microstructure is not so fine, because intermetallic particles (the dark areas) are observed on the free (top) side of the ribbon. In the URSA, a high-entropy alloy is formed. The ability to form such an alloy is increased with the number of elements in the system,

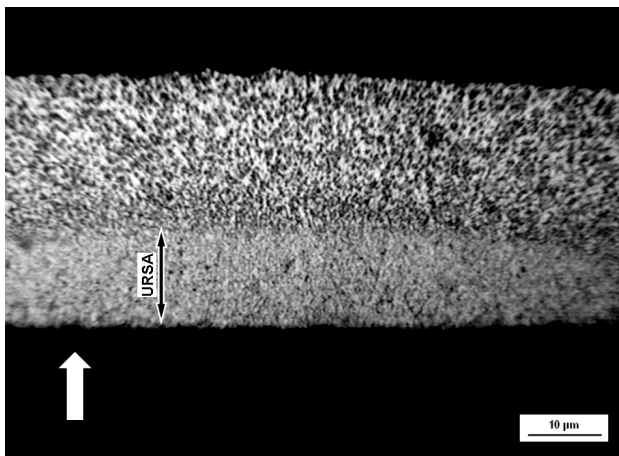


Figure 2: LM micrograph of a cross-section of a rapidly solidified ribbon of the AlCr5Fe3Ce1 alloy

Slika 2: Posnetek prereza hitro strjenega traku zlitine AlCr5Fe3Ce1

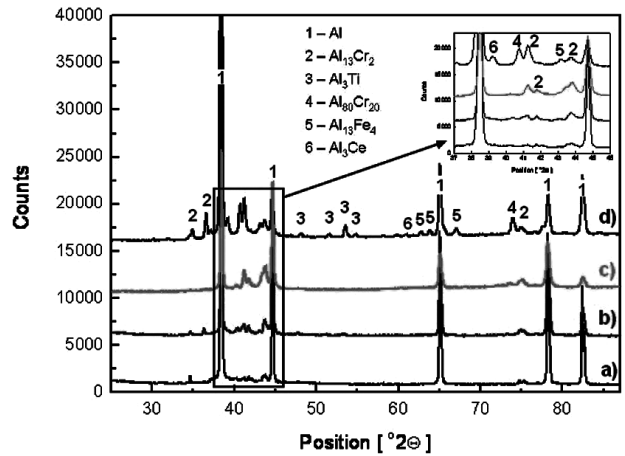


Figure 3: XRD patterns of: a) AlCr2, b) AlCr4Ce1, c) AlCr4Fe3 and d) AlCr5Fe3Ce1 alloys

Slika 3: Rentgenski posnetki zlitin: a) AlCr2, b) AlCr4Ce1, c) AlCr4Fe3 in d) AlCr5Fe3Ce1

especially with the number of transition metals. For this reason, the URSA of the AlCr5Fe3Ce1 (quaternary) alloy is much larger than that of the AlCr4Ce1 (ternary) alloy.

According to XRD (**Figure 3**), the AlCr5Fe3Ce1 alloy is composed of the fcc-Al, Al₁₃Cr₂, Al₁₃Fe₄, Al₃Ti and Al₃Ce crystalline intermetallic phases and the Al₈₀(Cr,Fe)₂₀ decagonal quasicrystalline phase. The AlCr4Ce1 alloy, on the other hand, contains neither Al₁₃Fe₄ nor the quasicrystalline Al₈₀(Cr,Fe)₂₀ – therefore, strongly increasing the MPFA due to the so called "confusion principle".^{14,15}

The fcc-Al matrix grain size determined with the Scherrer formula and Rietveld analysis is given in **Table 2**. The values are different because of the used methods and their limitations, but the grain-size trend is in sufficient agreement. The total amount of the alloying elements (Cr, Ti, Fe, Ce) in the AlCr2 alloy is significantly lower than in the other alloys. This results in a lower number of crystallization nuclei of the intermetallic phases during the solidification and in a huge grain size of the AlCr2 alloy.

Table 2: Grain size of the fcc-Al matrix in nm determined with the Scherrer formula and Rietveld analysis

Tabela 2: Velikost zrn fcc-Al osnove v nm, določena po Scherrerjevi enačbi in z Rietveldovo analizo

Alloy	Scherrer formula	Rietveld analysis
AlCr2	232	118
AlCr4Ce1	123	76
AlCr4Fe3	49	50
AlCr5Fe3Ce1	46	32

The addition of the mass fraction 1 % Ce causes a mild grain refinement. The reason for this is not only a higher amount of the alloying elements. The possibility

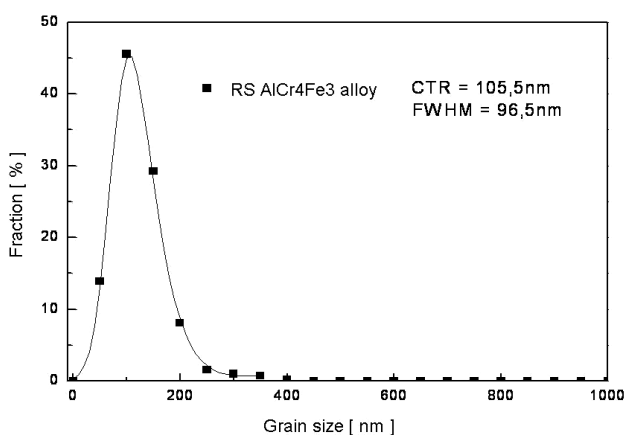


Figure 4: Grain-size distribution of the RS AlCr4Fe3 alloy
Slika 4: Razporeditev velikosti zrn hitro strjene zlitine AlCr4Fe3

of an intermetallic-phase formation increases with the Ce addition and so this addition supports the alloy metastability on the basis of the confusion principle. The Ce addition also enables the existence of an alloy melt at lower temperatures, because the Al-Ce system exhibits a eutectic. The Fe addition has a strong effect on the grain-size refinement, as it can be seen from the difference between the grain sizes of the AlCr4Ce1 and AlCr5Fe3Ce1 alloys. A very small grain size of the RS materials is caused by a suppression of the diffusion rate due to a very high quenching rate. Surprisingly, the AlCr4Fe3 and AlCr5Fe3Ce1 alloys exhibited almost the same grain sizes. This was the reason for determining the grain sizes of these alloys also with an image analysis and the results of the grain-size distribution are given in **Figures 4** and **5**. The values of the grain size determined from the XRD pattern are about half of the values determined from the TEM image. This is usual because what is seen, in a TEM micrograph, as single grains, can be more coherent diffracting domains for the X-ray methods. However, all the methods showed that the grain sizes of the AlCr4Fe3 and AlCr5Fe3Ce1 alloys are

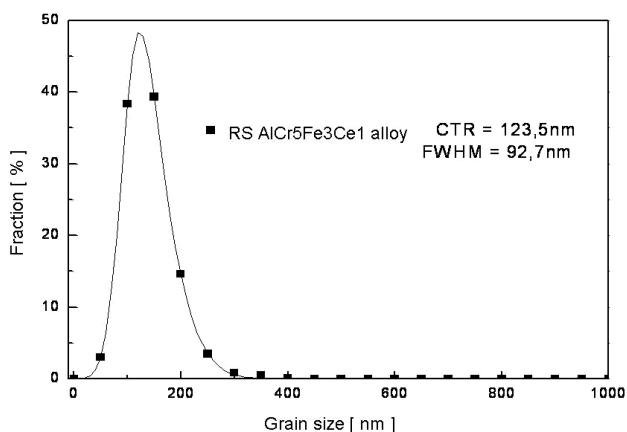


Figure 5: Grain-size distribution of the RS AlCr5Fe3Ce1 alloy
Slika 5: Razporeditev velikosti zrn hitro strjene zlitine AlCr5Fe3Ce1

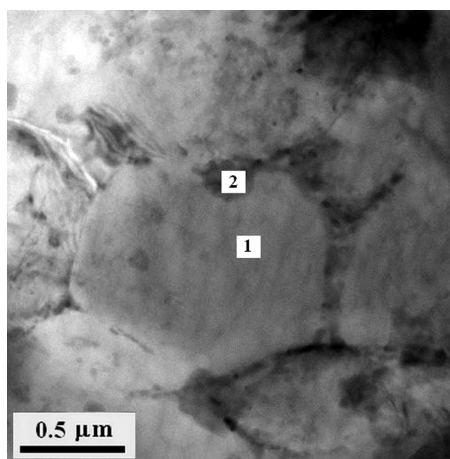


Figure 6: TEM micrograph of a cross-section of a rapidly solidified ribbon of the AlCr4Ce1 alloy (1 – Al grains, 2 – Al₁₃Cr₂)

Slika 6: TEM-posnetek prereza hitro strjenega traku zlitine AlCr4Ce1 (1 – Al zrna, 2 – Al₁₃Cr₂)

approximately the same. In the Fe-containing alloys the grain refinement is predominantly caused by the Fe addition and the influence of Ce on the grain size is almost negligible. The interaction of Al and Fe in a melt and during the solidification is so strong that it probably leads to a primary formation of very fine intermetallic phases. These phases can act as solidification nuclei for the fcc-Al matrix. These phases are then located at the grain boundaries or at the triple points of the matrix grains, protecting the alloys from a consequent grain coarsening.¹⁶

Figure 6 presents the structure of the AlCr4Ce1 alloy composed of the Al grains and intermetallic particles containing mainly Al and Cr. These intermetallics are most likely Al₁₃Cr₁₂, see the XRD patterns in **Figure 3**. The microstructure of the AlCr5Fe3Ce1 alloy is shown

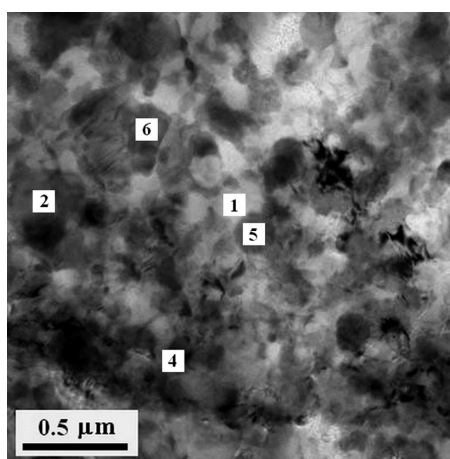


Figure 7: TEM micrograph of a cross-section of a rapidly solidified ribbon of the AlCr5Fe3Ce1 alloy (1 – Al grains, 2 – Al₁₃Cr₂, 4 – Al₈₀(Cr,Fe)₂₀, 5 – Al₁₃Fe₄, 6 – Al₃Ce)

Slika 7: TEM-posnetek prereza hitro strjenega traku zlitine AlCr5Fe3Ce1 (1 – Al zrna, 2 – Al₁₃Cr₂, 4 – Al₈₀(Cr,Fe)₂₀, 5 – Al₁₃Fe₄, 6 – Al₃Ce)

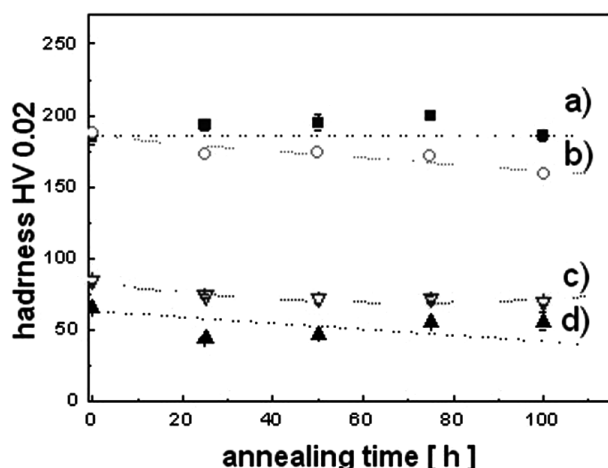


Figure 8: Room-temperature hardness dependence on the annealing time at 400 °C for: a) AlCr5Fe3Ce1, b) AlCr4Fe3, c) AlCr4Ce1 and d) AlCr2 alloys

Slika 8: Odvisnost trdote pri sobni temperaturi od časa žarjenja pri 400 °C za zlitine: a) AlCr5Fe3Ce1, b) AlCr4Fe3, c) AlCr4Ce1 in d) AlCr2

in **Figure 7**. Beside the Al grains and Al₁₃Cr₂ intermetallics in **Figure 7**, there are also spherical particles of the Al₈₀(Cr,Fe)₂₀ quasicrystalline phase as well as the Al₁₃Fe₄ and Al₃Ce phase particles.

Figure 8 shows the dependence of the room-temperature hardness on the annealing time after annealing at 400 °C. The microstructure of the AlCr5Fe3Ce1 alloy is supposed to be very stable because its hardness value did not change even after 100 h of annealing. The hardness of the other alloys slightly decreased. The Fe addition also caused a significant increase in the initial hardness of the rapidly solidified ribbons. In comparison with the AlCr5Fe3Ce1 alloy the hardness of the AlCr4Fe3 alloy slightly decreased with time. This suggests that the Ce addition stabilizes the alloy. The Al₃Ce particles, present in the AlCr5Fe3Ce1 alloy, are placed mainly at the grain boundaries suppressing the grain coarsening during the thermal exposure.

4 CONCLUSION

An addition of a few mass fractions of Fe significantly modifies the microstructure and the hardness of the rapidly solidified Al-Cr-Ti alloys. This results in an increase in the thickness of the ultra-rapidly-solidified areas of ribbons. It also causes a decrease in the fcc-Al matrix grain size and a significant increase in the hardness of the RS ribbons. An influence of the Fe addition on the thermal stability of the alloy during the heat treatment was not observed.

An addition of a very small amount (1 %) of Ce leads to the thermal stabilization of the alloy at the elevated temperatures of about 400 °C. The influence of Ce on the matrix grain size was not observed in the Al-Cr-Fe-Ti alloy. In the Al-Cr-Ti alloy, the Ce addition causes a mild decrease in the grain size.

Acknowledgement

This work was financially supported by the Czech Science Foundation (project No. P108/12/G043).

5 REFERENCES

- ¹ A. Inoue et al., *NanoStructured Materials*, 11 (1999), 221
- ² K. Saksl et al., *Journal of applied physics*, 97 (2005), 113507
- ³ M. Galano et al., *Acta Materialia*, 57 (2009), 5107
- ⁴ P. Jurči et al., *Mater. Tehnol.*, 41 (2007) 6, 283–287
- ⁵ H. Yang et al., *Journal of Non-Crystalline Solids*, 354 (2008), 3473
- ⁶ H. W. Jin et al., *Journal of Materials Science*, 36 (2001), 2089
- ⁷ C. Zhang et al., *Materials Science and Engineering A*, 323 (2002), 226
- ⁸ C. Dong et al., *Journal of Physics: Conference Series*, 98 (2008), 012015
- ⁹ K. Song et al., *Journal of Alloys and Compounds*, 440 (2007), L8
- ¹⁰ O. D. Neikov et al., *Materials Science and Engineering A*, 447 (2008), 80
- ¹¹ S. H. Wang et al., *Journal of Alloys Compounds*, 441 (2007), 135
- ¹² P. Rizzi et al., *Materials Science and Engineering A*, 304–306 (2001), 574
- ¹³ High Score Plus 2, user manual
- ¹⁴ A. L. Greer, *Science*, 267 (1995), 1947
- ¹⁵ M. P. Miller et al., *Bulk Metallic Glasses*, Springer-Verlag, 2007, 51
- ¹⁶ C. J. Ehrstrom et al., *Materials Science and Engineering A*, 186 (1994), 55–64

SHRINKAGE BEHAVIOR OF A SELF-COMPACTING CONCRETE

VEDENJE SAMOZGOŠČEVALNEGA BETONA PRI KRČENJU

Nasr-Eddine Bouhamou, Nadia Belas, Karim Bendani, Abdelkader Mebrouki

LCTPE Laboratory, Civil Engineering Department, University of Mostaganem, Algeria
bendanik@yahoo.fr

Prejem rokopisa – received: 2013-03-01; sprejem za objavo – accepted for publication: 2013-03-26

This paper presents the influence of the mixing constituents on the behavior of self-compacting concretes (SCCs), especially, the effect of the paste volume in their fresh and hardened state. It explains the roles of the pore network and the microstructure of the hydrates in drying and autogenous shrinkage of SCCs. Several tests such as slump flow, L-box, sieve stability, bleeding, mechanical strength, free shrinkage (drying and autogenous shrinkage) and microstructural tests (mineralogical characterization, porosimetric distributions) were carried out in order to understand the roles played by various components likely to influence the formulation of an SCC. The results obtained offer interesting prospects to optimize a SCC using local materials in Algeria. This study has allowed the development of various SCC formulations that fulfill the rheological criteria such as good deformability, low bleeding, low segregation and a better mechanical performance.

Keywords: self-compacting concrete, limestone fillers, porosimeter, drying shrinkage, autogenous shrinkage, mechanical strength

Članek opisuje vpliv primešanih dodatkov na vedenje samozgoščevalnega betona (SCC) na volumen v svežem in v strjenem stanju. Razložena je vloga mreže por in mikrostrukture hidratov pri sušenju in avtogenem krčenju SCC. Da bi razumeli vlogo posameznih delov in sestavin, ki opredeljujejo SCC, je bilo izvršenih več preizkusov, kot pojevanje toka, L-Box, stabilnost pri sejanju, izcejanje, mehanska trdnost, prosto krčenje (sušenje in avtogeno krčenje), mikrostrukturni preizkusi (mineraloška karakterizacija, razporeditev por). Dobljeni rezultati dajejo zanimive možnosti za optimiranje SCC z uporabo lokalnih mineralov v Alžiriji. Ta študija je omogočila različne formulacije SCC, ki izpolnjujejo reološka merila, kot je dobra deformabilnost, manj izcejanja, manj segregacij in boljše mehanske zmogljivosti.

Ključne besede: samozgoščevalni beton, polnila iz apnenca, porozimeter, krčenje pri sušenju, avtogeno krčenje, mehanska trdnost

1 INTRODUCTION

Self-compacting concrete is a fluid mixture suitable for being placed in the structures with a congested reinforcement without any vibration. Such concrete should have a low viscosity during the pouring to ensure the high-flow ability, and moderate viscosity to resist segregation and bleeding. Moreover, it must maintain its homogeneity during the transportation, placing and curing to ensure an adequate structural performance and long-term durability.

However, despite the interesting features that they offer, in particular, in their fresh state, some drawbacks of their long-term behavior can hinder their use. Indeed, the physicochemical phenomena inherent to the free shrinkage of SCCs have not yet been clearly specified. If it seems, from the formulation point of view, that one controls the proportioning of various components, to obtain a suitable fluidity, by preserving a good homogeneity and even a high mechanical strength,^{1,2} it should also be noted that the problem of the strains remains to be treated.

This research was undertaken in this context and must give answers to several questions, some of them concerning the progression of mechanical and physical properties of concrete with time. The objective of the

current work, using the local materials, is to acquire some knowledge explaining the shrinkage behavior of SCCs with variations in the relevant constituents, in particular, the volume of paste. The results obtained in this study will help us to have a more precise idea about the values of shrinkage and to determine the difference between the SCC and the ordinary concrete (OC), adopting an optimum formulation.

2 MATERIALS AND METHODS

2.1 Materials used

2.1.1 Cement

The cement used is CPJ CEM II/A 32.5, obtained from the Zahana factory (in the west of Algeria). Its physical and chemical properties in weight percent are given in **Table 1**.

2.1.2 Limestone fillers

The limestone used is from the Kristel quarry (in the west of Algeria). The sample analyzed is essentially constituted of limestone ($w(\text{CaCO}_3) = 85.45\%$) containing also a considerable quantity of silica ($w(\text{SiO}_2) = 10.81\%$). Its physical and chemical properties in mass fractions are given in **Table 1**.

Table 1: Physical properties and chemical analysis of the cement and limestone fillers

Tabela 1: Fizikalne lastnosti in kemijska analiza cementa ter polnil iz apnenca

Properties	Cement	Limestone fillers
Physical properties		
Bulk density (g/cm ³)	1.09	0.87
Specific gravity (g/cm ³)	3.00	2.66
Fineness (Blaine) (cm ² /g)	3100	2880
Chemical analysis (mass fractions, w/%)		
SiO ₂	21.93	10.81
CaO	63.87	47.51
MgO	0.21	0.21
Fe ₂ O ₃	4.26	0.76
Al ₂ O ₃	6.81	0.31
SO ₃	1.31	–
Loss on ignition	1.83	40.69
Free CaO	0.13	–
Carbonates	–	85.45
CO ₂	–	37.60
H ₂ O	–	3.09

2.1.3 Aggregates

Table 2 gives the aggregate properties for all the mixes used in this study.

Table 2: Physical properties of the aggregates

Tabela 2: Fizikalne lastnosti agregatov

	Marine sand (Sm)	Quarry sand (Sc)	Gravel (G)	
Grade	0/2	0/3	3/8	8/15
Composition	siliceous	limestone	limestone	limestone
Specific gravity (g/cm ³)	2.64	2.66	2.67	2.67
Absorption (%)	–	–	1.28	0.93

2.1.4 Admixture

A Viscocrete 20 HE superplasticizer, non-colored, containing acrylic copolymer, developed by the company of Sika, France, and complying with NF EN 934-2, was used for all the SCC mixes. This high-range water-reducing admixture has a dry extract content of 40 % and a unit mass of 1.085.

For the ordinary concrete (OC), the water-reducing superplasticizer used was a Plastiment BV 40. This

Table 3: Mix proportioning

Tabela 3: Mešalna razmerja

Description	V _{paste} (%)	Mix proportioning (kg/m ³)								
		Cement	Limestone fillers	Efficient water	Viscocrete 20 HE	Plastiment BV 40	Sm	Sc	G (3/8)	G (8/15)
SCC1	35	375.5	94	188	3.76	–	601	259	346	519
SCC2	37.5	400	100	200	4	–	578	249	333	499
SCC3	40	429	107	215	4.29	–	554	239	319	479
OC	34	350	–	175	–	5.25	129	576	204	947

admixture has a dry extract content of 36.6–40.4 % and a unit mass of 1.185.

2.2 Concrete mixtures

Three self-compacting concretes and one ordinary vibrated concrete were designed to study the effect of the paste volume on the SCC behavior in its fresh and hardened states.

The superplasticizer proportioning and the water/cement and filler/cement ratios were maintained constant for all the SCC mixes, i.e., Sp = 1 %, W/C = 0.5 and F/C = 0.25.

For the ordinary vibrated concrete, the mix was obtained using the Dreux-Gorisse method and the same W/C ratio as for the SCC was used for comparison. The compositions of different mixes are given in **Table 3**.

2.3 Tests on the fresh concrete

The fresh-state characterization of the SCC was limited to the tests recommended by the French Association of Civil Engineering (AFGC),³ i.e., the mini slump flow, L-box, sieve stability and bleeding.

2.4 Tests on the hardened concrete

2.4.1 Mechanical strengths

The samples used to determine the compressive mechanical strength for different concretes studied, are cylindrical test tubes with an diameter 11 cm and height 22 cm. Once removed from the mold, they were preserved in water for (1, 7, 28 and 90) d.

2.4.2 Free shrinkage

The shrinkage strains were measured using a contractometer on the prismatic test tube with the dimensions of 7 cm × 7 cm × 28 cm, fulfilling two requirements:

- to obtain the total shrinkage with hydrous exchange of the material with the environment;
- to measure the autogenous shrinkage, without hydrous exchange with the environment, by wrapping the test tubes in one or two aluminum sticker sheets.

After the removal from the mold (after 24 h), the total- and autogenous-shrinkage measurements are, at the beginning, worked out at very short times, followed by a periodic increase.

2.4.3 Measure of porosity

With the mercury intrusion porosimetry (MIP), the samples are introduced into a chamber, the chamber is evacuated, the samples are surrounded by mercury and the pressure on mercury is gradually increased. As the pressure increases, mercury is forced into the pores on the surface of the sample. By tracking the pressure and intrusion volumes during the experiment, it is possible to measure the connecting pore necks of a continuous system or the breakthrough pressure in a discontinuous system. The pore width corresponding to the highest rate of the mercury intrusion per change in the pressure is known as the "threshold", "critical" or "percolation" pore width. Using this technique, one also measures the total porosity of a sample as that corresponding to the volume of the mercury intruding at the maximum experimental pressure, divided by the bulk volume of the unintruded sample.

The humidity exchanges of the concrete with the external media are then linked to the porous structure. The knowledge of the concrete porosity can thus prove to be useful when estimating the relative differences between the microstructural formulations of the SCCs that are likely to explain the results obtained for the shrinkage with respect to its composition. In this context, the porosities of different SCC formulations were characterized (after about 300 d, i.e., the last period of the shrinkage measurement). The measurements were realized in the civil engineering laboratory of La Rochelle (France) by means of a mercury porosimeter Autopore III from Micrometrics (ASTM D4404-10). The range of the measurement was from 3 nm to 200 μm.

3 RESULTS AND ANALYSIS

3.1 Fresh state

The response of the characterization tests performed on the prepared concrete is given in Table 4.⁴

Table 4: Influence of the W/C and F/C ratios on the behavior of SCC in the fresh state

Tabela 4: Vpliv razmerij W/C in F/C na vedenje SCC v svežem stanju

Tests	SCC1	SCC2	SCC3
	$V_{paste} = 35\%$	$V_{paste} = 37.5\%$	$V_{paste} = 40\%$
Slump flow (mm)	570	700	750
L-box H2/H1	0.73	0.87	0.91
Sieve stability π (%)	5.66	7.68	15.01
Bleeding (%)	0.93	1.15	3.15

The volume of paste is supposed to play two roles in SCC. Initially, it fluxes the material by limiting the contacts between the aggregates. Then, it splits off the gravels sufficiently to avoid a formation of clusters against the reinforcements, responsible for the flow blocking. It is supposed that a minimum volume of paste is needed to fulfill the two functions.

Table 4 shows that among the tested concretes, only one presents a slump shorter than 60 cm. It is clear that an increase in the volume of paste contributes to a significant improvement in workability. This improvement is principally due to the reduction of the coarse aggregate content and, moreover, an increase in the volume, in particular, in the crushed aggregates, induces an important friction.⁵ This is the case of the SCC with a volume of paste of 35 %.

The results obtained from the L-box test given in Table 4 show a good proportioning between the volume of paste and the h_2/h_1 ratio of the concretes. The SCC with a volume of paste of 35 % showed a poor flow in the L-box test with the blocking h_2/h_1 ratio not exceeding 0.80.

For this purpose, it is noted that a paste content of approximately 35 % does not allow an SCC to fulfill the requirements of the AFGC.

Contrary to the slump and L-box tests, the concrete with the 40 % volume of paste was at the extreme limit to the domain of self-compactness since the percentage of its latency is slightly higher than 15 %.

This concrete also developed a poor stability with respect to bleeding, as its percentage exceeded 3 ‰. This segregation is principally due to the increase in the volume of paste compared to that of the aggregates.

3.2 Hardened state

3.2.1 Evolution of the compressive mechanical strength

An SCC presenting a good workability must contain enough volume of paste to cover the aggregate surface in order to minimize the frictions between the particles, on the one hand, and, on the other hand, an additional quantity of paste is necessary to obtain a better workability.⁶ When injected into the pores of the aggregates, this paste is called the matrix and its apparent properties are affected by the geometric arrangement of the skeleton.

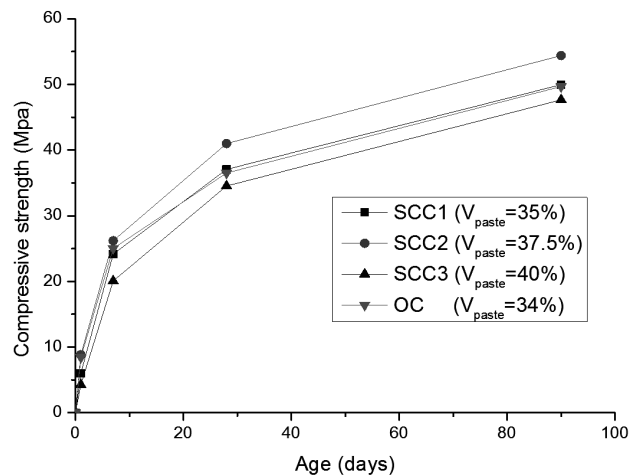


Figure 1: Influence of the volume of paste on the compressive strengths of SCCs

Slika 1: Vpliv količine paste na tlačno trdnost SCC

More precisely, it is the average distance between two coarse adjacent aggregates, called the maximum thickness of the paste, which reflects the topology influence of the skeleton: the shorter the distance, the higher is the concrete strength. It is supposed that there is a minimum volume of paste supporting this condition.

Figure 1 shows the effect of the volume of paste on the compressive strength after (1, 7, 28 and 90) d. At the first approximation, it is the density of the paste that varies with respect to its volume percentage. It is noted that the volume of paste within the interval (37.5–40 %) contributes to the increase in the strengths for two aging periods before causing their decrease when its rate exceeds the critical value of about 37.5 %.

There is only one explanation for that: within the volume-of-paste interval (37.5–40 %), the quantity of paste is important and the distance between the aggregates is larger, causing the frictions between them and, consequently, engendering the weaker strengths.

The compressive strength deviation for SCC/OC observed in **Figure 1** can be explained with a higher proportion of the paste used for SCC (376 l/m³ against 341 l/m³ for OC) and the absence of the limestone fillers in OC which may have had a negative effect upon the density.⁷

3.2.2 Free shrinkage

The concrete starts to undergo geometric strains as soon as its installation in the framework has been completed. These dimensional changes develop in different directions and are governed by various physical and chemical phenomena. They take place in the material free from stresses, creating a need for a loaded material.

3.2.2.1 Autogenous shrinkage

The development of autogenous shrinkage begins as soon as the concrete begins to settle and it will stabilize after a few months. This is linked to the auto-drying, i.e.,

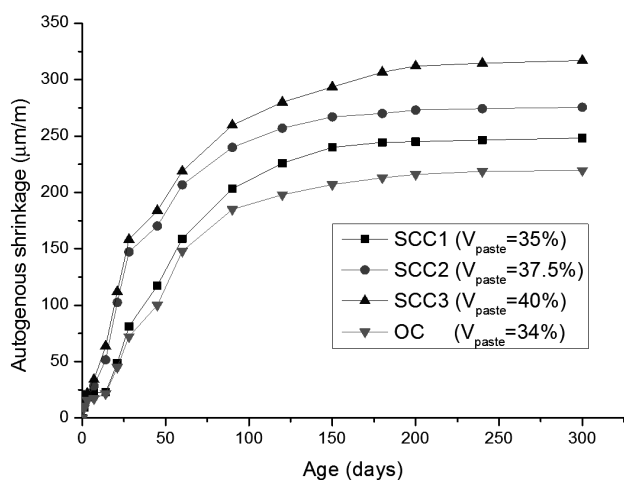


Figure 2: Influence of the volume of paste on the autogenous shrinkage of SCC

Slika 2: Vpliv količine paste na avtogeno krčenje SCC

the internal-humidity decrease due to the water consumption by the hydrates.⁵

The volume of paste in the concrete is generally much lower than in the mortar. And yet, it is the paste which retracts and not the aggregate skeleton, which, on the contrary, obstructs the shrinkage. Therefore, it can be concluded that it is the volume-of-paste proportioning that mainly governs the shrinkage values.

It is observed in **Figure 2** that the autogenous shrinkage increases with the volume of paste. The shrinkage progress, with respect to the volume of paste, does not seem to be linear. This is perhaps due to the skeleton-structure variation.

The autogenous shrinkage after 300 d is about 317 µm/m for the SCC with the V_{paste} of 40 % and 275 µm/m for the SCC with the V_{paste} of 37.5 %, showing a difference of 42 µm/m. The SCC with the V_{paste} of 35 % presents a shrinkage of 248 µm/m, i.e., a reduction of 69 µm/m compared to the first formula. These results reveal that the recorded autogenous strains on the SCC with the V_{paste} of 40 % are much higher than those measured on the two other SCCs. This highlights the importance of the aggregate content. In fact, the strains measured on the concrete are the effective strains of this heterogeneous material, consisting of the aggregates and the paste (cement + fillers + superplasticizer + water). And yet, the aggregates restrict the straining of the paste due to the physical/chemical process linked to hydration. Therefore, an aggregate-content reduction and an increase in the volume of paste allow much higher effective strains.

Indeed, the effective strains are determined with the respective parameters (especially the elastic properties, but also the dry density of the granular mixture).

At last, it can be said that the autogenous shrinkage of an SCC increases with an increase in the volume of paste. The reason is that only the paste creeps. The volume of paste is also a parameter that influences the shrinkage. The same result was reported in the literature.^{8,9}

The results show that, on the whole, the autogenous shrinkage of an SCC is greater than that of the ordinary concrete (OC). After the first three months, the observed difference between the two types of concrete varied from 10 % to 40 %, i.e., having a strain range of 1.1 to 1.4 (**Figure 2**).

3.2.2.2 Shrinkage due to drying and weight loss

Figure 3 shows a variation in the shrinkage time due to drying, for an SCC with respect to the volume of paste. This shrinkage can be considered to be due only to the evaporation of the water contained in the hydrated cement paste that develops from the surfaces when exposed to external ambience.

The drying shrinkage increases with an increase in the volume of paste. Two distinct phases appear in the strains developed: during the first phase of six months

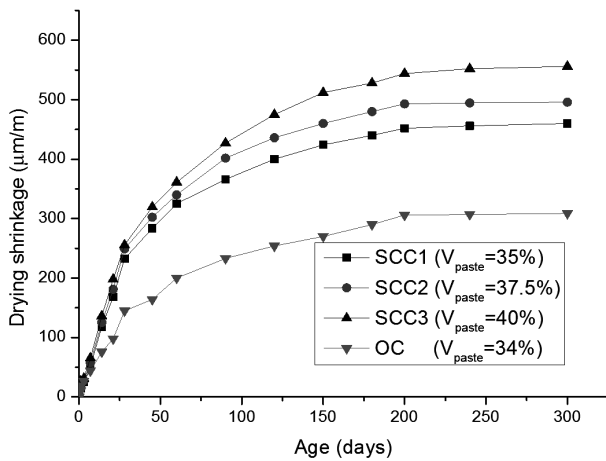


Figure 3: Influence of the volume of paste on the drying shrinkage of SCC

Slika 3: Vpliv količine paste na krčenje pri sušenju SCC

the evolution speed is high and in the second phase it slows down significantly to become constant. These results are very compatible with those obtained from reference.⁹

The strain analysis of the SCCs shows that the formulation with the V_{paste} of 40 % is characterized with a higher drying shrinkage than that of the two other formulations ($V_{paste} = 37.5 %$ and $V_{paste} = 35 %$) after 300 d; the differences are 60 $\mu\text{m/m}$ when compared to the SCC with the V_{paste} of 37.5 % and 96 $\mu\text{m/m}$ compared to the SCC with the V_{paste} of 35 %, corresponding to the increase range of 12 % and 21 %, respectively.

The differences in drying shrinkage between the SCC and the OC shown in Figure 4 are explained with the paste proportioning that is very important for the SCCs (the minimum proportioning for the SCCs is higher by 35 l/m^3), leading to a much higher volume of hydrates in the SCCs than in the OC and, therefore, creating a very important volumetric strain.

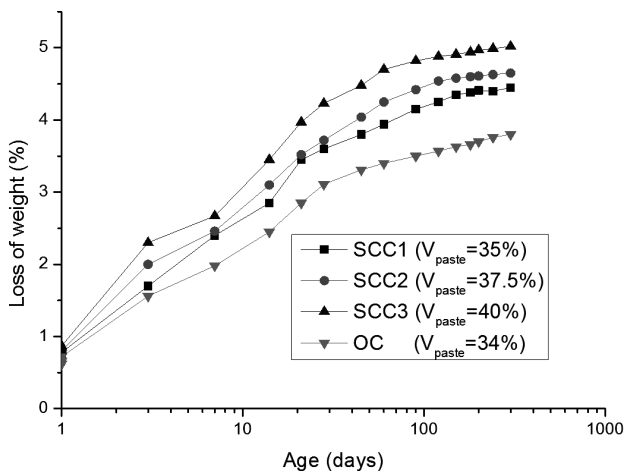


Figure 4: Loss of weight with respect to the volume of paste – a logarithmic scale

Slika 4: Zmanjšanje mase glede na količino paste – logaritemsko merilo

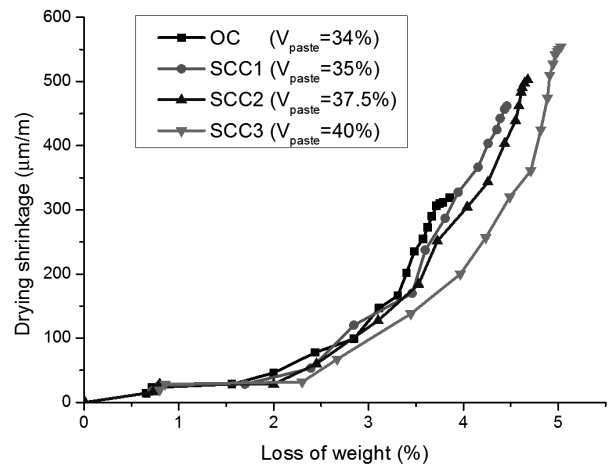


Figure 5: Drying shrinkage versus the loss of mass

Slika 5: Krčenje pri sušenju v primerjavi z zmanjšanjem mase

On the other hand, Figure 4 shows that the water-quantity variation for all the concretes is approximately linear as long as the water evaporation continues with a logarithmic time scale. All the concretes continue to hydrate and the evaporated quantity of water is then the function of the volume of paste.

Figure 5 brings an additional proof of the influence of the volume of paste on the shrinkage due to drying. In fact, different evolution curves of the shrinkage due to drying, with respect to weight loss, show that after the first evaporation of water with no consequences on the shrinkage, there is the second stage, where the shrinkage progresses with the water consumption.

It is observed that the weight losses for the SCC and OC are different, but also that the drying-shrinkage evolution with respect to the weight loss can be considered as linear.

3.2.2.3 Total shrinkage

The relative results for the SCC total shrinkage during 300 d are presented in Figure 6. From the quantitative point of view, the experimental value for the total shrinkage of the SCC containing a higher quantity of paste (40 %), after 300 d, is 873 $\mu\text{m/m}$. The values, for the same time, for the two other formulations are as follows: 771 $\mu\text{m/m}$ for the SCC containing 37.5 % of paste and 708 $\mu\text{m/m}$ for the SCC containing 35 % of paste.

The shrinkage of the SCC with the V_{paste} of 35 % is slightly lower than that of the SCC with the V_{paste} of 37.5 %, but it shows a defect in the stability, observed during the L-box test, causing a problem according to the AFGC recommendations.

The observed experimental data reveal significant differences between the total shrinkages of the SCCs. This deviation can be seen as a consequence of the volume-of-paste increase.

The SCCs are more susceptible to deformability than the OC (Figure 6) because of a higher quantity of paste.

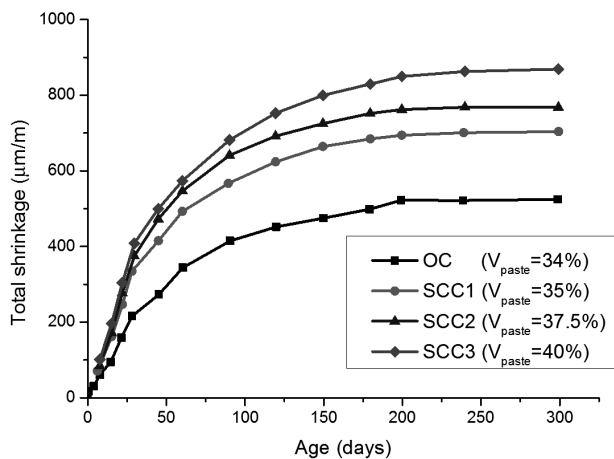


Figure 6: Influence of the volume of paste on the total shrinkage
Slika 6: Vpliv količine paste na celotno krčenje

While making this conclusion, we neglect, however, the fact that the SCC paste does not have the same composition as the OC paste (additions, superplasticizer, water quantity). Besides, E. Proust⁸ has found an opposed tendency of the other concretes. B. Persson¹⁰ has shown that, with the same strength, there will be no behavioral difference between SCC and OC, in spite of the volume-of-paste deviation.

On the other hand, Y. Klug and K. Holschemacher¹¹ found repeatedly in a large database that the total SCC shrinkage was higher, by 10 % to 50 %, than that of the OC. The SCC shrinkage was also found to be higher than that of the OC by other researchers.¹²⁻¹⁴

3.3 Study of porosity

The results obtained from the porosimetry test for the SCCs with respect to different values of paste proportioning ($V_{paste} = 35\%$, $V_{paste} = 37.5\%$ and $V_{paste} = 40\%$) are shown in **Figures 7 and 8**.

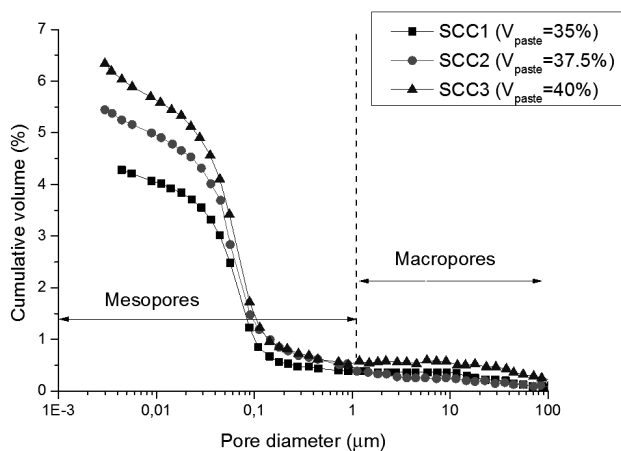


Figure 7: Cumulative volume of the mercury intrusion into the sample versus the pore diameter

Slika 7: Kumulativni volumen vdora živega srebra v vzorec v primerjavi s premerom por

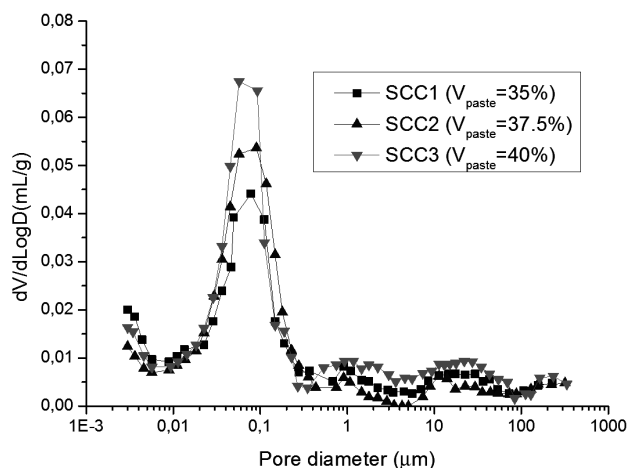


Figure 8: Differential volume of the mercury intrusion into the sample versus the pore diameter

Slika 8: Diferenčni volumen vdora živega srebra v vzorec v primerjavi s porami

In **Figure 7**, it is observed that the cumulative volume of the SCC pores containing a higher paste proportioning (40 %) becomes more important than those of the two other SCCs (the V_{paste} of 35 % and the V_{paste} of 37.5 %) as the pore size decreases. This seems to be in accordance with the autogenous shrinkage obtained for these concretes.

As far as the shrinkage due to drying is concerned, the smallest pores ($<0.01\ \mu\text{m}$) in the SCC with the V_{paste} of 40 % have a greater proportioning than those of the SCC with the V_{paste} of 37.5 % and the SCC with the V_{paste} of 35 %. The experimental results given in section 3.2.2 reveal, effectively, that the drying shrinkage of the SCC with a high quantity of paste ($V_{paste} = 40\%$) is greater than in the case of the two other formulations ($V_{paste} = 37.5\%$ and $V_{paste} = 35\%$).

On the other hand, it is noted on the graph of **Figure 8**, for all the SCCs, that the porosities are closer in a very marked peak zone, between $0.02\ \mu\text{m}$ and $0.2\ \mu\text{m}$, and, leaving aside the presence of the remainder of the peak in the zone (10–100 μm) for the SCC with the V_{paste} of 40 % and the SCC with the V_{paste} of 35 %, the other formulation shows a low porosity for higher pore sizes. The paste corresponding to this SCC ($V_{paste} = 37.5\%$) must appear on this scale as a homogenous and, consequently, tougher material.

Figure 8 shows, in fact, that a lower macroporosity difference (0.1 %) seems to explain a much higher mechanical strength of the corresponding SCCs (section 3.2.1).

4 CONCLUSION

In this study, it is confirmed that it is possible to produce SCCs with the Algerian local materials having the same properties as those known internationally. Therefore, it is advisable to pay attention to the import-

ance of the mix proportioning, which is of great influence, in particular, the W/C and F/C ratios, to achieve the best required properties of an SCC.

Based on the obtained results, it has been shown that, in the tested range (35–37.5 %), the volume of paste contributes to an increase in the SCC strength. In the range of 37.5–40 %, the paste proportioning has a significant influence on the concrete behavior resulting in a remarkable fall in the strength.

The SCC shrinkage is directly proportional to the paste proportioning. The presence of a net difference between the values for the tested SCC shrinkage seems to indicate that the volume of paste is also a principal parameter affecting the shrinkage.

The results obtained from the mercury-intrusion porosimetry test support certain assumptions put forward and allow us to explain, in a pertinent manner, the behavior of the SCCs in their hardened state. In fact, the microstructural study of the samples has confirmed that the hydration process is not the same for different SCCs, depending on the paste quantity. The volumetric porosity also shows relative differences in the SCC microstructure formulations, confirming the results obtained experimentally.

Finally, taking into account the relative measurement uncertainties, it is believed that the stabilization of the SCC strains will be faster than that for the OC, for which the tendency to stabilization seems to differ with time. Therefore, certain reduced deviations can be observed over a long term. More tests made over several years will be necessary for a better quantification of this phenomenon.

5 REFERENCES

- ¹ H. Okamura, K. Ozawa, M. Ouchi, Self-compacting concrete, *Structural Concrete, J. adv. concrete technology*, 1 (2003) 1, 5–15
- ² M. Shahul Hameed, A. S. S. Sekar, V. Sarswathy, Strength and permeability characteristics study of self-compacting concrete using crusher rock dust and marble sludge powder, *Arab J. Sci. Eng.*, 37 (2012), 561–574
- ³ AFGC, Les bétons autoplaçants, Recommandations provisoires, French Association of Civil Engineering, 2000
- ⁴ N. Bouhamou, N. Belas, H. Mesbah, A. Mebrouki, Y. Ammar, Etude du comportement à l'état frais des bétons autoplaçants à base de matériaux locaux, *Canadian Journal of Civil Engineering*, 35 (2008) 7, 653–662
- ⁵ A. Neville, Propriétés des bétons, Centre de Recherche International du Béton, Editions Eyrolles, 2000
- ⁶ S. G. Oh, T. Nogushi, F. Tomosawa, Toward mix design for rheology of self-compacting concrete, Proc. First International Rilem Symposium on Self-Compacting Concrete, Rilem, 1999
- ⁷ K. H. Khayat, Utility of statistical models in proportioning self-consolidating concrete, Proc. First International Rilem Symposium on Self-Compacting Concrete, Rilem, 1999
- ⁸ E. Proust, Retrait et fluage des bétons autoplaçants – vers une compréhension des comportements différés, Doctorat Thesis, Institut National des Sciences Appliquées, Toulouse, 2002
- ⁹ P. Turcry, Retrait et fissuration des bétons autoplaçants – Influence de la formulation, Doctorat thesis, Ecole Centrale de Nantes et l'Université de Nantes, Nantes, 2004
- ¹⁰ B. Persson, Creep, shrinkage and elastic modulus of self-compacting concrete, Technical Report, Japan Society for Promotion of Science, Lund Institute of Technology, Division of Building Materials, Lund University, Lund, 1997
- ¹¹ Y. Klug, K. Holschemacher, Comparison of hardened properties of self-compacting and normal vibrated concrete, Proc. Third International Rilem Symposium on Self-Compacting Concrete, Rilem, 2003
- ¹² J. Ambroise, J. Pera, S. Rols, Les bétons autonivelants, *Annales du Bâtiment et des Travaux Publics*, 1 (1997), 37–41
- ¹³ C. Hu, B. Barbieri, Comparaison des retraits des bétons autonivelants et d'un béton fluide traditionnel, *Sciences des Matériaux et Propriétés des bétons 1^{ères} rencontres internationales*, Toulouse, 1998, 265–272
- ¹⁴ S. Rols, J. Ambroise, J. Pera, Development of admixture for self-leveling concrete, 5th CANMET/ACI Int. Conf. on Superplasticizer and Other Chemical Admixtures in Concrete, SP 173, Rome, 1997, 493–509

FAILURE MODE OF M130 MARTENSITIC STEEL RESISTANCE-SPOT WELDS

NAČIN PORUŠITVE UPOROVNIH TOČKASTIH VAROV PRI MARTENZITNEM JEKLU M130

Majid Pouranvari¹, Seyed Mostafa Mousavizadeh²

¹Materials and Metallurgical Engineering Department, Dezful Branch, Islamic Azad University, Dezful, Iran

²Department of Materials Engineering, Faculty of Engineering, Hakim Sabzevari University, Sabzevar, Iran
mpouranvari@yahoo.com

Prejem rokopisa – received: 2013-03-04; sprejem za objavo – accepted for publication: 2013-03-25

This paper discusses the transition from the interfacial to the pullout failure mode for the M130 martensitic, advanced high-strength steel (AHSS) during a quasi-static tensile-shear test. It was studied whether the conventional/industrial weld-size criteria can produce pullout failure modes for M130 spot welds. The minimum fusion-zone size required to ensure the pullout failure mode during the tensile-shear test is estimated using an analytical model, taking into account the weld metallurgical characteristics, with good accuracy. Based on the theoretical analysis it was concluded that the failure-mode transition in M130 resistance-spot welds is influenced by the sheet thickness, the fusion-zone hardness and the intercritical heat-affected-zone hardness.

Keywords: martensitic steel, resistance-spot welds, failure mode, HAZ softening

Ta članek obravnava prehod od medploskovnega do iztrganega načina porušitve pri M130 martenzitnem naprednem visokotrnostnem jeklu (AHSS) med kvazistatičnim natezno-strižnim preizkusom. Raziskano je bilo, ali je pri običajnih kriterijih industrijskih zvarov mogoče dobiti porušitev z iztrganjem pri točkastih zvarih M130. Z analitičnim modelom, ki upošteva metalurške značilnosti zvara, je bilo mogoče z dobro zanesljivostjo določiti minimalno področje zlivanja za porušitev z iztrganjem med natezno-strižnim preizkusom. Na podlagi teoretičnih analiz je bilo ugotovljeno, da na prehod načina porušitve pri M130 uporovno varjenih zvarih vplivajo debelina pločevine, trdota področja zlivanja in interkritična trdota toplotno vplivanega področja.

Ključne besede: martenzitno jeklo, uporovno varjeni zvari, način porušitve, mehčanje HAZ

1 INTRODUCTION

Advanced high-strength steels (AHSSs) have been introduced to vehicle designs in an effort to improve the collision-energy management and passenger safety, while maintaining or reducing the vehicle weight that, in turn, creates a better fuel economy.¹ Due to a very high strength and low formability, martensitic advanced high-strength steels (AHSSs) are good candidates for high-stiffness, load-transferring barriers and anti-intrusion barriers (e.g., A- and B-pillar reinforcements, rocker reinforcements, roof rails, front and rear bumpers, side-wall members, cross beams and door beams) improving crash management and protection of passengers during side-impact collisions.²

Resistance-spot welding is the predominant joining process in the automotive industry.³⁻⁵ The failure mode of resistance-spot welds (RSWs) is a qualitative measure of mechanical properties.^{4,5} **Figure 1** shows a schematic representation of the fracture surfaces in the main failure modes during a mechanical testing of the spot welds. Basically, spot welds can fail in two distinct modes described as follows:⁶⁻¹¹

1. Interfacial failure (IF) mode, in which a fracture propagates through the fusion zone. It is believed that

this failure mode has a detrimental effect on the crashworthiness of the vehicles.

2. Pullout failure (PF) mode, in which a failure occurs due to a withdrawal of the weld nugget from one sheet. In this mode, a fracture may be initiated in the BM, HAZ or HAZ/FZ depending on the metallurgical and geometrical characteristics of the weld zone

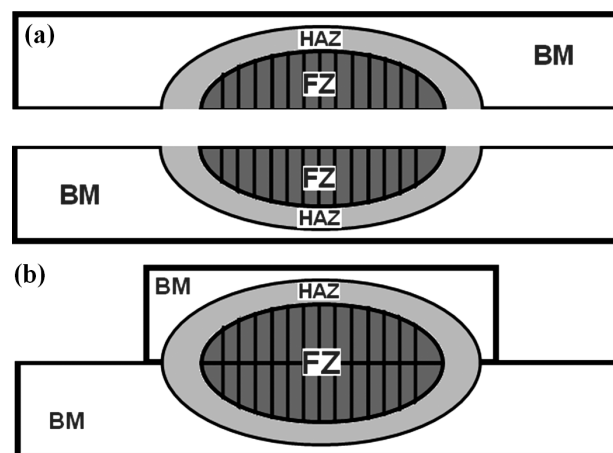


Figure 1: Schematic representation of: a) interfacial, b) pullout failure modes

Slika 1: Shematski prikaz načina porušitve: a) medploskovna, b) z iztrganjem

and the loading conditions. Generally, the PF mode exhibits the most satisfactory mechanical properties.

Thus, vehicle crashworthiness, as the main concern in the automotive design, can be dramatically reduced if spot welds fail due to the interfacial mode. The pullout failure mode indicates, during a quality control, that the same weld would have indeed been able to transmit a high level of force, thus, causing a severe plastic deformation in its adjacent components and an increased strain-energy dissipation in crash conditions. Therefore, it is necessary to adjust the welding parameters so that the pullout failure mode is guaranteed.

The RSWs of AHSSs exhibit a higher tendency to fail in the interfacial failure mode than those of traditional steels (i.e., low-carbon and HSLA steels).⁵⁻¹⁰ There are several size criteria for resistance-spot welds included in industrial standards. "The effectiveness of these criteria for evaluating AHSS spot welds, however, has not been adequately addressed in the automotive welding community; it was simply adopted from the mild steel practice and applied to AHSS spot welds".¹² The failure mode of the AHSS spot welds is a complex phenomenon causing an interaction among the geometrical factors, weld metallurgical properties and the loading mode. Consequently, it is necessary to develop a spot-weld sizing criterion based on the failure mode to reach a deeper understanding of the factors governing the failure mode of spot welds.

In this paper, the failure-mode transition of M130 martensitic steel resistance-spot welds under the tensile-shear loading condition is studied. The objectives of this study are:

1. to examine whether the existing weld-size criteria can produce the pullout failure mode for M130 spot welds;
2. to determine the critical fusion-zone size ensuring the pullout failure mode of M130 spot welds.

2 EXPERIMENTAL PROCEDURE

An M130 martensitic sheet with a thickness of 2 mm was used as the base metal in this study. The chemical composition and mechanical properties of the M130 used in this study are given in **Table 1**. Spot welding was performed using a 120 kVA AC pedestal-type resistance-spot welding machine, operating at 50 Hz and controlled by PLC. Welding was conducted using a 45°,

Table 1: Chemical composition and mechanical properties of the investigated M130 steel

Tabela 1: Kemijska sestava in mehanske lastnosti preiskovanega jekla M130

Chemical composition (w/%)					Tensile properties	
C	Mn	Si	S	P	YS* (MPa)	UTS** (MPa)
0.11	0.53	0.07	0.02	0.02	851	960

*Yield strength

** Ultimate tensile strength

truncated-cone, RWMA class 2 electrode with a face diameter 8 mm. To study the effects of the weld FZ size on the failure mode and mechanical properties, spot welding was performed in various welding conditions. The welding time, electrode force and electrode holding time after current-off were selected on the basis of the thickness of the base material and were kept constant at 0.5 s, 4.5 kN and 0.2 cycles. The welding current was changed step by step from 5 kA to 12.5 kA. The step size was 0.5 kA.

The quasi-static tensile-shear test samples were prepared according to the ANSI/AWS/SAE/D8.9-97 standard.¹³ **Figure 2a** shows the sample dimensions during the tensile-shear test. Since the tensile-shear specimen is asymmetrical, two shims with the same thickness were added at the grip sections of the specimen to ensure an alignment and to reduce the sheet bending and nugget rotation. The tensile-shear tests were performed at the cross-head speed of 2 mm/min with an Instron universal testing machine. The peak load and failure energy were extracted from the load-displacement curve (**Figure 2b**). The failure modes were determined by observing the weld fracture surfaces.

Microhardness test, a technique that has proven to be useful for quantifying the microstructure/mechanical property relationship, was used to determine the hardness profile. The hardness profile in the diagonal direction was obtained using the Vickers microhardness testing with an indenter load of 10 g and a speed of 10

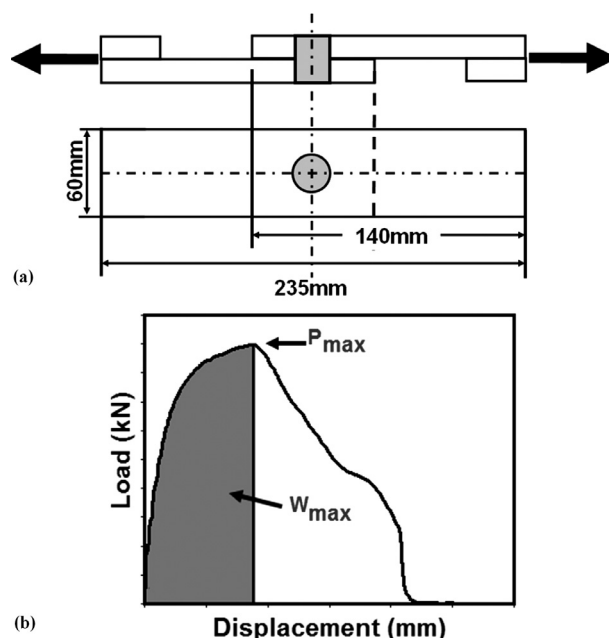


Figure 2: a) Tensile-shear specimen dimensions, b) a typical load-displacement curve with the extracted parameters; P_{max} : peak load, W_{max} : energy absorption

Slika 2: a) Dimenzije vzorcev za natežno-strižni preizkus, b) značilna krivulja obremenitev – raztezek s parametri; P_{max} : največja obremenitev, W_{max} : absorpcija energije

indentations/min. The indentations were made on three paths with a 0.3 mm spacing.

3 RESULTS AND DISCUSSION

3.1 Hardness characteristics

Macrostructural characteristics of the RSWs, particularly the fusion-zone size, the microstructural and hardness characteristics, play important roles in their failure behavior and failure mode.¹⁴⁻¹⁶ Rapid heating and cooling induced by the resistance-spot-welding thermal cycles significantly alter the microstructure in the joint zone. A typical macrostructure of M130 RSW is shown in **Figure 3a** indicating that there are distinct zones in the weldment including:

1. the fusion zone (FZ) or weld nugget, melted during the welding process and later resolidified, showing a cast structure. The macrostructure of the weld nugget consists of columnar grains;
2. the heat-affected zone (HAZ) that is not melted but it undergoes microstructural changes during welding;
3. the base metal (BM).

Figure 3b shows a typical hardness map of the M130 spot welds. The average hardness of the BM is about 300 HV. The average hardness of the FZ is 360 HV, which is about 1.2 times higher than the hardness of the BM. The microstructure of both BM and FZ is almost martensitic. Therefore, the higher hardness of the FZ, compared to the BM, can be related to the higher cooling rate during RSW. It has been reported that an increasing cooling rate can increase the dislocation density in the martensitic laths increasing its hardness.

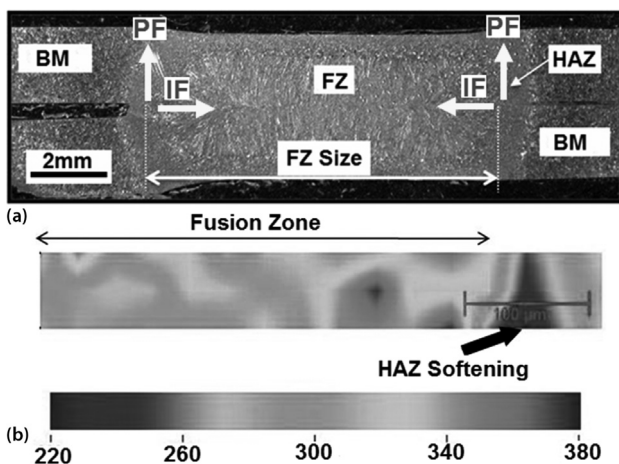


Figure 3: a) Typical macrostructure of M130 martensitic steel resistance-spot weld. Failure paths in the interfacial failure (IF) mode and pullout failure (PF) mode are also shown in the macrograph with the arrows. b) Typical hardness map

Slika 3: a) Značilna makrostruktura uporovnega točkastega zvara pri martenzitnem jeklu M130. S puščicami so prikazane poti porušitve pri medploskovni porušitvi (IF) in pri porušitvi iz ztrganjem (PF). b) Značilna razporeditev trdote

A reduction in the hardness (softening), with respect to the BM, was observed in the HAZ. The minimum hardness of the HAZ is about 215 HV (i.e., the maximum hardness reduction of 85 HV). The observed softening can be related to the following reasons:

1. In the intercritical HAZ (ICHAZ) region, the peak temperature is ranging between A_{c1} and A_{c3} and the BM microstructure transforms into ferrite plus austenite during heating. Due to the fast welding cooling rates, austenite can subsequently transform into martensite. Therefore, the formation of an allotriomorphic ferrite phase in the ICHAZ leads to a hardness reduction with respect to the fully martensitic BM.
2. In the subcritical HAZ (SCHAZ), the peak temperature is below A_{c1} resulting in tempering of the metastable martensite. This issue causes a reduction in the hardness with respect to the BM.

3.2 Failure-mode analysis

Figure 4 shows the effect of the FZ size on the failure mode of M130 welds. As can be seen, the increasing FZ size alters the failure mode from the interfacial to the pullout mode. There is a critical FZ size, above which the pullout failure mode is guaranteed. According to **Figure 4**, the minimum FZ size of 9.2 mm is required to ensure the PF mode.

In order to study the effect of the failure mode on the mechanical performance of M130 resistance-spot welds, box plots of peak load and energy absorption are shown in **Figures 5a** and **5b**, respectively. As can be seen in **Figure 5**, the average peak load of those spot welds that failed in the IF is lower than the peak load of the spot welds that failed in the PF mode. Therefore, due to its significant impact on the joint reliability, the failure mode has been an interesting issue of some recent studies. The transition from the IF mode to the PF mode is generally related to the increase in the FZ size above the

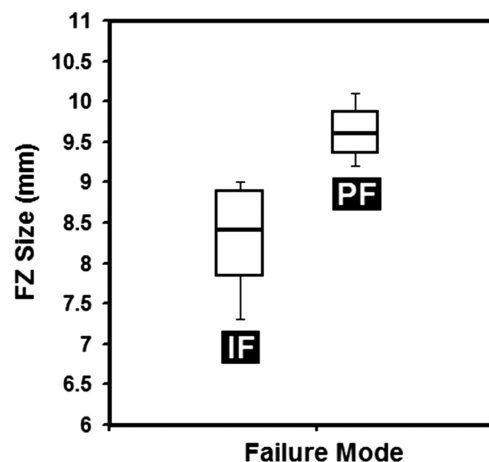


Figure 4: Effect of the FZ size on the failure mode of M130 martensitic steel resistance-spot welds

Slika 4: Vpliv velikosti FZ na način porušitve uporovnega točkastega zvara pri martenzitnem jeklu M130

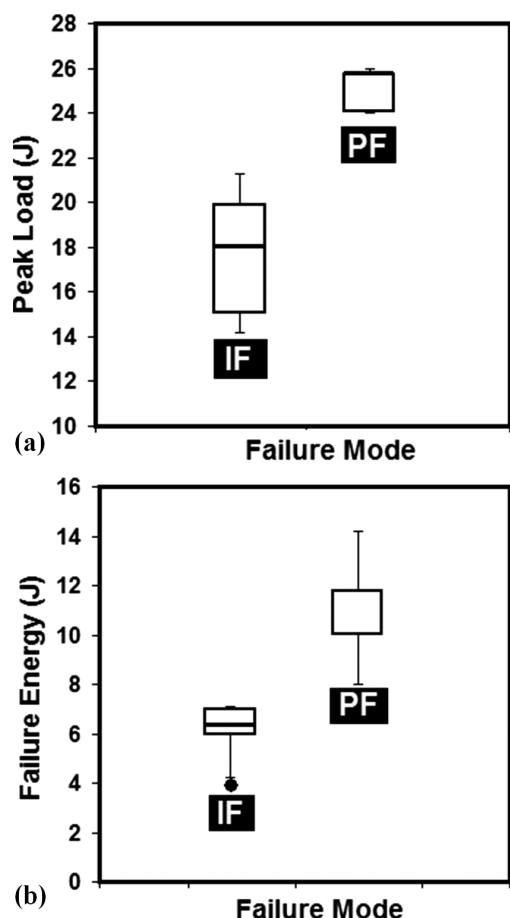


Figure 5: Box plots of: a) peak load (P_{max}) and b) failure energy (W_{max}) versus failure mode for M130 martensitic steel resistance-spot welds

Slika 5: Prikaz: a) največje obremenitve (P_{max}) in b) energije porušitve (W_{max}) glede na način porušitve točkasto uporovno varjenih zvarov martenzitetnega jekla M130

minimum value. In the following sections, the failure-mode transition is compared with the existing criterion for the weld-nugget sizing of a spot weld. For practical purposes, it is interesting to compare the experimentally determined minimum FZ size required to obtain the PF mode with the existing industrial standards for weld-nugget sizing. Various industrial standards have recommended a minimum weld size for a given sheet thickness:

1. According to AWS/ANSI/AISI,¹² the weld-button sizing used to ensure that the weld size was large enough to carry the desired load, is based on equation (1):

$$D = 4t^{0.5} \tag{1}$$

where D is the weld-nugget size and t is the sheet thickness (mm).

2. According to the Japanese JIS Z3140¹⁷ and German DVS2923¹⁸ standards the required weld size is specified according to equation (2):

$$D = 5t^{0.5} \tag{2}$$

3. The minimum weld-nugget size (equation 3) and the nominal weld size (equation 4) are also frequently used in certain industries:¹⁹

$$D = 0.69 (1.65t - 0.007)^{0.5} \tag{3}$$

$$D = 0.86 (1.65t - 0.007)^{0.5} \tag{4}$$

Figure 6 compares the experimentally determined critical FZ size for the spot welds made on M130 steel 2 mm and the weld size recommended by the industry. As can be seen, the most common weld-sizing criteria of $4t^{0.5}$ and $5t^{0.5}$ are not sufficient to produce a weld with the PF mode. Also, equation (3) and equation (4) are not sufficient to avoid the interfacial failure. Despite the fact that the industrial recommendations work well for obtaining the pullout mode of low-carbon steels, the sizing based on these recommendations does not guarantee the PF mode during the tensile-shear testing of the AHSS spot welds. This is due to the fact that these recommendations ignore the effect of metallurgical factors on the failure mode so that these models include only the sheet thickness for the sake of simplicity. Radakovic and Tumuluru²⁰ used finite-element modeling to predict the resistance-spot-weld failure mode and the loads in the shear-tension tests of advanced high-strength steels (AHSS). In the finite-element model, the base material, the heat-affected zone and the fusion-zone properties were assumed to be homogeneous. According to their finite-element modeling results, the critical fusion-zone size can be expressed as follows:

$$D_C = 4t \tag{5}$$

According to their results, the critical weld size for a thick sheet 2 mm is 8 mm. However, the experimental value for a thick M130 2 mm is 9.2 mm, which is above the recommended value of this mode. Indeed, this model assumes the mechanical properties across the weldment to be homogenous and does not take into account the HAZ softening. In the following section an analytical

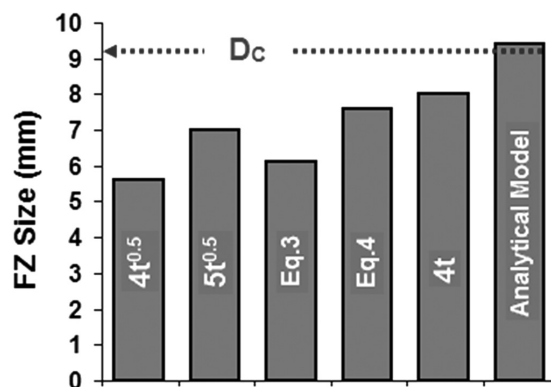


Figure 6: Comparison of the experimentally determined critical FZ zone (D_C) for M130 steel 2 mm with the thickness-based recommendations. The predicated value of D_C obtained with the analytical model is also shown.

Slika 6: Primerjava eksperimentalno določenega kritičnega področja FZ (D_C) za jeklo M130 s priporočljivo debelino. Prikazana je tudi napovedana vrednost za D_C , dobljena z analitičnim modelom.

model considering the weld hardness characteristics is used to determine the critical FZ size to ensure the pull-out failure mode.

3.3 Prediction of the failure mode taking into account metallurgical factors

The failure of the resistance-spot welds during the tensile-shear test can be described as a competition between the shear plastic deformation of the fusion zone (i. e., the IF mode) and the necking of the base metal or HAZ (i. e., the PF mode).^{11,16} Spot welds usually fail in the mode requiring less force during a fracture. It is well documented that the driving force for the IF is the shear stress along the sheet/sheet interface, while the driving force for the PF is the tensile stress around the weld nugget.^{11,16} In order to develop a model that predicts the failure mode, the first necessary step is to develop the equations for calculating the required force for each failure mode.

First, we have to consider the peak load of the spot welds in the interfacial mode. Considering the nugget as a cylinder with a specific (D) diameter and ($2t$) height, the failure load of the interfacial failure mode (F_{IF}) can be expressed with equation (6):

$$F_{IF} = \pi/4 D^2 \tau_{FZ} \quad (6)$$

where τ_{FZ} is the shear strength of the weld nugget.

Now, the peak load of the spot weld in the pullout failure mode is considered. It is assumed that, in the pullout failure mode, the failure is initiated when the maximum experienced radial tensile stress at the nugget circumference reaches the ultimate tensile strength of the failure location. Therefore, the failure load in the PF mode can be expressed as:

$$F_{PF} = \pi D t \sigma_{PFL} \quad (7)$$

where σ_{PFL} is the ultimate tensile strength of the pullout failure location. In the case of M130, where there is significant softening in the ICHAZ, the peak load in the PF mode can be expressed as follows:

$$F_{PF} = \pi D t \sigma_{ICHAZ} \quad (8)$$

where σ_{ICHAZ} is the tensile strength of the ICHAZ. To obtain the critical nugget diameter, D_C , equations (6) and (8) are intersected resulting in equation (9):

$$D_C = 4t\sigma_{ICHAZ}/\tau_{FZ} \quad (9)$$

The spot welds with $D < D_C$ tend to fail via the interfacial mode, contrary to the welds with $D > D_C$ that tend to fail via the preferred pullout mode.

A direct measurement of the mechanical properties of different regions of a spot weld is difficult. It is well known that there is a direct relationship between the tensile strength of a material and its hardness. The shear strength of a material can be related linearly to its tensile strength using a constant coefficient, f . Therefore, equation 9 can be rewritten as follows:

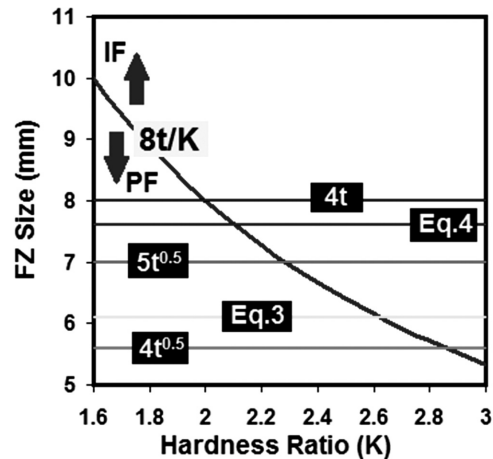


Figure 7: Comparison of the mode prediction and thickness-based recommendations when the sheet thickness (t) is 2 mm. The hardness ratio (K) is defined as the ratio of the FZ hardness to the pullout-failure-location hardness.

Slika 7: Primerjava napovedane vrste porušitve in priporočil debeline, če je debelina pločevine (t) 2 mm. Razmerje trdote (K) je določeno kot razmerje trdote FZ in lokalne trdote pri iztrganju.

$$D_C = 4tH_{ICHAZ}/fH_{FZ} \quad (10)$$

Now, to validate the model, the experimental results are compared with the analytical results. In the case of the M130 martensitic steel, the average FZ hardness is approximately 380 HV and the hardness of the softened zone in the ICHAZ is about 225 HV. Therefore, the hardness ratio of the FZ to the failure location is about 1.68. According to the Tresca criteria, the ratio of the ultimate shear strength to the ultimate tensile strength, f , is 0.5. By substituting these values in equation (10), the critical fusion-zone size is calculated to be 9.4 mm. Figure 6 shows that this value is a reasonable estimation of the critical FZ size.

Figure 7 compares the analytical model and the existing criteria for a sheet 2 mm. As can be seen, the sizing based on $4t^{0.5}$, Eq.3, $5t^{0.5}$, Eq.4 and $4t$ criteria is not appropriate for obtaining the PF mode when the hardness ratios are smaller than 2.85, 2.65, 2.3, 2.1 and 2, respectively. As the hardness ratio is reduced, the discrepancy between the analytical model and the industrial sizing criteria is increased.

4 CONCLUSIONS

In this work, the failure-mode transition of M130 martensitic resistance-spot welds is investigated. The following conclusions can be drawn from this work:

1. A reduction in the hardness (softening), with respect to the BM, was observed in the HAZ. The heat-affected-zone softening reduced the strength of the HAZ, resulting in the strain localization and, hence, causing the PF mode.
2. There is a critical FZ size ensuring the pullout failure mode during the tensile-shear test. According to the

theoretical analysis presented in this study, the failure-mode transition of the M130 spot welds is governed by the sheet thickness, FZ hardness and ICHAZ hardness.

3. The existing industrial weld-nugget sizing criteria are not sufficient to ensure the pullout failure mode during the tensile-shear testing of the M130 resistance-spot welds. The proposed model can predict the failure mode with good accuracy.

5 REFERENCES

- ¹ M. Pouranvari, Influence of Welding Parameters on Peak Load and Energy Absorption of Dissimilar Resistance Spot Welds of DP600 and AISI1008 Steels, *Canadian Metallurgical Quarterly*, 50 (2011), 381–388
- ² Committee on Automotive Applications: AHSS – application guidelines, Version 4.1, International Iron and Steel Institute, Washington DC, 2009
- ³ M. Pouranvari, *Metalurgija-Journal of Metallurgy*, 16 (2010), 187–194
- ⁴ X. Sun, E. V. Stephens, M. A. Khaleel, Effects of fusion zone size and failure mode on peak load and energy absorption of advanced high strength steel spot welds under lap shear loading conditions, *Eng. Fail. Anal.*, 15 (2008), 356–367
- ⁵ P. Podrzaj, S. Simoncic, Resistance spot welding control based on fuzzy logic, *Int. J. Adv. Manuf. Technol.*, 52 (2011), 959–967
- ⁶ M. Pouranvari, E. Ranjbarnoodeh, Dependence of the fracture mode on the welding variables in the resistance spot welding of ferrite-martensite DP980 advanced high-strength steel, *Mater. Tehnol.*, 46 (2012) 6, 665–671
- ⁷ M. Pouranvari, S. P. H. Marashi, Critical Review of Spot Welding of Automotive Steels: Process, Structure and Properties, *Sci. Technol. Weld. Joining*, 18 (2013), 361–403
- ⁸ M. Pouranvari, S. P. H. Marashi, Key factors influencing mechanical performance of dual phase steel resistance spot welds, *Sci. Technol. Weld. Joining*, 15 (2010), 149–155
- ⁹ V. H. Baltazar Hernandez, M. L. Kuntz, M. I. Khan, Y. Zhou, Influence of weld size and microstructure of dissimilar AHSS resistance spot welds, *Sci. Technol. Weld. Joining*, 13 (2008), 769–776
- ¹⁰ M. S. Khan, S. D. Bhole, D. L. Chen, G. Boudreal, E. Biro, J. V. Deventer, *Canadian Metallurgical Quarterly*, 48 (2009), 303–310
- ¹¹ M. Pouranvari, H. R. Asgari, S. M. Mosavizadeh, P. H. Marashi, M. Goodarzi, Effect of weld nugget size on overload failure mode of resistance spot welds, *Sci. Technol. Weld. Joining*, 12 (2007), 217–225
- ¹² X. Sun, E. V. Stephens, M. A. Khaleel, Effects of Fusion Zone Size and Failure Mode on Peak Load and Energy Absorption of Advanced High-Strength Steel Spot Welds, *Welding Journal*, 86 (2007), 18s–25s
- ¹³ Recommended Practices for Test Methods and Evaluation the Resistance Spot Welding Behavior of Automotive Sheet Steels, ANSI/AWS/SAE D8.9-97, 1997
- ¹⁴ M. Pouranvari, S. P. H. Marashi, Similar and dissimilar RSW of low carbon and austenitic stainless steels: effect of weld microstructure and hardness profile on failure mode, *Mater. Sci. Technol.*, 25 (2009), 1411–1416
- ¹⁵ M. Pouranvari, Failure mode transition in similar and dissimilar resistance spot welds of HSLA and low carbon steels, *Canadian Metallurgical Quarterly*, 51 (2012), 67–74
- ¹⁶ M. Pouranvari, S. P. H. Marashi, D. S. Safanama, Failure mode transition in AHSS resistance spot welds. Part II: Experimental investigation and model validation, *Materials Science and Engineering A*, 528 (2011), 8344–8352
- ¹⁷ Japanese Industrial Standard, Method of Inspection for Spot Welds, JIS Z 3140, 1989
- ¹⁸ German Standard, Resistance Spot Welding, DVS 2923, 1986
- ¹⁹ K. W. Ewing, M. Cheres, R. Thompson, P. Kukuček, Static and impact strengths of spot welded HSLA and low carbon steel joints, SAE 820281, Society of Automotive Engineers, Warrendale, PA, 1982
- ²⁰ D. J. Radakovic, M. Tumuluru, Predicting resistance spot weld failure modes in shear tension tests of advanced high-strength automotive steels, *Welding Journal*, 87 (2008) 4, 96-s–105-s

SYNTHESIZING A NEW TYPE OF MULLITE LINING

SINTEZA NOVE VRSTE OBLOGE IZ MULITA

Zagorka Aćimović¹, Anja Terzić², Ljubiša Andrić³, Ljubica Pavlović³,
Marko Pavlović¹

¹University of Belgrade, Faculty of Technology and Metallurgy, Belgrade, Serbia

²Institute for Materials Testing, Belgrade, Serbia

³Institute for Technology of Nuclear and Other Mineral Raw Materials, Belgrade, Serbia
anja.terzic@institutims.rs

Prejem rokopisa – received: 2013-03-07; sprejem za objavo – accepted for publication: 2013-03-27

Various possibilities for developing new mullite-based refractory linings that can be applied in a casting process were investigated and are presented in this paper. An optimization of the refractory-lining composition design with the controlled rheological properties was achieved by applying different lining components and altering the lining-production procedure. Mullite was used as a high-temperature filler. A mullite sample was tested with the following methods: X-ray diffraction analysis, differential thermal analysis and scanning-electron microscopy. The particle shape and particle size were analyzed with the program package for an image analysis called OZARIA 2.5. It was proved that an application of this type of lining has a positive effect on the surface quality, structural and mechanical properties of the castings of Fe-C alloys obtained by casting into sand molds, according to the method of expandable patterns (the EPC casting process).

Keywords: refractory lining, mullite, quality of casting, EPC casting process

V članku so predstavljene različne možnosti za razvoj nove mulitne ognjevdružne obloge, uporabne pri postopku ulivanja. Optimiranje sestave ognjevdružne obloge s kontroliranimi reološkimi lastnostmi je bilo doseženo z uporabo različnih sestavin obloge in s spremembo postopka izdelave obloge. Muli je bil uporabljen kot visokotemperaturno polnilo. Vzorec mulita je bil preiskovan z naslednjimi metodami: z rentgensko difrakcijo, diferenčno termično analizo in vrstično elektronsko mikroskopijo. Oblika in velikost zrn sta bili določeni s programsko opremo za analizo slik OZARIA 2.5. Dokazano je bilo, da uporaba te vrste obloge ugodno vpliva na kvaliteto površine, strukturo in mehanske lastnosti ulitkov iz Fe-C zlitin pri ulivanju v pečene forme po metodi ekspanzirane pene (EPC-postopek ulivanja).

Ključne besede: ognjevdružna obloga, mulit, kvaliteta ulitkov, EPC-postopek ulivanja

1 INTRODUCTION

The main role of a lining is the formation of an efficient, unbreakable and firm refractory barrier which separates the sandy substrate from the liquid metal flow. For such a role, certain lining properties are required: high refractoriness, suitable gas permeability, simple application, good adhesion to a sandy mold and polymer model, simple adjustment of the lining-layer thickness and high drying rate. These requirements can be successfully fulfilled with an optimization of the lining composition and production technology.¹⁻³

The basic characteristic of the EPC casting process is that the patterns and gating of molds made of polymers stay in the cast until the liquid-metal inflow occurs. The pattern-decomposition kinetics is the function of the liquid-metal temperature, with which the pattern comes in contact. The important factors influencing the pattern decomposition and, consequently, the evaporation process, besides temperature and pattern density, are: type of refractory lining, thickness of the lining layers covering the evaporable pattern, type and size of the sand grains and their granulation, permeability of the sandy model, gating of the mold construction, etc.⁴⁻⁷ Manufacturing the castings with the projected application quality by means of the EPC process has not been investigated enough and, thus, there is a need for a systematic

research of the 'triad' including structure/properties/technology, to which special attention was paid in this paper.

The mullite was chosen as the refractory-lining filler due to the following properties: low thermal conductivity ($6 \text{ W m}^{-1} \text{ K}^{-1}$);⁸ low coefficient of the linear thermal expansion ($5.4 \cdot 10^{-6} \text{ }^\circ\text{C}^{-1}$ at $25 \text{ }^\circ\text{C}$);⁹ high thermal-shock resistance (quenching/500) and high maximum-use temperature of $1650 \text{ }^\circ\text{C}$;¹⁰ flexural strength of 180 MPa ; elastic modulus of 151 GPa ; compressive strength of 1310 MPa ; hardness of 1070 kg mm^{-2} ; extreme resistance to liquid-metal absorption;⁶ no gas production when in contact with liquid metal. Different additive types and various quantities were tested in order to enable the best possible absorption between the additives and the refractory filler particles and, thus, the maintenance of the filler in a dispersed state and prevention of the filler build-up or segregation.

2 EXPERIMENTAL WORK

For the synthesis of mullite ($3\text{Al}_2\text{O}_3 \cdot 2\text{SiO}_2$) the mixture of kaolin and alumina was used with an addition of a mineralizer (1 % of NaF). Alumina was added in order to achieve the mullite stoichiometric ratio of 3 : 2. The crushing of the reactive components and the homo-

genization were performed in a planetary ball mill PM 100 with sintered, aluminium-oxide grinding balls. After the homogenization and an addition of the mineralizer, the mixture was wetted with water and, subsequently, pressed in the mold with the 100 N/mm² pressure and, afterwards, dried. The synthesis of mullite was performed by means of isothermal heating in the laboratory high-temperature 'Netzsch' furnace at the temperature of 1450 °C, with the heating rate of 10 °C/min in air atmosphere.

The lining compositions were defined (Table 1) and the lining-component preparation methods were determined.

Table 1: Composition of refractory mullite-based linings

Tabela 1: Sestava ognjevdružne obloge na osnovi mulita

Component	Refractory lining based on alcohol	Refractory lining based on water
ararsid14156519 Refractory filler	Mullite with the grain size of 35–40 µm, 90–94 %	Mullite with the grain size of 40 µm, 93–95 %
Binding agent	Colophonium (C ₂₀ H ₃₀ O ₂), 2.5 %	Bentonite, 2.5%; Bindal H, 0.5%; Na ₃ P ₃ O ₃ , 1–3 %
Additive/ suspension	Bentone 25, 0.8–1 %	Carboxymethyl-cellulose, 0.5–1 %
Solvent	Alcohol	Water

Refractory linings were applied to the sandy molds with a brush. During the application of the refractory lining on the polymer model using the technique of immersion into the tank with a lining, the process parameters were: the suspension density of 2 g/cm³, and the suspension temperature of 25 °C. The drying procedure was as follows: for the water-based linings, the duration of drying the first layer was 2 hours and the final layer was dried for 24 h; for the alcohol-based linings burning was used. The thickness of the lining layer on the model after drying was 0.5–1 mm.

For casting, Fe-C alloys were used. The casting temperature was 1350 °C. For the production of sandy molds, the mold mixture based on quartz sand was used, with the mean grain size being 0.17 mm, with an addition of bentonite (3 %) and dextrin (0.5 %). To produce the EPC-casting-process molds, dry quartz sand with the mean grain size of 0.25 mm was used and evaporable models were made of polystyrene with the density of 20 kg/m³.

The mineral-phase composition of mullite was analyzed by means of X-ray powder diffraction (an XRD-Philips PW-1710 diffractometer). DTA was performed with a Shimadzu DTA-50 apparatus. The microstructure of the samples was characterized with the scanning-electron-microscopy method (SEM) using a JEOL JSM-6390 Lv microscope. Distribution of the refractory filler and bonding agent in a lining suspension was conducted with a polarized-light optical microscope of the passing-light JENAPOL type (Carl Zeiss – Jena). The analysis of the

particle size and shape factor was conducted with the PC software OZARIA 2.5.

3 RESULTS AND DISCUSSION

In Figure 1 the results of the X-ray structural analysis of mullite powder are shown. The mean grain size of the refractory filler was between 35–40 µm, the grain-shape mean factor was 0.63, which means that the grains are round and suitable for the production of homogeneous linings.

A DTA curve for the mullite sample is presented in Figure 2. It can be concluded that mullite has a high refractoriness and, thus, it is suitable for casting Fe-C alloys.

In Figure 3, the results of the qualitative mineralogical analysis of the filler based on mullite are shown. The analysis shows that the mullite particles are principally of equal size and morphology, but there are also some differences in the particle size. This is favorable

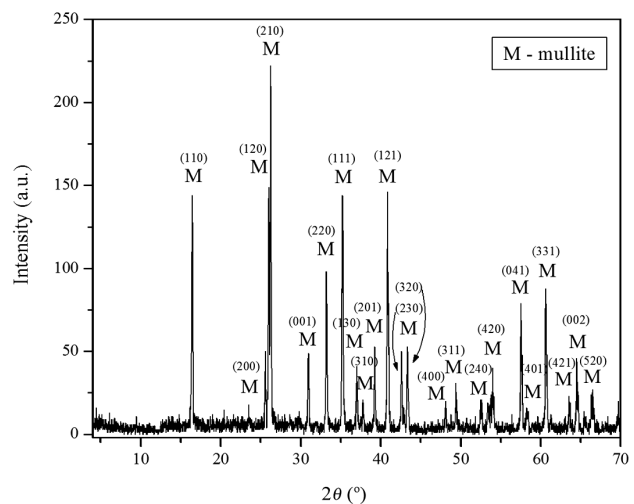


Figure 1: X-ray diffractogram of mullite
Slika 1: Rentgenski difraktogram mulita

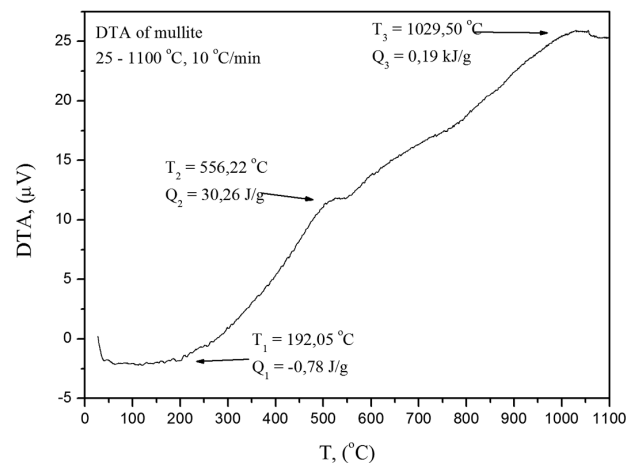


Figure 2: DTA curve of mullite
Slika 2: DTA-krivulja mulita

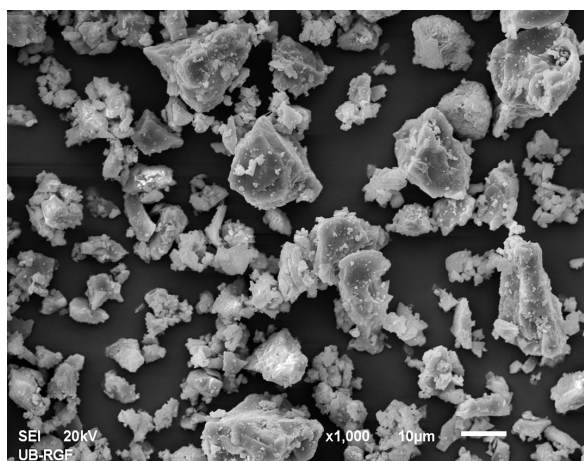


Figure 3: Mullite particles (SEM)
Slika 3: SEM-posnetek zrn mulita

since the particles of diverse granulations contribute to forming an equalized, continuous lining layer on the polymer pattern, due to a better harmony between the particles.

A histogram of the mullite-powder particle size is given in **Figure 4**, while **Figure 5** represents a histogram of the mullite-particle shape factor.

Microstructural analyses of the lining filler and the suspension samples proved that the filler particles have predominantly a uniform size and morphology. The filler particles were mainly oval (**Figure 5**). The filler particles with the sizes of 20–40 µm were predominantly present, making 50 % of the total mullite-particle granulate (**Figure 4**). It was estimated that the oval-shaped particles of various grain sizes contribute to the forming of a uniform and consistent lining layer on the mold and model surfaces due to the stronger interrelations among the particles, which was proved with the results of the lining-property tests. The sediment-stability test performed on all three types of refractory linings showed that solid

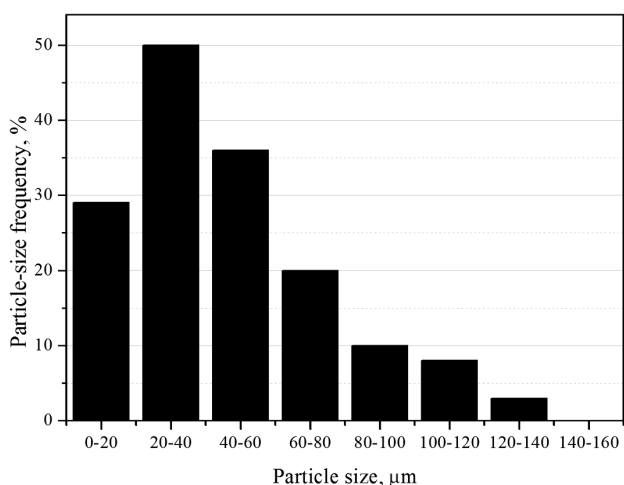


Figure 4: Mullite-particle size frequency
Slika 4: Velikostna razporeditev mulitnih zrn

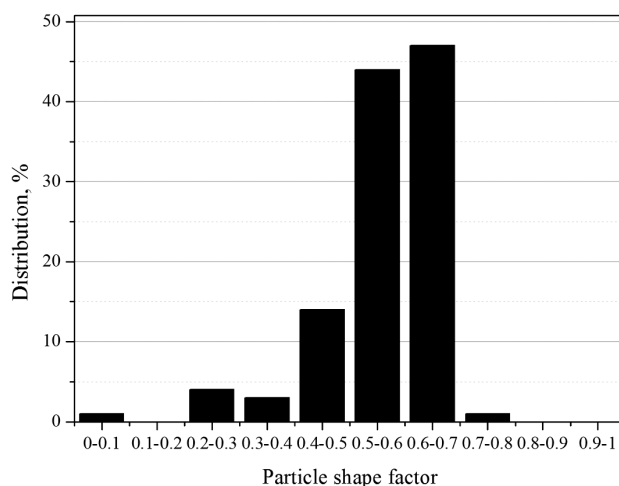


Figure 5: Distribution of the particle-shape factor of mullite
Slika 5: Razporeditev faktorja oblike zrn mulita

matters build up to the amount of 5–8 %, which is in accordance with the lining-quality requirements.

The homogeneity of the refractory-filler distribution also depends on the suspension preparation and application technology. The filler-particle concentration and the adhesion have a significant influence on the suspension rheological properties. In the case of an increase in the concentration of the filler in suspension, it was established that the adhesion forces among mullite particles were also increased and that, under the influence of rheological additives and binding agents, constant and uniform coating layers might be formed on the applied surfaces. The lining adheres easily to the surfaces applied and does not get cracked or wiped out after drying, which was proved after a visual examination of several test samples (**Figure 6**).

An application of diluted linings or the linings whose components are not homogenized enough with careful stirring does not create a good surface adhesion. Furthermore, in this case dried lining layers are not uniform, while the linings applied in thicker layers often crack after drying (**Figure 7**).



Figure 6: Appearance of the mullite-based lining on a test sample without visible flaws

Slika 6: Videz obloge na osnovi mulita na preizkusnem vzorcu brez vidnih napak



Figure 7: Appearance of the mullite-based lining on a test sample with visible flaws

Slika 7: Videz obloge na osnovi mulita na preizkusnem vzorcu z vidnimi napakami

Due to the results of preliminary testing and visual examination of the samples, further tests were carried out using a lining with the density of 2000 kg/m³. The lining components were carefully stirred during the application in order to achieve a homogeneous filler distribution in the suspension.

The experiment showed that alcohol-based linings are suitable for an application in sandy molds and cores. Both alcohol-based and water-based linings applied did not penetrate the test-tube surfaces made of polystyrene.

Applications of the three types of linings, during the processes of casting, in the sandy molds, and the EPC casting procedure enable a production of the castings with advanced quality settings. The prepared linings with a 2000 kg/m³ density were applied in two layers and, after drying, it was noted that constant, thin lining layers were formed on the molds and polymer models. This method provided a good gas permeability of the lining layers, enabling a faster liquid-metal cooling in the mold and a formation of a tiny-grain cast structure, confirmed with the results of testing the structural and mechanical properties of the castings. The application of thin lining layers positively influences the porosity reduction of the castings.

4 CONCLUSION

The investigation showed that the linings based on synthesized mullite met the casting-application requirements creating an acceptable casting-surface finish. This justifies the applied sintering regime at 1450 °C for the mullite synthesization. The investigated linings showed a possibility of an easy application on the sandy molds and polymer models: the linings evenly flew down during the pouring and they were easily applied with a brush without leaving traces, a leakage or a formation of coat drops or lumps. After drying, the lining surfaces were smooth, the layers had an even thickness and the models did not show any bubbling, cracks or peeling. The linings added stiffness to the cluster and allowed the foam-decomposition products to escape. The application of the linings

in thinner layers, approximately 0.5–1 mm, due to improved permeability, showed that the cast quality was higher, having no visible flaws (porosity, bubbles or cracks). Although all the investigated refractory linings gave satisfying properties, water-based linings are more ecologically and economically sustainable than alcohol-based linings.

Further research on improving this type of refractory linings will be done in terms of improved properties of the mullite-based filler using a mechanical activation process enhancing an improvement of the lining rheological properties and the lining suspension stability. Also, further research of the types of refractory linings investigated in this paper will concentrate on the mechanical properties of metal castings in order to confirm the connection between the mechanical performances and the advanced morphological characteristics of the linings.

Acknowledgements

This investigation was supported and funded by the Ministry of Education, Science and Technological Development of the Republic of Serbia and it was conducted within projects 33007, 172057 and 45008.

5 REFERENCES

- ¹ F. G. Martins, C. A. Silva de Oliveira, Study of full-mold casting process for Al–Si hypoeutectic alloys, *Journal of Materials Processing Technology*, 179 (2006), 196–201
- ² M. R. Barone, D. A. Caulk, A foam ablation model for lost foam casting of aluminum, *International Journal of Heat and Mass Transfer*, 48 (2005), 4132–4149
- ³ H. Gökce, D. Agaogullari, M. Lütfi Övecoglu, I. Duman, T. Boyraz, Characterization of microstructural and thermal properties of steatite/cordierite ceramics prepared by using natural raw materials, *Journal of the European Ceramic Society*, 31 (2011), 2741–2747
- ⁴ R. E. Moore, *Refractories, Structure and Properties*, Encyclopedia of Materials: Science and Technology, Press, Oxford 2001, 8079–8099
- ⁵ A. Prstić, Z. Aćimović - Pavlović, S. Grujić, M. Đuričić, Lj. Andrić, Different ceramic linings for application in foundry, *Proceedings of the 43rd October Conference on Mining and Metallurgy, Kladovo*, 2011, 79–82
- ⁶ J. Stjernberg, B. Lindblom, J. Wikström, M. L. Antti, M. Odén, Microstructural characterization of alkali metal mediated high temperature reactions in mullite based refractories, *Ceramics International*, 36 (2010) 2, 733–740
- ⁷ U. Steinhauser, W. Braue, J. Göring, B. Kanka, H. Schneider, A new concept for thermal protection of all-mullite composites in combustion chambers, *Journal of the European Ceramic Society*, 20 (2000) 5, 651–658
- ⁸ G. Brunauer, F. Frey, H. Boysen, H. Schneider, High temperature thermal expansion of mullite: an in situ neutron diffraction study up to 1600 °C, *Journal of the European Ceramic Society*, 21 (2001), 2563–2567
- ⁹ N. M. Rendtorff, L. B. Garrido, E. F. Aglietti, Thermal shock resistance and fatigue of Zircon–Mullite composite materials, *Ceramics International*, 37 (2011) 4, 1427–1434
- ¹⁰ N. Rendtorff, L. Garrido, E. Aglietti, Mullite–zirconia–zircon composites: Properties and thermal shock resistance, *Ceramics International*, 35 (2009), 779–786

INFLUENCE OF PROCESSING FACTORS ON THE TENSILE STRENGTH OF 3D-PRINTED MODELS

VPLIV PROCESNIH DEJAVNIKOV NA NATEZNO TRDNOST TRIDIMENZIONALNO TISKANIH MODELOV

Tomislav Galeta, Ivica Kladarić, Mirko Karakašić

J. J. Strossmayer University of Osijek, Mechanical Engineering Faculty in Slavonski Brod, Trg Ivane Brlić-Mažuranić 2, 35000 Slavonski Brod, Croatia
tgaleta@sfsb.hr

Prejem rokopisa – received: 2013-03-08; sprejem za objavo – accepted for publication: 2013-05-21

Since the models produced with three-dimensional printing are not as strong as the ones made with the other rapid prototyping technologies, the main objective of this research was to determine the influence of selected processing factors on the tensile strength and to determine the factor combination that provides the highest strength. Test samples were prepared on a 3D printer with variations in the layer thickness, building orientation and infiltrant type. The secondary objective was to evaluate the application of more affordable alternative infiltrants used instead of genuine infiltrants. The results of the tensile test revealed that the strength of 3D-printed samples comes mainly from the infiltrants, but it may be additionally increased by selecting the best combination of the other two processing factors. The strength of the samples infiltrated with alternative infiltrants was equivalent to that obtained with genuine infiltrants, thus confirming the use of alternative infiltrants.

Keywords: rapid prototyping, three-dimensional printing, tensile strength

Modeli, ki so proizvedeni s tridimenzionalnim tiskanjem, niso tako močni v primerjavi z drugimi tehnologijami hitrega prototipiranja, zato je bil glavni cilj raziskave ugotoviti, kakšen vpliv imajo izbrani procesni dejavniki na natezno trdnost, in kombinacijo, ki zagotavlja največjo trdnost. Vzorci za preizkuse so bili pripravljene na tridimenzionalnem tiskalniku s spreminjanjem debeline plasti, smeri nalaganja in vrste veziva. Dodaten cilj je bil oceniti uporabo dostopnejših nadomestnih vezivnih sredstev, namesto originalnih. Rezultati preizkusa natezne trdnosti so pokazali, da je trdnost 3D tiskanih vzorcev najbolj odvisna od vezivnega sredstva, mogoče pa jo je povečati z izbiro najboljše kombinacije drugih dveh procesnih dejavnikov. Trdnost vzorcev, ki so bili infiltrirani z alternativnimi vezivnimi sredstvi, je bila enakovredna tisti, pridobljeni z originalnimi vezivnimi sredstvi, kar potrjuje uporabo alternativnih vezivnih sredstev.

Ključne besede: hitro prototipiranje, tridimenzionalno tiskanje, natezna trdnost

1 INTRODUCTION

The models produced with three-dimensional printing (3DP) are not as strong as the ones made with the other rapid prototyping (RP) technologies. Several authors emphasized the issue of the 3DP strength in their researches. Pilipović et al.¹ compared the properties of the samples made with two similar RP procedures: the samples produced with "the stipulated standard 3DP procedure" showed mechanical properties that were inferior to those of the samples produced with the hybrid Polyjet procedure. The results obtained in that paper and frequent customer demands for better tensile properties motivated us to perform further research in order to improve the strength of the models produced on the considered model of 3DP machines. An initiative research was performed and its results were published in a master's degree thesis² and in our papers published in conferences.^{3,4}

There is a constant effort of the researchers to improve the strength and other mechanical properties of 3DP models. This is evident from the number of recently published papers. Patirupanusara et al. performed studies to enhance the mechanical properties of 3DP specimens on the basis of polymethyl methacrylate.^{5,6} Suwanprateeb

found that the use of light-cured acrylate resin as an infiltrant can enhance the flexural modulus and the flexural strength of natural-polymer-based 3DP parts to be close to the general use of polymethyl methacrylate resin.⁷ Chumnanklang et al. revealed that pre-coated particles would yield a stronger 3DP hydroxyapatite part.⁸ Hydroxyapatite is widely used as a medical, highly biocompatible bone-substitute material. Furthermore, several researchers gave their contributions on the subjects closely related to the mechanical properties of 3DP models.⁹⁻¹³

The overall work on the enhancement of 3DP mechanical properties can also be noticed on the market. The manufacturers of 3DP systems frequently deliver new enhanced models of printers, together with improved materials, system software or improved alternative spare parts for the existing models. These efforts will reduce the damages to 3DP models that occur during exploration. However, from the 3DP owner's point of view, it should be stressed that most damages occur on green models, i.e., before post-processing and infiltration (**Figure 1**), although customers are usually not informed about such damages. In the previous research², the obtained average tensile strength of green samples was 0.95 MPa. However, if the samples were dried in the

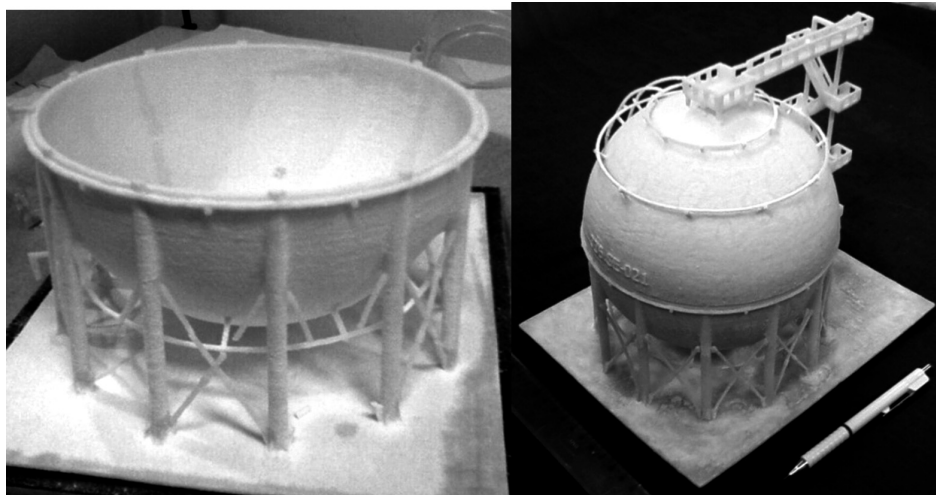


Figure 1: 3DP model of a spherical gas tank – damaged (left) and repaired with infiltration (right)
Slika 1: 3DP-model okroglega rezervoarja plina – poškodovan (levo) in popravljen z infiltriranjem (desno)

oven for at least two hours at 55 °C, the average tensile strength of green samples increased to 1.52 MPa.

Original equipment manufacturers (OEM) constantly make additional efforts to enhance the mechanical properties of the green 3DP model. OEM efforts result in new base materials, printer upgrades and a development of new 3DP machines.

The main objective of our research was to determine the influence of the selected 3DP processing factors on the tensile strength and to determine the factor combination that provides the highest strength. The secondary objective was to evaluate the application of the alternative infiltrants that we used instead of the genuine manufacturer’s infiltrants for the considered 3DP system. If the obtained properties are equivalent, the use of the alternative infiltrants can help to reduce the printing costs and to acquire infiltrants from the more available alternative suppliers. For this purpose we carried out a set of experiments on the considered 3DP system.

2 TESTING THE EQUIPMENT AND SAMPLE MATERIALS

The 3D printer, used for these experiments, was model Z310, a product of Z Corporation. It is a low-cost, monochrome 3D printer suitable for the RP education or for small and medium-sized companies. The printer firmware version was 10.158 and the test samples were prepared in printer software ZPrint version 7.5.23^{14,15} (**Figure 2**).

The considered 3D printer combines the layered approach of RP technologies and conventional ink-jet printing. It prints a binder fluid through a conventional ink-jet print head into the powder, one layer onto another, from the lowest model cross-section to the highest one (**Figure 3**). After printing, the printed models are dried in the building box (**Figure 4**), then removed from the powder bed, de-powdered with compressed air, dried in the oven and infiltrated for the maximum strength.

There are several base materials, i.e., powder types available for the above mentioned 3D printer. For our

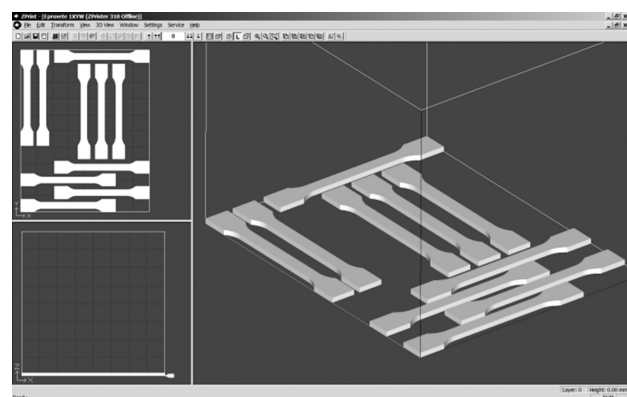


Figure 2: Test-sample build setup in software ZPrint
Slika 2: Razporeditev preizkusnih vzorcev s programsko opremo ZPrint

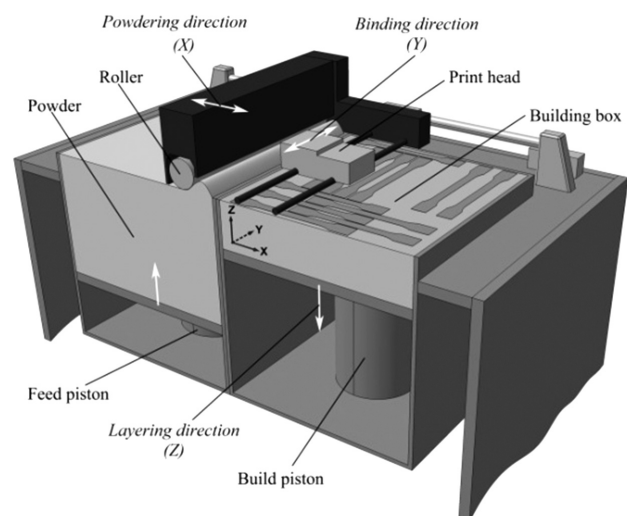


Figure 3: 3D printer main components – a section view
Slika 3: Glavni sestavni deli 3D-tiskalnika – pregled komponent

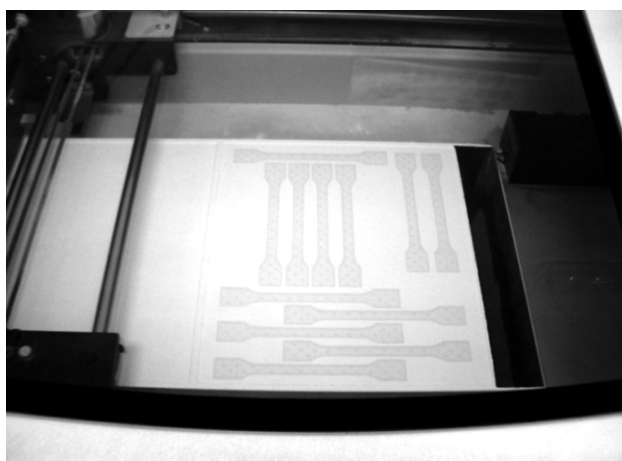


Figure 4: Test-sample 3D printing

Slika 4: 3D-tiskanje preizkusnih vzorcev

experiment, we used the plaster-based zp130 powder with an appropriate binder, zb56. The zp130 powder is recommended for the accuracy and for delicate models. It is a mixture of plaster, vinyl polymer and sulphate salt.¹⁶

All the test samples were dried twice before the infiltration, as recommended in^{15,17}: first in the printer's building box for one hour and then, after de-powdering, in the oven for at least two hours at 55 °C.

After drying, the samples were infiltrated with an appropriate infiltrant, taking into account the appropriate combination of the experiment. The applied infiltrants were: cyanoacrylate-based Loctite 406¹⁸; epoxy-resin-based Loctite Hysol 9483¹⁹ and normal-wax Cera Alba. We applied the alternative infiltrants that are the most similar to the corresponding genuine manufacturer's infiltrants: Loctite 406 instead of Z-Bond²⁰; Loctite Hysol 9483 instead of Z-Max; and normal-wax Cera Alba instead of Paraplast X-TRA Wax.²¹

Subsequent to the infiltration, i.e., prior to the tensile-strength test, all the samples rested in room conditions for a minimum of 24 h to obtain the final strength, as recommended for the epoxy-resin infiltrant.²² We measured the dimensions of the test samples with a digital caliper Lux Profi, model 572587, with a measurement range of 0–150 mm and an accuracy of 0.01 mm.

The tensile test was performed at room temperature on the tensile-testing machine ZMGi 250 made by VEB Thuringer Industriewerk with the jaw-motion speed of 1 mm/min.

3 DESIGN OF THE EXPERIMENT

The models for the tensile tests used in our experiments were those defined with standard ISO 527:1993. The nominal dimensions of the test sample are presented in **Figure 5**. The dimensions measured for the tensile test were: the neck width (W_i) and the height (H). The other linear dimensions like the total length (L) and the width

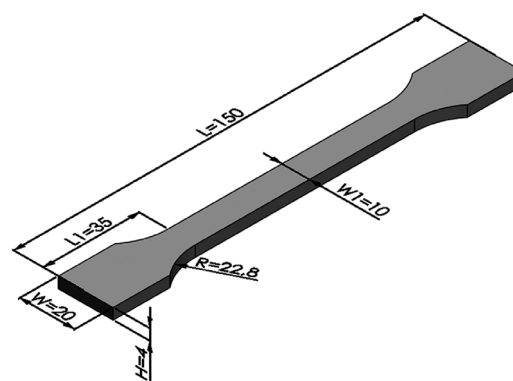


Figure 5: Test sample

Slika 5: Preizkusni vzorec

at the end (W) were controlled according to the requirements of the tensile test.

We considered the combinations of the following processing factors: the layer thickness, the building orientation and the infiltrant type. Every combination of the processing factors was denoted with an appropriate unique label made of three characters (**Table 1**).

In the considered ZPrint software version, the layer thickness can be selected from two possible values: 0.1 mm or 0.0875 mm. The first thickness is the default for the printer and it is, therefore, marked with number 1 at the beginning of the label for a particular combination of the factors. Congruently, the second thickness is marked with number 2 in a combination label. The lower layer thickness provides for finer printed models than the higher or coarser layer thickness, with the lower roughness notable especially on the beveled edges and faces.

The sample model can be oriented in any possible direction inside the printer building box. We considered two main directions: the 1st direction denotes the orientation of a sample's largest L dimension towards the building X axis and the 2nd direction denotes its orientation towards the Y axis. Thereby, the samples were aligned at the bottom plane of the building box. In the experiment label for a particular combination of the factors, the mark for the sample orientation is in the second place of the label, expressed with letters X or Y , respectively.

The orientation towards the building Z axis was omitted since it significantly prolonged the printing time: for example, to print five samples oriented with their largest L dimensions towards the building X axis, it takes only 15 min for 39 printed layers; the same time and the same number of layers are necessary when the samples are oriented towards the building Y axis; but when they are oriented towards the Z axis, the process is prolonged to 3 hours and 51 min for 1476 layers.

Although all the other orientations are also available to be combined, additional combinations were omitted in order to reduce the total number of the experiments.

However, if the results of the experiments had indicated a significant influence of the orientation on the tensile strength, additional experiments could have been easily performed.

The type of the infiltrant is marked with the letter at the end of the label for a particular combination of the factors. The letters used for a particular infiltrant type are: W for wax, E for epoxy resin and C for cyanoacrylate.

For every particular experiment, i.e., particular combination of factors in each set, six test samples were printed. During the first tests with the probationary 3D-printed samples, most of the samples tended to slip out of the tensile-testing machine jaws. Therefore, additional rubber pads were inserted between the clamping surfaces in order to ensure a sufficient grip of the machine jaws holding a test sample.

4 RESULTS

The dimensions that have the biggest influence on the test results were measured and analyzed prior to the tests: the test-sample neck width (W_1) and the height (H).

The results of measuring the neck height revealed that most of the samples exceed the limits of tolerance specified with the standard ((10 ± 0.2) mm). A correc-

tion to the exceeding dimension can be performed with the afterward processing (e.g., sanding) or this excess can be prevented prior to 3D printing. The prevention can be performed during the model preparation in the printer software with an appropriate anisotropic scale factor as presented in our published research.²³ The measured values of the neck height or thickness of the samples, H , are mainly within the limits of tolerance specified with the standard ((4 ± 0.2) mm). The neck width and the sample height multiplied together determine the cross-sectional area A_0 of the test samples (Table 2). The cross-sectional area A_0 of the test samples is used later to calculate the tensile strength.

The last two rows in the table contain the calculated values: the arithmetic mean and the standard deviation.

The results of the tensile test are expressed with the values of the breaking force, F_m , and presented in Table 3. In the previous researches it was proved that the breaking force of 3DP samples is very close or, often, equal to the maximum testing force^{1,2}; consequently, the breaking force values are considered to narrow the focus of the research.

Table 1: Combinations of the processing factors and experiment labels

Tabela 1: Kombinacije procesnih dejavnikov in oznaka preizkusa

Layer thickness	0.1 mm						0.0875 mm					
	Wax		Epoxy resin		Cyanoacrylate		Wax		Epoxy resin		Cyanoacrylate	
Orientation	X	Y	X	Y	X	Y	X	Y	X	Y	X	Y
Experiment label	1XW	1YW	1XE	1YE	1XC	1YC	2XW	2YW	2XE	2YE	2XC	2YC

Table 2: Neck cross-sectional area (A_0) of the test samples

Tabela 2: Prerez (A_0) preizkusnih vzorcev

Experiment label	Area A_0/mm^2											
	1XW	1YW	1XE	1YE	1XC	1YC	2XW	2YW	2XE	2YE	2XC	2YC
1	41.94	43.60	42.32	43.28	43.42	44.49	43.23	44.13	42.84	43.08	44.27	44.24
2	41.35	43.59	41.69	42.95	44.07	43.52	43.19	43.48	42.70	42.89	43.58	44.95
3	42.28	42.44	41.00	40.59	44.33	42.95	43.73	43.45	43.40	44.61	44.27	44.24
4	41.47	42.50	40.85	41.13	44.51	43.20	43.22	43.58	42.72	44.25	43.58	44.95
5	44.96	42.67	42.42	41.56	43.20	43.66	47.60	44.90	46.46	45.33	49.85	50.80
6	43.93	43.93	42.22	41.71	42.92	43.14	45.63	46.63	45.70	45.39	49.90	50.11
\bar{x}	42.66	43.12	41.75	41.87	43.74	43.49	44.43	44.36	43.97	44.26	45.91	46.55
S	1.46	0.66	0.69	1.05	0.65	0.55	1.81	1.24	1.67	1.08	3.09	3.05

Table 3: Breaking force

Tabela 3: Sila ob porušitvi

Experiment label	Force F_m/N											
	1XW	1YW	1XE	1YE	1XC	1YC	2XW	2YW	2XE	2YE	2XC	2YC
1	119	104	237	327	174	177	115	137	366	421	163	223
2	134	154	273	321	154	185	116	126	358	299	214	206
3	100	138	278	256	121	160	121	146	338	483	225	156
4	121	120	230	276	161	143	131	151	380	502	233	123
5	93	112	273	279	137	163	126	105	251	303	208	246
6	133	128	290	295	165	167	101	126	295	332	252	192
\bar{x}	116.67	126.00	263.50	292.33	152.00	165.83	118.33	131.83	331.33	390.00	215.83	191.00
S	16.91	18.15	24.16	27.55	19.62	14.54	10.42	16.63	49.19	90.96	30.14	45.00

Table 4: Tensile strength
Tabela 4: Natezna trdnost

Experiment label	Tensile strength R_m /MPa											
	1XW	1YW	1XE	1YE	1XC	1YC	2XW	2YW	2XE	2YE	2XC	2YC
1	2.84	2.39	5.60	7.55	4.01	3.98	2.66	3.10	8.54	9.77	3.68	5.04
2	3.24	3.53	6.55	7.47	3.49	4.25	2.69	2.90	8.38	6.97	4.91	4.58
3	2.37	3.25	6.78	6.31	2.73	3.73	2.77	3.36	7.79	10.83	5.08	3.53
4	2.92	2.82	5.63	6.71	3.62	3.31	3.03	3.47	8.90	11.35	5.35	2.74
5	<u>2.07</u>	2.62	6.44	6.71	3.17	3.73	2.65	2.34	5.40	6.68	4.17	4.84
6	3.03	2.91	6.87	7.07	3.84	3.87	2.21	2.70	6.46	7.31	5.05	3.83
\bar{x}	2.74	2.92	6.31	6.97	3.48	3.81	<u>2.67</u>	2.98	7.58	8.82	4.71	4.09
S	0.44	0.42	0.56	0.49	0.47	0.31	0.26	0.42	1.37	2.08	0.64	0.89

The typical breakage outlook presents a fragile fracture without the previously observable plastic deformation (**Figure 6**). Moreover, the locations of the breakage are not concentrated in the middle of the sample-neck length but accidentally distributed along the neck length. Such accidental distribution of the breakage location indicates an internal structural inconsistency and its significant influence on the mechanical properties of 3DP models.

The maximum tensile stress (R_m), i.e., the tensile strength is calculated from the results with the following formula:

$$R_m = \frac{F_m}{A_0} \quad (1)$$

5 ANALYSIS AND DISCUSSION

The maximum particular tensile strength of 11.35 MPa was achieved for the 4th sample from the set labeled as 2YE, i.e., the sample was printed with a finer layer thickness of 0.0875 mm, infiltrated with epoxy resin and oriented towards axis Y. The particular value is shaded with gray and underlined continuously in **Table 4**.

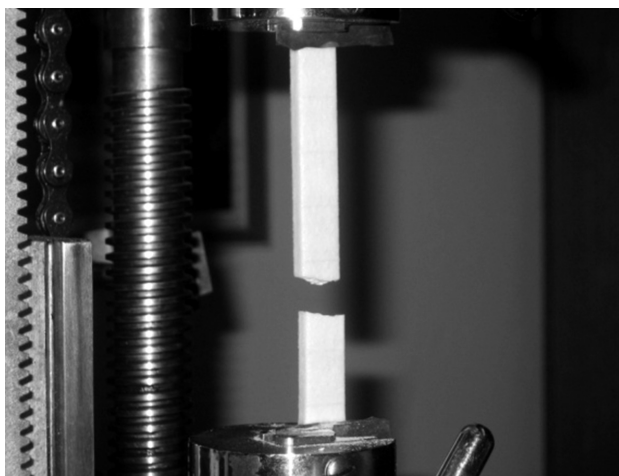


Figure 6: Typical breakage outlook
Slika 6: Značilni videz porušenega vzorca

The minimum particular tensile strength of 2.07 MPa was achieved for the 5th sample from the set labeled as 1XW, i.e., the sample was printed with a coarser layer thickness of 0.1 mm, infiltrated with wax and oriented towards axis X. This overall lowest value is shaded with light gray and has a dotted underline in **Table 4**.

An overview of the sorted average tensile strengths, presented in **Figure 7**, reveals the strongest and the weakest experiment sets. The strongest experiment set is the one that includes the strongest particular sample, labeled as 2YE. Although this set also showed the highest standard deviation referring to the significant diversity of the strength values, it has the highest average strength. However, the weakest experiment set was not the one including the weakest particular sample, labeled as 1XW. The weakest average strength was revealed by the set labeled as 2XW, having also the lowest standard deviation.

The samples infiltrated with epoxy resin obtained the highest strength in comparison with the other infiltrant types. Among the epoxy-infiltrated samples, the ones having a finer layer thickness (2YE and 2XE) showed a higher strength than those with a coarser thickness (1YE and 1XE). However, it should be noted that the results for the finer thickness are significantly more dispersed than the results for the coarser thickness: the standard deviation for the 2YE set is 2.08 MPa, for 2XE it is 1.37

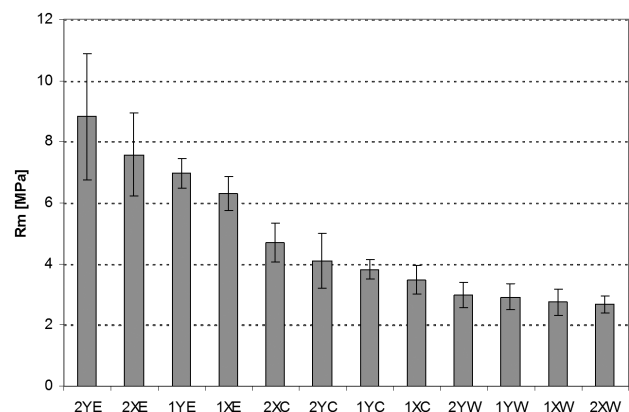


Figure 7: Sorted average tensile strength
Slika 7: Razporeditev povprečne natezne trdnosti

MPa, while for 1YE it is only 0.49 and for 1XE only 0.56. The orientation of the epoxied samples towards building axis *Y* provided a somewhat better strength than those oriented towards axis *X*. The samples infiltrated with cyanoacrylate obtained a medium strength. The cyanoacrylated samples with a finer layer thickness also showed a higher strength than those with a coarser thickness, being similar to the epoxied samples. However, a different orientation of these samples did not cause any obvious difference in the strength.

The waxed samples acquired the lowest strength. The orientation of the waxed samples towards building axis *Y* gave a slightly better strength than the orientation towards axis *X*. The variation in the layer thickness did not show any discrepancy in the strength.

In order to verify the observed principles and relationships between the sample strength and the processing factors, we carried out a factorial analysis of the variance (ANOVA) and summarized the results in **Table 5**. The abbreviations used for the processing factors are: LT – layer thickness; O – orientation; I – infiltrant. ANOVA confirms a major influence of the infiltrant type and a minor influence of the other observed processing factors on the resulting strength of the 3DP samples. The variances in the processing-factor combinations (LT*O, LT*I, O*I, LT*O*I) also indicate a minor influence of the considered combinations on the tensile strength.

Table 5: ANOVA of the tensile strength and the processing factors

Tabela 5: ANOVA natezne trdnosti in procesni dejavniki

Factors	SS	DOF	MS	Var	P	F (0.95)
LT	10.61	1	10.61	14.38	0.00	4
O	2.23	1	2.23	3.02	0.09	4
I	272.47	2	136.24	184.55	0.00	4
LT*O	0.03	1	0.03	0.04	0.85	4
LT*I	7.37	2	3.68	4.99	0.01	4
O*I	3.68	2	1.84	2.49	0.09	4
LT*O*I	1.85	2	0.93	1.25	0.29	4
Error	44.29	60	0.74			

To evaluate the application of alternative infiltrants on our samples instead of the genuine, manufacturer's infiltrants, the results are compared with those obtained for the genuine infiltrants² and presented in **Figure 8**. In both researches, the samples were printed with the same model of 3D printer but with different printers. The tensile tests were performed with the same tensile-testing machines.

The genuine epoxied samples show a significantly better average strength when compared to the overall average strength of the alternative epoxied samples. However, it should be noted that only five genuine epoxied samples were tested in the comparative research where the samples were printed with a finer layer thickness, directed towards building orientation *Y* and laid with the narrow side on the bottom of the building box. Therefore, it should be compared with the test involving

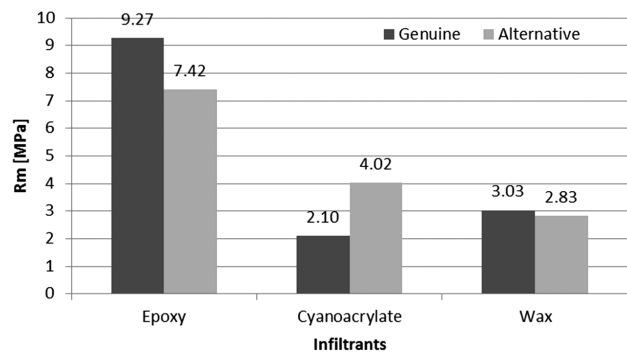


Figure 8: Comparison of the average tensile strengths for the alternative and genuine infiltrants

Slika 8: Primerjava povprečne natezne trdnosti med alternativnim in originalnim vezivnim sredstvom

six appropriate alternative epoxied samples labeled as 2YE, with the average strength of 8.82 MPa (**Table 4**).

The alternative cyanoacrylated samples show a much better average strength when compared to the overall average strength of the genuine cyanoacrylated samples. There were sufficient numbers of samples and combinations of the factors in the two researches for them to be compared: 40 genuine cyanoacrylated samples distributed over 5 distinctive combinations of the processing factors² and 24 alternative cyanoacrylated samples used with 4 factor combinations. Since the strength of the cyanoacrylated samples can also be influenced by the residual moisture²⁴ and the moisture was not measured, we must express some reservation about the results of the comparison between the cyanoacrylated samples.

The genuine and alternative waxed samples reveal almost equal average strengths after a comparison between sufficient numbers of samples (genuine: 50, alternative: 24) and combinations of factors in both researches.

Furthermore, if the results are compared with the previous research published in¹, it can be noticed that the average values of the measured strength correspond to the published values with an evident improvement for the epoxied samples and a smaller decrease for the cyanoacrylated samples than in the previous research. The improvement for the epoxied samples is most likely due to an improved combination of the processing factors used for more samples.

6 CONCLUSIONS

The strength of 3D-printed samples mainly comes from the infiltrants. The results obtained from the conducted experiments clearly confirm a major role of the infiltration type, putting ahead epoxy resin as the strongest one, followed by cyanoacrylate and wax. If the maximum strength is required, as it is common for functional prototypes or molding models, then an additional increase in the strength can be obtained by selecting the best combination of the other two processing factors.

In the case of the infiltration with epoxy resin, to obtain the maximum strength, the model should have a finer layer thickness, i.e., 0.0875 mm. The infiltration with epoxy resin is the slowest one since additional time is necessary for the resin to obtain full strength, usually one day at room temperature or two hours in a heated oven at 70 °C.²⁴

Also, the most important dimension of the printed model should be oriented towards building direction *Y*, if possible taking into account the size of the model and the size of the building box. The most probable reason for this is a coincidence between the orientations of axis *Y* and the movement of the printing head – the direction of the binding-material application, so that the direction of the binding-material application coincides with the longitudinal direction of the test-tube orientation along axis *Y*. On the other hand, the orientation of test tubes along axis *X* coincides with the powdering direction, so the application of the binding material is performed transversely to the direction of the orientation of the test tube, so it is expected that the value of the tensile strength is lower. The only exceptions are the cases of 2XC and 2YC, where the average tensile strength is higher in the direction of axis *X*. However, a higher standard deviation of set 2YC implies possible impurities in the powder and post-processing differences.

Although the infiltration with cyanoacrylate provides a clear white color of a 3D-printed model, different from a dim yellow one obtained with epoxy or wax, the experiments did not confirm cyanoacrylate as the best choice when the strength of a model is required. The cyanoacrylate infiltration is the most expensive solution,²⁵ but it still remains to be the only solution if two or more models have to be joined or mated together after 3D printing, when a large model is divided due to a limitation of the building-box size. A cyanoacrylated model should be 3D printed with a finer layer thickness of 0.0875 mm and the most important dimension of the printed model should be oriented towards building direction *X* to obtain the highest possible strength.

The infiltration with wax, the cheapest available solution, is also the weakest solution. However, such a low strength can still satisfy customer demands, because many 3D-printed models are produced only for representative purposes without special demands on the mechanical properties. Neither the orientation nor the layer thickness has a significant influence on the resulting strength of a 3D-printed model infiltrated with wax.

The evaluation of the alternative infiltrants, applied instead of the genuine manufacturer's infiltrants, revealed that the obtained levels of the strength are equivalent to those obtained with genuine infiltrants for the considered 3DP system. Therefore, the use of alternative infiltration solutions has been confirmed with respect to the tensile strength.

Although it is possible that some of the presented conclusions are valid for similar machines or even rapid

prototyping techniques, all the conclusions should be considered only for the selected 3D printer and the selected materials. New materials and new equipment for 3D printing are developed constantly and may demand new analyses.

Acknowledgements

The work presented in this paper was financially supported by the Ministry of Science, Education and Sports, Republic of Croatia, through the scientific project No. 152-1521473-3111. Special thanks to Professor Pero Raos, Professor Milan Kljajin and system engineer Miroslav Mazurek for supporting the work presented in this paper; to Vedran Galeta for the assistance in the experiments; and to Professor Željka Rosandić for proofreading the manuscript.

7 REFERENCES

- 1 A. Pilipović, P. Raos, M. Šercer, Experimental analysis of properties of materials for rapid prototyping, *The International Journal of Advanced Manufacturing Technology*, 40 (2009) 1–2, 105–115
- 2 A. Fajić, Analiza utjecaja procesnih parametara tehnologije 3D printanja na svojstva prototipa, Master degree thesis, Mašinski fakultet, Univerzitet Džemal Bijedić, Mostar, 2007
- 3 A. Fajić, D. Tiro, T. Galeta, Effects of Processing Parameters on Hardness of 3D Printed Parts, *Proceedings of 11th International Research/Expert Conference Trends in the Development of Machinery and Associated Technology TMT 2007*, Hammamet, Tunis, 2007
- 4 A. Fajić, D. Tiro, T. Galeta, A. Topčić, Research of 3D Printing Process Characteristics, *Proceedings of 5th Research/Expert Conference with International Participation – QUALITY 2007*, Neum, 2007
- 5 P. Patirupanusara, W. Suwanpreuk, T. Rubkumintara, J. Suwanprateeb, Properties improvement of three-dimensionally printed polymethyl methacrylate by bis-GMA-based resin infiltration, *Polymer Testing*, 26 (2007) 4, 519–525
- 6 P. Patirupanusara, W. Suwanpreuk, T. Rubkumintara, J. Suwanprateeb, Effect of binder content on the material properties of polymethyl methacrylate fabricated by three dimensional printing technique, *Journal of Materials Processing Technology*, 207 (2008) 1–3, 40–45
- 7 J. Suwanprateeb, Strength improvement of critical-sized three dimensional printing parts by infiltration of solvent-free visible light-cured resin, *Journal of Materials Science: Materials in Medicine*, 17 (2006) 12, 1383–1391
- 8 R. Chumnanklang, T. Panyathanmaporn, K. Sitthiseripratip, J. Suwanprateeb, 3D printing of hydroxyapatite: Effect of binder concentration in pre-coated particle on part strength, *Materials Science and Engineering C*, 27 (2007) 4, 914–921
- 9 C. X. F. Lam, X. M. Mo, S. H. Teoh, D. W. Hutmacher, Scaffold development using 3D printing with a starch-based polymer, *Materials Science and Engineering C*, 20 (2002) 1–2, 49–56
- 10 J. Stampfl, R. Liska, New Materials for Rapid Prototyping Applications, *Macromolecular Chemistry and Physics*, 206 (2005) 13, 1253–1256
- 11 J. Suwanprateeb, Comparative study of 3DP material systems for moisture resistance applications, *Rapid Prototyping Journal*, 13 (2007) 1, 48–52
- 12 K. Lu, W. T. Reynolds, 3DP Process for Fine Mesh Structure Printing, *Powder Technology*, 18 (2008) 6, 490–499

- ¹³ D. Dimitrov, K. Schreve, N. de Beer, Advances in three dimensional printing – state of the art and future perspectives, *Rapid Prototyping Journal*, 12 (2006) 3, 136–147
- ¹⁴ D. Webster, *ZPrint 7.5 Software Manual*, Z Corporation, Burlington, 2007
- ¹⁵ D. Webster, *ZPrinter 310/DESIGNmate Mx Hardware Manual*, Z Corporation, Burlington, 2006
- ¹⁶ Material Safety Data Sheet zp130 Powder, Z Corporation, Burlington, 2007
- ¹⁷ D. Webster, *Z-Max™ User Guide High-Strength Epoxy Infiltrant*, Z Corporation, Burlington, 2007
- ¹⁸ Loctite 406 Technical Data Sheet, Henkel Europe, Burlington, 2008
- ¹⁹ Loctite Hysol 9483 Technical Data Sheet, Henkel Europe, 2003
- ²⁰ Z-Bond 101 Medium Strength Cyanoacrylate Material Safety Data Sheet, Z Corporation, Burlington, 2005
- ²¹ Paraplast X-TRA Wax Material Safety Data Sheet, Tyco Healthcare/Kendall, Mansfield, 2004
- ²² Z-Max User Guide, Z Corporation, Burlington, 2007
- ²³ T. Galeta, M. Kljajin, M. Karakašić, Geometric Accuracy by 2-D Printing Model, *Strojniški vestnik – Journal of Mechanical Engineering*, 10 (2008) 10, 725–733
- ²⁴ Z-Bond User Guide, Z Corporation, Burlington, 2007
- ²⁵ T. Galeta, M. Kljajin, M. Karakašić, Cost Evaluation of Shell and Compact Models in 3D Printing, *Výrobné Inžinierstvo – Manufacturing Engineering*, 7 (2008) 3, 27–29

NON-SINGULAR METHOD OF FUNDAMENTAL SOLUTIONS FOR THE DEFORMATION OF TWO-DIMENSIONAL ELASTIC BODIES IN CONTACT

NESINGULARNA METODA FUNDAMENTALNIH REŠITEV ZA DEFORMACIJO DVO-DIMENZIONALNIH STIKAJOČIH SE ELASTIČNIH TELES

Qingguo Liu¹, Božidar Šarler^{1,2,3}

¹University of Nova Gorica, Nova Gorica, Slovenia

²IMT, Ljubljana, Slovenia

³Center of Excellence BIK, Solkan, Slovenia
qingguo.liu@ung.si, bozidar.sarler@imt.si

Prejem rokopisa – received: 2013-03-11; sprejem za objavo – accepted for publication: 2013-10-10

The development of an effective new numerical method for the simulation of the micromechanics of multi-grain systems in contact is developed in the present paper. The method is based on the Method of Fundamental Solutions (MFS) for two-dimensional plane strain isotropic elasticity and employs the Kelvin Fundamental Solution (FS). The main drawback of MFS is the presence of an artificial boundary, outside the physical boundary, for positioning the source points of the FS, which is difficult or impossible in multi-body problems. In order to remove the singularities of the FS the point sources are replaced by the distributed sources over circular disks. The values of the distributed sources are calculated in a closed form in the case of the Dirichlet boundary conditions. In the case of the Neumann boundary conditions the respective values of the derivatives of the FS are calculated indirectly from the considerations of the solution of simple displacement fields. A problem of two, four and nine bodies in contact is tackled. The newly developed method is verified based on a comparison with the classic MFS. The numerical method will form a part of the microstructure-deformation model, coupled with the macroscopic thermo-mechanics simulation system for continuous casting, hot rolling and heat treatment.

Keywords: isotropic elasticity, plane strain, Navier's equation, displacement and traction boundary conditions, non-singular method of fundamental solutions, Kelvin's fundamental solution

V članku opisujemo učinkovito novo numerično metodo za simulacijo mikromehanike sistemov z več zrn v stiku. Ta temelji na metodi fundamentalnih rešitev (MFR) za dvo-dimenzionalne probleme izotropnih elastičnih ravninskih deformacij in uporablja Kelvinovo fundamentalno rešitev (FR). Bistvena slabost MFR je prisotnost fiktivnega roba zunaj fizikalnega roba za postavitev izvornih točk FR, kar je težavno ali nemogoče pri problemih z več telesi. Z odstranitvijo nesingularnosti FR smo točkovne izvire nadomestili s porazdeljenimi izviri po krogih. Vrednosti porazdeljenih izvirov so izračunane v analitični obliki za Dirichletove robne pogoje. Pri Neumann-ovih robnih pogojih so vrednosti odvodov FR izračunane posredno pri upoštevanju rešitev preprostih polj premika. Obravnavani so sistemi z dvema, štirimi in devetimi telesi v stiku. Nova metoda je verificirana na podlagi primerjave s klasično MFR. Uporabljena bo v deformacijskem modelu mikrostrukture, povezanim z makroskopskim termomehanskim sistemom za simulacijo kontinuirnega ulivanja, vročega valjanja in toplotne obdelave.

Ključne besede: izotropna elastičnost, ravninska deformacija, Navierove enačbe, robni pogoji premika in vlečenja, nesingularna metoda fundamentalnih rešitev, Kelvinova fundamentalna rešitev

1 INTRODUCTION

The physical modelling of metallurgical processes¹ consists of modelling the relations between the process parameters and the macroscopic velocity, temperature, concentration, and stress fields, and the relations between these fields and the evolution of the microstructure. In such multi-scale modelling, the transport phenomena and solid mechanics on the level of microstructure play an important role and have to be properly computationally modelled.^{2,3} We have, in the recent years, developed a completely new generation of meshless methods, based on local collocation with radial basis functions, for solving these models on different scales. The main advantage of the method is in their similar structure in 2 and 3D, no need for polygonisation, ease of coding, high accuracy, robustness and flexibility. The method has already been developed for modelling very complex

phenomena such as macro-segregation on the macroscopic level⁴ as well as dendritic growth on the micro-level.⁵ An extension of the meshless method, based on a collocation with a fundamental solution (Method of Fundamental Solutions (MFS)), for the simulation of the deformation of the multiple grains in an ideal mechanical contact is presented in the present paper. An extension of the represented method with anisotropic and plastic deformation capabilities will be used in our future thermo-mechanical calculations for the microstructure evolution in metallurgical processes.⁶

The main idea of MFS consists of approximating the solution of the partial differential equation by a linear combination of fundamental solutions, defined in source points. The expansion coefficients are calculated by collocation or least-squares fit of the boundary conditions. The fundamental solution is usually singular in the

source points and this is the reason why the source points are located outside the domain in the MFS. Then, the original problem is reduced to determining the unknown coefficients of the fundamental solutions and the coordinates of the source points by requiring the approximation to satisfy the boundary conditions and hence solving a non-linear problem. If the source points are a priori fixed, then the coefficients of the MFS approximation are determined by solving a linear problem. The MFS has become very popular in recent years because of its simplicity. Clearly, it is applicable when the fundamental solution of the partial differential operator of the governing equation (or of the system of governing equations) of the problem under consideration is known. The MFS has been widely used⁷ for the solution of problems in linear elasticity.

In the traditional MFS, the fictitious boundary, positioned outside the problem domain, is required to place the source points. This is very impractical or even impossible, particularly when solving multi-body problems. In recent years, various efforts have been made, aiming to remove this barrier in the MFS, so that the source points can be placed directly on the real boundary.⁸⁻¹² In the present paper, we use a non-singular MFS based on⁸ to deal with the 2D multi-body isotropic elasticity problems. The application of a non-singular method of fundamental solutions (NMFS) in two-dimensional isotropic linear elasticity has been originally developed in.¹³ We extend these developments to multi-body problems in the present paper. We respectively use area-distributed sources covering the source points to replace the concentrated point sources. This NMFS approach also does not require information about the neighbouring points for each source point, thus it is a truly mesh-free boundary method. The derivatives of the fundamental solution in the distributed source points are calculated by adopting the methodology in⁹ from the Laplace to Kelvin fundamental solution.

The rest of the paper is structured as follows. The solution procedure is given for MFS and NMFS. Numerical results with 1, 4 and 9 bodies in contact are given, followed by conclusions and further research.

2 GOVERNING EQUATIONS OF ELASTICITY FOR THE MULTI-BODY PROBLEM

We consider a two-dimensional domain Ω with the boundary Γ , divided into M sub-domains $\Omega = \Omega_I \cup \Omega_{II} \cup \dots \cup \Omega_M$ with boundaries $\Gamma = (\Gamma_I \cup \Gamma_{II} \cup \dots \cup \Gamma_M) - \Gamma_{I-II} - \dots - \Gamma_{I-M} - \dots - \Gamma_{(M-I)-M}$ as shown in **Figure 1**. Each of the domains is occupied by an isotropic, ideally elastic material with different material properties, in general. Let us introduce a two-dimensional Cartesian coordinate system with orthonormal base vectors \mathbf{i}_x and \mathbf{i}_y , and coordinates p_x and p_y of point P with the position vector $\mathbf{p} = p_x \mathbf{i}_x + p_y \mathbf{i}_y$. The solid is governed by Navier's equations for plane strain problems, which are the conditions for

equilibrium, expressed with the displacement \mathbf{u} . The following governing equations are valid in the sub-domain $\Omega_m, m = I, II, \dots, M, \mathbf{p} \in \Omega_m$:

$$\frac{2(1-\nu_m)}{1-2\nu_m} \frac{\partial^2 u_x(\mathbf{p})}{\partial p_x^2} + \frac{\partial^2 u_x(\mathbf{p})}{\partial p_y^2} + \frac{1}{1-2\nu_m} \frac{\partial^2 u_y(\mathbf{p})}{\partial p_x \partial p_y} = 0$$

$$\frac{2(1-\nu_m)}{1-2\nu_m} \frac{\partial^2 u_y(\mathbf{p})}{\partial p_y^2} + \frac{\partial^2 u_y(\mathbf{p})}{\partial p_x^2} + \frac{1}{1-2\nu_m} \frac{\partial^2 u_x(\mathbf{p})}{\partial p_x \partial p_y} = 0$$

where ν_m represents the Poisson ratio in the subdomain Ω_m . The boundary Γ is divided into two not necessarily connected parts $\Gamma = \Gamma^D + \Gamma^T$. On the part Γ^D the displacement (Dirichlet) boundary conditions are given, and on the part Γ^T the traction (Neumann) boundary conditions are given:

$$\chi_I u_{\zeta I}(\mathbf{p}) + \chi_{II} u_{\zeta II}(\mathbf{p}) + \dots + \chi_M u_{\zeta M}(\mathbf{p}) = \bar{u}_{\zeta}(\mathbf{p})$$

$$\zeta = x, y, \mathbf{p} \in \Gamma^D$$

$$\chi_I t_{\zeta I}(\mathbf{p}) + \chi_{II} t_{\zeta II}(\mathbf{p}) + \dots + \chi_M t_{\zeta M}(\mathbf{p}) = \bar{t}_{\zeta}(\mathbf{p})$$

$$\zeta = x, y, \mathbf{p} \in \Gamma^T$$

where:

$$\chi_m = \begin{cases} 1, & \mathbf{p} \in \Gamma_m \\ 0, & \mathbf{p} \notin \Gamma_m \end{cases}$$

On the interface between different regions, displacement continuity and traction equilibrium conditions have been assumed:

$$u_{\zeta m}(\mathbf{p}) - u_{\zeta k}(\mathbf{p}) = 0 \quad \zeta = x, y, \mathbf{p} \in \Gamma_m \cap \Gamma_k$$

$$t_{\zeta m}(\mathbf{p}) + t_{\zeta k}(\mathbf{p}) = 0 \quad \zeta = x, y, \mathbf{p} \in \Gamma_m \cap \Gamma_k$$

$$m, k = I, II, \dots, M$$

The strains $\varepsilon_{\zeta\xi}$; $\zeta, \xi = x, y$ are related to the displacement gradients by:

$$\varepsilon_{\zeta\xi} = \frac{1}{2} \left(\frac{\partial u_{\zeta}}{\partial p_{\xi}} + \frac{\partial u_{\xi}}{\partial p_{\zeta}} \right)$$

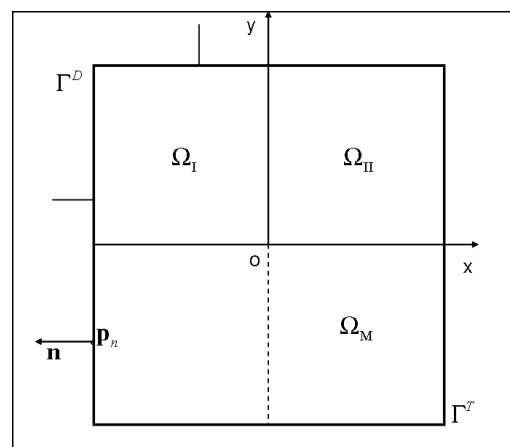


Figure 1: A scheme of the multi-region problem. Each of the sub-domains can have different elastic properties.

Slika 1: Shema problema z več območji. Vsako podobmočje ima lahko različne elastične lastnosti.

The stress components $\sigma_{\zeta\xi}$; $\zeta, \xi = x, y$ are for the plane-strain cases related to the strains through Hooke's law:

$$\sigma_{\zeta\xi} = \lambda_m \delta_{\zeta\xi} (\varepsilon_{xx} + \varepsilon_{yy}) + 2\mu_m \varepsilon_{\zeta\xi} \quad (6)$$

where $\mu_m = E_m / 2(1 + \nu_m)$ is the shear modulus of elasticity, E_m is a constant, known as the modulus of elasticity, or Young's modulus, $\lambda_m = 2 \nu_m \mu_m / (1 - 2\nu_m)$ is the Lamé constant, and $\delta_{\zeta\xi}$ is the Kronecker delta:

$$\delta_{\zeta\xi} = \begin{cases} 1, & \zeta = \xi \\ 0, & \zeta \neq \xi \end{cases} \quad (7)$$

3 SOLUTION PROCEDURE

The fields on each of the sub-domains are represented by collocation with fundamental solutions in the boundary points. The collocation needs to satisfy the boundary conditions between different regions and outer boundaries. In a numerical implementation of MFS and NMFS, we assume that one boundary collocation point belongs to only two regions at once. In order to keep the formulation simple we do not put the discretisation points on the corners that might belong to three or more regions at once. Explicit expressions for Kelvin's fundamental solution of elastostatics, used in the collocation, are given¹⁴ in a two-dimensional plane-strain situation by:

$$U_{\zeta\xi}(\mathbf{p}, \mathbf{s}) = \frac{1}{8\pi\mu(1-\nu)} \left\{ (3-4\nu) \lg\left(\frac{1}{r}\right) \delta_{\zeta\xi} + \frac{(p_\zeta - s_\zeta)(p_\xi - s_\xi)}{r^2} \right\} \quad (8)$$

$\zeta, \xi = x, y$

where the material properties depend on the position in a subdomain. $U_{\zeta\xi}(\mathbf{p}, \mathbf{s})$ represents the displacement in the ζ direction at point \mathbf{p} due to a unit point force acting in the ξ direction at point \mathbf{s} . $r = \sqrt{(p_x - s_x)^2 + (p_y - s_y)^2}$ is the distance between the collocation point \mathbf{p} and the source point \mathbf{s} .

It can be shown that the following u_x and u_y satisfy the governing Eq. (1):

$$\begin{aligned} u_x(\mathbf{p}) &= \sum_{n=1}^N \tilde{U}_{xx}(\mathbf{p}, \mathbf{p}_n) \alpha_n + \sum_{n=1}^N \tilde{U}_{xy}(\mathbf{p}, \mathbf{p}_n) \beta_n \\ u_y(\mathbf{p}) &= \sum_{n=1}^N \tilde{U}_{yx}(\mathbf{p}, \mathbf{p}_n) \alpha_n + \sum_{n=1}^N \tilde{U}_{yy}(\mathbf{p}, \mathbf{p}_n) \beta_n \end{aligned} \quad (9)$$

$$\mathbf{p} \notin \sum_{n=1}^N A(\mathbf{p}_n, R)$$

where α_n and β_n represent arbitrary constants and $\alpha_n = \alpha_{nm}, \beta_n = \beta_{nm}, N = N_m$ when $\mathbf{p} \in \Omega_m$. N_m is the number of $\mathbf{p} \in \Gamma_m, m = I, II, \dots, M$. $A(\mathbf{p}_n, R)$ (Figure 2) represents a circle with radius R , centred around $\mathbf{p}_n \cdot \mathbf{p}_n = \mathbf{s}$ represents points on the physical boundary. \mathbf{p} and \mathbf{p}_n belong to the same sub-domain. The quantity $U_{\zeta\xi}(\mathbf{p}, \mathbf{p}_n)$ is singular when $\mathbf{p} = \mathbf{p}_n$. We use the following de-singularization technique, proposed by⁶, for evaluating the singular values:

$$\tilde{U}_{\zeta\xi}(\mathbf{p}, \mathbf{p}_n) = \begin{cases} U_{\zeta\xi}(\mathbf{p}, \mathbf{p}_n) & \mathbf{p} \neq \mathbf{p}_n \\ \frac{1}{\pi R^2} \int_{A(\mathbf{s}, R)} U_{\zeta\xi}(\mathbf{p}, \mathbf{p}_n) dA & \mathbf{p} = \mathbf{p}_n \end{cases} \quad (10)$$

The tractions can be expressed as:

$$\begin{aligned} t_x(\mathbf{p}) &= \sum_{n=1}^N T_{xx}(\mathbf{p}, \mathbf{p}_n) \alpha_n + \sum_{n=1}^N T_{xy}(\mathbf{p}, \mathbf{p}_n) \beta_n \\ t_y(\mathbf{p}) &= \sum_{n=1}^N T_{yx}(\mathbf{p}, \mathbf{p}_n) \alpha_n + \sum_{n=1}^N T_{yy}(\mathbf{p}, \mathbf{p}_n) \beta_n \end{aligned} \quad (11)$$

where:

$$\begin{aligned} T_{xx}(\mathbf{p}, \mathbf{p}_n) &= \left[\frac{2\mu(1-\nu)}{1-2\nu} \frac{\partial U_{xx}(\mathbf{p}, \mathbf{p}_n)}{\partial p_x} + \frac{2\mu\nu}{1-2\nu} \frac{\partial U_{yx}(\mathbf{p}, \mathbf{p}_n)}{\partial p_y} \right] n_{nx} + \\ & \left[\mu \frac{\partial U_{xx}(\mathbf{p}, \mathbf{p}_n)}{\partial p_y} + \mu \frac{\partial U_{yx}(\mathbf{p}, \mathbf{p}_n)}{\partial p_x} \right] n_{ny} \\ T_{yy}(\mathbf{p}, \mathbf{p}_n) &= \left[\frac{2\mu(1-\nu)}{1-2\nu} \frac{\partial U_{yy}(\mathbf{p}, \mathbf{p}_n)}{\partial p_x} + \frac{2\mu\nu}{1-2\nu} \frac{\partial U_{xy}(\mathbf{p}, \mathbf{p}_n)}{\partial p_y} \right] n_{nx} + \\ & \left[\mu \frac{\partial U_{xy}(\mathbf{p}, \mathbf{p}_n)}{\partial p_y} + \mu \frac{\partial U_{yy}(\mathbf{p}, \mathbf{p}_n)}{\partial p_x} \right] n_{ny} \\ T_{yx}(\mathbf{p}, \mathbf{p}_n) &= \left[\mu \frac{\partial U_{yx}(\mathbf{p}, \mathbf{p}_n)}{\partial p_x} + \mu \frac{\partial U_{xx}(\mathbf{p}, \mathbf{p}_n)}{\partial p_y} \right] n_{nx} + \\ & \left[\frac{2\mu(1-\nu)}{1-2\nu} \frac{\partial U_{yx}(\mathbf{p}, \mathbf{p}_n)}{\partial p_y} + \frac{2\mu\nu}{1-2\nu} \frac{\partial U_{xx}(\mathbf{p}, \mathbf{p}_n)}{\partial p_x} \right] n_{ny} \\ T_{xy}(\mathbf{p}, \mathbf{p}_n) &= \left[\mu \frac{\partial U_{xy}(\mathbf{p}, \mathbf{p}_n)}{\partial p_x} + \mu \frac{\partial U_{yy}(\mathbf{p}, \mathbf{p}_n)}{\partial p_y} \right] n_{nx} + \\ & \left[\frac{2\mu(1-\nu)}{1-2\nu} \frac{\partial U_{xy}(\mathbf{p}, \mathbf{p}_n)}{\partial p_y} + \frac{2\mu\nu}{1-2\nu} \frac{\partial U_{yy}(\mathbf{p}, \mathbf{p}_n)}{\partial p_x} \right] n_{ny} \end{aligned} \quad (12)$$

$t_\zeta = t_{\zeta m}, T_{\zeta\xi} = T_{\zeta\xi m}, n_{n\zeta} = n_{n\zeta m}, \zeta, \xi = x, y$ when $\mathbf{p} \in \Omega_m$.

The coefficients α_n and β_n are calculated from a system of $(2N_I + 2N_{II} + \dots + 2N_M) \times (2N_I + 2N_{II} + \dots + 2N_M)$ algebraic equations, obtained by collocating the boundary conditions:

$$\mathbf{Ax} = \mathbf{b} \quad (13)$$

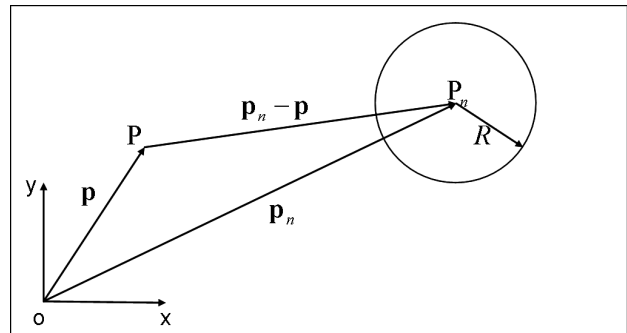


Figure 2: Distributed source on a disk $A(\mathbf{p}_n)$
 Slika 2: Porazdeljeni izviri na disku $A(\mathbf{p}_n)$

where \mathbf{A} is composed of $\tilde{U}_{\zeta\xi}(\mathbf{p}, \mathbf{p}_n)$ and $\tilde{T}_{\zeta\xi}(\mathbf{p}, \mathbf{p}_n)$, \mathbf{x} is composed of α_n and β_n , and \mathbf{b} is composed of u_ζ , t_ζ and 0. The explicit form of the elements of the algebraic equation system (13) can be found in.¹¹

The diagonal terms $\tilde{T}_{\zeta\xi}(\mathbf{p}_l, \mathbf{p}_l)$, $\zeta, \xi = x, y, l = 1, \dots, N_I + \dots + N_M$, in Eq. (13) are determined indirectly for the collocation points on Γ^T . For this purpose, the method proposed in⁷ for potential problems is applied to determine the diagonal coefficients of Eq. (13). In the approach, we first assume two simple solutions. The first simple solution is $\bar{u}_x(\mathbf{p}) = p_x + c_x$, $\bar{u}_y(\mathbf{p}) = 0$ everywhere. The second simple solution is $\bar{u}_x(\mathbf{p}) = 0$, $\bar{u}_y(\mathbf{p}) = p_y + c_y$ everywhere. We solve them for the corresponding $\alpha_n^{(1)}$, $\beta_n^{(1)}$ and $\alpha_n^{(2)}$, $\beta_n^{(2)}$ using only the displacement boundary condition. From these two solutions, we can also know:

$$\frac{\partial u_x^{(1)}(\mathbf{p})}{\partial p_x} = 1, \quad \frac{\partial u_x^{(1)}(\mathbf{p})}{\partial p_y} = \frac{\partial u_y^{(1)}(\mathbf{p})}{\partial p_x} = \frac{\partial u_y^{(1)}(\mathbf{p})}{\partial p_y} = 0 \tag{14}$$

$$\frac{\partial u_x^{(2)}(\mathbf{p})}{\partial p_x} = \frac{\partial u_x^{(2)}(\mathbf{p})}{\partial p_y} = \frac{\partial u_y^{(2)}(\mathbf{p})}{\partial p_x} = 0, \quad \frac{\partial u_y^{(2)}(\mathbf{p})}{\partial p_y} = 1$$

By substituting $\alpha_n^{(1)}$, $\beta_n^{(1)}$ and $\alpha_n^{(2)}$, $\beta_n^{(2)}$ and Eq. (9) into Eq. (14), we can obtain the diagonal terms $\tilde{T}_{\zeta\xi}(\mathbf{p}_l, \mathbf{p}_l)$, $\zeta, \xi = x, y, l = 1, \dots, N_I + \dots + N_M$. The constant c should be selected in such a way that all the points in the upper cases do not move the same distance. So that the denominators in the upper derivations are not zero.

By knowing all the elements A_{ij} and b_k of the system (13), we can determine all the values of α_n and β_n . Subsequently, we can calculate the displacement for all the domain points using Eq. (9).

4 NUMERICAL EXAMPLES

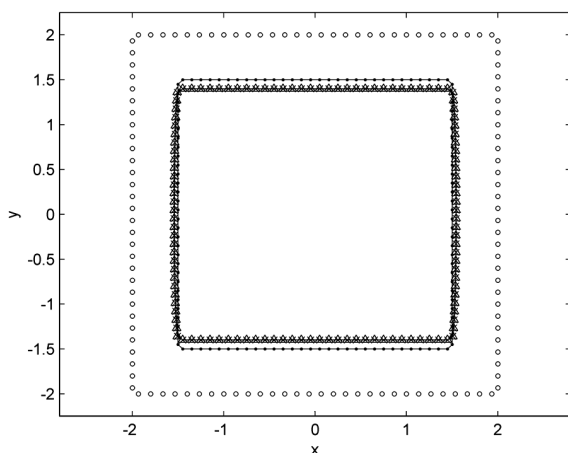


Figure 3: The deformation calculated with MFS and NMFS for a one-domain case with $E = 1\text{N/m}^2$, $\nu = 0.3$ and $N = 120$ (●: collocation points, ○: source points, ×: MFS solution, Δ: NMFS solution)

Slika 3: Deformacija, izračunana z MFR in NMFR, za primer z enim območjem z $E = 1\text{N/m}^2$, $\nu = 0,3$ in $N = 120$ (●: kolokacijska točka, ○: izvorna točka, ×: MFR-rešitev, Δ: NMFR-rešitev)

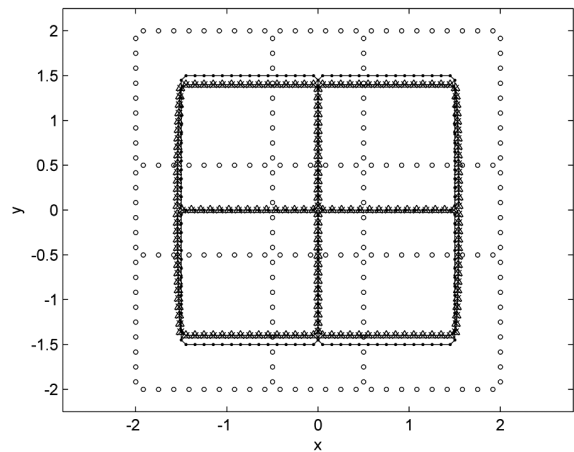


Figure 4: The deformation calculated with MFS and NMFS for a four-domain case $E_I = E_{II} = \dots = E_{IV} = 1\text{N/m}^2$, $\nu_I = \nu_{II} = \dots = \nu_{IV} = 0.3$ and $N = 240$ (●: collocation points, ○: source points, ×: MFS solution, Δ: NMFS solution). The position of the source points in MFS is on squares around each of the square physical domains.

Slika 4: Deformacija, izračunana z MFR in NMFR, za primer s štirimi območji $E_I = E_{II} = \dots = E_{IV} = 1\text{N/m}^2$, $\nu_I = \nu_{II} = \dots = \nu_{IV} = 0,3$ in $N = 240$ (●: kolokacijska točka, ○: izvorna točka, ×: MFR-rešitev, Δ: NMFR-rešitev). Pozicija izvornih točk je na kvadratih okoli vsakega od štirih kvadratnih domen.

We consider a square with side $a = 3\text{m}$ centred around $p_x = 0\text{m}$, $p_y = 0\text{m}$ for testing the performance of the method. We distinguish three sub-examples. In the first one, the whole square is occupied by one material, with the material properties $E = 1\text{N/m}^2$, $\nu = 0.3$, in the second one, the square is split into four parts with the same material properties as in the first example $E_I = E_{II} = \dots = E_{IV} = 1\text{N/m}^2$, $\nu_I = \nu_{II} = \dots = \nu_{IV} = 0.3$, and in the third one, the square is split into nine parts with the same

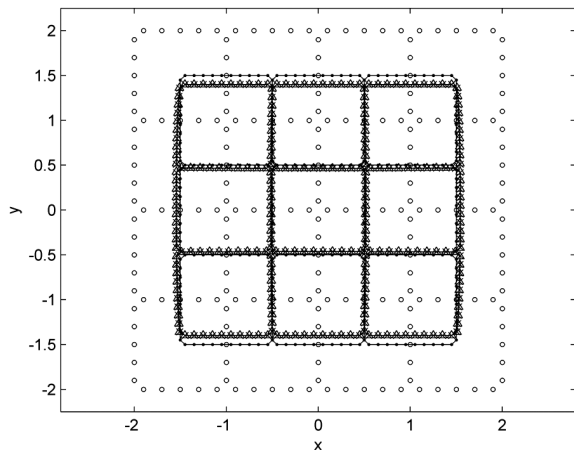


Figure 5: The deformation calculated with MFS and NMFS for a nine-domain case $E_I = E_{II} = \dots = E_{IV} = 1\text{N/m}^2$, $\nu_I = \nu_{II} = \dots = \nu_{IV} = 0.3$ and $N = 360$ (●: collocation points, ○: source points, ×: MFS solution, Δ: NMFS solution). The position of the source points in MFS is on squares around each of the square physical domains.

Slika 5: Deformacija, izračunana z MFR in NMFR, za primer z devetimi območji $E_I = E_{II} = \dots = E_{IV} = 1\text{N/m}^2$, $\nu_I = \nu_{II} = \dots = \nu_{IV} = 0,3$ in $N = 360$ (●: kolokacijske točke, ○: izvorne točke, ×: MFR-rešitev, Δ: NMFR-rešitev). Pozicija izvornih točk je na kvadratih okoli vsakega od štirih kvadratnih domen.

material properties as in the first example $E_I = E_{II} = \dots = E_{IX} = 1\text{N/m}^2$ $\nu_I = \nu_{II} = \dots = \nu_{IX} = 0.3$. We considered the solution of the Navier equations in this square subject to the boundary conditions $\bar{u}_x = 0\text{m}$, $\bar{u}_y = -0.1\text{m}$ on the points of the north side with $p_y = 1.5\text{m}$; $\bar{u}_x = 0\text{m}$, $\bar{u}_y = 0.1\text{m}$ on the south side with $p_y = -1.5\text{m}$ and on the east $p_x = 1.5\text{m}$ and west $p_x = -1.5\text{m}$ sides $\bar{t}_x = 0\text{N/m}^2$, $\bar{t}_y = 0\text{N/m}^2$ is set. A plot of the deformation, calculated with the defined three sub-examples is shown in **Figures 3, 4 and 5**, respectively. The following parameters were used $R = d/5$, $R_I = d_I/5$, ..., $R_{IX} = d_{IX}/5$, where d , d_m , $m = \text{I, II, ..., IX}$ are the smallest distances between two nodes on the boundary, R_m is the radius of the circle centred the point $\mathbf{p}_n \in \Gamma_m$, $c_x = c_y = c_{xI} = c_{yI} = L = c_{xIX} = c_{yIX} = 4$. The distance of the fictitious boundary from the true boundary for the MFS is set to $R_M = 5d$, $R_{MI} = 5d_I$, ..., $R_{MIX} = 5d_{IX}$.

Figures 3, 4 and 5 show good agreement between the solution for a one-domain region and a solution recalculated with the four and nine regions in ideal mechanical contact and with the same material properties. The maximum absolute difference in displacements between the values in **Figures 3 and 4** at the outer boundary are $\Delta u_x = 0.0417\text{m}$, $\Delta u_y = 0.0886\text{m}$, and between **Figures 3 and 5** $\Delta u_x = 0.0017\text{m}$, $\Delta u_y = 0.0012\text{m}$, respectively.

5 CONCLUSION

A new, non-singular method of fundamental solutions¹³ is extended in the present paper to solve multi-dimensional linear elasticity problems. In this approach, the singular values of the fundamental solution are integrated over small circular discs, so that the coefficients in the system of equations can be evaluated analytically and consistently, leading to an extremely simple computer implementation of this method. The method essentially gives the same results as the classic MFS. It has the advantage that the artificial boundary is not present; however, at the expense of solving three times the systems of algebraic equations in comparison with only one solution in MFS. The main advantage of the method is that the discretisation is performed only on the boundary of the domain and no polygonisation is needed, like in the finite-element method. The NMFS method, presented in this paper, can be adapted or extended to handle many related problems, such as three-dimensional elasticity, anisotropic elasticity, and multi-body problems, which all represent directions for

our further investigations. The advantage of not having to generate the artificial boundary is particularly welcome in these types of problems. The method will be used in the future for the calculation of multigrain deformation problems in steel and aluminium alloys, with realistic grain shapes, obtained from the microscope images. The developed method is believed to represent a most simple state-of-the-art way to numerically cope with these types of problems.

Acknowledgement

This paper forms a part of the project L2-3651 Simulation and Optimisation of Casting, Rolling and Heat Treatment Processes for Competitive Production of Topmost Steels, supported by the Slovenian Research Agency (ARRS) and Štore Steel company. The Centre of Excellence for Biosensors, Instrumentation and Process Control (COBIK) is an operation financed by the European Union, European Regional Development Fund and the Republic of Slovenia.

6 REFERENCES

- ¹ B. Šarler, R. Vertnik, S. Šaletič, G. Manojlović, J. Cesar, Berg-Huettenmaenn. Monatsh., 150 (2005), 300–306
- ² T. Mura, Micromechanics of Defects in Solids, 2ed, Martinus Nijhoff Publishers, Netherlands 1987
- ³ M. Braccini, M. Dupeux, Mechanics of Solid Interfaces, Wiley, New York 2012
- ⁴ G. Kosec, M. Založnik, B. Šarler, H. Ccombeau, CMC: Computers, Materials & Continua, 22 (2011), 169–195
- ⁵ A. Z. Lorbiecka, B. Šarler, CMC: Computers, Materials & Continua, 18 (2010), 69–103
- ⁶ U. Hanoglu, S. Islam, B. Šarler, Mater. Tehnol., 45 (2011) 6, 545–547
- ⁷ Y. S. Smyrlis, Mathematics of Computation, 78 (2009), 1399–1434
- ⁸ Y. J. Liu, Engineering Analysis with Boundary Elements, 34 (2010), 914–919
- ⁹ B. Šarler, Engineering Analysis with Boundary Elements, 33 (2009), 1374–1382
- ¹⁰ D. L. Young, K. H. Chen, J. T. Chen, J. H. Kao, CMES: Computer Modeling in Engineering & Sciences, 19 (2007), 197–222
- ¹¹ D. L. Young, K. H. Chen, C. W. Lee, Journal of Computational Physics, 209 (2005), 290–321
- ¹² W. Chen, F. Z. Wang, Engineering Analysis with Boundary Elements, 34 (2010), 530–532
- ¹³ Q. G. Liu, B. Šarler, CMES: Computer Modeling in Engineering and Sciences, 91 (2013), 235–266
- ¹⁴ D. E. Beskos, Boundary Element Methods in Mechanics, Elsevier, Amsterdam 1987, 33

REMOVAL OF SURFACE IMPURITIES FROM QCM SUBSTRATES WITH THE LOW-PRESSURE OXYGEN-PLASMA TREATMENT

ODSTRANJEVANJE POVRŠINSKIH NEČISTOČ S QCM-PODLAG Z OBDELAVO V NIZKOTLAČNI KISIKOVI PLAZMI

Rok Zaplotnik¹, Darij Kreuh², Alenka Vesel¹

¹Jožef Stefan Institute, Department of Surface Engineering and Optoelectronics, Jamova cesta 39, 1000 Ljubljana, Slovenia

²Eklptik, d. o. o., Teslova 30, 1000 Ljubljana, Slovenia
rok.zaplotnik@ijs.si

Prejem rokopisa – received: 2013-03-12; sprejem za objavo – accepted for publication: 2013-03-25

A novel method for cleaning quartz crystals used in QCM is presented. Crystals were covered with a thin film of impurities containing protein fibrinogen, sodium stearate and sodium chloride. Samples were exposed to the oxygen plasma created by an electrodeless radiofrequency discharge in the H-mode. The oxygen pressure was fixed to 10 Pa, the nominal power of the RF-generator was 200 W, the reflected power was about 24 W, and the treatment times were up to 40 s. The plasma was characterized with optical emission spectroscopy. During the treatment of the samples the spectral features indicating a removal of impurities appeared in the optical spectra. The temporal evolution of characteristic optical features allowed for a real-time monitoring of the cleaning procedure. All the spectral features have been normalized to the temporal evolution of the atomic oxygen line at 615 nm. The CO features appeared in the first few seconds of the plasma treatment indicating a preferential removal of organic components. The Na atomic line at 589 nm became measurable after a few seconds of the plasma treatment, increasing for about 10 s and decreasing thereafter until it became very low after about 35 s. The results clearly indicate the applicability of oxygen plasma for a rapid removal of impurities from the surface of quartz crystals. Organic impurities are removed in a very short time due to an extremely high affinity of oxidation, while inorganic impurities can be removed only with a prolonged treatment when the thermal effects become important.

Keywords: protein fibrinogen, oxygen plasma, surface cleaning, etching

V članku predstavljamo novo metodo čiščenja QCM-podlag iz kremenovega kristala. Kristale smo prekrili s tanko plastjo nečistoč, ki so vsebovale protein fibrinogen, natrijev stearat in natrijev klorid. Vzorce smo izpostavili kisikovi plazmi, ustvarjeni z brezelektrodno radiofrekvenčno razelektrovitvijo v H-načinu. Obdelovali smo jih pri konstantnem tlaku 10 Pa, časi obdelave so bili do 40 s, moč RF-generatorja je bila 200 W, odbita moč pa okoli 24 W. Značilnosti plazme smo merili z optično emisijsko spektroskopijo. Med obdelavo vzorcev so se na optičnem spektru pojavile emisijske spektralne črte, ki jasno nakazujejo odstranjevanje nečistoč. Časovni potek teh črt nam je omogočil spremljanje postopka čiščenja v realnem času. Vse emisijske črte smo normalizirali s časovnim potekom kisikove atomske črte pri 615 nm. V prvih nekaj sekundah so se v spektrih pojavile emisijske črte molekule CO, kar nakazuje odstranjevanje organskih komponent. Intenziteta natrijeve emisijske črte pri 589 nm postane merljiva po nekaj sekundah plazemske obdelave, se večja približno 10 s, doseže maksimum in se nato manjša, dokler ne doseže nizkih vrednosti pri 35 s. Rezultati jasno prikazujejo uporabnost kisikove plazme pri hitrem odstranjevanju nečistoč s površin kremenovih kristalov. Organske nečistoče očistimo v zelo kratkem času zaradi visoke afinitete oksidacije, medtem ko anorganske nečistoče lahko odstranimo le z daljšimi obdelavami, ko termični efekti postanejo pomembni.

Ključne besede: protein fibrinogen, kisikova plazma, čiščenje površin, jedkanje

1 INTRODUCTION

Quartz crystal microbalance (QCM) is one of the most accurate devices for determining thin-film thickness.¹⁻⁶ The method is based on measuring the resonance frequency of the oscillating crystals, depending on the mass of the material deposited on the quartz crystal.⁷ Quartz crystals are rarely used several times if the deposited material is not removed properly, making this technique rather expensive. In the vacuum practice crystals are often cleaned and reused in order to reduce costs. Several techniques for removing the surface impurities have been applied and most of them use wet chemical cleaning. Not only is this technology unfriendly to the environment, it often does not ensure an atomically clean surface. One can use different solvents for removing specific impurities such as organic solvents for removing organic materials and acids or bases for re-

moving inorganic impurities. The latter may destroy the samples if not used properly. In many practical applications hundreds of samples should be measured and the cleaning of crystals may represent a major concern especially because the atomic cleanliness of a surface is not always guaranteed. In order to overcome this problem we have developed an alternative technique for removing the surface impurities that is based on an application of highly aggressive oxygen plasma.⁸

2 EXPERIMENTAL WORK

Commercially available QCM crystals have been used for the experiments. The crystals were covered with about a 100-nm thick film containing a mixture of fibrinogen, sodium citrate and sodium chloride. A commercially available lyophilized mixture of these materials

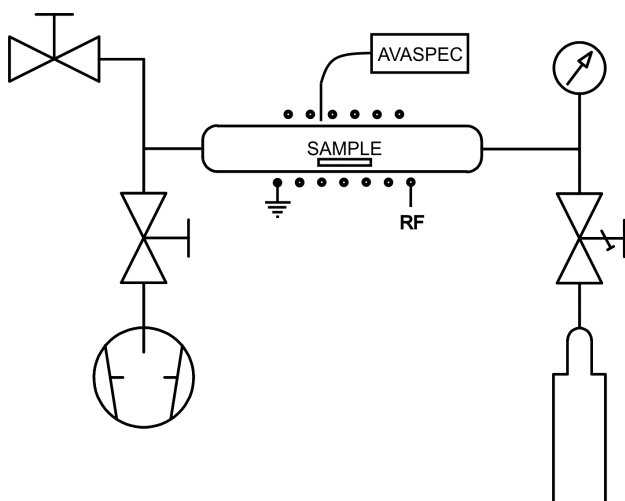


Figure 1: Schematic of the experimental set-up
Slika 1: Shema eksperimentalne postavitve

(Fibrinogen, Fraction I, type III from human plasma) was purchased from Sigma-Aldrich, dissolved in MilliQ water in order to obtain a 0.1 % solution, applied on a quartz crystal and distributed evenly by spinning it at 500 r/min. The samples were mounted into a vacuum system presented schematically in **Figure 1**. The system is pumped with a two-stage rotary pump with the nominal pumping speed of $80 \text{ m}^3 \text{ h}^{-1}$. Commercially available oxygen is leaked into the system on the other side, so the oxygen pressure during continuous pumping is 10 Pa. The pressure is measured with a precise pressure gauge MKS Baratron 722A. Plasma was excited inside a glass tube with a diameter of 4 cm. A copper coil was connected to an RF-generator via a matching network. The generator operated at the standard frequency of 13.56 MHz and the nominal power variable up to 1000 W. During the current experiment the applied power was 200 W and the reflected power was 24 W, so the plasma was well matched with the generator. Luminous plasma was concentrated within the coil indicating almost a pure H-mode of the electrical discharge.

The plasma was characterized with optical emission spectroscopy. We used a spectrometer AVASPEC 3648 and the integration time was fixed to 50 ms. Such an integration time, rather unusual for a characterization of luminous plasma in the H-mode, was applied in order to let the major peaks oversaturate and detect the minor peaks and bands.

3 RESULTS

A typical spectrum of gaseous plasma at the absence of any sample is presented in **Figure 2**, while a spectrum of plasma during the treatment of a quartz crystal contaminated with a film of impurities is shown in **Figure 3**. Both spectra show oversaturated major atomic lines, but the spectral features corresponding to the etching of

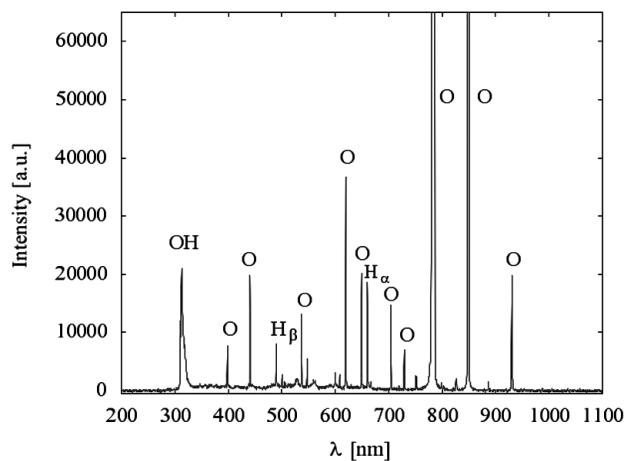


Figure 2: Typical optical spectrum of oxygen plasma at the absence of a sample

Slika 2: Značilni optični spekter kisikove plazme brez vzorca

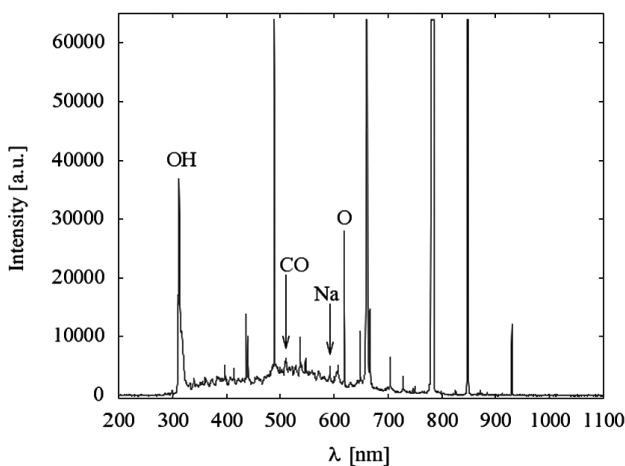


Figure 3: Typical optical spectrum of oxygen plasma at the presence of a sample

Slika 3: Značilni optični spekter kisikove plazme pri obdelavi vzorca

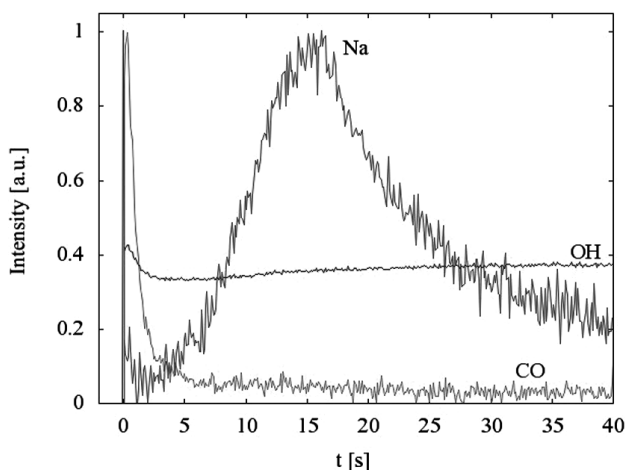


Figure 4: Temporal evolution of specific spectral features during the plasma cleaning of the quartz crystal contaminated with a 100-nm thick film of impurities

Slika 4: Časovni potek določenih emisijskih spektralnih črt med plazemskim čiščenjem kremenovega kristala z nanoseno debelo plastjo nečistoč 100 nm

surface impurities are clearly visible in **Figure 3**. Selected spectral features during the plasma treatment of a sample are presented in **Figure 4**. These spectral features have been normalized to the temporal evolution of the atomic oxygen line at 615 nm.

4 DISCUSSION

Optical spectra of oxygen plasma during the treatment of quartz crystals, contaminated with surface impurities, have been collected continuously for 40 s. A spectrum without a sample was also measured and it is presented in **Figure 2**. As expected, neutral oxygen-atom atomic lines prevail. The absence of any molecular bands just indicates a well-known characteristic of plasma, created by the RF-discharge in the H-mode – an almost 100 % dissociation rate. Such a very high dissociation rate is due to a very low coefficient for a heterogeneous surface recombination of O-atoms on the glass surface as well as the absence of three body collisions at 10 Pa that could otherwise allow for a gas-phase recombination. Plasma is therefore almost 100 % dissociated and many oxygen atoms are probably found in the excited states that are metastable. Such atoms are chemically extremely reactive and will interact with organic as well as some inorganic impurities even at room temperature. Well pronounced spectral features peaking at 309 nm correspond to OH radicals. This peak is due to the presence of water vapour in our vacuum system that has never been baked. Water molecules dissociate to OH and H radicals in a rather powerful discharge. The spectral features presented in **Figure 3** are different. Not only are the hydrogen atomic lines corresponding to Balmer series much higher, but other features are observed as well. The most significant one is the broad continuum that has been assigned to various transitions of CO radicals.^{9,10} Also, the Na atomic line at 589 nm is clearly visible. The existence of these two features indicates a substantial etching of the surface impurities deposited on quartz crystals.

The time evolution of some spectral features is shown in **Figure 4**. Let us first discuss the extremely sharp peak of the OH radical found just after turning on the discharge. As mentioned earlier, our system was frequently vented and never baked so that the surfaces are covered with adsorbed water molecules. As soon as the discharge is turned on the molecules desorb and quickly dissociate in gaseous plasma and are excited by the inelastic collisions with free electrons. Since the amount of water molecules on the surfaces is rather low, practically all the molecules desorb in a very short time. This is the reason of the sharp peak observed in **Figure 4**. For the next few seconds the intensity of the OH peak slowly decreases until it becomes constant. Such a decrease cannot be attributed to the desorption of water molecules from the discharge tube, as it is probably due to the oxidation of organic impurities containing hydrogen. This hypothesis is sound with the behaviour of the CO peak. This peak

appears immediately after turning on the discharge. Since it is absent in the plasma created in an empty tube, it can be attributed to the oxidation of organic materials. The fact that the peak appears only in the first few seconds of the plasma treatment indicates a rapid oxidation of organic impurities. Such a rapid oxidation is probably due to a rather high density of excited oxygen atoms in plasma. As mentioned earlier such metastable atoms are chemically extremely reactive. The sodium peak is also presented in **Figure 4**. The temporal evolution of this peak is completely different from the OH and CO peaks. The sodium peak becomes measurably high after about 5 s and its intensity is the highest after about 15 s. Oxygen plasma is obviously aggressive enough to react also with this sort of impurities.

5 CONCLUSIONS

A novel method for cleaning quartz crystals was presented. The method is ecologically benign since it does not produce any wastes. The method allows for a rapid removal of organic impurities since about a thick film 100 nm of fibrinogen with stearates is effectively removed in a few seconds. As expected, inorganic impurities such as sodium chloride are more resistant and it, therefore, takes a longer time to remove them. It is worth mentioning that oxygen plasma does not interact with silicon dioxide so that the properties of quartz crystals are preserved.

Acknowledgements

The authors acknowledge the financial support from the Slovenian Research Agency through project L7-4035 (Toward ecologically benign alternative for cleaning of delicate biomedical instruments).

6 REFERENCES

- B. D. Vogt, E. K. Lin, W. I. Wu, C. C. White, *Journal of Physical Chemistry B*, 108 (2004) 34, 12685–12690
- F. Höök, B. Kasemo, T. Nylander, C. Fant, K. Sott, H. Elwing, *Analytical Chemistry*, 73 (2001) 24, 5796–5804
- T. Indest, J. Laine, L. S. Johansson, K. Stana-Kleinschek, S. Strnad, R. Dworzak, V. Ribitsch, *Biomacromolecules*, 10 (2009) 3, 630–637
- F. Caruso, K. Niikura, D. N. Furlong, Y. Okahata, *Langmuir*, 13 (1997) 13, 3422–3426
- M. M. Ayad, M. A. Shenashin, *European Polymer Journal*, 39 (2003) 7, 1319–1324
- T. Indest, J. Laine, K. Stana-Kleinschek, L. Fras-Zemljic, *Colloids Surfaces A*, 360 (2010) 1–3, 210–219
- A. Doliska, A. Vesel, M. Kolar, K. Stana-Kleinschek, M. Mozetic, *Surface and Interface Analysis*, 44 (2012) 13, 56–61
- M. Mozetic, *Mater. Tehnol.*, 44 (2010) 4, 165–171
- N. Glavan Vukelic, M. Biscan, S. Milosevic, *Spectral simulations of CO molecular emission observed in inductively coupled radio frequency plasmas*, *Proceedings of the 3rd International Conference on Advanced Plasma Technologies*, Bohinj, 2010, 38–43
- A. Vesel, M. Mozetic, A. Drenik, M. Balat-Pichelin, *Chemical Physics*, 382 (2011) 1–3, 127–131

STRUCTURAL, OPTICAL AND ELECTRICAL STUDIES ON Si-DOPED POLYMER ELECTROLYTES

ŠTUDIJ STRUKTURE, OPTIČNE IN ELEKTRIČNE LASTNOSTI ELEKTROLITOV POLIMEROV, DOPIRANIH S Si

Amit Saxena^{1,2}, Pramod Kumar Singh², Bhaskar Bhattacharya²

¹Department of Physics, Hindustan College of Science and Technology, Farah, Mathura- 281122, India

²Material Research Laboratory, School of Engineering and Technology, Sharda University, G. Noida 201310, India
saxena.electronics@gmail.com

Prejem rokopisa – received: 2013-03-25; sprejem za objavo – accepted for publication: 2013-04-02

In this paper we have studied the modification of the structural, optical and electrical properties of a polymer electrolyte film of polyethylene oxide complexed with sodium iodide (PEO:NaI) by doping with Si particles. Structural studies were carried out using Fourier-transform infrared spectroscopy (FTIR) and X-ray diffraction (XRD) measurements. The surface morphology of the polymer electrolyte film doped with Si particles was studied using polarized optical microscopy (POM). For the electrical properties, the electrical conductivity of the films was measured using complex impedance spectroscopy. The ionic transference number measurement (t_{ion}) was carried out and explained in detail to support the electrical conductivity data.

Keywords: polymer electrolyte, FTIR, XRD, POM, ionic conductivity

V tem članku smo preučevali spremembe strukture, optičnih in električnih lastnosti polimernih elektrolitskih plasti polietilen oksida, kompleksiranega z natrijevim jodidom (PEO:NaI) po dopiranju z delci Si. Študij strukture je bil opravljen z uporabo infrardeče spektroskopije s Fourierjevo transformacijo (FTIR) in z rentgensko difrakcijo (XRD). Morfologija površine tanke plasti polimernega elektrolita, dopiranega z delci Si, je bila preučevana s svetlobno mikroskopijo s polarizirano svetlobo (POM). Od električnih lastnosti je bila izmerjena električna prevodnost plasti s kompleksno impedančno spektroskopijo. Izvršeno in razloženo je bilo merjenje številke ionske transference (t_{ion}), ki prispeva k podatkom o električni prevodnosti.

Ključne besede: elektrolit iz polimera, FTIR, XRD, POM, ionska prevodnost

1 INTRODUCTION

Ion-conducting solid polymer electrolytes are arguably the most attractive materials today because of their potential applications in various electrochemical devices, such as dye-sensitized solar cells, supercapacitors, rechargeable batteries, sensors, etc.¹⁻⁷ For electrochemical applications, the electrolytes must be ironically conductive, and at the same time electrode must be compatible with it. Good quality, mechanically strong, semi-crystalline films could be obtained, but unfortunately in most cases the obtainable conductivity is too low (10^{-7} – 10^{-8} S/cm), while for an efficient device we need at least three-to-four orders of magnitude higher conductivity (10^{-3} – 10^{-4} S/cm). To achieve this conductivity value, different approaches have been proposed in the literature, like the use of plasticizers, copolymerization, the formation of blends, changing polymer chain length, composite formation, etc. Of these, composite formation is quite attractive and many composites/blends with various types of dispersoid have been reported in the literature.⁸⁻¹⁰ In this communication, we report an important observation that if semiconducting Si particles are used in forming a composite, a significant conductivity enhancement as well as a structural change can be obtained.

2 EXPERIMENTAL

Before forming the composite, the weight amount of polymer (PEO) and salt (NaI) are taken and films are prepared using a standard solution cast technique. The cation-to-monomer ratio was kept fixed at ≈ 0.065 for all the samples. The different stoichiometric ratios of the semiconducting Si powder (different size) were taken as the dopant to form the composite electrolyte and added to the ion-conducting polymer electrolyte solution. The resultant Si-doped polymer electrolyte solutions were stirred continuously. The final viscous solutions thus obtained were poured into a polypropylene Petri dish. The films, so prepared, were subjected to different characterizations.

To confirm the interaction between the polymer and the semiconductor, Fourier-transform infrared (FTIR) spectra were recorded in the attenuated total reflectance (ATR) mode using a Bruker Tensor 27 spectrometer with a resolution of 4 cm^{-1} in the vibrational frequency range 600 – 3600 cm^{-1} . The X-ray diffraction (XRD, Rigaku D/MAX-RC 12 kW) patterns of the samples were taken with 2θ values ranging from 15° to 65° at a scanning rate of $10^\circ/\text{min}$. The surface morphologies of the composite polymer film were studied with an optical microscope (OM, Leica DM LB) under a cross polarizer.

In order to evaluate the ionic conductivity of the polymer electrolyte film, impedance spectroscopic tech-

niques were used. The conductivities of the polymer films were evaluated from the bulk resistance by ac complex impedance analysis over a frequency range of 100 Hz to 1 MHz. The transference numbers (t_{ion}) of the Si-doped polymer electrolyte composite sample are measured using Wagner's polarization method.² In this method the sample is placed between two electrodes in such a way that it minimizes the contact resistance. In an ideal case one of the electrodes is blocking, whereas the other is non-blocking. In the present case we have used stainless-steel electrodes. A dc potential is applied across the sample in such a way that mobile ion species move towards the non-blocking electrode and a small polarization current flows, and finally the sample becomes polarized. The initial total current I_i and the final residual current I_f are used to evaluate the ionic transference number:

$$T_{ion} = \frac{I_{initial} - I_{final}}{I_{initial}}$$

3 RESULT AND DISCUSSION

3.1 FTIR study

The composite natures of the Si-doped polymer electrolyte and the host polymer electrolyte (PEO:NaI) were confirmed using the FTIR spectra of different samples. **Figure 1** shows the recorded infrared spectra of the PEO:NaI (line 1) and PEO:NaI doped with Si polymer electrolyte films (line 2). Peaks corresponding to various conformations of the polymer chain could be identified.^{11–13} No additional peaks were observed in the FTIR spectra of the Si-doped polymer electrolyte (line 2) other than the host polymer electrolyte (line 1).

This affirms the composite nature of the films. Additionally, the absence of any other peak re-confirms that no chemical reaction takes place between the host and

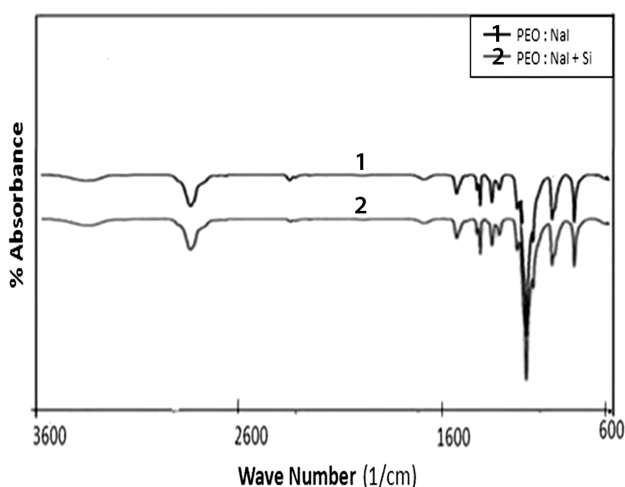


Figure 1: The FTIR spectra of the Si-doped polymer film (line 2) and polymer electrolyte film (PEO:NaI) without Si-doping (line 1)

Slika 1: FTIR-spektra s Si dopirane polimerne plasti (linija 2) in polimerne elektrolitske plasti (PEO:NaI) brez dopiranja s Si (linija 1)

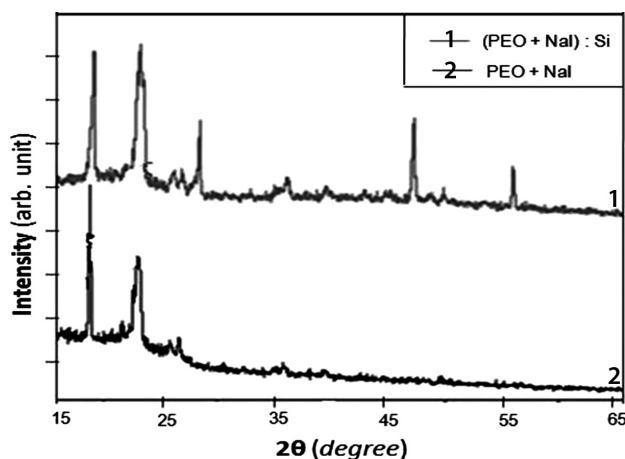


Figure 2: XRD pattern of pure PEO:NaI (line 2) and PEO:NaI doped with Si particles (line 1) polymer electrolyte films

Slika 2: XRD-posnetek čistega PEO:NaI (linija 2) in PEO:NaI, dopiranega z delci Si (linija 1) polimerne elektrolitske plasti

the doped semiconductor. The recorded X-ray diffraction patterns of the Si-doped polymer electrolyte as well as the host polymer electrolyte (without Si-doping) are shown in **Figure 2**. It is well known that the PEO shows a partially crystalline nature, containing a broad hollow between $2\theta = 15^\circ$ and 20° . The Si-doped polymer electrolyte films seems superimposed on this broad hollow.¹⁰ No other peak than the host and the semiconductors clearly confirms the composite nature, as we observed in our FTIR study, discussed earlier.

3.2 Surface study using polarized optical microscopy (POM)

The surface features of polymer electrolyte films with and without Si are further characterized by polarized optical microscopy (POM). **Figure 3** shows the POM photographs of different samples. It was clear that the pure PEO film (**Figure 3a**) shows well the semi-crystalline nature in which large size spherulites are tightly interconnected with each other. Adding NaI into the PEO matrix (**Figure 3b**), the spherulite size becomes small, while the amorphous region (black portion) is

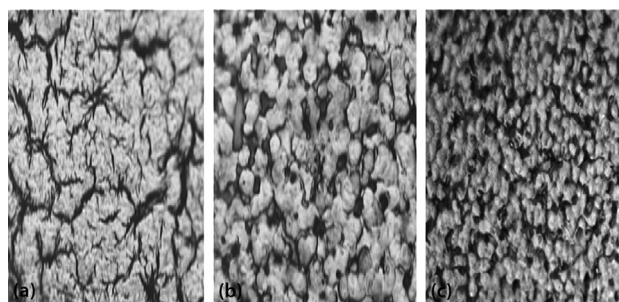


Figure 3: Polarized optical micrographs of: a) pure PEO, b) PEO:NaI and c) Si-doped PEO:NaI polymer electrolyte films

Slika 3: Optični posnetki v polarizirani svetlobi: a) čisti PEO, b) PEO:NaI in c) s Si dopirana PEO:NaI polimerne elektrolitske plasti

increased. It was also noticed that the amorphous region further increases after the Si doping (Figure 3c) and Si is preferred to obtain the assembled amorphous region. This shows good agreement with our FTIR and XRD measurements.

3.3 Electrical studies

The complex impedance spectroscopy was used to calculate the bulk electrical conductivity of the polymer electrolyte films.^{14–18} We used pressure-contacted stainless-steel electrodes and connected it with the CH instruments electrochemical workstation (Model CHI604D) with the frequency range 100 Hz to 1 MHz. The electrical conductivity (σ) was evaluated using the formula:

$$\sigma = G \frac{l}{A}$$

where σ is the ionic conductivity, G is the conductance ($G = 1/R_b$ where R_b is the bulk resistance), l is the thickness of the film and A is the area of the polymer sample. The cole-cole plot (complex impedance plot) of a typical sample of PEO + NaI doped with the mass fraction 10 % of Si is shown in Figure 4.

The calculated ionic conductivity values are plotted in Figure 5. Figure 5 shows the conductivity vs. composition plot of Si-doped PEO:NaI polymer electrolyte films calculated from various impedance plots. Since the PEO shows a very low conductivity at room temperature ($10^{-9} \text{ S cm}^{-1}$), we have added a small amount of NaI to improve its conductivity. It is clear from the figure that the conductivity increases with increasing Si concentration and the conductivity maxima obtained at the mass fraction of 10 % Si concentration with conductivity value of $4.4 \cdot 10^{-6} \text{ S cm}^{-1}$. This enhancement in conductivity is attributed to the enhancement in the amorphous region by doping with Si particles, which is clearly affirmed by our POM data, discussed earlier.

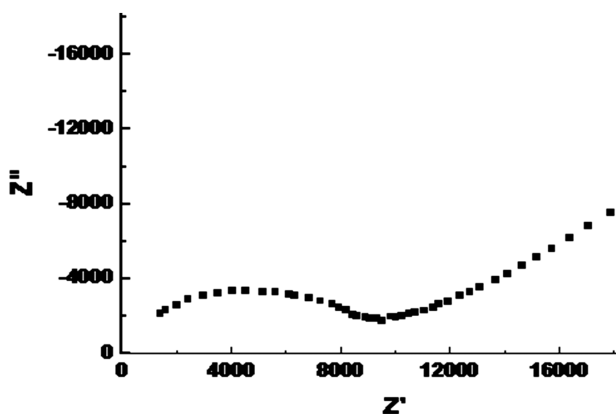


Figure 4: Cole-cole plot of PEO:NaI + 10 % Si polymer electrolyte system

Slika 4: Cole-cole diagram PEO:NaI + 10 % Si sistema elektrolitskega polimera

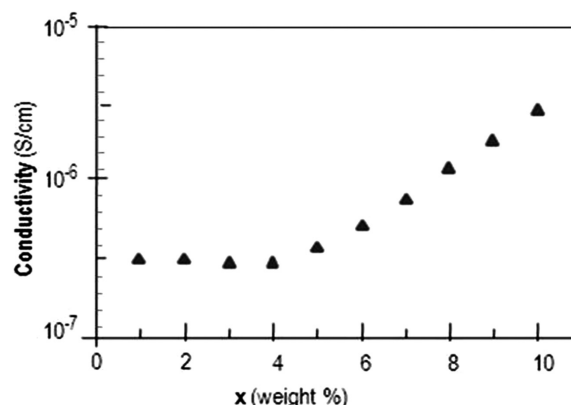


Figure 5: Ionic conductivity (σ) vs. concentration of NaI plot in Si-doped PEO:NaI polymer electrolyte system

Slika 5: Ionska prevodnost (σ) v odvisnosti od koncentracije NaI v sistemu s Si dopiranega PEO:NaI elektrolitskega polimera

3.4 Ionic transference number measurement

The total ionic transference numbers of the Si-doped polymer electrolyte samples are calculated using Wagner's polarization method. Figure 6 shows the variation of the current with the time plot for PEO:NaI + 8 % Si composite polymer electrolyte film. It can be observed that the current initially decreases rapidly as the time increases. The initial current is due to ionic behaviour, but after a short time the sample becomes polarized and the current is decreased due to the lack of ions. Finally, there are no ions, but a very small number of electrons are still being present inside the sample, which are responsible for the residual current. The transference number calculated in the present system is 0.99, which shows that the system is mostly due to ionic behaviour and is a good candidate for a solid electrolyte.

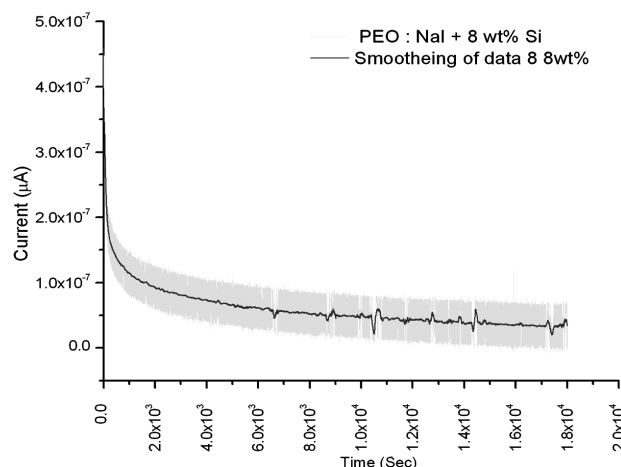


Figure 6: Time vs. current plot for PEO:NaI + 8 % Si composite polymer electrolyte

Slika 6: Čas v odvisnosti od toka za kompozitni polimerni elektrolit PEO:NaI z masnim deležem 8 % Si

4 CONCLUSIONS

A composite polymer electrolyte based on Si-doped PEO:NaI has been developed and characterized. Electrical conductivity measurements show the enhancement in the electrical conductivity by Si doping. IR as well as XRD affirmed the composite nature of the polymer electrolyte samples. Polarized optical microscopy (POM) confirmed the enhancement in the amorphous region by Si doping, which is a well-known condition for conductivity enhancement. Ionic transference number measurements (T_{ion}) suggest that the developed composite polymer electrolytes are ionic in nature.

Acknowledgement

This work was supported by DST project (SR/S2/CMP-0065/2010) government of India.

5 REFERENCES

- ¹ J. R. MacCallum, C. A. Vincent (eds.), *Polymer Electrolyte Reviews*, 1, 2, Elsevier Science Publishers Ltd., New York 1989, 1991
- ² P. V. Wright, *Br. Polym. J.*, 7 (1975), 319
- ³ D. E. Fenton, J. M. Parker, P. V. Wright, *Polymer*, 14 (1973), 589
- ⁴ S. Chandra, *Superionic solids: principles and applications*, North Holland, Amsterdam 1981
- ⁵ A. F. Nogueira, J. R. Durrant, M. A. De Paoli, *Advanced Materials*, 13 (2001), 826
- ⁶ A. Chandra, P. K. Singh, S. Chandra, *Solid State Ionics*, 154–155 (2002), 15
- ⁷ P. Kumar, P. K. Singh, B. Bhattacharya, *Ionics*, 17 (2011), 721–725
- ⁸ P. V. Braun, P. Osenar, S. I. Stupp, *Nature*, 380 (1996), 327
- ⁹ R. Singh, N. A. Jadhav, S. Majumder, B. Bhattacharya, P. K. Singh, *Carbohydrate Polymers*, 91 (2013), 682
- ¹⁰ B. Bhattacharya, J. Y. Leem, J. Geng, H. T. Jung, J. K. Park, *Langmuir*, 25 (2009), 3276
- ¹¹ B. L. Papke, M. A. Ratner, D. F. J. Shriver, *Electrochem. Soc.*, 129 (1982), 1434
- ¹² J. Y. Lee, B. Bhattacharya, D. W. Kim, J. K. Park, *J. Phys. Chem. C*, 112 (2008), 12576
- ¹³ G. Socrates, *Infrared and Raman Characteristic Group Frequencies*, 3rd ed., John Wiley & Sons, Ltd., New York 2005
- ¹⁴ P. K. Singh, B. Bhattacharya, R. K. Nagarale, *Journal of Applied Polymer Science*, 118 (2010), 2976
- ¹⁵ P. K. Varshney, S. Gupta, *Ionics*, 17 (2011), 479
- ¹⁶ A. Chandra, S. Chandra, *Phys Rev B*, 49 (1994), 630
- ¹⁷ P. K. Singh, K. W. Kim, K. I. Kim, N. G. Park, H. W. Rhee, *Journal of Nanoscience and Nanotechnology*, 8 (2008), 5271
- ¹⁸ P. K. Singh, B. Bhattacharya, *Optoelectronics and Advanced Materials-Rapid communications*, 7 (2013), 157

ELECTROLESS Ni-B-W COATINGS FOR IMPROVING HARDNESS, WEAR AND CORROSION RESISTANCE

NANAŠANJE Ni-B-W S CEMENTACIJSKIM GALVANIZIRANJEM ZA IZBOLJŠANJE TRDOTE, OBRABE IN ODPORNOSTI PROTI KOROZIJI

Ali Imre Aydeniz¹, Ali Göksenli¹, Gökce Dil¹, Faiz Muhaffel², Cagdas Calli²,
Behiye Yüksel³

¹TU Istanbul, Mechanical Engineering Department, 34437 Istanbul, Turkey

²TU Istanbul, Mechanical Metallurgical and Materials Eng. Dep., 34469 Maslak, Istanbul, Turkey

³Istanbul Aydin University, Dep. of Mechanical Engineering, 34668 Istanbul, Turkey
aydenizal@itu.edu.tr

Prejem rokopisa – received: 2013-03-26; sprejem za objavo – accepted for publication: 2013-04-08

In this study the formation of a Ni-B-W coating on steel using an electroless plating process and evaluation of the hardness, wear and corrosion resistance was analyzed. The Ni-B-W coating was prepared using an alkaline borohydride-reduced electroless nickel bath. Scanning electron microscopy (SEM) of the cross-sectional view of the Ni-B-W coating was analyzed and the layer characteristics were investigated. The Ni-B-W coating was characterized using XRD. The study reveals that the Ni-B-W coating is amorphous in the as-plated condition and after heat treatment at 450 °C for 1 h the Ni-B-W coatings crystallize and produce nickel and nickel borides. The hardness of the as-plated and heat-treated Ni-B-W coatings were compared with Ni-B coatings. In both coatings the hardness increased with heat treatment. The wear resistance of Ni-B-W coatings annealed at different temperatures was analyzed using a ball-on-flat test. The wear resistance of the coating increased with heat treatment and reached a maximum value at 400 °C. An optical microscope and EDS analysis were applied on the wear tracks to determine the wear mechanism. Ductile failure and an abrasive wear mechanism were dominant for the coating heat treated up to 400 °C. Network cracks and shearing marks were detected for the coatings annealed at 450 °C and above, indicating brittle failure. For investigating the corrosion characteristics of the coatings, immersion tests in 5 % H₂SO₄ and 10 % HCl acidic solutions for seven days were applied. According to the corrosion test results, the Ni-B-W coatings showed good corrosion resistance in the H₂SO₄ solutions.

Keywords: electroless plating, hardness, wear resistance, corrosion resistance, Ni-B-W coating

V tej študiji je bil analiziran postopek cementacijskega galvaniziranja za nanašanje Ni-B-W na jeklo in analizirana je bila trdota, obraba in korozijska odpornost. Nanos Ni-B-W je bil pripravljen z uporabo alkalne z borhidridom reducirane cementacijske galvanske kopeli niklja. Z vrstičnim elektronskim mikroskopom (SEM) je bil analiziran prečni prerez nanosa Ni-B-W in preiskane so bile značilnosti plasti. Nanos Ni-B-W je bil karakteriziran z XRD. Študija je odkrila, da je nanos Ni-B-W amorfen v nanesenem stanju, po toplotni obdelavi pri 450 °C, 1 h je bil nanos Ni-B-W kristaliziran in nastali so nikelj in nikljevi boridi. Primerjani sta bili trdota nanesenega in toplotno obdelanega nanosa Ni-B-W. V obeh primerih je trdota narasla s toplotno obdelavo. S preizkusom s kroglico na ploskvi je bila preizkušena obrabna odpornost nanosa Ni-B-W, žarjenega pri različnih temperaturah. Odpornost proti obrabi se je povečevala s toplotno obdelavo in je dosegla najvišjo vrednost pri 400 °C. Svetlobni mikroskop in EDS analiza sta bila uporabljena na obrabljeni tečini, da bi ugotovili mehanizem obrabe. Žilav prelom in mehanizem abrazijske obrabe sta prevladovala pri nanosu, segretem do 400 °C. Pri nanosu, segretem na 450 °C in višje, se je pojavila mreža razpok in znaki striženja, kar kaže na krhek prelom. Za ugotavljanje korozijskih lastnosti so bili uporabljeni preizkusi s potapljanjem sedem dni v raztopino 5 % H₂SO₄ in 10 % HCl. Pri korozijskem preizkusu je nanos Ni-B-W pokazal dobro korozijsko odpornost v raztopini H₂SO₄.

Gljučne besede: cementacijsko galvaniziranje, trdota, odpornost proti obrabi, odpornost proti koroziji, Ni-B-W nanos

1 INTRODUCTION

Electroless deposition is a chemical deposition technology, involving the deposition of metals from a solution onto surfaces without applying an external electric voltage.¹ The coating forms a uniform layer, independent of the substrate geometry, with good adhesion.² As reducing agents for the electroless nickel, hypophosphite and borohydrite have been used.³ The main advantages of Ni-P coatings are their low cost, ease of control and high corrosion resistance.⁴ The Ni-B coatings have exhibited interesting properties, like improved hardness and wear resistance.⁵ The as-plated Ni-B coatings' hardness can be further increased by

applying a heat treatment up to 1200 VHN, which could make it an alternative for chromium coatings.⁶ Also, the columnar structure of Ni-B coatings is useful in adhesive wear due to the good lubrication characteristics.⁷ The major limitations of Ni-B coatings are their high costs, poor control of the coating conditions and a low corrosion resistance compared to Ni-P coatings.⁸ To improve the properties of Ni-B coatings, a second metal salt into nickel solutions, such as W, Mo or Co, is added.⁹⁻¹¹ Among these metals, tungsten is an attractive metal due to its excellent, electrical, wear and corrosion resistance. Up to now, only a few analyses were carried out on the preparation and tribological-corrosion analyses of Ni-B-W coatings.^{9,12}

2 EXPERIMENTAL PROCEDURES

Plain carbon steel samples with dimensions of 10 mm × 10 mm × 30 mm were used as the substrate material. The plain carbon steel substrates were grinded, polished and then soaked in trichloroethylene. After which they were cleaned with a detergent at 70 °C. Lastly, the samples were placed in a 30 % HCl solution for 2 min, followed by a rinse in distilled water. The cleaned substrates were subsequently placed in a bath. For the electroless Ni-B-W bath, sodium borohydride was preferred. The stabilizer used was lead tungstate. To prevent the precipitation of nickel hydroxide, complexing agents such as ethylenediamine are required in the bath. The bath composition and the operating conditions used for preparing the Ni-B-W coatings are given in **Table 1**.

Table 1: Composition of the bath and the experimental parameters used for electroless Ni-B-W coatings

Tabela 1: Sestava kopeli in eksperimentalni parametri, uporabljeni pri cementacijskem galvaniziranju Ni-B-W nanosa

Operation	Plating bath composition	Condition
Electroless Ni-B-W	NiCl ₂ 24 g/L	pH = 13.5 ± 0.2 T = (88 ± 2) °C t = 2 h
	EDA 60 mL/L	
	KOH 26.5 g/L	
	NaBH ₄ 120 g/L	
	NaOH 263 g/L	
	PbWO ₄ 2.6 g/L	
	EDTA 13 g/L	
	Na ₂ WO ₄ 2H ₂ O 40 g/L	

A 2.6 mL reducing solution and a 2.6 mL stabilizing solution were added to the heated bath every 30 min during the coating procedure. A scanning electron microscope (SEM) was used to obtain the surface morphology and the cross-section of the Ni-B-W layer. A microhardness tester with a Vickers indenter load of 100 g and an indentation time of 20 s was used. The dry sliding wear performances of the selected coatings were evaluated in atmospheric conditions using a ball-on-flat

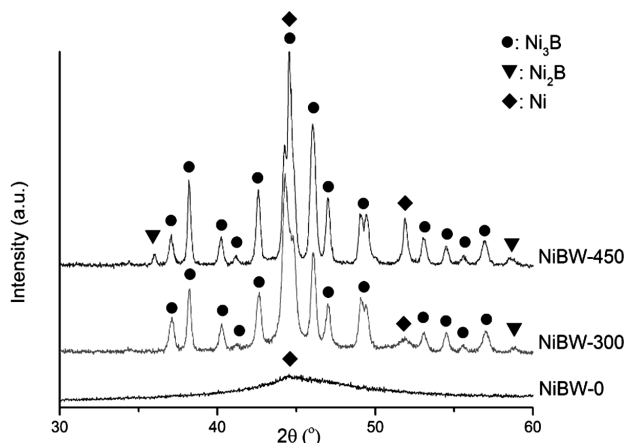


Figure 1: XRD pattern of the Ni-B-W coating

Slika 1: XRD-posnetek nanosa Ni-B-W

wear tester. The wear tests were carried out by applying a normal load of 5 N with a diameter 6 mm aluminum oxide (Al₂O₃) ball. The stroke and sliding speed of the balls on the coatings were 5 mm and 10 mm/s. To evaluate the wear mechanisms, wear tracks were studied using light microscopy, SEM and energy-dispersive spectrometry (EDS). To evaluate the corrosion resistance and the possible passivation behavior of the samples, immersion tests in different media were carried out.

3 RESULTS AND DISCUSSION

The chemical composition of the coating was analysed using EDS. The amount of tungsten in the coating was in mass fraction 1.1 %. The XRD patterns of the Ni-B-W coatings on a steel substrate in the as-plated and heat-treated (300 °C and 450 °C) conditions are analyzed in **Figure 1**. For the as-deposited condition, the coating was an amorphous phase. At 300 °C, crystallization started to occur. After the examination, the existence of Ni₃B peaks after the heat treatment at 450 °C proved the crystallization of the Ni-B-W layer.

The surface morphology of the Ni-B-W coating (**Figure 2a**) after heat treatment shows the formation of the developed crystallites.

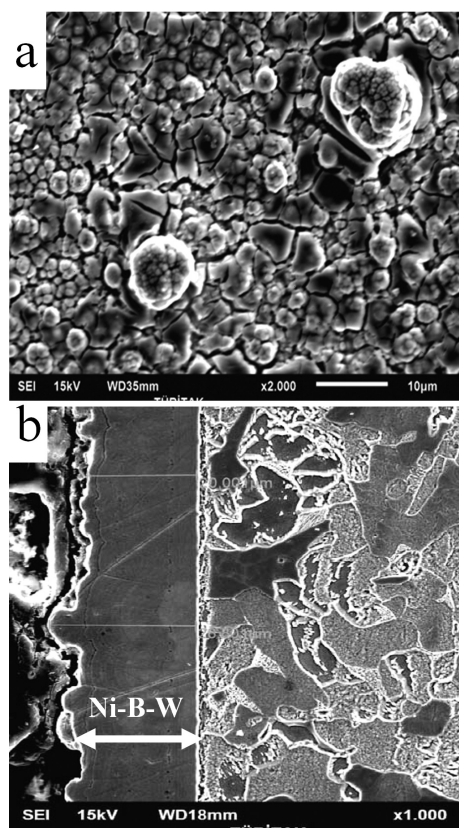


Figure 2: a) Surface morphology of heat-treated Ni-B-W coating and b) the cross-section morphology of the Ni-B-W coating detected by SEM

Slika 2: a) Morfologija površine toplotno obdelanega nanosa Ni-B-W in b) morfologija prereza nanosa Ni-B-W (SEM)

The spherical nodules, which can be seen in **Figure 2a**, are formed because of the precipitation of crystalline nickel and nickel borides (Ni₃B) in the coatings. From the cross-section morphology of the as-plated Ni-B-W coatings detected by SEM it is clear that the coating is uniform and is closely connected to the substrate, indicating good adhesion to the substrate. The thickness of the coating is 28 μm.

The microhardness of the Ni-B and Ni-B-W coatings after different heat-treatment temperatures are given in **Table 2**. The microhardness of the coatings increased with an increase of the heat-treatment temperature. This is due to the formation of micro-grains and a hard nickel boride phase (Ni₃B) in the Ni-B-W coatings, which was confirmed by the XRD measurements. The Ni-B coating reached its maximum hardness after the heat treatment at 350 °C, with 1131 VHN, and the Ni-B-W coating at 400 °C, with 1278 VHN.

Table 2: Micro-Vickers hardness of Ni-B and Ni-B-W coatings after different heat-treatment temperatures

Tabela 2: Trdota po mikrovikersu nanosu Ni-B in Ni-B-W po toplotni obdelavi pri različnih temperaturah

Temperature (°C)	Ni-B	Ni-B-W
300	979	995
350	1131	1147
400	1109	1278
450	987	1247
500	599	1116

The evaluation of the friction coefficients and the wear resistance of the steel, as-plated and heat-treated Ni-B-W coatings, are presented in **Table 3**. It is clear that applying the heat treatment increases slightly the friction coefficient. The results of the wear tests on different electroless coatings were analyzed using a profilometer, by measuring the wear track area after 100 m of sliding distance (**Table 3**).

Table 3: Coefficient of friction, wear track area of as-plated and heat-treated Ni-B-W coatings

Tabela 3: Koeficient trenja, velikost področja s sledovi obrabe pri nanosenem in toplotno obdelanem nanosu Ni-B-W

Annealing temp.	Fric. coeff.	Wear track area (μm ²)	Rel. wear resist.
Steel	0.48	859	1.00
As-plated	0.53	231.2	3.71
350 °C	0.62	134.3	6.39
400 °C	0.54	90.1	9.53
450 °C	0.54	399.5	2.15
550 °C	0.58	670.8	1.28

The specific wear rates of all the coatings indicate a better wear resistance than the steel. Although the as-deposited coatings show the lowest value of friction coefficient, the wear rate of the as-deposited sample is higher than the steel. The best wear resistance was achieved for the samples annealed at 400 °C. This is

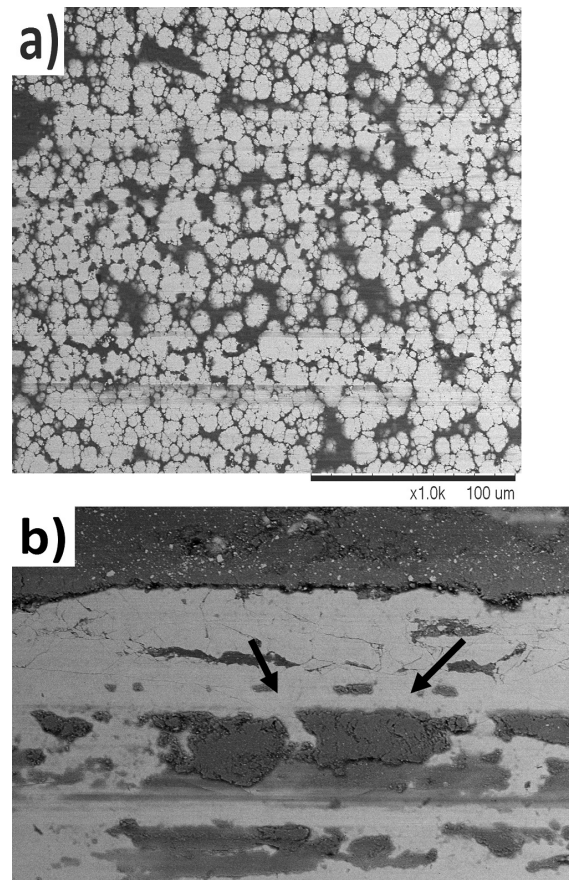


Figure 3: Wear tracks after the wear tests on the Ni-B-W coatings annealed at: a) 400 °C, b) 550 °C

Slika 3: Sledovi obrabe po preizkusu obrabe pri nanosu Ni-B-W po žarjenju na: a) 450 °C in b) 550 °C

because of the maximum hardness of the coatings achieved by heating at this temperature. When heated beyond this temperature, the specific wear resistance decreased due to the softening of the coatings by grain coarsening. The EDS analyses of the wear tracks on the coated samples show that the wear-track depth does not reach the substrate.

To understand the wear mechanism of the different coatings, wear-track patterns produced by the Al₂O₃ ball were studied (**Figure 3**).

The wear tracks of the as-plated and the coating annealed at 400 °C show a similarity. In both coatings, grooves along the sliding direction are observed. Also, high plasticity is detected, indicating micro-cutting, which is a typical ductile failure mechanism. No pits are detected. Therefore, it can be concluded that an abrasive wear mechanism is dominant. A network of cracks and shearing marks are observed for the coatings annealed at 450 °C (**Figure 3b**) and 550 °C. For a detailed investigation of the wear mechanism, an EDS analysis was carried out on the wear tracks to detect aluminum, which would originate from the Al₂O₃ friction ball, indicating the presence of adhesive wear. The EDS analysis indicates that in the case of the as-plated and 400 °C

annealed coatings, the layers are dominated by nickel and contain aluminum of only 0.8 % in terms of weight. In the annealed coatings at 450 °C and 550 °C, the amount of aluminum increased slightly (to 1.7 % Al). This indicates that with the annealed coatings at 450 °C and above, the adhesive wear mechanism is also active in addition to the abrasive wear mechanism. Another important factor is the effect of tungsten on the wear mechanism. As mentioned before, by annealing the coating beyond 400 °C, a phase transformation from an amorphous to a crystalline structure is detected. With the formation of the crystalline structure, grains start to occur, resulting in the formation of grain boundaries. These boundaries act as diffusion channels for the tungsten to move from the inside to the coating surface, causing the formation of a dense and brittle tungsten oxide film on the surface. This brittle tungsten oxide film is also an additional reason for the formation of a network of cracks after the wear tests for the coatings annealed at 450 °C and above.

For analyzing the corrosion resistance of the coatings, immersion tests were carried out. Steel, Ni-B and Ni-B-W coatings were immersed in 10 % HCl and 5 % H₂SO₄ acid solutions for 7 d and the weight loss was measured each day (**Table 4**).

Table 4: Weight loss of steel and as-plated Ni-B and Ni-B-W coatings in different acids, mg

Tabela 4: Zmanjšanje mase jekla, nanosenega Ni-B in nanosa Ni-B-W v različnih kislinah, mg

Day	Steel		Ni-B		Ni-B-W	
	HCl	H ₂ SO ₄	HCl	H ₂ SO ₄	HCl	H ₂ SO ₄
1	11.1	390.6	0.1	12.9	17.8	15.4
2	14.2	791.4	1.2	76.7	19.7	21.9
3	18.1	1201.5	4.6	209.1	36.0	30.6
4	23.7	1564.3	9.6	472.4	56.9	58.3
5	26.6	1890.5	13.8	729.8	92.7	102.4
6	35.7	2219.5	14.7	1049.6	145.5	112.5
7	40.8	2357.5	26.5	1460.0	219.1	241.4

The corrosion rate of the as-plated Ni-B coatings in both the HCl and H₂SO₄ solutions is lower compared to the steel. The corrosion rate of the Ni-B-W coating in HCl solutions is the highest; however, the corrosion rate in the H₂SO₄ solution is the lowest. Therefore, it can be concluded that Ni-B-W coatings can be used in a H₂SO₄ environment.

4 CONCLUSION

Ni-B and Ni-B-W coatings were prepared on steel by electroless deposition using dual baths. The Ni-B-W coatings are amorphous in their as-plated condition, but after a heat treatment at 450 °C for 1 h, the Ni-B-W coatings crystallize and produce nickel and nickel borides. SEM of the cross-section view of the coatings show that the coatings are uniform and the compatibility is good. The hardness and specific wear resistance of the Ni-B-W coating increased with the heat treatment and reached maximum values at 400 °C. Above 400 °C, the hardness and wear resistance decreased due to grain coarsening. After analyses of the wear profiles it was concluded that ductile failure occurred in the coatings up to 400 °C and that abrasive wear is the dominant wear mechanism. With coatings at 450 °C and above, surface cracks are determined and the adhesive wear mechanism is also active in addition to the abrasive wear mechanism. The formation of a tungsten oxide layer due to the crystallization was also a reason for the formation of network cracks. The results of the immersion test in acid solutions show that a Ni-B-W coating could provide electrochemical protection in a H₂SO₄ environment. It can be concluded that electroless Ni-B-W coatings will be a useful replacement for Ni-B coatings.

5 REFERENCES

- ¹ B. Oraon, G. Mujamdar, B. Ghosh, *Materials and Design*, 29 (2008), 1412–1418
- ² A. Contreras, C. Leon, O. Jimenez, E. Sosa, R. Perez, *Applied Surface Science*, 253 (2006) 2, 592–599
- ³ T. Saito, E. Sato, M. Matsuoka, C. Iwakura, *J. Of Applied Electrochemistry*, 28 (1998), 559–563
- ⁴ Y. F. Shen, W. Y. Xue, Z. Y. Liu, L. Zuo, *Surface & Coating Tech.*, 205 (2010), 632–640
- ⁵ F. Bulbul, *Met. Mater. Int.*, 26 (2011), 67–75
- ⁶ K. H. Lee, D. Chang, S. C. Kwon, *Electrochimica*, 50 (2005), 4538–4543
- ⁷ I. Baskaran, R. Kumar, T. S. N. Narayanan, A. Stephen, *Surface & Coating Tech.*, 200 (2006), 6888–6894
- ⁸ K. Krishnaveni, T. S. N. Narayanan, S. K. Seshadri, *Surface & Coating Tech.*, 190 (2005), 115–121
- ⁹ A. B. Drovosekov, M. V. Ivanov, V. M. Krutskikh, E. N. Lubnin, Y. M. Polukarov, *Protection of metals*, 41 (2005), 55–62
- ¹⁰ Z. Y. Jin, P. Li, Z. Zheng, D. Xiao, *Materials and Corrosion*, 62 (2011), 1–6
- ¹¹ T. S. N. Narayanan, A. Stephan, S. Guruskanthan, *Surface & Coating Tech.*, 179 (2004), 179–185
- ¹² R. A. Yildiz, A. Goksenli, B. Yüksel, F. Muhaffel, A. Aydeniz, *Adv. Materials Res.*, 651 (2013), 263–268

PHYSICAL AND NUMERICAL MODELLING OF A NON-STATIONARY STEEL FLOW THROUGH A SUBENTRY SHROUD WITH AN INNER METERING NOZZLE

FIZIKALNO IN NUMERIČNO MODELIRANJE NESTACIONARNEGA TOKA JEKLA SKOZI POTOPLJEN IZLIVEK Z NOTRANJO ŠOBO

Karel Michalek¹, Markéta Tkadlečková¹, Karel Gryc¹, Jiří Cupek²,
Michal Macura³

¹VŠB-Technical University of Ostrava, Faculty of Metallurgy and Materials Engineering, Department of Metallurgy and Foundry and Regional Materials Science and Technology Centre, Ostrava, Czech Republic

²Třinecké Železářny, Inc., Třinec, Czech Republic

³Vesuvius Česká republika, a.s., Třinec, Czech Republic
karel.michalek@vsb.cz

Prejem rokopisa – received: 2013-04-02; sprejem za objavo – accepted for publication: 2013-05-23

The paper presents new knowledge about physical and numerical modelling of a non-stationary steel flow into a mould through a subentry shroud with an inner, pressed metering nozzle. The physical and numerical modelling was realized under the conditions of the Department of Metallurgy and Foundry at VSB-Technical University of Ostrava. A special type of the subentry shroud is used during continuous casting of steel in Třinecké železářny, a.s. During continuous casting of steel, two unfavourable phenomena were observed. In the first case, it was not possible to increase the casting speed, though the diameter of the metering nozzle was extended. In the second case, a fluctuation of the casting speed among individual casting strands was detected. These two problems did not allow an improvement of the performance of the casting machine. Therefore, the physical and numerical modelling was performed. Attention was focused on the verification of the effect of the inner diameter of the nozzle body and internal diameter of the metering nozzle on the resulting volume flow rates. Four diameters of the metering nozzle – (16; 17; 17.5; 18) mm – were tested. The physical modelling was done on a 1 : 1 model constructed from Plexiglas. The numerical modelling was realized in the ANSYS FLUENT software. On the basis of the results of the modelling study and in cooperation with the VESUVIUS company, a new type of the profile of the subentry shroud with a metering nozzle was designed. The first experimental results in the steel plant led to an increase in the productivity of the continuous-casting machine.

Keywords: steel, continuous-casting machine, subentry shroud, metering nozzle, physical and numerical modelling

Članek predstavlja novo znanje o fizikalnem in numeričnem modeliranju nestacionarnega toka jekla v kokilo skozi potopljen izlivek z notranjo šobo. Fizikalno in numerično modeliranje je bilo izvršeno v Oddelku za metalurgijo in livarstvo na VSB Tehniški univerzi, Ostrava. V Třinecké železářny, a. s., se uporabljajo posebne izvedbe potopljenih izlivkov med kontinuirnim ulivanjem jekla. Pri tem sta bila opažena dva neželena pojava. Pri prvem ni bilo mogoče povečati hitrosti litja, čeprav je bil povečan premer notranjega izlivka, pri drugem pa je bilo opaženo spreminjanje hitrosti litja med posameznimi žilami. Ta dva pojava nista omogočila izboljšanja zmogljivosti livne naprave. Zato je bilo izvršeno fizikalno in numerično modeliranje. Pozornost je bila usmerjena na preverjanje vpliva notranjega premera telesa izlivka in notranjega premera izlivne šobe na stopnje pretoka. Preizkušeni so bili štirje premeri (16; 17; 17,5 in 18) mm notranjega izlivka. Fizikalni model je bil izdelan na modelu 1 : 1, izdelanem iz pleksi stekla. Numerični model je bil izdelan s programsko opremo ANSYS FLUENT. Na osnovi rezultatov in s sodelovanjem podjetja VESUVIUS je bila konstruirana nova vrsta potopnega izlivka z notranjo izlivno šobo. Prvi preizkusi v jeklarni so omogočili povečanje produktivnosti naprave za kontinuirno ulivanje.

Ključne besede: jeklo, naprava za kontinuirno ulivanje, potopni izlivek, izlivna šoba, fizikalno in numerično modeliranje

1 INTRODUCTION

A special type of the subentry shroud with an inner, pressed metering nozzle is used during continuous casting of steel on the CCM No.2 in Třinecké železářny, a.s. (TŽ, a.s.). A metering nozzle serves here as a stabilizing element adjusting the volume flow rate of the steel. However, while using this type of the nozzle two adverse effects were observed:

- 1) It was not possible to increase the casting speed when increasing the diameter of the metering nozzle.
- 2) Fluctuations of the casting speed in individual casting streams were detected.

Both of these factors eliminated the possibility of increasing the performance of the entire casting machine.

Due to a long-term mutual cooperation, the TŽ, a. s., team contacted the research team at the Department of Metallurgy and Foundry at VSB-TU Ostrava, which has extensive experience in the optimization of metallurgical processes using modelling methods.¹⁻⁴ The sophisticated methodology of the experiments and a well-selected system of physical and numerical modelling results, transformed into the operational experience with verified use of the similarity theory, provide an opportunity to address the other fundamental technological problems.⁵⁻⁷ Physical and numerical modelling was used to study the

behaviour of a steel flow through an inner metering nozzle. Its goal was to assess the behaviour of the steel flow through the nozzle, analyse its causes and propose solutions in the form of a new geometry of the inner, pressed metering nozzle of the subentry shroud. The parameters such as the influences of the inner diameter of the body of the subentry shroud and the inner diameter of the metering nozzle on the resulting volume flow rates at a constant hydrostatic (ferrostatic) height above the subentry shroud (a constant steel height in the tundish) were tested. The efforts were aimed at finding the limiting factor that restricts the increase in the rate of the steel flow through the subentry shroud even when the diameter of the inner metering nozzle is increased.

2 ANALYSIS OF THE PROBLEM

Fluctuations of the casting speed during the casting of steel on the CCM No. 2, equipped with the shrouds with inner metering nozzles, are perfectly evident from **Figures 1 and 2**. **Figure 1** shows the behaviour of the casting speed on individual casting strands (CS) during a sequence of heats cast using the subentry shrouds equipped with inner metering nozzles. See **Figure 2** for an example of the behaviour of the casting speed at a constant steel weight in the tundish. The following was determined:

- When using the subentry shrouds equipped with metering nozzles, the variability of the casting speed is much greater than when regulating it with the stopper rods only.
- The casting speed (or the steel flow through the nozzle) is slightly dependent on the weight of the steel in the tundish (or on the steel height in the tundish) – **Figure 1**.
- Despite the nearly constant weight of the steel in the tundish, the casting speed increased in some cases – **Figure 2**.

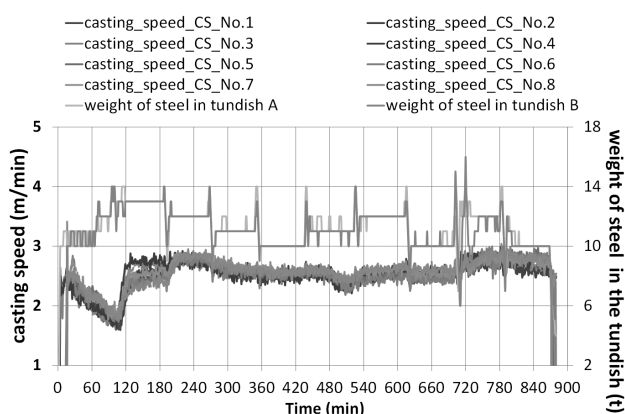


Figure 1: Example of the behaviour of the casting speed on individual casting strands during a sequence of heats cast using subentry nozzles equipped with metering nozzles

Slika 1: Primer vedenja hitrosti ulivanja na posamezni livni žili med sekvenčnim ulivanjem talin z uporabo potopljenega izlivka, opremljenega z notranjo izlivno šobo

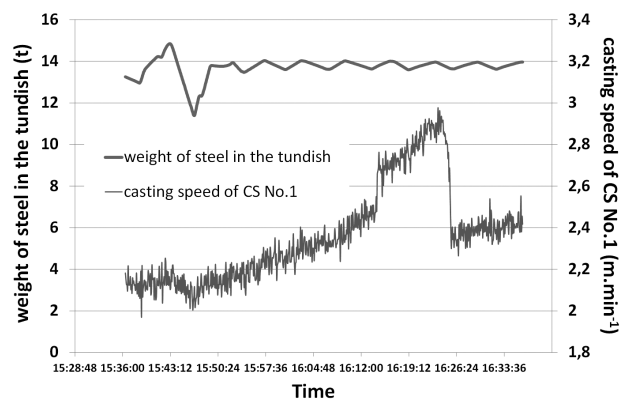


Figure 2: Example of the behaviour of the casting speed on casting strand No.1 at a constant weight of the steel in the tundish

Slika 2: Primer vedenja hitrosti litja na livni napravi št. 1 pri konstantni masi jekla v vmesni ponovci

- Fluctuations in the volume flow rate indicate the presence of a non-stationary flow in the nozzle.
- An inability to further increase the casting speed while increasing the metering-nozzle diameter shows the existence of an undetermined limiting factor affecting the flow, which limits the volume flow of the steel through the subentry shroud.

On the basis of the calculation of the volume flow rate for the casting speed of 2.5 m min^{-1} and the cast dimensions of $150 \text{ mm} \times 150 \text{ mm}$, it was found that:

- The rate of the volume flow of the liquid steel through the nozzle with the inner diameter of 20 mm is approximately 60 L min^{-1} .
- The calculated Re criterion reaches approximately 89,000.
- The value noted above is specified for circular cross-sections far beyond the critical value of the transition from the laminar to the turbulent flow. In other words, we can expect that, within the nozzle, the steel flow is of a strong turbulent character, which, of course, bears the risk of large-scale non-stationarities of the steel flow, especially if the diameter of the nozzle is, at some spot/location, made even narrower (in the area of the inner, pressed metering nozzle).
- It is likely that the hydraulic resistance of the subentry shroud below the metering nozzle was so high that an increase in the metering-nozzle diameter could no longer allow a further increase in the steel flow rate (the casting speed).

To confirm these partial, theoretical conclusions, the researchers decided to assess the nature of the steel flow using physical and numerical modelling.

3 PHYSICAL MODELLING

Physical modelling was performed with a nozzle constructed from Plexiglas on the geometric scale of $1 : 1$ (**Figure 3a**). The following diameters of the metering

nozzles were tested: (16; 17; 17.5 and 18) mm, having the outlets (the internal diameters of the nozzles below the metering nozzles) of 20 mm and 24 mm, hereafter referred to as nozzle A and nozzle B. The submersion of a nozzle below the surface of the steel in the mould was in all the cases identical – 120 mm. This value corresponds to the central part of the bottom zirconium protection.

Given that when applying the geometric scale of 1 : 1, both identity criteria, Re and Fr , are maintained, we can assume there is a significant agreement between the phenomena occurring in the flow in the actual nozzle and in its model in terms of the character of the flow, swirl and stationarity (stability). It is evident that the thermal processes that may affect the steel flow cannot be detected with this type of modelling. In particular, it is the influence of the temperature on the steel viscosity, erosion and corrosion of the material of a nozzle (that is contingent upon the flow rate of steel and its temperature) and the associated change in the internal profile of the nozzle, which may be essential for the stability of the flow and its fluctuations.

4 NUMERICAL MODELLING

Physical modelling was also complemented with numerical modelling of the steel-flow behaviour in the original nozzle with the metering nozzles having the diameters of (17; 17.5 and 18) mm and with an outlet of only 20 mm in diameter. Numerical modelling of the steel flow through a subentry shroud with inner metering nozzles was performed using the simulation package ANSYS WORKBENCH, providing a 3D modeller called DesignModeler, a generator of a computational mesh and the CFD software FLUENT. The nozzle geometry was

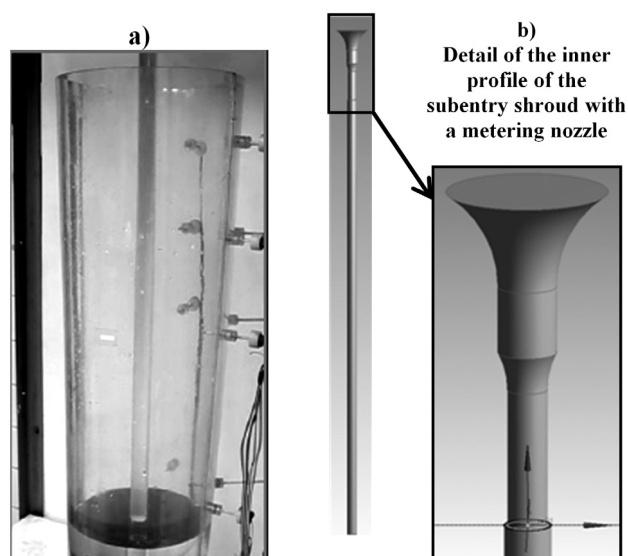


Figure 3: a) Physical model, b) 3D CAD model of the metering nozzle of the subentry shroud

Slika 3: a) Fizikalni model, b) 3D CAD model notranje izlivne šobe potopljenega izlivka

modelled on the 1 : 1 scale. The 3D CAD geometry of the nozzle, including a detailed view of the area of the metering nozzle is shown in **Figure 3b**.

The volume mesh was automatically generated for the nozzle. The entrance into the nozzle was defined as the PRESSURE INLET and the exit from the nozzle was defined as the PRESSURE OUTLET. These boundary conditions allow a definition of the input parameters when the input speed is not known exactly, but the pressure indicated by the height of the steel in the tundish is known. The total pressure defined the pressure-input condition, which is the sum of the hydrostatic and dynamic pressure.⁸

The hydrostatic pressure is defined by the product of the steel height in the tundish with the steel density and gravitational acceleration. The dynamic pressure is defined as the square of the flow speed multiplied by the density of steel and one-half.⁸

The pressure outlet was defined in a similar way to the inlet pressure. However, only the hydrostatic/ferrostatic output pressure, the turbulence intensity and the hydraulic diameter need to be specified. The pressure outlet was the same for all simulated variants.

The steel flow was simulated to be incompressible and turbulent with the turbulence-model $k-\epsilon$ standard having a standard wall function. The gravity of 9.81 m s^{-2} was considered in the z axis. In the simulation, the operating conditions and material properties listed in **Table 1** were defined.

Table 1: Operating conditions and material properties of the steel at the temperature of 1843 K

Tabela 1: Delovne razmere in materialne lastnosti jekla pri temperaturi 1843 K

Condition	Value	Unit
Operating pressure	101325	Pa
Operating temperature	1843	K
Operating density	7030	kg m^{-3}
Heat capacity	750	$\text{J kg}^{-1} \text{K}^{-1}$
Heat conductivity	41	$\text{W m}^{-1} \text{K}^{-1}$
Viscosity	0.006995	Pa s

The study focused on the effect of the inner geometry of the nozzle on the rate of the flow through the nozzle. Attention was also focused on the character of the velocity and pressure field inside the nozzle. The results were also complemented with the distribution of the shear stress on the walls of the nozzle, allowing a prediction of the risk of erosion of the nozzle material.

5 DISCUSSION OF RESULTS

5.1 Effect of the metering-nozzle diameter and nozzle-outlet diameter on volume flow rates

The effect of the diameter of the metering nozzle and the diameter of the nozzle outlet on the achieved maximum volume flow rates at a constant hydrostatic (ferro-

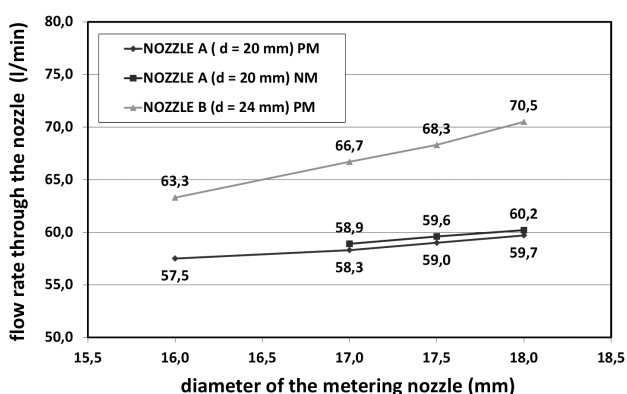


Figure 4: Effect of the metering-nozzle diameter and nozzle-outlet diameter on the volume flow through the subentry shroud for a 120 mm submersion in the mould

Slika 4: Vpliv premera notranje izlivne šobe in izstopni premer izlivka na volumenski tok skozi potopljen izlivek pri potopitvi 120 mm v kokilo

static) height above the nozzle (the constant steel height in the tundish) obtained with physical (PM) and numerical modelling (NM) is shown in **Figure 4**.

The main findings that can be defined from the graph above are as follows:

- An increase in the metering-nozzle diameter results in the increases in the volume flow rates for both types of nozzle, A and B (with the outlet diameters of 20 mm and 24 mm).
- The nozzle with the outlet diameter of 20 mm shows an increase in the volume flow rate of only 1.4 L min^{-1} (or 1.3 L min^{-1} according to the results of the numerical simulation) when switching from the metering-nozzle diameter 17 mm to 18 mm. This increase corresponds to a very small increase in the casting speed, i.e., 0.06 m min^{-1} .
- The nozzle with an outlet diameter of 24 mm shows a more noticeable increase in the volume flow rate, i.e., 3.8 L min^{-1} , representing an increase in the casting speed by 0.16 m min^{-1} .
- A very good agreement of the results of the physical and numerical modelling for the nozzle outlet of 20 mm is evident.

To sum up the results stated above, we can conclude that when we use the nozzle with a 20-mm outlet diameter, the flow rate can be increased only very slightly by simply increasing the diameter of the metering nozzle. This is due to a great hydraulic resistance of the nozzle located below the metering nozzle, which prevents a bigger increase in the volume flow rate. An increase in the flow rate can only be achieved by increasing the input ferrostatic pressure (the height of the steel in the tundish), but only to a very limited extent. A more significant increase in the volume flow rate and, thus, the casting speed can be expected after increasing the diameter of the nozzle below the metering nozzle from 20 mm to 24 mm, when the diameter of the

metering nozzle has already started to perform the actual role of the flow-rate restrictor.

5.2 Fluctuation of the rate of the volume flow through the subentry shroud/nozzle

The fluctuation of the flow rate (and, in practice, of the casting speed) is an interesting phenomenon that may be associated with the changes in ferrostatic conditions, especially with a change in the flow character in the nozzle itself.

A change in ferrostatic conditions may be related to a change in the steel weight in the tundish, i.e., with a change in the height of the steel in the tundish. As the flow rate is not only a function of the height of the steel in the tundish, but, more accurately, a function of the distance between the height of steel in the tundish and the height of steel in the mould, it is also necessary to take into account the change in the elevation position of the tundish, which is sometimes made to allow an even wear of the outer surface of the nozzle. A shift in the steel-level distances by 10 cm will change the volume flow rate of the model by 1.33 L min^{-1} and, in the operating conditions, it will change the casting speed by 0.055 m min^{-1} .

However, a far more significant factor is the character of the steel flow rate in the nozzle. **Figure 5** shows the flow character displayed with the velocity vectors in the cross-section of a nozzle. **Figure 5** shows that an increase in the metering-nozzle diameter (17 mm \rightarrow 17.5 mm \rightarrow 18 mm) leads to a slight decrease in the maximum velocity in the area of the metering nozzle, while the area of the medium speed of 3.2 m s^{-1} slightly increases below the metering nozzle and in the nozzle-outlet area. On the other hand, the walls of the nozzle show a slowdown of the casting strand due to the presence of the so-called laminar sublayer⁹, which is a typical phenomenon in a highly turbulent flow of a liquid in the pipelines. The velocity of the steel flow is, thus, not the same in the entire section of the nozzle, as shown in the detailed views of the distribution of the velocity vectors at the nozzle outlets.

The velocity distribution also determines the distribution of the pressure of the flowing steel in a nozzle. As confirmed with the detailed views of the pressure profiles at the metering nozzles (**Figure 6**) an enlarged diameter of a metering nozzle results in a reduction of the pressure (or, as noted above, of the maximum speed). On the other hand, below the metering nozzles, as shown by the details in **Figure 6**, the bigger the metering-nozzle diameter, resulting in a slight increase in the volume flow rate, the bigger is the area with the maximum pressure field near the nozzle outlet. However, if one looks closely, an increase in the area with the maximum pressure field is very subtle, which could be related, as stated above, to a large hydraulic resistance, which also prevents a higher increase in the volume flow rate.

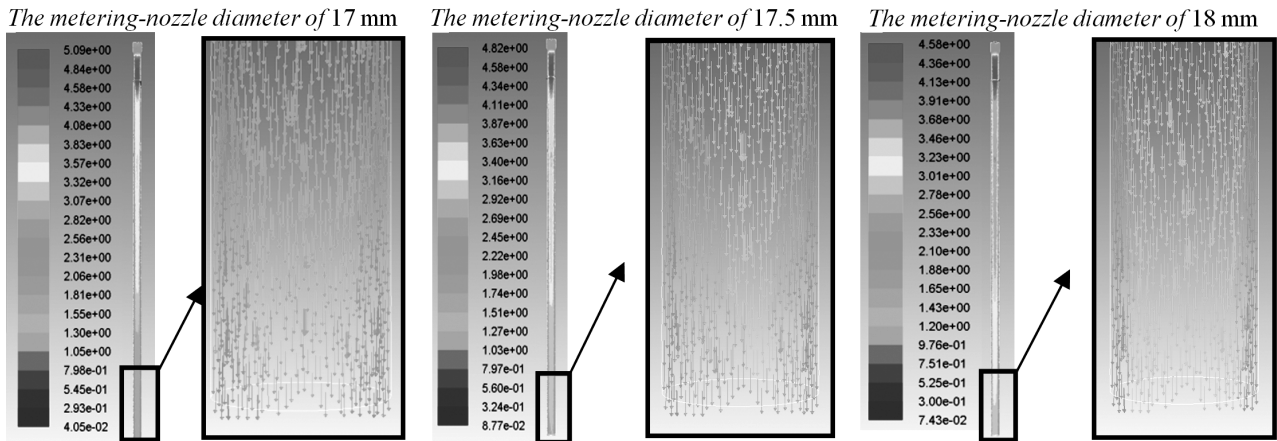


Figure 5: Steel-flow characteristics in the nozzles displayed with the velocity vectors (m s^{-1}) in the cross-sections of the nozzles with detailed views at the nozzle outlets for individual nozzles with the metering-nozzle diameters

Slika 5: Značilnosti toka jekla v šobi, prikazane z vektorji hitrosti (m s^{-1}) na prerezu šobe z detajlnim pogledom pri izstopu iz šobe za posamezne šobe s premeri notranjih šob

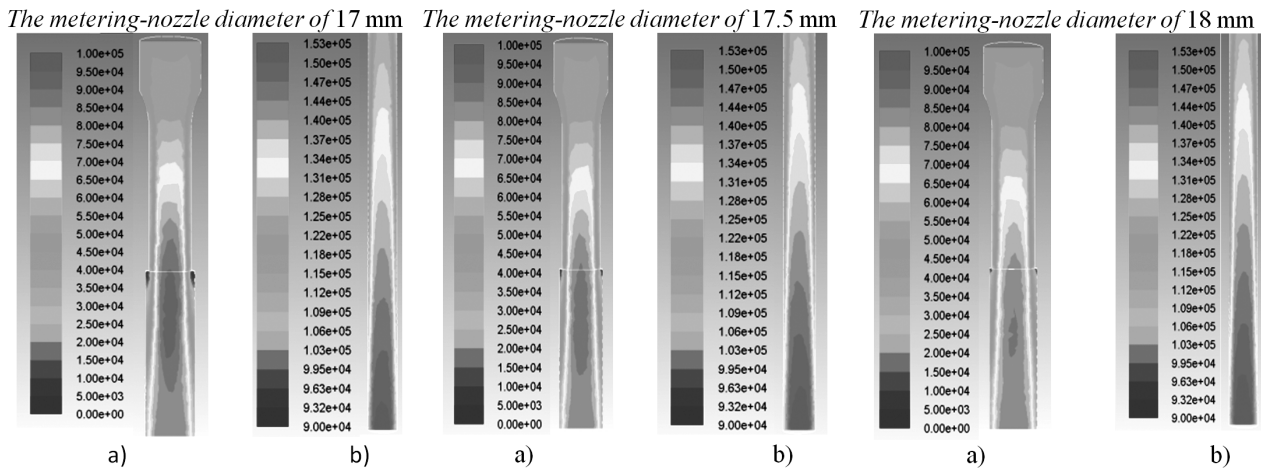


Figure 6: Detailed views of the pressure profiles (Pa): a) in the metering nozzles and b) in the areas of the nozzle outlets

Slika 6: Podroben prikaz profilov tlaka (Pa): a) v notranji izlivni šobi in b) na področju izstopa iz šobe

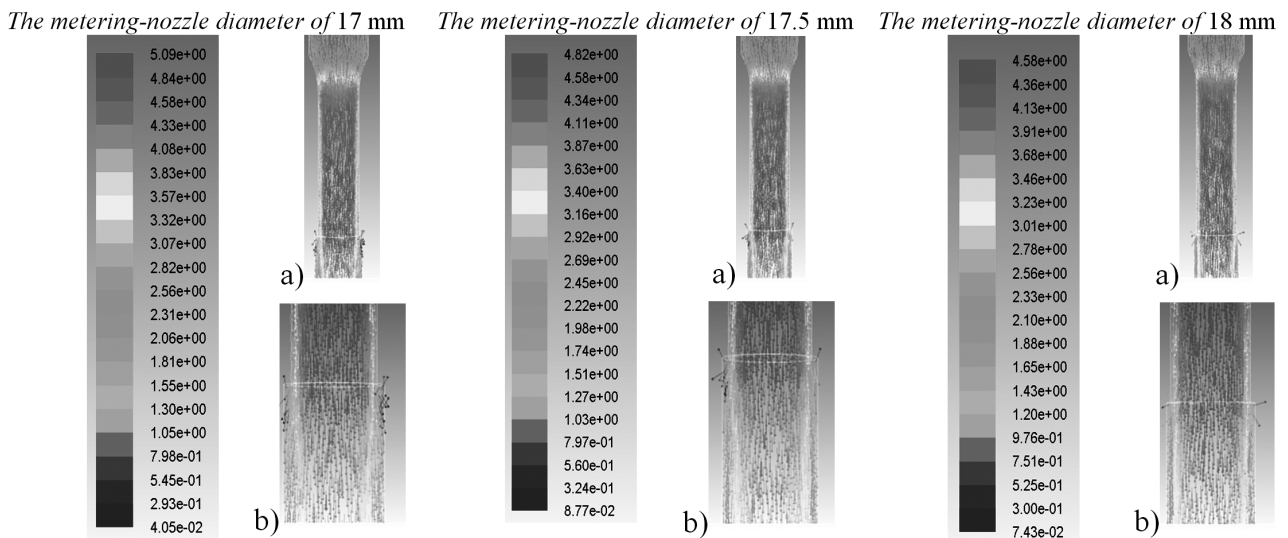


Figure 7: a) Character of the steel flows in the nozzles shown with the velocity vectors (m s^{-1}) at the cross-sections of the nozzles – in the metering nozzles and b) details just below the metering nozzles

Slika 7: a) Vedenje toka jekla v šobi, prikazano z vektorji hitrosti (m s^{-1}) na prerezu šobe – notranje šobe in b) detajl tik pod izlivno šobo

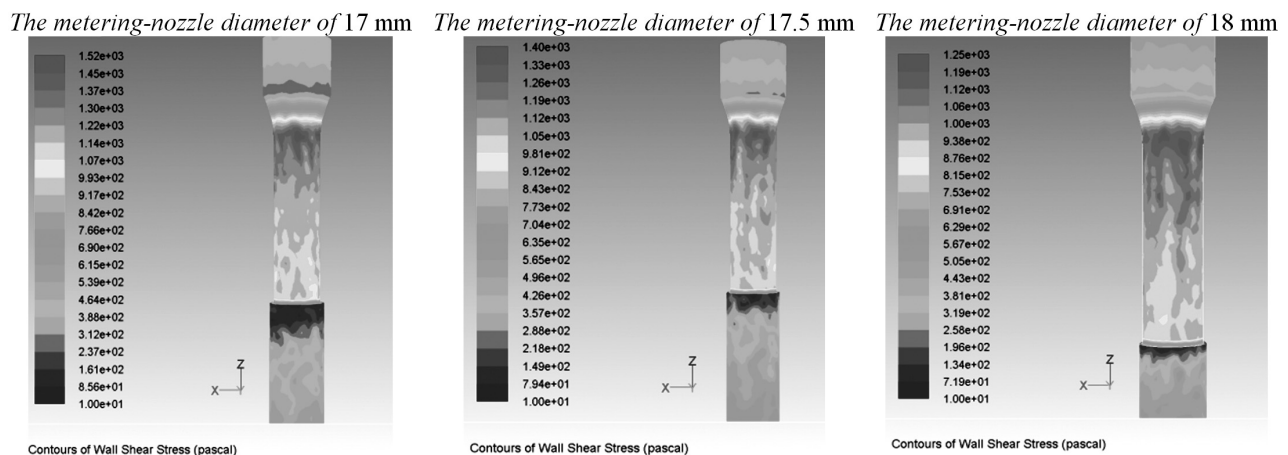


Figure 8: Distribution of the shear-stress profile (a risk of erosion) on the walls of the outlets for individual diameters of the metering nozzles
Slika 8: Razporeditev strižnih napetosti (rizik erozije) na stenah pri izhodu za posamezni premer notranjega izlivka

As explained above, the flow fluctuations may be caused by a high Re number of the steel flow in the nozzle. A particularly critical point can be considered to be the narrowing in the metering nozzle. See **Figure 7a** for a detailed view of the behaviour of the flow in the metering nozzle and see **Figure 7b** for the way of the velocity distribution just below the metering nozzle, where the nozzle is expanded to a diameter 20 mm. By observing the velocity vectors, a velocity profile can be noted, from which it is obvious that the strand is being strongly held back on the metering-nozzle walls. In the area of the burst expansion just below the metering nozzle, a "weak spot" is visible, where the velocity is minimum, and where the minimum contact of the nozzle walls with the flowing steel can be expected. An intense steel strand begins to flow around the wall approximately 3 cm below the metering-nozzle extension. This area may be, thus, prone to a greater erosion of the internal profile of the nozzle.

It is understandable that during the casting a profile may change (due to erosion, corrosion, fouling, etc.), which greatly and adversely affects the flow character and, thus, the stationarity of the flow fluctuations and the emergence of steel-flow fluctuations. A more significant impact of the metering-nozzle wear will more likely apply to a smaller diameter of the metering nozzle, as evidenced with the distribution of the shear stress on the nozzle walls in **Figure 8**. The size of the shear stress signals a danger of erosion. The most significant risk of erosion is at the inlet to the metering nozzle. In the area of the burst expansion below the metering nozzle, a "weak spot", as mentioned above, with a length of approximately 2 cm can be seen as well as the impact of the strand on the walls of the nozzle and, thus, there is a potential danger of a further significant erosion at a distance of approximately 3 cm below the metering nozzle. The shear-stress results confirmed the earlier finding that an increase in the diameter of the metering nozzle

influences the length of the "weak spot", which is reduced at the extension below the metering nozzle.

When designing the metering nozzles, the principles resulting from the design of the nozzles must be followed. In general, in the recommended design the angle of the leading edges at the narrowing should be less than 10° and, in the critical cases, it should be 5° . In other words, at the connection of the metering nozzle to the body of the nozzle there should be no sharp transition; neither should there be one at the end of the metering nozzle (the drainage edge).

These conclusions were also confirmed experimentally on the physical model. It was also found that in the case of a sharp transition at a metering nozzle, it was not possible to provide a stable flow rate; the fluctuations amounted to 10 % of the volume flow rate values.

6 DESIGN OF A NEW NOZZLE PROFILE

Based on the above results, a design of a new structure (the inner profile) of the subentry nozzle was created in cooperation with the engineers at TŽ, a. s., and the staff of the VESUVIUS company, which should provide a greater volume flow of the steel (and, thus, higher casting speeds) and also eliminate the pulsation.

In the new construction design of the nozzle (the C nozzle) the lower end of the metering nozzle was moved 510 mm away from the nozzle outlet and the inner diameter of the nozzle above the metering nozzle was enlarged to 30 mm. The inner diameter of the nozzle below the metering nozzle remained the same (20/22 mm), as well as the metering-nozzle profile with a 17.5 mm diameter. A comparison of the original and modified geometry is shown in **Figure 9**.

Prior to manufacturing an operational variant and mounting the nozzle for the first test, a verification of the impact of the diameters of the metering nozzles on the volume flow rates, as well as the occurrence of non-stationarity of the flow were carried out using



Figure 9: Comparison of the inner profiles of the original and new nozzles

Slika 9: Primerjava notranjega profila originalnega izlivka in novega izlivka

physical and numerical modelling. Physical modelling was performed using the same methodology with the nozzles on a geometric scale of 1 : 1, and with the interchangeable metering nozzles of the diameters of (16, 17, 17.5 and 18) mm. Numerical modelling was performed for the geometry of the new nozzle on the scale of 1 : 1 with only the metering nozzle of the 17.5 mm diameter. The exact same input and output parameters of the calculation were used in the simulations, including the final step of the calculation. **Figure 10** shows the effect of the diameter of the metering nozzle on the volume

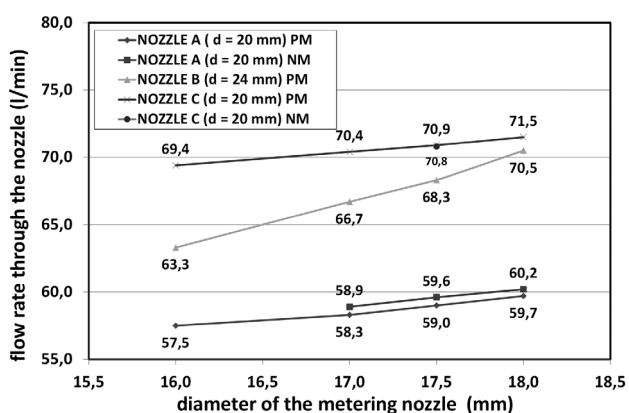


Figure 10: Effect of the metering-nozzle diameter on the rates of the volume flows through subentry nozzles A, B, C at a 120 mm submersion

Slika 10: Vpliv premera izlivka na hitrosti pretoka volumna skozi potopljeno šobo A, B, C pri potopitvi 120 mm

flow rates. To enable a comparison, the previously discussed dependences on the metering nozzle in the inlet part of a nozzle are also shown.

As evident from **Figure 10**, there was an increase in the flow rate for all the tested diameters of the metering nozzles at nozzle C during both physical and numerical modelling in comparison with nozzles A and B. It can be noted that the curve behaviour for nozzle C is shifted in relation to the curve of nozzle A by approximately 11 L min⁻¹, which is an increase by 18 % to 20 %. For the casting speed of 2.5 m min⁻¹ this would mean an increase to 2.9 m min⁻¹ or 3 m min⁻¹.

Similarly to nozzle A, a relatively low dependence of the volume flow rate on the diameter of the metering nozzle was registered in nozzle C. The cause may be the same: a poorly proportioned diameter of the nozzle below the metering nozzle. Increasing the diameter to approximately 25 mm would result in a greater incline of nozzle C and, thus, to a further increase in the flow through a subentry nozzle. These nozzles are significantly more sensitive to potential erosion in the metering nozzle.

Operational tests of the new subentry nozzle of type C resulted in an increase in the casting speed of the first casting sequence from 2.4 m min⁻¹ to 2.8 m min⁻¹, representing an increase by 17 %. The situation was similar with the second and third test sequences of the heats.

7 CONCLUSIONS

The current type of the subentry shroud equipped with metering nozzles used in the continuous casting of steel on the CCM No. 2 in Třinecké železářny, a.s., did not allow a performance improvement of the casting machine even if the diameter of the metering nozzle was increased. For this reason, physical and numerical modelling was conducted, the goal of which was to assess and justify the behaviour of the steel flow and suggest a possible solution. On the basis of theoretical calculations and performed physical and numerical modelling, the following was found:

An inability to increase the casting speeds by further increasing the diameters of the metering nozzles in the subentry nozzles is due to a too small diameter of the nozzle-A outlet (20/22 mm) and, in particular, due to its length (approximately 1000 mm). Both parameters increase the hydraulic resistance and limit a further increase in the volume flow rate of the steel.

Fluctuations in the volume flow rate (and, thus, the casting speed) may be related to the turbulent nature of the flow; a metering nozzle and its implementation can have a significant impact; for this reason it should not have sharp leading and output edges – it is recommended that an angle is up to 5° and, at the maximum, up to 10°.

On the basis of the knowledge obtained with the physical and numerical modelling, a new type of nozzle,

known as type-C nozzle, has been proposed. Here a shift of the lower end of the metering nozzle to a distance of 510 mm from the nozzle outlet, and an enlargement of the inner diameter of the nozzle above the metering nozzle to 30 mm were carried out.

Operational testing of the subentry nozzle led, during the first sequence, to an increase in the casting speed from 2.4 m min⁻¹ to 2.8 m min⁻¹, an increase by 17 %, and similar results were achieved during the second and third test sequences of the heats.

Acknowledgements

This paper could not have been realized without the financial support from Třinecké železářny, a. s., and close cooperation with Vesuvius Česká republika, a. s. Further acknowledgement is owed to the project No. CZ.1.05/2.1.00/01.0040 "Regional Materials Science and Technology Centre", within the frame of the operation programme "Research and Development for Innovations" financed from the Structural Funds and from the state budget of the Czech Republic.

8 REFERENCES

- ¹ K. Michalek, K. Gryc, M. Tkadlečková, D. Bocek, Model study of tundish steel intermixing and operational verification, *Archives of metallurgy and materials*, 57 (2012) 1, 291–296
- ² K. Michalek, M. Tkadlečková, K. Gryc, P. Klus, Z. Hudzieczek, V. Sikora, P. Štřasák, Optimization of argon blowing conditions for the steel homogenization in ladle by numerical modelling, *Proc. of the 20th Anniversary International Conference on Metallurgy and Materials, Metal 2011, Brno, 2011*, 143–149
- ³ K. Gryc, K. Michalek, M. Tkadlečková, Z. Hudzieczek, Physical Modelling of Flow Pattern in 5-strand Asymmetrical Tundish with Baffles, *Proc. of the 19th International Conference of Metallurgy and Materials, Metal 2010, Rožnov p. Radhoštěm, 2010*, 42–46
- ⁴ M. Tkadlečková, K. Michalek, K. Gryc, Z. Hudzieczek, J. Pindor, P. Štřasák, J. Morávka, Comparison of extent of the intermixed zone achieved under different boundary conditions of continuous billets casting, *Proc. of the 19th International Conference of Metallurgy and Materials, Metal 2010, Rožnov p. Radhoštěm, 2010*, 47–52
- ⁵ J. Stetina, L. Klimes, T. Mauder, F. Kavicka, Final-structure precondition of continuously cast billets, *Mater. Tehnol.*, 46 (2012) 2, 155–160
- ⁶ J. Stetina, F. Kavicka, The influence of the chemical composition of steel on the numerical simulation of a continuously cast slab, *Mater. Tehnol.*, 45 (2011) 4, 363–367
- ⁷ J. Pieprzyca, Z. Kudlinski, Determining transition zone size in continuous casting by the method of modelling, *Stahl und Eisen*, 124 (2004), 51–53
- ⁸ ANSYS FLUENT, Users Guide
- ⁹ M. Kozubková, Modelling of fluid flow, VŠB-Ostrava, Ostrava, 2008 (in Czech), www.338.vsb.cz/PDF/Kozubkova-Fluent.pdf

RESEARCH OF THERMAL PROCESSES FOR THE CONTINUOUS CASTING OF STEEL

RAZISKAVE TERMIČNIH DOGAJANJ PRI KONTINUIRNEM ULIVANJU JEKLA

**Marek Velicka, David Dittel, Rene Pyszko, Miroslav Prihoda, Miroslav Vaculik,
Pavel Fojtik, Jiri Burda**

VSB – Technical University of Ostrava, Faculty of Metallurgy and Materials Engineering, 17. listopadu 15, 708 33 Ostrava, Czech Republic
marek.velicka@vsb.cz

Prejem rokopisa – received: 2013-04-03; sprejem za objavo – accepted for publication: 2013-04-08

The article deals with the determination of the basic indicators of heat transfer in the continuous casting of steel, which can be described as an unsteady process with complicated boundary conditions for the solution. An analytical solution of this problem is practically impossible and, therefore, mathematical modelling is applied with a certain simplification of the real conditions and with a description of those criteria that influence the most the process of solidification and cooling. Using a simulation program and the knowledge of input parameters, it was possible to predict the distribution of the thermal field of a continuously cast blank in the course of its casting. Simulations also allowed us to deal with the issues of the inner structure, surface quality, mechanical properties of a continuously cast blank, metallurgical length, change in the thickness of a strand shell and over-heating of steel. Some results obtained with numerical simulations are documented for concrete examples.

Keywords: continuous casting of steel, modelling, heat transfer, shell, mould

Članek obravnava določanje osnovnih pokazateljev prenosa toplote pri kontinuirnem ulivanju jekla, ki se lahko opišejo kot nestabilen proces s kompliciranimi robnimi pogoji za rešitev. Analitska rešitev tega problema je praktično nemogoča, zato je bilo uporabljeno matematično modeliranje z nekaterimi poenostavitvami realnih pogojev in z opisom tistih meril, ki najbolj vplivajo na proces strjevanja in ohlajanja. S programom za simulacijo in poznanjem vhodnih parametrov je bilo mogoče predvideti razporeditev temperaturnega polja kontinuirno ulite gredice med njenim ulivanjem. Uporaba simulacije je omogočila opis notranje strukture, kvalitete površine, mehanskih lastnosti kontinuirno ulite gredice, metalurške dolžine, spreminjanja debeline strjene skorje in pregretja jekla. Nekateri rezultati, dobljeni z numerično simulacijo, so prikazani za konkretne primere.

Ključne besede: kontinuirno ulivanje jekla, modeliranje, prenos toplote, skorja, kokila

1 INTRODUCTION

Mathematical precise description of thermal processes during the continuous casting of steel is very difficult, since the process of cooling and solidification of a continuously cast blank is influenced by many factors.

For this reason it is necessary to find, with the help of mathematical and physical modelling, the criteria that have the biggest influence on the solidification and cooling of a continuously cast blank. Understanding the thermal processes taking place during the continuous casting of steel is of crucial importance because it enables a prediction of a formation of defects, an enhancement of the thermal processes during continuous casting, the optimum locations for cooling nozzles or a minimisation of breakout risks, etc.¹

It is evident, that it is impossible to optimise the process of continuous casting of steel only by modelling. A very close interaction with the results of experimental measurements is always necessary since these results introduce, into the system, characteristic features of a concrete continuous-casting machine. At present, it is possible to perform, with the use of sophisticated software, not only the thermal calculations but also the

calculations of stress conditions, and also to predict segregation during the continuous casting of steel. The finite-element method or finite-difference method are used most frequently as the calculation algorithm in this software.

This paper deals with the solution of thermal processes during the continuous casting of round steel blanks with a diameter of 410 mm, using the simulation software based on the explicit finite-element method.

2 THERMAL FIELD OF A CONTINUOUSLY CAST BLANK

The kinetics of an unsteady thermal field is described with the Fourier partial differential equation.² If we want to describe the thermal field of a moving, continuously cast blank, it is necessary to take into account, in the transverse direction, also the rate of casting, by transforming the classical Fourier equation to the Fourier-Kirchhoff equation:

$$\frac{\partial t}{\partial \tau} = a \cdot \nabla^2 t + \frac{q_v}{c_p \cdot \rho} \quad (1)$$

where $a/(m^2/s)$ is the temperature-conductivity coefficient, $\nabla^2/(m^{-2})$ is the Laplace's operator, $c_p/(J/kg K)$ is

the specific heat capacity, ρ /(kg/m³) is the density and q_v /(W/m³) is the inner heat source.

This equation can only be solved with the conditions of monovalency of the solution, which, in the classical concept, are divided into geometric, physical, surface and initial conditions. Physical conditions are generally created with the chemical composition of the cast steel, geometric conditions are created with the shape of the cast products, and the initial condition is closely linked to the temperature of the liquid steel in a tundish. Numerous researches concerning the continuous casting of steel³⁻⁶ combined with modelling physical models use the Neumann surface condition for the mould and the Fourier condition for the secondary and tertiary cooling.

3 SIMULATION MODELLING

For numerical modelling, the ProCAST program tool was used, which is based on the implicit finite element method. Alternatively, an original program code Tefis based on the explicit finite difference method, specially designed for numerical modelling of the continuously cast blank temperature field, was used. The program Tefis enables real-time simulations too. The second method requires compliance with a numeric stability condition, which describes mutual dependence between fineness of the calculation mesh and calculation time step.

Fluid Velocity (m/min)

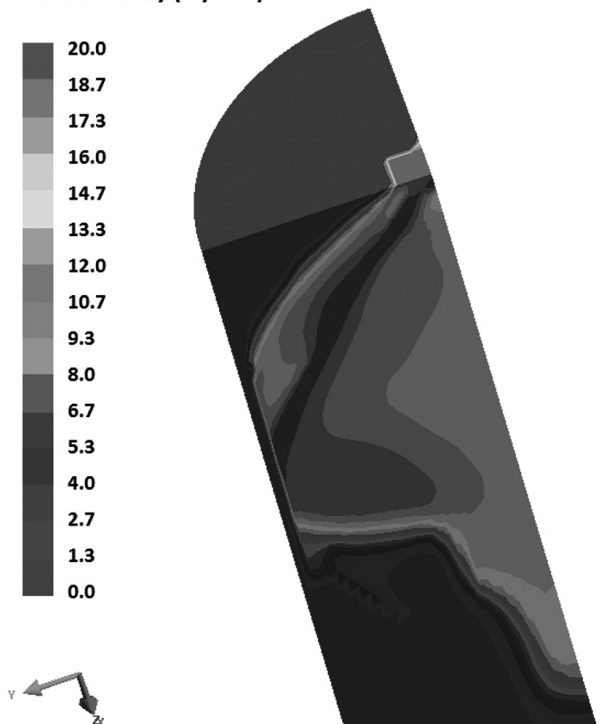


Figure 1: Velocity vectors of a blank

Slika 1: Vektor hitrosti v gredici

Fraction Solid

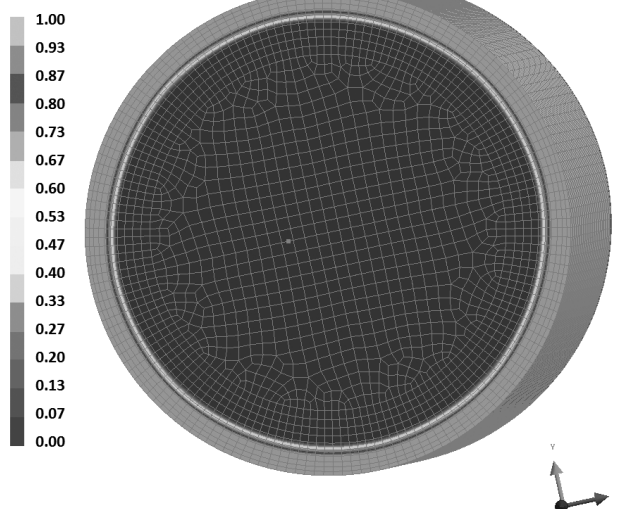


Figure 2: Calculation mesh of a blank

Slika 2: Računska mreža gredice

An application of program ProCAST consists of five modules, which are functionally mutually interconnected. The first module is used for defining the body geometry and for selecting the fineness and the shape of the calculation mesh. It is then necessary to determine the physical, initial and surface conditions that may be modified in line with the requirements of the next module. After correctly entering the initial calculation parameters, the main calculation module of the software launches the program.

The program allows a graphical visualisation of the calculated results and an export of the values, graphs and images for further processing. The program can launch a calculation in two modes – the thermal and flow modes. The results of the thermal mode give the thermal fields of a round, continuously cast blank without the velocity vectors of liquid steel. If it is also required to visualise the velocity vectors, then it is necessary to activate the flow mode (Figure 1).

Distribution of the temperatures during the solidification or cooling is calculated in the nodal points of the whole volume of a continuously cast blank (Figure 2).

The program also comprises a vast database of the information about cast steel grades, including their thermophysical properties (density, specific heat capacity, heat conductivity, viscosity, etc.).

4 RESULTS OF NUMERICAL SIMULATIONS

Within the research two steel grades of different chemical compositions used for the production of continuously cast blanks with a diameter of 410 mm were subjected to a simulation (Table 1). The following influences were analysed: the influence of the chemical composition, the casting rate, overheating of the steel above the liquidus temperature, the influence of the mol-

ten-steel level in the mould on the resulting technological parameters, generally represented with the metallurgical length, the length of the liquid phase, the surface temperatures of a continuously cast blank at the outlets of the primary and secondary cooling zones, and the thickness of the strand shell.

Table 1: Chemical composition of the steel in mass fractions, w/%

Tabela 1: Kemijska sestava jekla v masnih deležih, w/%

Brand of the steel	Chemical composition, w/%				
	C	Mn	Si	P	S
Steel A	0.168	1.350	0.381	0.013	0.007
Steel B	0.913	0.342	0.246	0.009	0.004

The chemical compositions, especially the carbon contents, have a principal influence on the heat removal in all the zones of the continuous-casting machine. In the case of low-carbon steels the biggest shrinkage of the strand shell occurs as a result of a peritectic reaction as well as a considerable deceleration of its growth, which is manifested by a reduction of the heat-flow density through the mould wall to its minimum. Another result of this reaction is an increased occurrence of surface defects of a continuously cast blank, particularly of surface cracks.

The casting rate is related to the dimensions of a continuously cast blank, the type of steel and the type of mould. Higher values of the casting rate cause a shorter stay of a continuously cast blank in the mould, which increases the surface temperatures and, simultaneously, also the local values of the thermal-flow density.

It may be stated on the basis of the performed simulations that, with respect to investigating the influence of the casting rate on the metallurgical length and the length of the liquid phase, their very strong linear dependence is evident and is best characterised with a high value of the slope in the regression equations (Figure 3).

The growth of the strand shell with the changing casting rate (Figure 4) confirms the previous scientific research works,^{7,8} which document the fact that the para-

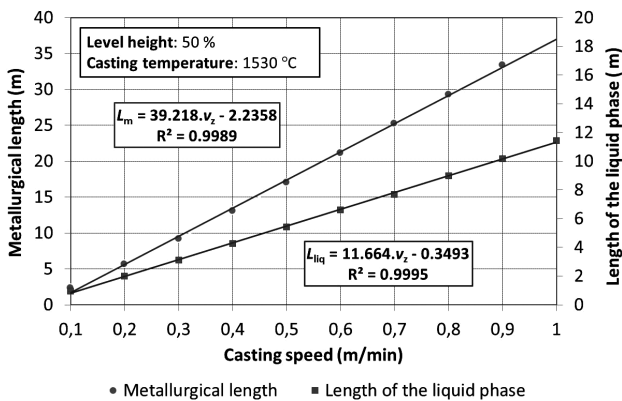


Figure 3: Influence of the metallurgical length depending on the casting speed in the case of steel A

Slika 3: Vpliv metalurške dolžine v odvisnosti od hitrosti litja v primeru jekla A

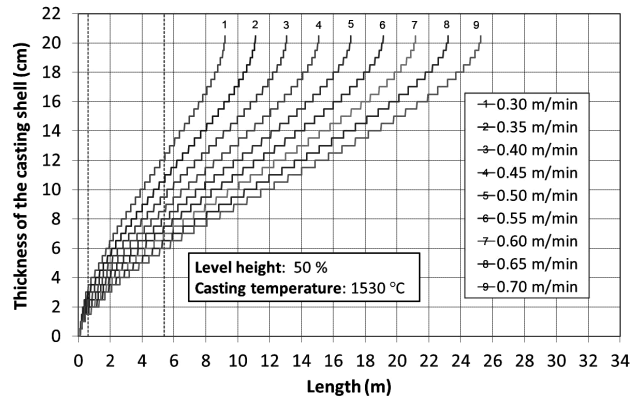


Figure 4: Increase in the thickness of the casting shell depending on the casting speed in the case of steel A

Slika 4: Povečanje debeline skorje, v odvisnosti od hitrosti litja v primeru jekla A

abolic law may be used for the solidification of an ingot to a distance of approximately 75 % of the diameter of a continuously cast blank from the ingot mould surface. When this critical value is exceeded, the differences are more pronounced, as it is known that the solidification of round, continuously cast blanks accelerates towards their centre, in comparison to the ingot mould.

The thickness of the shell can determine the results of the logarithmic equation for steel A:

$$\xi = (-1.490 \cdot 10^{-2} \cdot \ln v_z + 1.683 \cdot 10^{-1}) \cdot \tau^{(-6.378 \cdot 10^{-3} \cdot \ln v_z + 5.874 \cdot 10^{-1})} \quad (2)$$

And for steel B, the following applies:

$$\xi = (-1.3690 \cdot 10^{-2} \cdot \ln v_z + 1.869 \cdot 10^{-1}) \cdot \tau^{(-9.369 \cdot 10^{-3} \cdot \ln v_z + 5.456 \cdot 10^{-1})} \quad (3)$$

where v_z /(m/s) is the specific casting rate and τ /s is the casting time.

Finally, an analysis of the influence of overheating of steel on the investigated technological parameters was made. Overheating of steel can be defined as the difference between the casting temperature and the liquidus

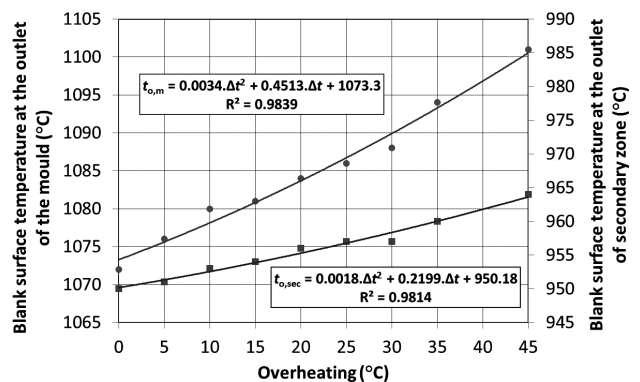


Figure 5: Blank-temperature change depending on the overheating of steel B

Slika 5: Sprememba temperature gredice glede na pregrevanje jekla B

temperature. This temperature difference should be, from the viewpoint of the operation, as small as possible, since it reduces the thermal stress and the energy intensity of the continuous casting of steel, as well as the scrap factor and the formation of surface cracks (**Figure 5**).

The results of the simulations also show that the greater is the overheating of steel, the later is the solidification of a continuously cast blank and the greater is the distance of this solidification from the molten-steel level. The overheating of steel in the interval from 0 °C to 45 °C increases the metallurgical length, on average, by 0.5 m, and a similar trend is characteristic of all steel grades. Even a greater influence of this parameter on the increase in the length of the liquid phase was confirmed. An increase in the overheating temperature by 40 °C above the liquidus temperature caused an elongation of the metallurgical length, on average by 3 %; however, the length of the liquid phase was increased even by 20 %, while the surface temperature of a continuously cast blank at the output from the primary and secondary cooling zones increased by up to 3 %.

5 CONCLUSION

The optimum configuration of the thermal mode of the continuous casting machine substantially influences the quality of the cast products. The processes participating in the cooling and solidification of a continuously cast blank show their physical characters in the complicated transfer phenomena of the heat and mass transfer. In order to allow a general solvability of these tasks, computer simulations are used making it possible to define the optimum parameters of the continuous casting of

steel. The casting rate, which influences practically all the casting parameters, appeared to be most important quantity.

Acknowledgements

The work was realised within the frame of the grant project No. SP 2013/53, under the financial support of The Ministry of Education, Youth and Sports.

6 REFERENCES

- ¹ Y. Xie, H. Yu, X. Ruan, B. Wang, Y. Ma, Mathematical modelling of mould temperature field during continuous casting of steel, *Journal of Materials Processing Technology*, 199 (2008) 1–3, 49–55
- ² I. L. Ferreira, J. E. Spinelli, J. C. Pires, A. Garcia, The effect of melt temperature profile on the transient metal/mold heat transfer coefficient during solidification, *Materials Science and Engineering A*, 408 (2005) 1–2, 317–325
- ³ J. X. Fu, J. S. Li, H. Zhang, X. Z. Zhang, Industrial Research on Broadening of Slab in Continuous Casting Process, *Journal of Iron and Steel Research International*, 17 (2010) 8, 20–24
- ⁴ M. Janik, H. Dyja, Modelling of three-dimensional temperature field inside the mould during continuous casting of steel, *Journal of Materials Processing Technology*, 157 (2004) 1, 177–182
- ⁵ S. Sanyal, J. K. Saha, S. Chandra, A Mathematical Model to Optimize Aluminium Wire Injection in Steel Melts, *Steel Research International*, 80 (2009) 8, 559–567
- ⁶ J. Stetina, F. Kavicka, The influence of the chemical composition of steels on the numerical simulation of a continuously cast slab, *Mater. Tehnol.*, 45 (2011) 4, 363–367
- ⁷ K. Stransky, J. Dobrovska, F. Kavicka, V. Gontarev, B. Sekanina, J. Stetina, Two numerical models of the solidification structure of massive ductile cast-iron casting, *Mater. Tehnol.*, 44 (2010) 2, 93–98
- ⁸ J. X. Fu, W. S. Hwang, J. S. Li, S. F. Yang, Z. Hui, Effect of Casting Speed on Slab Broadening in Continuous Casting, *Steel Research International*, 82 (2011) 11, 1266–1272

STATIONARY-CREEP-RATE EQUATIONS FOR TEMPERED MARTENSITE

ENAČBE ZA HITROST STACIONARNEGA LEZENJA ŽARJENEGA MARTENZITA

**Franc Vodopivec, Borut Žužek, Danijela A. Skobir Balantič, Monika Jenko,
Matjaž Godec, Darja Steiner Petrovič**

Institute of Metals and Technology, Lepi pot 11, 1000 Ljubljana, Slovenia
franc.vodopivec@imt.si

Prejem rokopisa – received: 2013-07-01; sprejem za objavo – accepted for publication: 2013-08-28

The stationary-creep equations including parameters as the average particle spacing or/and particle size are examined in terms of the effects of different equation parameters on the difference of calculated and experimental creep rate. It is concluded that the difference between the experimental creep rate and the creep rate deduced from the recently proposed creep equation is in the range of about $\pm 25\%$ if the effects of the steel composition and the changes in the particle size and spacing during the creep test are considered with sufficient accuracy.

Keywords: creep-resistant steel, creep equations, particle size and spacing, difference between the calculated and experimental creep rate

Enačbe za izračun hitrosti stacionarnega lezenja, ki vključujejo kot parametre povprečno velikost in oddaljenost izločkov, so analizirane s stališča razlike med eksperimentalno in izračunano hitrostjo lezenja. Sklep je: pred kratkim predložena enačba da razliko v razponu okoli 25 %, če so prav upoštevani vplivi sestave jekla in spremembe velikosti in oddaljenosti izločkov pri preizkusih lezenja.

Ključne besede: jeklo odporno proti lezenju, enačbe za izračun hitrosti lezenja, velikost in oddaljenost izločkov, razlika med izračunano in eksperimentalno hitrostjo lezenja

1 INTRODUCTION

Theoretical and semi-empirical constitutive equations were proposed for calculating the stationary (secondary) creep rate of high-chromium creep-resistant steels using as parameters physical constants, creep-test conditions, steel properties, microstructure as well as the average particle size and spacing¹⁻⁵. The equations were deduced applying different concepts of interaction between particle shape, size and spacing and mobile dislocations in the metal matrix. Also, more than 20 semi-empirical creep equations have been proposed⁶⁻⁸ so far using the rationalisation of the stress-strain-creep test results obtained for different steels. In these equations, the base parameters of microstructures of creep-resistant steels, matrix grain size and particle size and spacing are considered as constants based on the results of the creep tests. The recently derived creep equation is based on the disjunctive-matrix (**dm**) concept of particle stress transfer of acting stress on gliding and climbing of dislocation segments in the matrix after crossing the strait between two neighbour particles⁹. By specific angles of acting stress, matrix grain-dislocation slip plane and stress-transfer particle face, the dislocation gliding stress is decreased significantly, while the climb stress changes much less¹⁰. It was concluded that the creep rate depended on the dislocation glide velocity in disjunctive matrix^{9,10} which is proportional to the gliding

stress¹. The calculations have shown that in a disjunctive matrix with backstress due to opposite directions of the components of acting and transfer stress¹⁰, the gliding stress may be decreased by up to about four orders of magnitude. The concept of a **dm** stationary creep of tempered martensite allows a simple explanation of the effect of matrix grain size on the stationary-creep rate and of the transition from stationary to accelerating creep¹⁰. In this article, the accuracy and reliability of parameters of the equations, proposed so far for calculating the stationary-creep rate, such as volume share, particle size and/or spacing are examined.

2 STATIONARY-CREEP EQUATIONS

Equation (1) was deduced for a dislocation line advancing through a field of obstacles (particles) by locally climbing over them¹:

$$\dot{\epsilon} = \left(\frac{2\pi \cdot D \cdot G \cdot b}{f \cdot k \cdot T} \right) \cdot \left(\frac{\sigma}{G} \right) \quad (1)$$

where $\dot{\epsilon}$ is the creep rate (s^{-1}), D is the iron-diffusion rate in ferrite, G is the shear modulus at T , b is the Burgers vector, f is the volume fraction of particles in the matrix, k is the Boltzmann constant and σ is the acting stress.

It was stated that the equation is reasonable for the limit of density of mobile dislocations: $\rho < 1/(d/2)^2$. An

interaction of particles and mobile dislocations is considered including the volume share of carbide, f . In this work, experimental and calculated creep rates are obtained for the steel with the average particle sizes of $d_1 = 280$ nm and $d_2 = 420$ nm; the limits $\rho_1 = 1.96 \times 10^{14}$ m⁻² and $\rho_2 = 4.41 \times 10^{14}$ m⁻² are obtained, while $\rho = 0.978 \times 10^{14}$ m⁻² is deduced later for the examined steel. Thus, the validity limit $\rho < 1/(d/2)^2$ for equation (1) is fulfilled.

Equation (2)² was derived as an improvement of equation (1) considering the density of mobile dislocations (ρ) and particle spacing (λ):

$$\dot{\epsilon} = \frac{b^2 \cdot D \cdot \lambda \cdot \rho \cdot \sigma^2}{k \cdot T \cdot G} \quad (2)$$

For the detachment concept of stationary creep based on TEM observations of the detachment of the dislocation line from the free surface of oxide particles in aluminium, the creep equations (3) were derived³⁻⁵:

$$\dot{\epsilon} = \left(\frac{6\lambda \cdot \rho \cdot D}{b} \right) \cdot \exp^{-E} \quad (3)$$

$$E = G \cdot b^2 \cdot r \cdot \left((1-k) \left[\frac{1-k}{\sigma_d} \right] \right)^{3/2}$$

where E is the detachment activation energy, σ_d is the detachment stress and $k = T_p/T_m$ with the T_m dislocation line energy.

It was concluded¹¹⁻¹³ that equations (3) required significant improvements for the calculation of the stationary-creep rate of the creep-resistant steels strengthened with non-coherent particles.

Equation (2) was modified introducing the constants for the particle size and spacing, considering their dependence on temperature and rationalising the acting stress with the shear modulus or yield stress at the creep-test temperature. Reasonable fits of the experimental and calculated creep rates for different test temperatures were obtained with the stress exponents in the range from $n = 4.5$ to $n = 16$ and the creep activation energy significantly higher than the activation energy of iron diffusion in ferrite was calculated^{6-8,14-16}:

$$\dot{\epsilon} = C_1 \cdot \left(\frac{\sigma}{G} \right)^n \cdot \exp^{-C_2 \frac{(\sigma/G)}{RT}} \quad (4)$$

Based on the experimental data¹¹⁻¹³, with $C_1 = 4.3 \times 10^{-41}$ K s⁻¹ and $C_2 = 2.85 \times 10^7$, the stress exponent $n = 4.5$ and the activation energy of 680 kJ m⁻¹ was deduced¹⁶⁻¹⁸. Recently, only a small difference was found in the creep activation energy for the creep rates calculated considering a negligible change in the particle size and spacing¹⁹.

The simplified equation (5) includes the parameters of the previous equations and considers the effect of the particles as a difference of particle spacing and size ($\lambda - d$).⁹ The basis of the equation is the assumption that the mobile-dislocation driving energy is consumed mainly

for the lengthening of the dislocation segment due to the transition of the disjunctive-particle matrix. Based on the **dm** stationary-creep concept and experimental data, the stress exponent $n = 3.65$ was deduced and the obtained difference between the calculated and experimental creep rates was about 10 %.⁹ For the cube-shaped particles, the exponent up to $n \approx 4$ was deduced recently¹⁰:

$$\dot{\epsilon} = \frac{c \cdot b^2 \cdot \sigma^v \cdot \rho \cdot D \cdot (\lambda - d)}{k \cdot T \cdot G} \quad (5)$$

The creep rate ϵ in s⁻¹ is obtained in equation (5) and written as:

$$\dot{\epsilon} = c\alpha \frac{b^2 \cdot \sigma^v \cdot \rho \cdot D \cdot (\lambda - d)}{k \cdot T \cdot G} \text{ and } \alpha = \frac{\sigma^{3.65}}{\sigma^2} = 4.78 \cdot 10^3$$

The density of mobile dislocations was calculated as¹⁸:

$$\rho = \left(\frac{\sigma}{a \cdot M \cdot G \cdot b} \right)^2 \quad (6)$$

where $M = 3$ (the Taylor factor).

In **Table 1** for the tempered martensite with a uniform distribution of particles, the experimental creep rate, the creep rates calculated using equations (1), (2) and (5) with $c = 1$, $b = 2.5 \times 10^{-10}$ m, $\sigma = 170$ MPa, $\rho = 9.78 \times 10^{13}$ m⁻², $D = 1.19 \times 10^{-19}$ m² s⁻¹ (in¹⁹), $k = 1.38 \times 10^{-23}$ J K⁻¹, $G = 57.3 \times 10^3$ MPa, $T = 853$ K and $f = 0.037$ (in^{9,20}) are given.

Table 1: Creep rates calculated for two average particle sizes and spacings. In equation (1) shear stress $\sigma_g = \sigma_a/M = 170/3 = 56.6$ GPa and in equation (5) $n = 3.65$ were considered.

Tabela 1: Hitrosti lezenja, izračunane za dve povprečni velikosti izločkov in razdalji med njimi. V enačbi (1) je upoštevan strižni modul $\sigma_g = \sigma_a/M = 170/3 = 56.6$ GPa in $n = 3.65$.

Particles		Calc. creep rate, $\dot{\epsilon}/s^{-1}$			Exp. creep rate
Size	Spacing	$\dot{\epsilon}$			$\dot{\epsilon}$
D	λ	s ⁻¹			s ⁻¹
nm	nm	Eq. 1	Eq. 2	Eq. 5	
280	1065	$2.36 \cdot 10^{-11}$	$3.42 \cdot 10^{-9}$	$12.2 \cdot 10^{-8}$	$12.1 \cdot 10^{-8}$
420	1650		$5.42 \cdot 10^{-9}$	$18.9 \cdot 10^{-8}$	$21.2 \cdot 10^{-8}$

The difference between the experimental and calculated creep rate for equation (5) is reasonable. It is greater if deduced from equation (1), probably due to the substitution of the effects of segmentation of the dislocation line, the interaction dislocation segments and the particles with the volume fraction of particles. The lower creep rate deduced from equation (4) is ascribed to the assumption of an interaction between the mobile dislocations and the modified Orowan mechanism. However, by stationary creep, the applied stress is significantly lower than the Orowan stress. The creep rates quoted in this work were determined and calculated for 100 h tests with static-tensile stress of 170 MPa at 853 K. At this temperature, the Young modulus (E) for two high-chromium creep-resistant steels is $E_{853} = 57.3 \times 10^3$ MPa

= $0.82 \times E_{22}$ with the E_{22} Young modulus at room temperature²¹. Assuming that the effects of temperature on yield stress (σ_y) and Young modulus are equal, the experimental rates in **Table 2** were obtained as follows: $\sigma_{y853} \approx 0.82 \times \sigma_{y22} = 0.82 \times 400 = 328$ MPa. The ratio of the acting-creep stress to the yield stress, $\sigma/\sigma_y = 170/328 = 0.52$ at 853 K, makes the Orowan interaction between mobile dislocations and non-shearing particles improbable at the creep-test temperature.

3 ACCURACY AND RELIABILITY OF THE PARAMETERS IN EQUATION (5)

In creep-resistant steels, the ratio of numbers of iron atoms and atoms of the alloying elements is above 0.85. The difference between the parameters of chromium and iron is: $\Delta_a(\text{Cr-Fe}) = 2.88 \times 10^{-10} - 2.48 \times 10^{-10} = 0.4 \times 10^{-10}$ m. Theoretically, the maximum extension of ferrite lattice due to chromium atoms in the solid solution is $0.4 \times 0.15 = 0.06 \times 10^{-10}$ m, thus $0.06/2.48 = 0.024 \times 10^{-10}$ m. It is concluded that the effect of the difference in the Burgers vector due to alloying elements in solution in ferrite for creep-resistant steels is negligible.

The lattice parameters of ferrite and the Burgers vector are increased at the creep-test temperature because of the thermal expansion. The coefficient of linear thermal expansion of α iron is $11.8 \times 10^{-6} \text{ K}^{-1}$. Consequently, at the creep-test temperature, the lattice parameter is for $2.48 \times 10^{-10} \times 11.6 \times 10^{-6} \times 853 = 2.45 \times 10^{-12}$ m. Thus, the effect of increase in the α -Fe lattice at creep temperature is negligible.

The iron-diffusion rate was deduced from data in¹⁹. The values of activation energy for steels with 0.87 % Cr to 5 % Cr differ by less than 5 % from the average value. Considering the difference in D_0 it is concluded that the error due to differences in the diffusion rate is within ± 10 %.

The acting stress is included as a parameter in all theoretical and semi-empirical equations, while $n = 1$, $\sigma_a = 170$ MPa, $\sigma^{1.1} = 284$ MPa, $\sigma^{1.2} = 475$ MPa, $\sigma^{1.5} = 2116$ MPa and $\sigma^2 = 28900$ MPa. It is evident that already the difference of $n = 0.2$ generates the difference between the calculated and experimental creep rates of 2.8 times. The accuracy of the stress-exponent deduction depends on the accuracy of the assumed changes in particle content, size and spacing during the creep tests. The effect of the stress exponent is explained with the **dm** concept of the stationary creep¹⁰. It was, namely, calculated that the gliding stress in disjunctive parts of the matrix could be decreased by up to 10^4 times, with respect to the acting stress, to the backstress generated by the angles of acting stress, grain-dislocation slip plane and stress-transfer particle face. Thus, it seems reasonable to ascribe a great range of the quoted stress exponents ($n = 4.5$ to $n = 16$) to the undervaluation of the effect of changes of particle size and spacing during the experimental creep tests.

The mobile-dislocation density calculated using equation (5)¹⁸, $\rho = 0.978 \times 10^{14} \text{ m}^{-2}$, was checked using the relations suggested for copper²²:

$$\sigma_s = \frac{1}{2} \cdot G \cdot b \cdot \rho \quad \text{and} \quad \dot{\epsilon} = \rho \cdot v \cdot b \quad (7)$$

where σ_s is the acting shear stress ($\sigma_s = \sigma_a/3$), v is the dislocation velocity, while the other parameters are the same as in equation (5); it was obtained that $\rho = 1.04 \times 10^{14} \text{ m}^{-2}$. The difference between the two deduced mobile-dislocation densities of 5.3 % supports the conclusion that the accuracy of the calculations of the mobile-dislocation density deduced from equation (6) is of ± 10 %.

In the creep equations, the coefficient of iron diffusion in ferrite determined for the equilibrium content of vacancies is considered. The tensile stress increases the content of vacancies^{23,24} and the increase in the diffusion rate is deduced from this relation²⁴:

$$D_1 = \left(\frac{c_0}{c_1} \right) \cdot D_0 \quad (8)$$

where c_0 and D_0 are the vacancy content and diffusion rate at $\sigma = 0$, while c_1 and D_1 are the vacancy content and diffusion rate at the acting stress. It was deduced from data in²⁴ that $D_1 = 1.14D_0$. In the case of calculations of creep rate at the acting stress $\sigma_a = 170$ MPa, the effect of the increase of diffusion rate is relatively low with respect to the effect of the stress exponent, however, it should not be neglected in accurate calculations.

For the activation energy of iron diffusion in ferrite, $Q = \gamma$ and D_0 251 kJ/mol¹⁹ as 289 kJ/mol²² are quoted. The calculated diffusion rates at 853 K differ by several orders of magnitude. Thus, it is clear that the calculated creep-rate values are reliable only if deduced using reliable data in the deduction of iron diffusion in ferrite. In this case, the error in the calculation of the creep rates would be in the range of 10 %.

In modern high-chromium creep-resistant steels, the molar contents of carbide-forming vanadium and niobium are lower than the molar content of carbon, while the content of chromium is higher. Consequently, the particles of carbide $M_{23}C_6$ with a molar composition of $\text{Cr}_{18}\text{Fe}_3\text{Mo}_2$ ²³⁻²⁵ are stable up to the austenite temperature. The solubility of VC and NbC carbides in ferrite is higher and at 700 °C virtually all VC and a significant part of NbC are dissolved in ferrite. Consequently, the effects of the creep-testing temperature on the quantity, size and spacing of particles of different carbides may be different. It is greater for a lower content of carbide-forming elements in solution in ferrite and higher solid solubility of carbide.

From the data in²⁵, it is calculated that in the 0.18C11.4Cr steel with the particles size of 0.1 μm , $M_{23}C_6$ increase after 1000 h at 650 °C by about $\Delta d = 2$ %, and by about $\Delta d = 12$ % at 750 °C. According to

equation (5), the creep rate is proportional to $(\lambda - d)$. The particle spacing is deduced from²:

$$\lambda = \frac{4 \cdot d}{\pi \cdot f^{1/3}} \quad (9)$$

By constant volume share of carbide, an increase in average particle size of 12 %, the increase of particle spacing is $\Delta\lambda = 4\Delta d = 48$ % and, according to equation (5), the increase of difference between experimental and calculated creep rates of $(48 - 12)$ % = 36 %. The logical conclusion is that by stationary-creep tests, reliable data could be obtained only by a very limited change initial particles size and spacing. The difference between calculated and experimental creep rates would be even greater if the dissolution of the VC and NbC particles was omitted.

Assuming that after the tempering at 800 °C $M_{23}C_6$ particles are situated in the centre of cubes with edge e , equation (10) was deduced²⁰. Further, it was assumed that, in the micrograph plane, the sections of all cubes are squares with side e and with a particle in the square centre. The average size of the particle is than²⁰:

$$d = \frac{\pi \cdot F^{1/2} \cdot f^{1/3}}{4N_p^{1/2}} \quad (10)$$

where F is the surface area of the assessed micrograph and N_p is the number of the particles in the micrograph, f is the volume fraction of carbide calculated from the content of carbon in the steel and the previously quoted relation², $e = \lambda = (4d)/\pi f^{1/3}$. In equation (5) it is assumed that the cube edge and the square side lengths are equal. This assumption is partly incorrect, as the geometrical shape of a cube section depends on the angle between the section (micrograph) plane and the cube edge, which is, on average, a rectangle with the average side length $s = 1.205e = (e + e\sqrt{2})/2$ ¹⁰. The average spacing of the particles in the micrograph plane is then not $\lambda = \sqrt{F/N}$ but $\lambda' = 1.205 \sqrt{F/N}$ and equation (10) is inexact. However, the size of most of the particles is below the average size²⁵. On the SEM micrographs, the particles with the size of 25 nm are visible by magnification of 10^4 times. The dissolution velocity of particles, $v_d \approx d^3/d^2$, is inversely proportional to the particle surface area²⁶. As in equation (5) $(\lambda - d)$ is included, it is assumed that the omission of the particles unseen on the micrographs at the magnification of 5×10^3 would decrease the calculated creep rate by up to 10 % if interaction particle-mobile dislocation was independent of particle size.

The volume fraction of carbide f is a parameter in several equations and it is deduced considering the contents of carbon and of carbide-forming elements in steel^{2,20,27}. For high-chromium steels, the calculated value of f is accurate as the content of carbon is much higher than the content of chromium bound in $M_{23}C_6$. The calculation of the carbide-volume fraction is unreliable in case of a strong effect of temperature on the solubility

of particles of different carbides, i.e., VC and NbC carbides in creep resistant steels. In this case, the volume fraction of carbides is calculated with an acceptable accuracy up to about 650 °C when vanadium in niobium are virtually totally bound in VC and NbC and the difference in carbon is bound to $M_{23}C_6$.

4 ACCURACY OF EQUATION (10)

Equation (10)²⁰ was deduced assuming:

- a spherical shape of the particles with different sizes,
- the particles are situated in the centres of the cubes of different sizes;
- the particle spacing is equal to the cube edge, which is equal to the square side on the micrographs and $\lambda = (F/N)^{1/2}$ with F – surface and N – number of particles on the examined micrograph.

In **Table 2** the results of an assessment of the micrographs of the same specimen of the X20 steel, quenched and tempered for 400 h at 800 °C, are listed. The volume fraction of carbide $Cr_{18}Fe_3Mo_2C_6$, with $f = 0.045$, in the steel tempered at 800 °C²⁰ was deduced as:

$$f = \frac{C \cdot (18Cr + 3Fe + 2Mo + 6C)}{6C \cdot 7.04 \times V_{st}} \quad (11)$$

where C is the content of C in 100 g of steel in g; Cr, Fe, Mo and C are the atom weights; 7.04 is the specific weight of carbide (g/cm^3) and V_{st} is the volume of 100 g of steel.

Table 2: Results of assessment of micrographs of $M_{23}C_6$ particles in grip and gauge parts of a specimen after 100 h of creep tests with $\sigma = 170$ MPa and 853 K

Tabela 2: Rezultati analiz izločkov $M_{23}C_6$ na posnetkih iz merilnega in vpetega dela preizkušanca po preizkusu lezenja 100 h pri 853 K in 170 MPa

Magnification	Gauge, particles, μm		Grip, particles, μm	
	Spacing	Size	Spacing	Size
3500	0.68	0.19	0.72	0.20
5000	0.61	0.17	0.58	0.16
10000	0.55	0.15	0.55	0.15

The average particle spacing and size decrease with the micrograph magnification and reflect the discernibility of very small particles. By the magnification of 10^4 times, the particles of a size down to 25 nm are discerned. The omission of smaller particles would cause an error of about 10 % with respect to the particle spacing and size; however, this inaccuracy is diminished with the assumption that the section of the cubes in the micrograph plane is orthogonal to the cube edge, while the section is rectangular and the average particle spacing is, accordingly, greater. The resulting error is opposed to the error due to the number of very small particles undiscerned on the examined micrograph. The comparison of data suggests that by sufficient magnification of the micrographs and a sufficient number of counted parti-

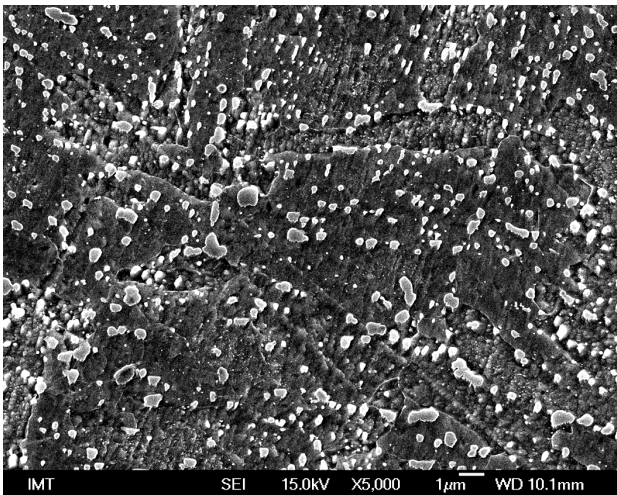


Figure 1: Particles in the gauge specimen part
Slika 1: Izločki v merilnem delu preizkušanca

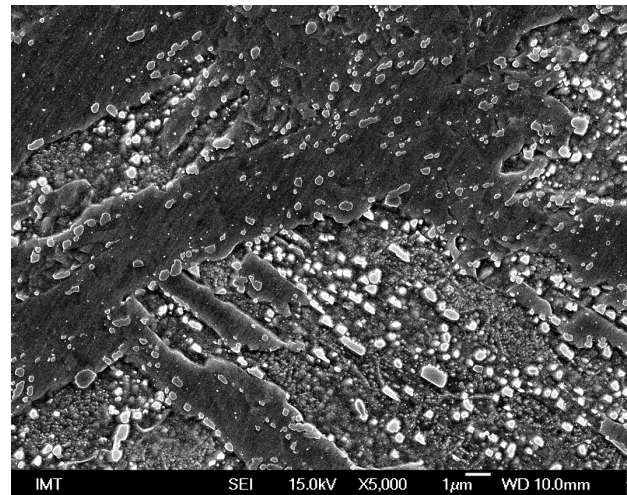


Figure 2: Particles in the grip specimen part with areas of inappropriate etching
Slika 2: Izločki v vpetem delu preizkušanca, ki ni bil pravilno jedkan

cles, the range of error of assessment the particle size and spacing is $\pm 10\%$.

The error could be significantly greater by insufficient surface quality of the SEM micrograph specimen. In **Figures 1** and **2** SEM micrographs of the same steel are shown. The surface quality of the specimen in **Figure 1** was sufficient and only $M_{23}C_6$ particles of different sizes are visible, while the quality of surface of the specimen in **Figure 2** was insufficient, as, in strongly etched areas, a great density of very small particles is visible due to an unsuited specimen preparation.

5 CONCLUSIONS

The accuracy of the quoted creep-rate equations, including as parameters particles size and spacing, depends on the accuracy of consideration of the changes due to the creep-test stress and temperature, and is related to:

- physical parameters at test temperature with a negligible change by change of test temperature;
- inaccuracies of the calculated changes in steel parameters: iron-diffusion rate in ferrite, shear modulus and mobile-dislocation density are in the range of $\pm 10\%$;
- changes of average particle-size spacing during the tests may be greater than 100% depending on the creep-test temperature, time and solubility of particles in ferrite;
- accuracy and reliability of the stress exponent as, due to the exponent change of 0.2, the calculated creep rate increases 2.8 times.

Thus, if the effects of enumerated changes of parameters are considered with sufficient accuracy, especially the change in the particle size and spacing, the stress coefficient was deduced from tests enabling the accurate changes of particle size and spacing, the diffe-

rence between the experimental creep rate and the rate calculated for tempered martensite using equation (5), should be in the range of $\pm 25\%$.

Acknowledgment

The authors thank the Slovenian Research Agency for the funding of this work.

6 REFERENCES

- ¹ M. F. Ashby, The mechanical effects of a dispersion of a second phase, Proc. of the 2nd Int. Conf. On Strength of Metals and Alloys, ASM, Metals Park, Ohio, 1970, 507–541
- ² E. Hornbogen, Einfluss von Teilchen einer zweiten Phase auf das Zeitverhalten, In: W. Dahl, W. Pitch, Festigkeits- und Bruchverhalten bei höheren Temperaturen, Verlag Stahleisen, Düsseldorf 1980, 31–52
- ³ E. Artz, D. S. Wilkinson, Acta Metall., 34 (1986), 1893–1898
- ⁴ E. Artz, J. Rösler, Acta Metall., 36 (1988), 1053–1060
- ⁵ J. Rösler, E. Artz, Acta Metall., 36 (1988), 1043–1051
- ⁶ K. H. Kloos, J. Granacher, M. Monses, Steel Res., 69 (1998), 446–453
- ⁷ S. R. Holdsworth, Constitutive equations for creep curves and predicting service life, In: F. Abe, T. U. Kern, R. Wiswanathan, Creep resistant steels, Woodhead Publ. Lim., Cambridge, England 2008, 403–420
- ⁸ B. Wilshire, H. Burt, Creep strain analysis for steel, In: F. Abe, T. U. Kern, R. Wiswanathan, Creep resistant steels, Woodhead Publ. Lim., Cambridge, England 2008, 421–445
- ⁹ F. Vodopivec, B. Žužek, M. Jenko, D. A. Skobir Balantič, M. Godec, Mater. Sci. Tech., 29 (2013) 4, 451–455
- ¹⁰ F. Vodopivec, F. Kafexhiu, B. Žužek, Stationary creep and glide stress for martensite with hypothetic cube particles, submitted to Mater. Sci. Tech.
- ¹¹ V. Sklenička, K. Kuharova, A. Dlouhy, J. Krejčí, Materials for Advanced Power Engineering, part I, In: D. Coutsoradis (ed.), Kluwer Academic Publishers, 1994, 435–444
- ¹² J. Čadek, V. Šustek, M. Pahutova, Mat. Sci. Eng. A, 225 (1997), 22–28

- ¹³ J. Čadek, V. Šustek, *High Temperature Materials and Processes*, 16 (1997), 97–107
- ¹⁴ A. Nagode, B. Ule, M. Jenko, L. Kosec, *Steel Res. Int.*, 78 (2007), 638–642
- ¹⁵ B. Ule, A. Nagode, *Materials Sci. Techn.*, 23 (2007), 1367–1374
- ¹⁶ B. Ule, A. Nagode, *Scripta Mater.*, 57 (2007), 405–408
- ¹⁷ B. Žužek, F. Vodopivec, B. Podgornik, M. Jenko, M. Godec, *Mater. Tehnol.*, 46 (2012) 6, 661–664
- ¹⁸ K. Maruyama, K. Sawada, J. Koike, *ISIJ Intern.*, 41 (2001), 641–653
- ¹⁹ H. Oikawa, Y. Iijima, *Diffusion behaviour of creep-resistant steels*, In: F. Abe, T. U. Kern, R. Wiswanathan, *Creep resistant steels*, Woodhead Publ. Lim., Cambridge, England 2008, 241–264
- ²⁰ F. Vodopivec, D. A. Skobir Balantič, M. Jenko, B. Žužek, M. Godec, *Mater. Tehnol.*, 46 (2012) 6, 633–636
- ²¹ Y. F. Yin, R. G. Faulkner, *Physical and elastic behaviour of creep-resistant steels*, In: F. Abe, T. U. Kern, R. Wiswanathan, *Creep resistant steels*, Woodhead Publ. Lim., Cambridge, England 2008, 217–240
- ²² R. W. K. Honeycombe, *The Plastic Deformation of Metals*, 2nd ed., Edward Arnold, London 1985, 10–14
- ²³ I. V. Valikova, A. V. Nazarov, *Simulation of Characteristics Determining Pressure Effects on Self Diffusion in BBC and FCC Metals*, *Physics of Metals and Metallography*, 109 (2010), 220–226
- ²⁴ J. W. Jang, J. Kwon, B. J. Lee, *Effect of stress on self-diffusion in bcc Fe. An atomistic simulation study*, *Scripta Mater.*, 63 (2010), 39–42
- ²⁵ F. Vodopivec, D. Steiner Petrovič, B. Žužek, M. Jenko, *Coarsening rate of M₂₃C₆ particles in a high chromium creep resistant steel*, *Steel Res. Int.*, 84 (2013) 11, 1110–1114
- ²⁶ J. W. Martin, R. D. Doherty, B. Cantor, *Stability of microstructure in metallic systems*, 2nd ed., Cambridge Un. Press, 1997, 254
- ²⁷ D. A. Skobir, F. Vodopivec, M. Jenko, S. Spaić, B. Markoli, *Z. Metallkd.*, 95 (2004) 11, 1020–1024

NUMERICAL CALCULATIONS OF STRESS-INTENSITY FACTORS FOR A WWER-1000 REACTOR PRESSURE VESSEL UNDER A PRESSURIZED THERMAL SHOCK

NUMERIČNI IZRAČUNI FAKTORJA INTENZITETE NAPETOSTI V REAKTORSKI TLAČNI POSODI WWER-1000 PRI TOPLOTNEM ŠOKU POD TLAKOM

Sergey Vladimirovich Kobelsky

G. S. Pisarenko Institute for Problems of Strength, National Academy of Science of Ukraine, Kiev, Ukraine
ksv@ipp.kiev.ua

Prejem rokopisa – received: 2013-07-24; sprejem za objavo – accepted for publication: 2013-10-03

Two methods of determining stress-intensity factors based on the calculations of J - and G -integrals are analyzed for a simulated emergency-cooling regime of a WWER-1000 reactor pressure vessel. A finite-element analysis of the convergence of the results determining the stress-intensity factors using different approaches and different finite-element meshes was done.

Keywords: reactor pressure vessel (RPV), finite-element method (FEM), J - and G -integral, crack, stress-intensity factor (SIF)

Analizirani sta bili dve metodi za določanje faktorja intenzitete napetosti na osnovi izračuna J - in G -integrala pri simuliranem režimu hitrega nujnega ohlajanja tlačne posode reaktorja WWER-1000. Narejena je bila analiza raztrosa rezultatov s končnimi elementi pri določanju faktorja intenzitete napetosti in različnih mrežah končnih elementov.

Ključne besede: tlačna posoda reaktorja (RPV), metoda končnih elementov (FEM), J - in G -integral, razpoka, faktor intenzitete napetosti (SIF)

1 INTRODUCTION

The safety control of nuclear power plants and, in particular, of reactor pressure vessels (RPV) as their most critical elements, is one of the important theoretical and practical problems. One of the promising ways of solving this problem is mathematical modeling of the kinetics of the thermomechanical state of a reactor pressure vessel, which requires solutions of non-stationary non-linear problems of thermomechanics. The computational justification for the strength of the RPV is carried out on the basis of an analysis determining fracture-mechanics parameter values, namely, stress-intensity factors (SIF).

The complexity of the problem under consideration, a large amount of computations and the necessity of performing multiple-choice calculations make it essentially impossible to justify the convergence of the obtained results when solving practical problems with the finite-element method (FEM).¹ In the majority of cases, for the structures of a complex shape, calculations are performed on finite-element meshes with a spacing of 0.5 mm to 1 mm in the vicinity of crack front points. At the same time, in the finite-element method, the convergence of numerical-calculation results is a necessary but not a sufficient condition for their reliability. The degree of reliability of the results can be enhanced by comparing the values of the analyzed parameters obtained with the use of various hypotheses or criteria.² It should be noted that

the conditions for attaining the numerical convergence cannot automatically be extended to another class of problems. Thus, the numerical-convergence conditions for the problem to be solved using the deformation-plasticity theory, cannot be fulfilled for the problem to be solved on the basis of the flow theory.

The goal of the present paper is to analyze the convergence of the results determining the SIF calculated using various concepts on different finite-element meshes.

2 PROBLEM STATEMENT

For typical emergency-cooling conditions, known as the pressurized thermal shock, two computational models of the WWER-1000 reactor pressure vessel (RPV), with a built-in crack and without it, are analyzed (**Figure 1**).

A circumferential semi-elliptical crack with the depth of $a = 15$ mm and the ratio $a/c = 1/3$ of the half-axis³ that is located at the level of welded joint No. 4 is postulated. The procedure of embedding the crack in the finite-element model of a pressure-vessel fragment is used.

3 METHOD OF CALCULATION AND THE SOFTWARE

The problem is solved in a three-dimensional formulation using a mixed finite-element method scheme

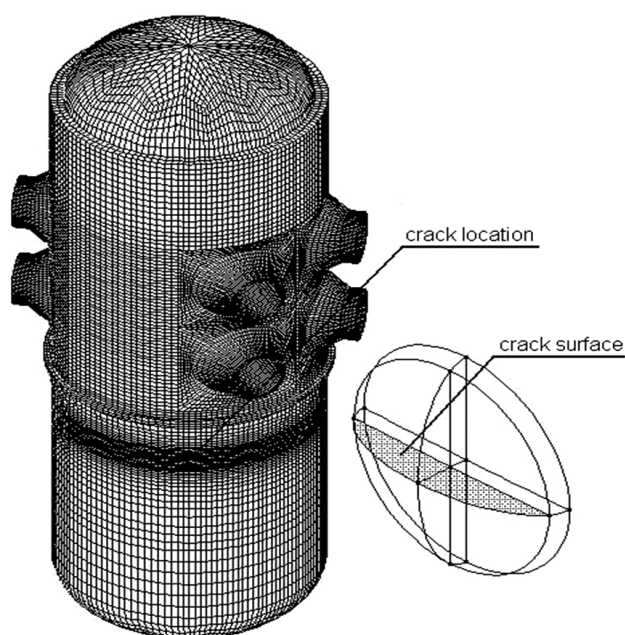


Figure 1: Computational model of the WWER-1000 reactor pressure vessel

Slika 1: Model za izračune tlačne posode reaktorja WWER-1000

(MFEM).⁴ The main advantage of the MFEM, as compared to the classical FEM approach in the form of the displacement method, is the possibility of ensuring the continuity of the approximation not only for displacements but also for stresses and strains as well as the possibility of accurately satisfying the static boundary conditions on the body surface. The mixed scheme is implemented in the SPACE&RELAX software package created at the G. S. Pisarenko Institute for Problems of Strength of the National Academy of Sciences of Ukraine.

The procedure of solving the problem includes three stages. At the first stage, the temperature fields are determined at the specified instants of time. At the second one, the fields of displacements, stresses and strains for the reactor-pressure-vessel (RPV) model are calculated taking into account the thermomechanical loading history. At the third stage, a refined calculation of the fields of displacements, stresses and strains is performed for the RPV fragment with a built-in crack, and the values of the stress-intensity factors (SIF) are determined.

When solving the problem of the elasto-plastic formulation, the loading process is divided into separate time steps, within each of which the elasto-plastic problem is solved considering the residual plastic strains determined at the previous step. To solve the elasto-plastic problem at the current stage of loading, a two-step iteration process is used. The problem of the plasticity theory is solved with the method of variable parameters of elasticity, whereas at the internal steps pertaining to elasticity, the problems are solved using the conjugate-gradient method with the zeroth-order initial approximation.

4 METHODS OF DETERMINING THE SIF VALUES

To determine the SIF values, the J -integral and G -integral concepts are used. In the problems of both the linear and nonlinear theories of elasticity as well as the deformation-plasticity theory, the J -integral value characterizes the energy-release rate for a virtual infinitesimal crack extension.^{5,6} The applicability of the J -integral concept is limited by the following requirements: the material is nonlinearly elastic and homogeneous; under elasto-plastic deformation, the load increases in proportion to one parameter, that is, the deformation-plasticity theory is applicable. The use of the J -integral in the flow theory has no theoretical justification.

In this paper, the method of equivalent volume integration (EVI) proposed by G. P. Nikishkov is used for the calculation of the J -integral value.⁷

The G -integral of the crack closure is defined as the work of adhesive forces acting in a body ahead of the crack front and preventing a separation of its surfaces when the crack propagates negligibly. For the instant of the crack growth onset when the value of the crack propagation can be considered as infinitesimal, the G -integral is calculated with formula:⁸

$$G = \frac{1}{2} \sigma \cdot \Delta \quad (1)$$

Here, σ is the stress calculated normally to the crack plane at the finite-element node located ahead of its front; Δ is the opening displacement calculated as a difference in the displacements normal to the crack plane for two mesh nodes adjacent to the crack front and lying on its different surfaces.

In contrast to the J -integral, the G -integral value remains meaningful when used in the flow theory for an arbitrary loading history, because it defines the specific work necessary for the crack growth onset in an elastic-plastic body. The G -integral value is likely to be meaningful only on condition that tensile (positive) stresses are acting at the crack tip.

Thus, it can be noted that when solving elasto-plastic problems with the flow theory for a complex law of loading, the use of the G -integral concept is more justified than the J -integral concept.

5 FINITE-ELEMENT MESH

Figure 2 illustrates a fragment of the finite-element mesh being constructed in the vicinity of the crack front. The mesh extending along the front consists of three parts – the core, the transition zone and the coarsening zone. The core size is selected to be small in comparison with the size of the transition zone (5–10 %). A mesh that is regular in the plane perpendicular to the crack front is constructed in the core. The size of the mesh spacing along the front is adjusted by assigning the

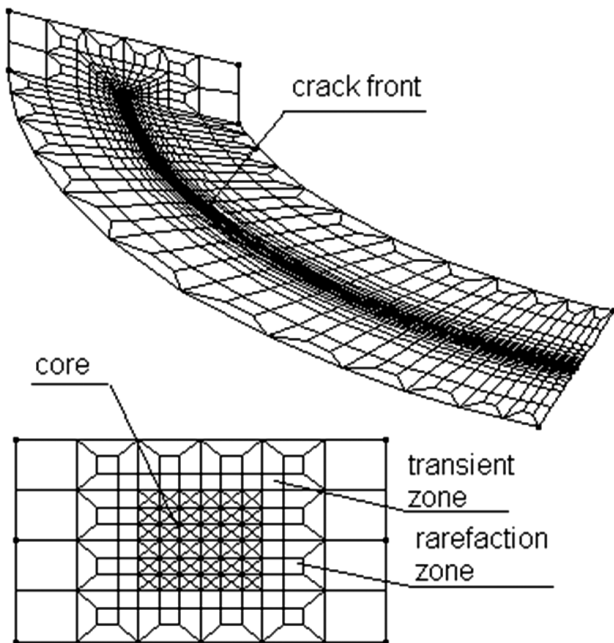


Figure 2: Finite-element mesh constructed in the vicinity of the crack front

Slika 2: Mreža končnih elementov, konstruirana v bližini čela razpoke

refinement factor whose value is selected so that, in the vicinity of the points of interest (e.g., the deepest point of the front), the ratio of the mesh spacing values along the front and in the plane directed to it does not exceed $10 \times 1 \times 1$. The fragment of the finite-element mesh constructed in the crack plane is shown in **Figure 3**.

The mesh shown in **Figure 3a** allows obtaining reliable data on the fracture parameters for the points located along the crack front (point 1 is the deepest point of the front) but does not allow evaluating their values at point 2 on the boundary between the base metal and the cladding. The mesh shown in **Figure 3b** makes it possible to obtain reliable data on the values of the stress-in-

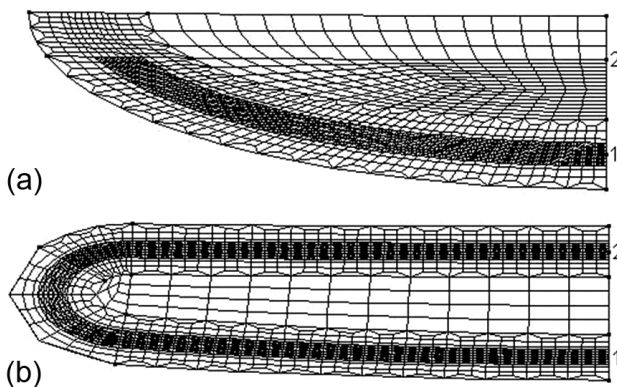


Figure 3: Finite-element mesh constructed in the crack plane: a) with an unclosed contour, b) with a closed contour

Slika 3: Mreža končnih elementov, postavljena v ravnini razpoke: a) z nezaprtem obrisom, b) z zaprtim obrisom

tensity factors and the corresponding integrals at points 1 and 2.

Unless otherwise specified, the results below were obtained using the unclosed crack model.

6 SOLUTION OF THE PROBLEM IN THE ELASTO-PLASTIC FORMULATION TAKING INTO ACCOUNT THE LOADING HISTORY

When solving the problem of the elasto-plastic formulation, taking into account the loading history, we analyzed the sensitivity of the SIF values determined with the following factors:

- the use of the initial RPV model with a built-in crack and without it;
- the use of different criteria for stopping the iterative process;
- the use of the finite-element meshes of different densities.

The SIF values presented in all the plots were normalized with the SIF value determined using the G -integral for the crack with the mesh parameters of $21 \mu\text{m} \times 5.5 \mu\text{m}$. Relative temperature $T - T_{k0}$ is set along the horizontal axis, where T_{k0} is the critical-brittleness temperature of the metal under the initial conditions.

6.1 Analysis of the influence of the crack presence in the initial RPV model and the used criteria for stopping the iteration process

In the method of variable elasticity parameters, the use of two criteria for stopping the iteration process is analyzed – based on the discrepancy (2) and the G -integral value (3):

$$\delta = \frac{(r_i, r_i)}{\sum_{j=1}^i (r_j, r_i)} \leq \varepsilon_r \quad (2)$$

$$\delta = \frac{(G_{i-k}, G_i)}{G_{i-k}} \leq \varepsilon_G \quad (3)$$

where r_i is the discrepancy vector, G_{i-k} and G_i are the G -integral values at the $i-k$ -th and i -th step iterations with respect to the non-linearity, $k \geq 1$ is the parameter, $\varepsilon_r = 1 \times 10^{-16}$, $\varepsilon_G = 1 \times 10^{-3}$.

Figure 4 shows the plots of the results for fracture parameters – CTOD and relative SIF values calculated using the G -integral for the problems that were solved on three meshes ($1000 \mu\text{m} \times 600 \mu\text{m}$, $400 \mu\text{m} \times 275 \mu\text{m}$, $47.5 \mu\text{m} \times 27.5 \mu\text{m}$) under the following conditions:

- the initial RPV model with a built-in crack, the stopping criterion is (2),
- the initial RPV model without a built-in crack, the stopping criterion is (3).

The analysis of the results allows one to conclude that it is unreasonable to build a crack into the initial full RPV model. The use of criterion (3) instead of criterion

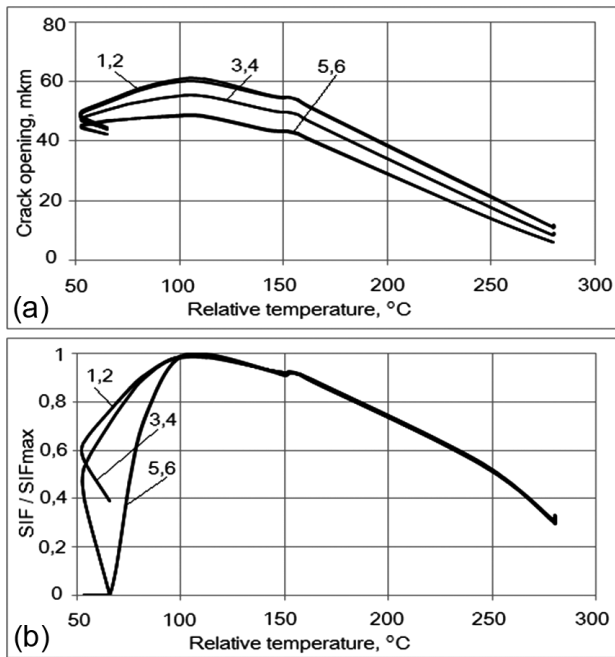


Figure 4: Plots showing the results of calculating the fracture parameters: a) is for the crack-tip opening displacement, b) is for the relative SIF values: 1 – 1000 $\mu\text{m} \times 600 \mu\text{m}$ (1), 2 – 1000 $\mu\text{m} \times 600 \mu\text{m}$ (2), 3 – 400 $\mu\text{m} \times 275 \mu\text{m}$ (1), 4 – 400 $\mu\text{m} \times 275 \mu\text{m}$ (2), 5 – 47.5 $\mu\text{m} \times 27.5 \mu\text{m}$ (1), 6 – 47.5 $\mu\text{m} \times 27.5 \mu\text{m}$ (2)

Slika 4: Prikaz rezultatov izračunov parametrov preloma: a) je za premik konice razpoke, b) je za relativne vrednosti SIF: 1 – 1000 $\mu\text{m} \times 600 \mu\text{m}$ (1), 2 – 1000 $\mu\text{m} \times 600 \mu\text{m}$ (2), 3 – 400 $\mu\text{m} \times 275 \mu\text{m}$ (1), 4 – 400 $\mu\text{m} \times 275 \mu\text{m}$ (2), 5 – 47,5 $\mu\text{m} \times 27,5 \mu\text{m}$ (1), 6 – 47,5 $\mu\text{m} \times 27,5 \mu\text{m}$ (2)

(2) did not lead to a noticeable difference in the results of the problem solution (the maximum difference in the SIF values was found to be less than 0.1 %) but made it possible to reduce considerably the total time of the solution (if the time of the problem solution with the use of criterion (2) can be taken to be a unity, then, with the use of criterion (3), the problem time was 0.55 for the mesh of 1000 $\mu\text{m} \times 600 \mu\text{m}$, 0.4 for the mesh of 400 $\mu\text{m} \times 275 \mu\text{m}$, and 0.7 for the mesh of 47.5 $\mu\text{m} \times 27.5 \mu\text{m}$).

The character of the SIF variation curves (Figure 4b) shows that the effect of the mesh-spacing value is minimum at the stages of active loading. However, with an increase in the spacing, the descending branch of the curve departs increasingly more to the right, showing a tendency to be vertical in the limit.

Particular attention should be given to the stress behavior during the mesh refinement – under unloading, a compressive stress zone occurs in the vicinity of the crack tip. The instant of time, at which this zone begins to be fixed, and its size are essentially dependent on the spacing value in the vicinity of the crack front. Thus, for the mesh of 1000 $\mu\text{m} \times 600 \mu\text{m}$, the compressive stresses did not occur at all, whereas for the mesh of 400 $\mu\text{m} \times 275 \mu\text{m}$ they appeared at the crack tip only, at the time instant of 6400 s.

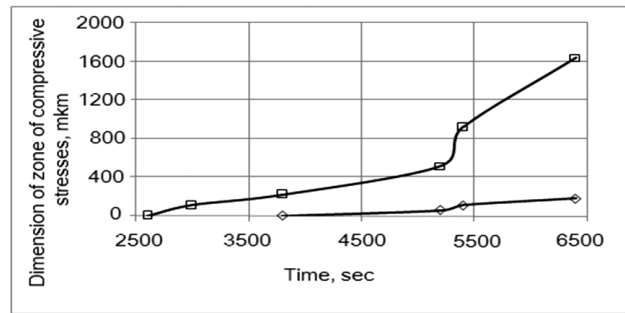


Figure 5: Plots of the time dependence of the compressive-stress-zone size in the vicinity of the crack tip: \square 21 $\mu\text{m} \times 5.5 \mu\text{m}$, \blacklozenge 47.5 $\mu\text{m} \times 27.5 \mu\text{m}$

Slika 5: Prikaz odvisnosti velikosti tlačne cone na čelu konice razpoke: \square 21 $\mu\text{m} \times 5,5 \mu\text{m}$, \blacklozenge 47,5 $\mu\text{m} \times 27,5 \mu\text{m}$

For the mesh of 21 $\mu\text{m} \times 5.5 \mu\text{m}$, the last SIF value was obtained for the time instant of 2000 s, whereas for the mesh of 1000 $\mu\text{m} \times 600 \mu\text{m}$, the SIF values were obtained up to the time instant of 6 400 s. The plots of the time dependence of the compressive-stress-zone size in the vicinity of the crack tip for the meshes of 47.5 $\mu\text{m} \times 27.5 \mu\text{m}$ and 21 $\mu\text{m} \times 5.5 \mu\text{m}$ are given in Figure 5.

6.2 Use of meshes of different densities

The solution of the problem with the finite-element method can be considered to be reliable only upon reaching the convergence. It is common practice to perform an analysis of the convergence by comparing the solutions obtained on two or more meshes, whose spacings differ by a factor of 2 to 5 times. Figure 6 compares the relative SIF values calculated on the meshes of 1000 $\mu\text{m} \times 600 \mu\text{m}$, 47.5 $\mu\text{m} \times 27.5 \mu\text{m}$ and 21 $\mu\text{m} \times 5.5 \mu\text{m}$ using the *J*- and *G*-integral concepts. At the stages of active loading, the greatest difference in the SIF values is $\approx 9 \%$ for the meshes of 1000 $\mu\text{m} \times 600 \mu\text{m}$ and 47.5 $\mu\text{m} \times 27.5 \mu\text{m}$, whereas for the mesh of 21 $\mu\text{m} \times 5.5 \mu\text{m}$ this differ-

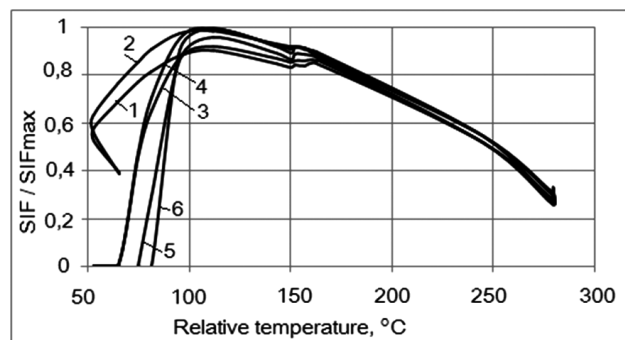


Figure 6: Plots of the relative SIF values calculated on different meshes using the *J*- and *G*-integral concepts: 1 – 1000 $\mu\text{m} \times 600 \mu\text{m}$ (*J*), 2 – 1000 $\mu\text{m} \times 600 \mu\text{m}$ (*G*), 3 – 47.5 $\mu\text{m} \times 27.5 \mu\text{m}$ (*J*), 4 – 47.5 $\mu\text{m} \times 27.5 \mu\text{m}$ (*G*), 5 – 21 $\mu\text{m} \times 5.5 \mu\text{m}$ (*J*), 6 – 21 $\mu\text{m} \times 5.5 \mu\text{m}$ (*G*)

Slika 6: Prikaz relativnih vrednosti SIF, izračunanih z različnimi mrežami, s konceptom *J*- in *G*-integrala: 1 – 1000 $\mu\text{m} \times 600 \mu\text{m}$ (*J*), 2 – 1000 $\mu\text{m} \times 600 \mu\text{m}$ (*G*), 3 – 47,5 $\mu\text{m} \times 27,5 \mu\text{m}$ (*J*), 4 – 47,5 $\mu\text{m} \times 27,5 \mu\text{m}$ (*G*), 5 – 21 $\mu\text{m} \times 5,5 \mu\text{m}$ (*J*), 6 – 21 $\mu\text{m} \times 5,5 \mu\text{m}$ (*G*)

ence is $\approx 3\%$. It can be noted that the SIF values determined using the G -integral concept turn out to be higher than those determined using the J -integral concepts, and also that with a decrease in the mesh-spacing value, the difference between the SIF values calculated with various methods decreases, too.

6.3 Determination of the allowable critical-brittleness temperature of the metal

The data of the SIF calculation for a circumferential under-the-cladding crack obtained using the J - and G -integral concepts is applied when determining the critical-brittleness temperature of the metal. A fracture-toughness curve is used, whose equation is given in^{3,9}. **Figure 7a** shows the plots of the temperature dependence of the relative SIF values $K_I(T)/K_{I\max}$ and the fracture toughness $K_{Ic}(T)/K_{Ic\max}$ for the three meshes ($1000\ \mu\text{m} \times 600\ \mu\text{m}$, $47\ \mu\text{m} \times 27.5\ \mu\text{m}$ and $21\ \mu\text{m} \times 5.5\ \mu\text{m}$) obtained using the J -integral concept. On the other hand, **Figure 7b** illustrates the plots obtained using the G -integral concept. **Table 1** summarizes the values of increments in the critical-brittleness temperature of metal ΔT_{ka} compared for the meshes of $1000\ \mu\text{m} \times 600\ \mu\text{m}$, $47\ \mu\text{m} \times 27.5\ \mu\text{m}$ and $47\ \mu\text{m} \times 27.5\ \mu\text{m}$, $21\ \mu\text{m} \times 5.5\ \mu\text{m}$.

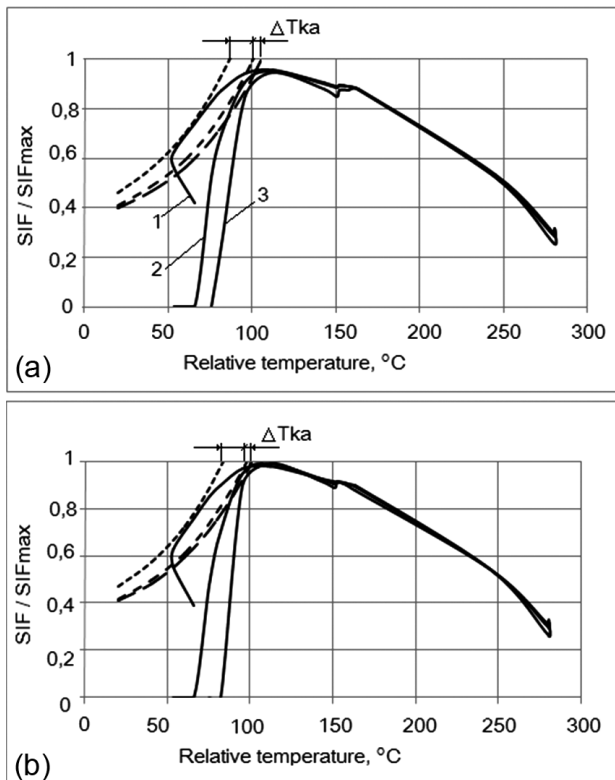


Figure 7: Determining the critical-brittleness temperature value of the metal: a) the J -integral concept; b) the G -integral concept: 1 – $1000\ \mu\text{m} \times 600\ \mu\text{m}$, 2 – $47.5\ \mu\text{m} \times 27.5\ \mu\text{m}$, 3 – $21\ \mu\text{m} \times 5.5\ \mu\text{m}$

Slika 7: Določanje vrednosti kritične temperature krhkosti kovine: a) koncept J -integrala, b) koncept G -integrala: 1 – $1000\ \mu\text{m} \times 600\ \mu\text{m}$, 2 – $47,5\ \mu\text{m} \times 27,5\ \mu\text{m}$, 3 – $21\ \mu\text{m} \times 5,5\ \mu\text{m}$

On the basis of the analysis of the results it is possible to draw a conclusion about their convergence when successively denser meshes are used.

The critical-brittleness temperature values of the metal obtained using the J -integral concept turned out to be less conservative than those obtained using the G -integral concept.

The critical-brittleness temperature value of the metal increases and becomes determined with lesser conservatism when performing a refinement of a finite-element mesh.

Table 1: Values of increments in the critical-brittleness temperature of the metal

Tabela 1: Vrednost korakov kritične temperature krhkosti kovine

Mesh, $\mu\text{m} \times \mu\text{m}$	ΔT_{ka} , J -	ΔT_{ka} , G -
$47 \times 27.5 \rightarrow 1000 \times 600$	14 °C	14 °C
$21 \times 5.5 \rightarrow 47 \times 27.5$	5 °C	3 °C

6.4 Analysis of the results obtained using the closed-crack model

Figure 8 shows the results of determining the SIF values at a deep point of the crack and at the midpoint of

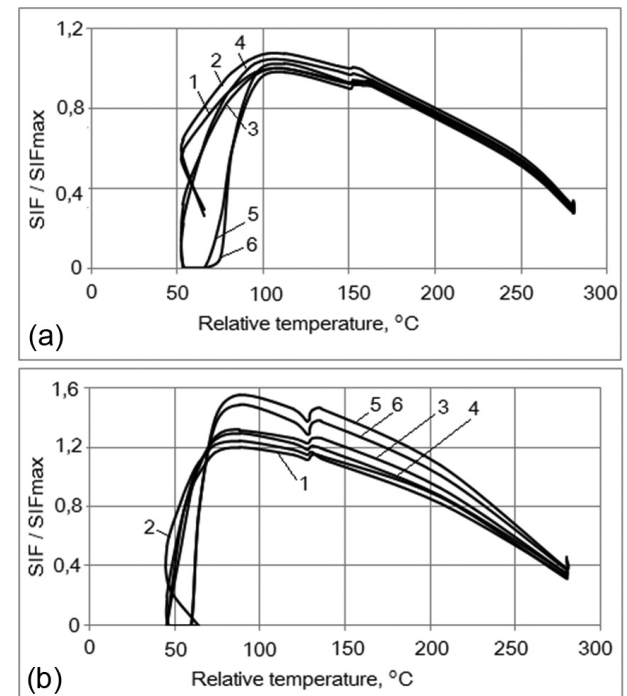


Figure 8: Plots of the relative SIF values calculated on different meshes using the J - and G -integral concepts: a) is for the deep point of the crack, b) is for the point at the boundary between the base metal and the cladding: 1 – $1100\ \mu\text{m} \times 360\ \mu\text{m}$ (J), 2 – $1100\ \mu\text{m} \times 360\ \mu\text{m}$ (G), 3 – $100\ \mu\text{m} \times 100\ \mu\text{m}$ (J), 4 – $100\ \mu\text{m} \times 100\ \mu\text{m}$ (G), 5 – $12\ \mu\text{m} \times 12\ \mu\text{m}$ (J), 6 – $12\ \mu\text{m} \times 12\ \mu\text{m}$ (G)

Slika 8: Relativne vrednosti SIF, izračunane z različnimi mrežami z uporabo koncepta J - in G -integrala: a) je za točko v globini razpoke, b) je za točko na meji med osnovnim materialom in oblogo: 1 – $1100\ \mu\text{m} \times 360\ \mu\text{m}$ (J), 2 – $1100\ \mu\text{m} \times 360\ \mu\text{m}$ (G), 3 – $100\ \mu\text{m} \times 100\ \mu\text{m}$ (J), 4 – $100\ \mu\text{m} \times 100\ \mu\text{m}$ (G), 5 – $12\ \mu\text{m} \times 12\ \mu\text{m}$ (J), 6 – $12\ \mu\text{m} \times 12\ \mu\text{m}$ (G)

the boundary between the base metal and the cladding with the use of the J - and G -integral concepts. For the deep point, the results obtained using the G -integral concept, as before, turned out to be more conservative than those obtained using the J -integral concept. At the same time, for the point at the boundary between the base metal and the cladding, the results obtained using the J -integral concept turned out to be more conservative than those obtained with the G -integral concept. For this point, the maximum difference in the SIF values determined using both concepts was approximately $\approx 5\%$.

7 CONCLUSIONS

The SIF determination methods based on the use of the J - and G -integral concepts were analyzed for a typical regime of the WWER-1000 RPV emergency cooling.

When solving the problem of an elastic and elasto-plastic formulation without taking into account the loading history, the difference in the SIF values is negligible, corresponding to the theoretical statements about the equality of J and G integrals.

The results of the SIF calculation obtained using the initial full model of the RPV – with a built-in crack and without it – practically coincide, which testifies to the uselessness of the crack embedding into the initial full model of the RPV. However, according to the requirements of the IAEA (International Atomic Energy Agency), a crack is to be built in the RPV fragment under consideration.

It was shown that when solving the problem of the elasto-plastic formulation on the basis of the flow theory under non-proportional loading, the SIF values obtained using J - and G -integral concepts are in agreement even at the stages of unloading, although the use of the J -integral concept under these conditions contradicts the theory statements.

The results of the SIF calculation using the G -integral concept are more conservative than those obtained using the J -integral concept.

The character of the temperature dependence of the fracture parameters – the stress at the crack tip and SIF –

at the stages of unloading was shown to be considerably dependent on the density of the employed finite-element mesh. With a decrease in the size of the finite element in the vicinity of the crack front, an increase in the size of the compressive-stress zone is observed, and the descending branch of the SIF curve tends to become practically vertical. The analysis of the behavior of the fracture-parameter curves points to the convergence of the results, which is a necessary condition for solving the problem with the finite-element method. However, the use of the temperature dependence of SIF constructed from the solution of the problem on a dense finite-element mesh for the purpose of determining the brittleness temperature of the metal results in obtaining, as far as we know, less conservative results than those obtained using the curve constructed from the problem solution on a coarse finite-element mesh.

8 REFERENCES

- ¹ Z. Chen, The finite element method – Its fundamentals and applications in engineering, World Scientific, New Jersey 2011
- ² D. Kovacevic, I. Budak, A. Antic, B. Kosec, Special finite elements; theoretical background and application, Technical Gazette, 18 (2011) 4, 649–655
- ³ Authorizing Document of the Operating Organization 0606-2005, Procedure of calculating for brittle fracture resistance of WWER nuclear reactor pressure vessels (RPV – BFR – 2004), St. Petersburg, Moscow, 2004
- ⁴ A.Yu. Chirkov, Mixed finite element method scheme for solving boundary-value problems of the elasticity theory and small elasto-plastic strains, Publishing House of the Institute for Problems of Strength, Kiev 2003
- ⁵ G. P. Cherepanov, Brittle Fracture Mechanics, Nauka, Moscow 1974
- ⁶ H. G. deLorenzi, On the energy release rate and the J -integral for 3-D crack configurations, Int. Journ. of Fracture, 19 (1982), 182–193
- ⁷ S. N. Atluri (ed.), Computational Methods in Fracture Mechanics, Mir, Moscow 1990
- ⁸ A. Yu. Chirkov, Development and implementation of the mixed finite element method in problems of vibration stability and structural element strength, PhD Thesis, Kiev, 2008 (in Russian)
- ⁹ Standard Document 0.03.391-09, Procedure for assessing the strength and in-service life of WWER RPV, Kiev, 2009

DISSOLUTION OF A COPPER WIRE DURING A HOT-DIPPING PROCESS USING A SnCu1 LEAD-FREE SOLDER

RAZTAPLJANJE BAKRENE ŽICE MED VROČIM OMAKANJEM PRI UPORABI SPAJKE BREZ SVINCA SnCu1

Darja Steiner Petrovič¹, Jožef Medved², Grega Klančnik^{2,3}

¹Institute of Metals and Technology, Lepi pot 11, 1000 Ljubljana, Slovenia

²University of Ljubljana, Faculty of Natural Sciences and Engineering, Aškerčeva 12, 1000 Ljubljana, Slovenia

³Institute for Foundry and Heat Treatment, Litostrojska 60, 1000 Ljubljana, Slovenia
darja.steiner@imt.si

Prejem rokopisa – received: 2013-09-04; sprejem za objavo – accepted for publication: 2013-10-28

Thermodynamic arguments and calculations were used to describe a complete dissolution of a copper wire in a SnCu1 lead-free solder during hot-dipping at 400 °C. For the calculation of the phase diagram the newly reviewed Gibbs energies of the phases were used. The experimental investigation involved a visual inspection, stereomicroscopy, scanning electron microscopy (FE-SEM/EDX) and a thermal analysis (DSC). The results showed that the dissolution of the copper wire during hot dipping at a selected working temperature can be attributed to the increased solubility of the copper in the liquid solder and a prolonged time of dipping. Thus, the applied temperature was too high for the geometry, the volume-to-surface ratio, of the selected fuse element. Laboratory simulation tests performed at 303 °C showed a much slower kinetics for the Cu pick-up.

Keywords: lead-free solder, copper, dissolution, hot dipping, thermodynamics

Neželeno raztapljanje tanke bakrene žice v kopeli spajke SnCu1 pri temperaturi 400 °C smo opisali s termodinamičnimi argumenti in izračuni. Za izračun faznega diagrama smo uporabili na novo optimirane Gibbsove energije posameznih faz. Eksperimentalno delo je obsegalo vizualni pregled, stereomikroskopijo, vrstično elektronsko mikroskopijo (FE-SEM/EDX) in termično analizo (DSC). Rezultati so pokazali, da je raztapljanje bakrene žice med omakanjem na izbrani delovni temperaturi posledica povečane topnosti bakra v talini spajke in predolgega časa omakanja za dano geometrijo bakrene žice, predvsem velikega razmerja med površino in prostornino. Laboratorijski simulacijski preizkusi, izvedeni pri temperaturi 303 °C, so pokazali veliko počasnejšo kinetiko raztapljanja tanke bakrene žice.

Ključne besede: spajke brez svinca, baker, raztapljanje, omakanje, termodinamika

1 INTRODUCTION

Fuses consist of one or more metallic conductors, known as the fuse element, and usually have a cylindrical or flat strip form. The surrounding media are granular silica quartz (SiO₂) in high-breaking-capacity (HBC) fuses, and boric acid in expansion fuses. The element and the surroundings are housed in a body of an insulating material (ceramic, fibre, melamine, etc.). The fuse element's edges are usually soldered to, or in an electric contact with, the fuse end caps.¹

Another process used in the electronics industry for the coating of copper wires is hot dipping. The process is carried out by immersing a pre-treated (e.g., cleaned, etched) substrate in a bath of a molten solder metal, or an alloy, for a specific time.

In recent years a new generation of solders has been developed in order to replace Pb-Sn solders with lead-free solder alloys. Many of the proposed alloy systems are Sn-rich alloys. Thermodynamic properties play a crucial role in the development of the new solder materials.²⁻⁵ Although a thermodynamic assessment cannot cover the whole situation relating to kinetic problems, the driving forces and formation energies of intermetallic compounds, which are the most important

parameters in the growth kinetics, may be subjected to the thermodynamics of the system. A precise thermodynamic assessment of a Cu-Sn system was given by Shim et al.² New data is not only essential for a new alloy design but also very important for understanding the reactions between solder alloys and substrate materials.

The major factors affecting a solder selection are the melting point of an alloy, the wetting characteristics, the cost, the availability, the environmental friendliness, etc. Reliability-related properties include the electrical and thermal conductivities, the mechanical strength, the shear and tensile properties, the fatigue resistance, the corrosion and oxidation resistance, the coefficient of thermal expansion and the formation of intermetallic compounds.⁶

The three major chemical properties affecting the use and the long-term reliability of solders⁶ are as follows:

- the solubility of Cu in the solder,
- the resistance to corrosion,
- the oxidation behaviour.

In the literature a lot of data about the formation of intermetallic compounds (IMCs) is available. Investigations of interfacial interactions and the formation of

IMCs involving a solid substrate and liquid soldering alloys have mainly focused on simple geometries, holding the solder joint above the melting temperature of the solder alloy at a single interface and then maintaining the system under isothermal conditions.⁷⁻⁹

The aim of the present case study was to highlight the thermodynamic background of an undesirable dissolution of a fuse element (in this case a copper wire) at the temperature of interest, in the process of hot dipping using an Sn-Cu lead-free solder. For the calculation of a phase diagram, the reviewed Gibbs energies of phases were modelled using substitutional and stoichiometric models. The optimized parameters are presented in Appendix A.

In the investigation, a visual inspection, chemical analysis, stereomicroscopy, scanning electron microscopy (FE-SEM/EDS) and thermal analysis (DSC) were carried out. In addition, thermodynamic calculations using ThermoCalc were performed in order to determine the failure analysis. The copper dissolution was investigated by hot dipping the Cu wire into a SnCu1 soldering bath.

2 EXPERIMENTAL WORK

The specimens under investigation were a mass fraction 99.9 % Cu wire and a lead-free solder declared as SnCu1, both of which are used in industrial production processes for special-purpose fuses (**Table 1**).

The cross-sections of the materials under investigation were metallographically prepared by grinding and polishing. FE-SEM/EDX analyses were performed on these cross-sections using a JEOL JSM 6500-F electron microscope. An X-Ray fluorescence spectrometer (Thermo Scientific Niton) was used to determine the chemical composition of the solder alloy.

The thermal analysis was performed using differential scanning calorimetry (DSC) in an STA-449 C Jupiter, Netzsch instrument. The DSC experiments were conducted under the static atmosphere of argon of a volume fraction 99.999 % purity to minimize the surface oxidation. The empty corundum crucible was taken as a reference. The linear temperature program for the heating was as follows: 25 °C to 280 °C to 25 °C. The heating rate was taken to be 5 K/min to minimize the effects relating to the apparatus and hysteresis of the characteristic temperatures (emphasis was given to a determination of the liquidus temperature). There was no isothermal step at the maximum temperature in order to avoid a possible loss of elements. The liquidus temperature was estimated assuming that the peak temperature of the last thermal event during heating represents the liquidus temperature.¹⁰ The solidus temperature was taken as the onset of the melting during heating. The construction of the tangents for the solidus temperature was made on the DSC cooling curve with an extrapolation of the peak slope down to the baseline.

The copper dissolution was investigated by hot dipping the Cu-wire in a SnCu1 soldering bath. The tests were performed at 400 °C and 303 °C. For the temperature control a K-type thermocouple was used, protected with a corundum tube and immersed into the soldering bath. The dipping was done in air atmosphere as the common procedure of preparing the SnCu coatings.

2.1 Thermodynamic model

The thermodynamic calculations for the Cu-Sn binary system were performed with ThermoCalc Classic (TCC). Additionally, a computer simulation of the solidification of the selected solder alloy was performed with the Scheil-Gulliver model for simulating the solidification path, knowing that an equilibrium distribution of the elements is inhibited with the relatively high cooling rates after the hot-dipping process. The thermodynamic calculations were done using various models for describing the Gibbs energies of phases.

2.2 Substitutional model

The disordered solution phases and their Gibbs free energies, G_m^P , of fcc, liquid and bcc are described with the following equation:

$$G_m^P = X_{Cu} {}^0G_{Cu}^P + X_{Sn} {}^0G_{Sn}^P + RT(X_{Cu} \ln X_{Cu} + X_{Sn} \ln X_{Sn}) + {}^{ex}G_m^P$$

where ${}^{ex}G_m$, X_{Cu} , R and T represent the excess molar Gibbs energy, the molar fraction of Cu, the gas constant (8.314 J mol⁻¹ K⁻¹) and the temperature (K) represent the molar Gibbs energy of pure Cu in the P phase (liquid, fcc, bcc). The Gibbs energy of pure element Cu in the P phase is given relative to SER (the standard element reference of 298.15 K). The excess contribution is modelled as:

$${}^{ex}G_m^P = X_{Cu} X_{Sn} ({}^0L_{CuSn}^P + {}^1L_{CuSn}^P (X_{Cu} - X_{Sn}) + {}^2L_{CuSn}^P (X_{Cu} - X_{Sn})^2)$$

representing a deviation from the ideal solution.

2.3 Stoichiometric model

The stoichiometric phases (Cu₃Sn, Cu₄₁Sn₁₁, Cu₁₀Sn₃ and Cu₆Sn₅) were modelled using the following formulation of the Gibbs energy with reference to the enthalpies of pure Cu and Sn in phase Φ (298.15 K):

$$G_m^{Cu_p Sn_q}(T) - p {}^0H_{Cu}^\Phi - q {}^0H_{Sn}^\Phi = \Delta_f G_{Cu_p Sn_q}(T) + p \cdot GSERCU(T) + q \cdot GHSERSN(T)$$

where $\Delta_f G_{Cu_p Sn_q}(T)$ represents the standard Gibbs free energy. Normally, this is represented with the linear temperature dependence:

$$\Delta_f G_{Cu_p Sn_q}(T) = a + b \cdot T$$

where a and b represent the optimized parameters. GHSERCU and GHSERSN are the Gibbs free energies of pure elements, Cu and Sn, also relative to the stable state at 298.15 K. The two-sublattice model can be represented with $(\text{Cu})_p(\text{Sn})_q$. The p and q symbols represent the atomic ratio (the location of a phase). The D03 phase, with a larger solubility, was modelled with a two-sublattice model: $(\text{Cu},\text{Sn})_{0.75}(\text{Sn},\text{Cu})_{0.25}$. More details are given in².

3 RESULTS AND DISCUSSION

Copper wire is used in the production of fuses. It has a widespread use in electronic applications due to its superior thermal and electrical conductivities. In this case study a commercial copper coil with a diameter $d = \pm 0.15$ mm was investigated (**Figure 1**).

Problems occurred when, in the industrial process of hot dipping, the Pb-Sn solder was replaced with a Sn-Cu lead-free solder (**Figure 2**). After a few seconds in the solder bath, declared as SnCu1, heated to $T = 400$ °C, the copper wire was completely dissolved.

The DSC melting curve of the solder material was performed to determine its liquidus temperature, which gives very important information required for determining the optimum parameters of hot dipping. The DSC melting curve obtained at a heating rate of 5 K/min is presented in **Figure 3**. The T_{onset} of the major endothermic reaction was around 223.9 °C. The enthalpy of this endothermic reaction was 48.15 J/g.

From the DSC response during heating, it is clear that the chemical composition of the investigated Sn-Cu alloy is very close to the eutectic composition. For non-eutectic compositions the melting curve would show a splitting into two separate peaks due to the sample containing the Cu solid solution in Sn and the eutectic.¹¹

Additionally, the chemical composition of the solder material of the Sn-Cu alloy system was identified using

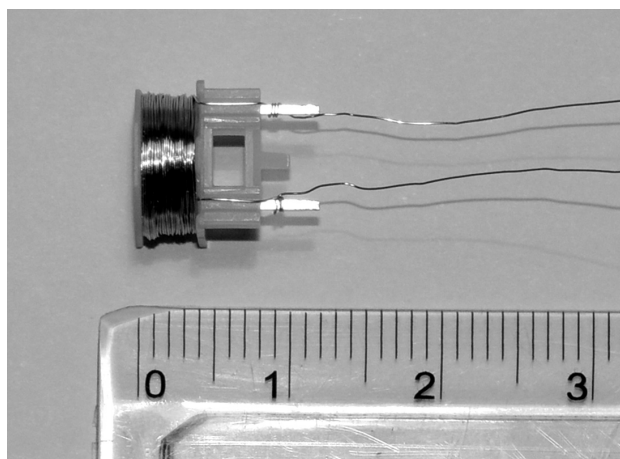


Figure 1: Fuse element (a Cu-coil)

Slika 1: Bakrena žica za varovalko

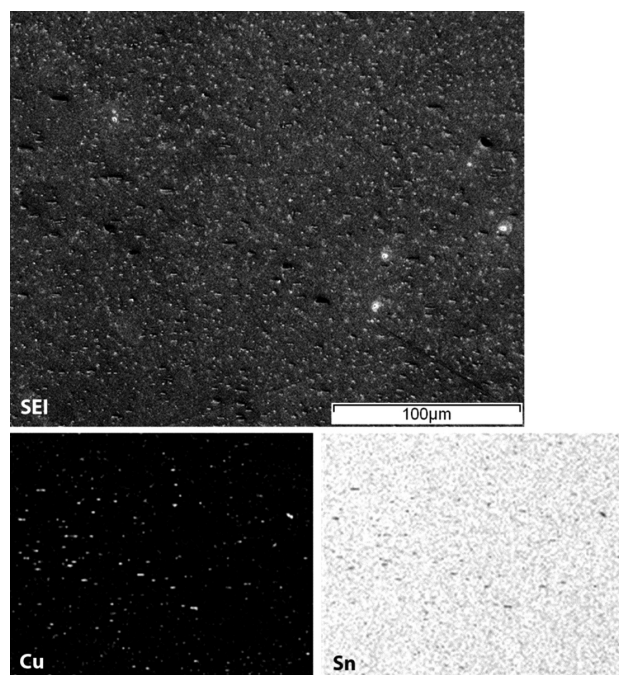


Figure 2: SE image and the corresponding X-ray elemental mapping showing the distribution of Cu and Sn in the solder

Slika 2: SEM-posnetek spajke in porazdelitev elementov Cu in Sn (EDX)

X-Ray fluorescence spectrometry. The chemical composition of the solder is given in **Table 1**.

Table 1: Chemical composition of the lead-free Sn-Cu solder in mass fractions ($w/\%$)

Tabela 1: Kemijska sestava spajke Sn-Cu v masnih deležih ($w/\%$)

	$w(\text{Sn})/\%$	$w(\text{Cu})/\%$
Solder Sn-Cu	99.183 ± 0.648	0.785 ± 0.034

The eutectic Sn-Cu solder alloy is one of the most popular lead-free alloys used for soldering in electronic applications.¹²

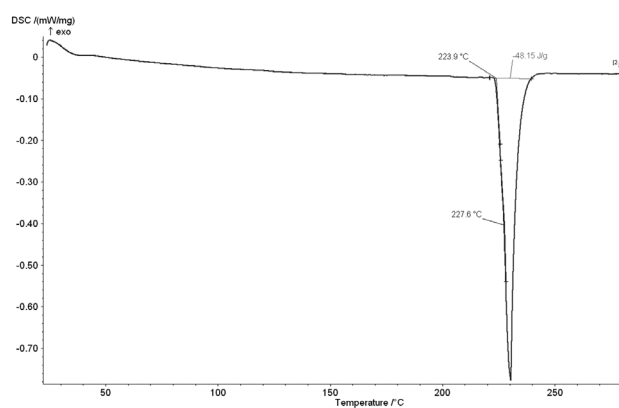


Figure 3: DSC heating curve for the solder material (the heating rate of 5 K/min)

Slika 3: DSC segrevalna krivulja za zlitino spajke (hitrost ogrevanja 5 K/min)

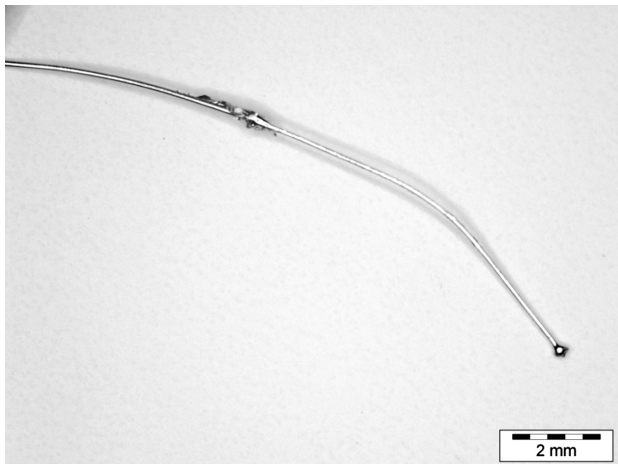


Figure 4: Cu wire after hot dipping in the SnCu1 bath at 303 °C for 10 s

Slika 4: Bakrena žica po omakanju pri temperaturi 303 °C, 10 s v kopeli SnCu1

Table 2: Average consumption of the Cu wire Δd during hot dipping at 303 °C in mass fractions

Tabela 2: Povprečno odtapljanje bakrene žice Δd med omakanjem pri 303 °C v masnih deležih

$T/^\circ\text{C}$	t/s	$\Delta d/\%$
303	10	30
303	20	60

The ability of a solder bath to pick up copper is directly related to the solubility of Cu in the major constituents.⁶ The dissolution kinetics of Cu in soldering reactions with Sn-Pb and Sn-Ag solders has already been described in^{13,14}.

In the present study the consumption of a Cu wire was investigated during the hot dipping of the wire into the soldering bath at 400 °C. At this temperature the soldering bath aggressively dissolves the whole of the Cu wire on contact. It has been reported that the suitable temperature to perform the soldering with the eutectic

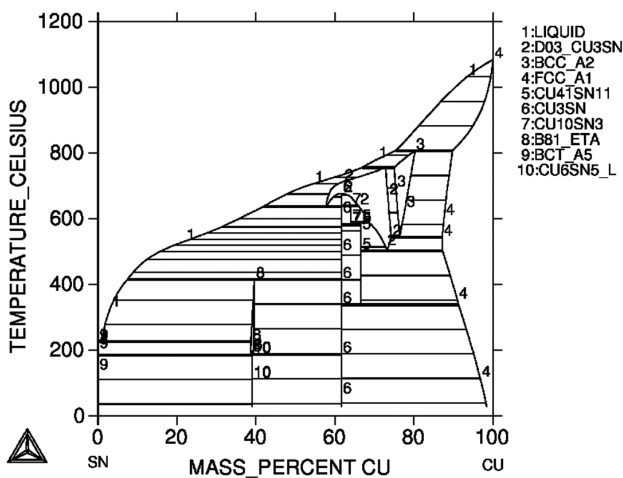


Figure 5: Binary phase diagram for Cu-Sn

Slika 5: Binarni fazni diagram Cu-Sn

Sn-0.7Cu alloy is 303 °C, because at this temperature the solder exhibits the lowest value of the surface tension.¹²

For this reason, comparison tests were also performed at 303 °C, showing much slower kinetics for the Cu pick-up. The results of the hot dipping at 303 °C are given in **Table 2**.

It was confirmed that a Cu wire with a diameter of approximately 140 μm to 153 μm is completely dissolved after a few seconds of being dipped in the solder bath at $T = 400$ °C. On the other hand, at $T = 303$ °C, the average Cu consumption measured after 10 s (**Figure 4**) and 20 s, as the difference between the initial diameter and that after hot dipping, was 30 % and 60 %, respectively.

The problem of the rapid dissolution of a Cu wire in a liquid solder can also be described using thermodynamic arguments. Using the CALPHAD method (CALculation of PHase Diagrams) the phase equilibria can be calculated with the relative Gibbs free energies of the phases present in a particular system.¹⁵ It is clear from the Cu-Sn phase diagram in **Figure 5** that the solid solubility of Cu in Sn at room temperature is practically zero. However, as the temperature increases, the solubility of Cu in Sn increases appreciably. The optimized parameters taken for the Cu-Sn system² are presented in Appendix A.

According to the Scheil-Gulliver model the liquidus temperature is 228 °C for Sn-0.7Cu (**Figure 6**). The calculated solidification process is in good agreement with the experimental one (**Figure 3**). With a decreasing temperature, the solidification of the liquid phase proceeds with the precipitation of Sn (the bct phase). Below 220 °C the precipitation of the fcc intermetallic takes place. The mass-fraction of all the stable phases in the Sn-0.7Cu system is presented in **Figure 7**.

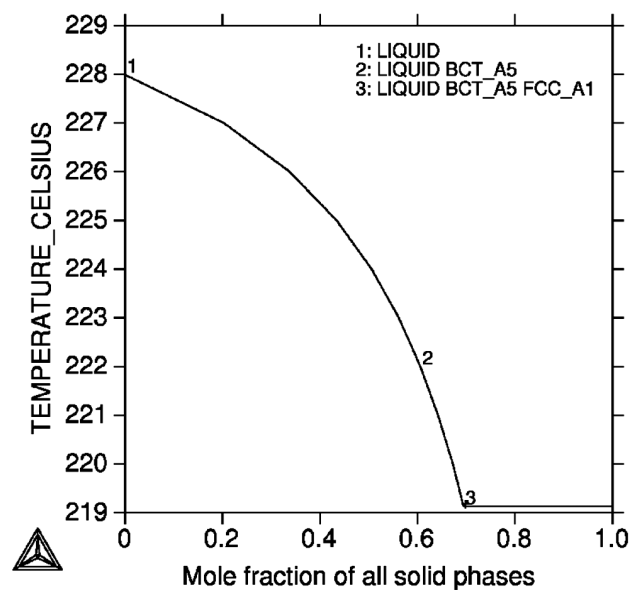


Figure 6: Solidification sequence of the Sn-0.7Cu alloy

Slika 6: Potek strjevanja zlitine Sn-0,7Cu

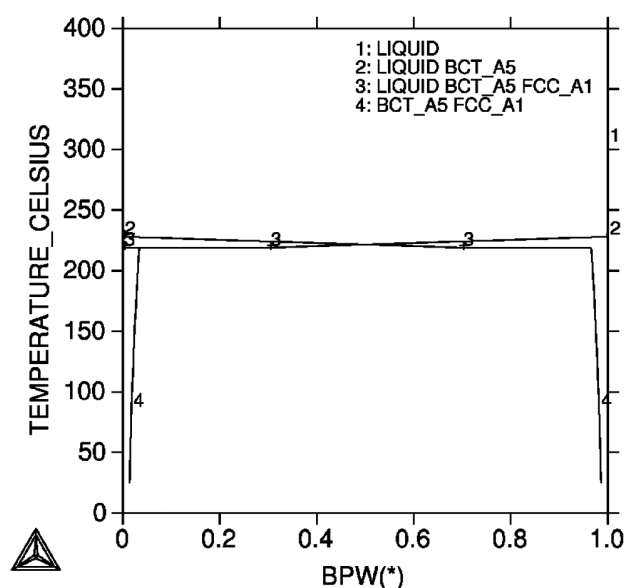


Figure 7: Mass fraction of stable phases in the Sn-0.7Cu system
Slika 7: Masni delež stabilnih faz v sistemu Sn-0,7Cu

During the soldering operation, materials from the solid substrate dissolve and mix with the solder, allowing a formation of intermetallic compounds (IMCs). It has been found that in Cu-Sn systems the formation of Cu_6Sn_5 is usually followed by Cu_3Sn .^{7,8} A compressive stress is generated as a result of the volume expansion during the growth of IMCs, especially Cu_6Sn_5 .^{16,17} The initial formation of Cu_6Sn_5 , followed by Cu_3Sn , can be attributed to a larger driving force for the precipitation of Cu_6Sn_5 during the early stages of the Cu/Sn reaction. Furthermore, the Cu/Sn interface is typically covered by a Cu_6Sn_5 layer within a few milliseconds. After a prolonged Cu_6Sn_5 layer growth, Cu_3Sn begins to appear at the Cu/ Cu_6Sn_5 interface.^{8,9}

The growth of IMCs as a result of the interactions between the eutectic Sn-0.7Cu solder and the Cu-based alloy was studied by Dariavach et al.¹⁸ A thick scallop layer of η - Cu_6Sn_5 and a thin layer of ε - Cu_3Sn were observed at the interface. The total thickness of IMCs and the grain size of the η -phase increased with the increasing soldering time.¹⁸ As the interfacial reaction occurs between the substrate and the molten solder, the liquid structure of the solder significantly affects the reaction and the formation of interfacial compounds.

4 CONCLUSIONS

The thermodynamic assessment of Shim et al.² was the basis for the thermodynamic description of a Sn-Cu system. The optimization was performed using ThermoCalc Classic (TCC). The optimized parameters of the phases of interest in the Sn-Cu system are listed in Appendix A. The thermodynamic data were used to describe a complete dissolution of a Cu wire in a SnCu1 lead-free solder during hot dipping at 400 °C.

The melting behaviour as well as the chemical analysis of the investigated solder declared as SnCu1 confirmed the chemical composition of Sn-Cu to be very close to the eutectic one. The measured liquidus temperature was approximately 228 °C.

According to the Sn-Cu binary phase diagram the solubility of copper in tin increases with the temperature.

A rapid dissolution of the copper wire during hot dipping at the working temperature $T = 400$ °C is attributed to the increased solubility of copper in a liquid solder. The applied temperature was too high for the geometry of the selected fuse element (0.15-mm thick copper wire).

The kinetics of the Cu dissolution in the Sn-Cu solder was much slower at 303 °C. The average copper consumption measured after 10 s and 20 s was approximately 30 % and 60 %, respectively.

Better results for hot dipping would be obtained by lowering the temperature of the solder bath so that the layer of intermetallic compounds (IMCs) would form on the interface between the solder bath and the copper fuse element. By lowering the working temperature for hot dipping, the solubility of copper in the solder would decrease and the nucleation of IMCs would be ensured.

Appendix A: Optimized parameters for the Sn-Cu phase diagram²

```
LIQUID
CONSTITUENTS: CU,SN
G(LIQUID,CU;0)-H298(FCC_A1,CU;0) =
  298.15<T< 1358.02:
+12964.736-9.511904*T-5.849E-21*T**7+GHSERCU
  1358.02<T< 3200.00: +13495.481-9.922344*T-3.642E+29*T**(-9)
+GHSERCU
G(LIQUID,SN;0)-H298(BCT_A5,SN;0) =
  100.00<T< 505.08: +7103.092-14.087767*T+1.47031E-18*T**7
+GHSERSN
  505.08<T< 3000.00: +6971.587-13.814382*T+1.2307E+25*T**(-9)
+GHSERSN
L(LIQUID,CU,SN;0) = -9002.8-5.8381*T
L(LIQUID,CU,SN;1) = -20100.4+3.6366*T
L(LIQUID,CU,SN;2) = -10528.4
BCC_A2
2 SUBLATTICES, SITES 1: 3
CONSTITUENTS: CU,SN : VA
G(BCC_A2,CU:VA;0)-H298(FCC_A1,CU;0) = +GCUBCC
G(BCC_A2,SN:VA;0)-H298(BCT_A5,SN;0) = +GSNBCC
L(BCC_A2,CU,SN:VA;0) = -44821.6+51.2164*T
L(BCC_A2,CU,SN:VA;1) = -6876.5-56.4271*T
BCT_A5
CONSTITUENTS: CU,SN
G(BCT_A5,CU;0)-H298(FCC_A1,CU;0) = +GCUBCT
G(BCT_A5,SN;0)-H298(BCT_A5,SN;0) = +GHSERSN
L(BCT_A5,CU,SN;0) = 21000
CU10SN3
2 SUBLATTICES, SITES .769: .231
CONSTITUENTS: CU : SN
G(CU10SN3,CU:SN;0)-0.769 H298(FCC_A1,CU;0)-0.231
H298(BCT_A5,SN;0) =
-6655-1.4483*T+.769*GHSERCU+.231*GHSERSN
CU3SN
```

2 SUBLATTICES, SITES .75: .25
 CONSTITUENTS: CU : SN
 $G(\text{CU3SN,CU:SN};0) - 0.75 \text{ H298}(\text{FCC_A1,CU};0) - 0.25 \text{ H298}(\text{BCT_A5,SN};0) =$
 $-8194.2 - 2043 * T + 7.75 * \text{GHSERCU} + 2.25 * \text{GHSERSN}$
 CU41SN11
 2 SUBLATTICES, SITES .788: .212
 CONSTITUENTS: CU : SN
 $G(\text{CU41SN11,CU:SN};0) - 0.788 \text{ H298}(\text{FCC_A1,CU};0) - 0.212 \text{ H298}(\text{BCT_A5,SN};0) =$
 $-6323.5 - 1.2808 * T + 7.788 * \text{GHSERCU} + 2.12 * \text{GHSERSN}$
 CU6SN5
 2 SUBLATTICES, SITES .545: .455
 CONSTITUENTS: CU : SN
 $G(\text{CU6SN5,CU:SN};0) - 0.545 \text{ H298}(\text{FCC_A1,CU};0) - 0.455 \text{ H298}(\text{BCT_A5,SN};0) =$
 $-6869.5 - 1.589 * T + 5.45 * \text{GHSERCU} + 4.55 * \text{GHSERSN}$
 CU6SN5_L
 2 SUBLATTICES, SITES .545: .455
 CONSTITUENTS: CU : SN
 $G(\text{CU6SN5_L,CU:SN};0) - 0.545 \text{ H298}(\text{FCC_A1,CU};0) - 0.455 \text{ H298}(\text{BCT_A5,SN};0) =$
 $-7129.7 + 4.059 * T + 5.45 * \text{GHSERCU} + 4.55 * \text{GHSERSN}$
 DO3
 2 SUBLATTICES, SITES .75: .25
 CONSTITUENTS: CU,SN : CU,SN
 $G(\text{DO3,CU:CU};0) - \text{H298}(\text{FCC_A1,CU};0) = +\text{GCUBCC}$
 $G(\text{DO3,SN:CU};0) - 0.25 \text{ H298}(\text{FCC_A1,CU};0) - 0.75 \text{ H298}(\text{BCT_A5,SN};0) =$
 $+116674.85 + 4.8166 * T + 7.75 * \text{GSNBCC} + 2.25 * \text{GCUBCC}$
 $G(\text{DO3,CU:SN};0) - 0.75 \text{ H298}(\text{FCC_A1,CU};0) - 0.25 \text{ H298}(\text{BCT_A5,SN};0) =$
 $-10029.85 + 0.0285 * T + 7.75 * \text{GCUBCC} + 2.25 * \text{GSNBCC}$
 $G(\text{DO3,SN:SN};0) - \text{H298}(\text{BCT_A5,SN};0) = +\text{GSNBCC}$
 $L(\text{DO3,CU:CU,SN};0) = -1857.8 - 2.5311 * T$
 $L(\text{DO3,CU:CU,SN};1) = -2.9894 * T$
 $L(\text{DO3,CU,SN:SN};0) = +45850 - 42.2191 * T$
 FCC_A1
 2 SUBLATTICES, SITES 1: 1
 CONSTITUENTS: CU,SN : VA
 $G(\text{FCC_A1,CU:VA};0) - \text{H298}(\text{FCC_A1,CU};0) = +\text{GHSERCU}$
 $G(\text{FCC_A1,SN:VA};0) - \text{H298}(\text{BCT_A5,SN};0) = +\text{GSNFCC}$
 $L(\text{FCC_A1,CU,SN:VA};0) = -11106.95 + 2.0791 * T$
 $L(\text{FCC_A1,CU,SN:VA};1) = -15718.02 + 5.92467 * T$

Acknowledgements

The authors would like to acknowledge ETI, d. d., Izlake, Slovenia, for the supply of the specimens. The work was also supported by the Slovenian Research Agency (Pr. No. P2-0050 and P2-0344).

5 REFERENCES

- C. S. Psomopoulos, C. G. Karagiannopoulos, Temperature distribution of fuse elements during the pre-arcing period, *Electric Power Sys Res*, 61 (2002), 161–167
- J. H. Shim, C. S. Oh, B. J. Lee, D. N. Lee, Thermodynamic assessment of the Cu-Sn system, *Z Metallkd*, 87 (1996), 205–212
- S. Amore, S. Delsante, N. Parodi, G. Borzone, Calorimetric Investigation of the Cu-Sn-Bi lead-free solder system, *J Therm Anal Calorim*, 92 (2008), 227–232
- W. Chen, J. Kong, W. J. Chen, Effect of rare earth Ce on the microstructure, physical properties and thermal stability of a new lead-free solder, *J Mining Metallurgy B*, 47 (2011), 11–21
- P. Fima, A. Gazda, Thermal analysis of selected Sn-Ag-Cu alloys, *J Therm Anal Calorim*, 112 (2013), 731–737
- M. Abteu, G. Selvaduray, Lead-free solders in microelectronics, *Material Sci Engin*, 27 (2000), 95–141
- M. S. Park, R. Arroyave, Early stages of intermetallic compound formation and growth during lead-free soldering, *Acta Mater*, 58 (2010), 4900–4910
- M. S. Park, R. Arroyave, Concurrent nucleation, formation and growth of two intermetallic compounds (Cu6Sn5 and Cu3Sn) during the early stages of lead-free soldering, *Acta Mater*, 60 (2012), 923–934
- M. S. Park, S. L. Gibbons, R. Arroyave, Phase-field simulations of intermetallic compound growth in Cu/Sn/Cu sandwich structure under transient liquid phase bonding conditions, *Acta Mater*, 60 (2012), 6278–6287
- W. J. Boettinger, U. R. Kattner, K. W. Moon, J. H. Perepezko, DTA and Heat-flux DSC Measurements of Alloy Melting and Freezing, Special publication 960-15, National Institute of Standards and Technology, Washington 2006, 1–90
- A. S. Pedersen, N. Pryds, S. Linderth, P. H. Larsen, J. Kjoller, The determination of dynamic and equilibrium solid/liquid transformation data for Sn-Pb using DSC, *J Therm Anal Calorim*, 64 (2001), 887–894
- P. K. N. Satyanarayan, Reactive wetting, evolution of interfacial and bulk IMCs and their effect on mechanical properties of eutectic Sn-Cu solder alloy, *Adv Colloid Interface Sci*, 166 (2011), 87–118
- H. K. Kim, K. N. Tu, Rate of consumption of Cu in soldering accompanied by ripening, *Appl Phys Lett*, 67 (1995), 2002–2004
- A. Sharif, Y. C. Chan, Dissolution kinetics of BGA Sn-Pb and Sn-Ag solders with Cu substrates during reflow, *Mater Sci Eng B*, 106 (2004), 126–131
- H. L. Lukas, S. G. Fries, B. Sundman, *Computational Thermodynamics, The Calphad Method*, Cambridge University Press, Cambridge 2007
- A. Skwarek, M. Pluska, J. Ratajczak, A. Czerwinski, K. Witek, D. Szwagierczak, Analysis of tin whisker growth on lead-free alloys with Ni presence under thermal shock stress, *Mater Sci Eng B*, 176 (2011), 352–357
- A. Skwarek, M. Pluska, A. Czerwinski, K. Witek, Influence of laminate type on tin whisker growth in tin-rich lead-free solder alloys, *Mat Sci Eng B*, 177 (2012), 1286–1291
- N. Dariavach, P. Callahan, J. Liang, R. Fournelle, Intermetallic growth kinetics for Sn-Ag, Sn-Cu, and Sn-Ag-Cu lead-free solders on Cu, Ni, and Fe-42Ni substrates, *J Electron Mater*, 35 (2006), 1581–1591

STRUCTURAL CHARACTERIZATION OF PLATINUM FOIL FOR NEURAL STIMULATING ELECTRODES USING A FOUR-POINT RESISTIVITY-MEASURING DEVICE

STRUKTURNE LASTNOSTI PLATINSKE FOLIJE ZA ELEKTRODE PRI STIMULACIJI ŽIVCEV, UGOTOVLJENE Z NAPRAVO ZA ŠTIRITOČKOVNO MERJENJE UPORNOSTI

**Polona Pečlin¹, Milan Bizjak², Marko Pribošek³, Matjaž Godec⁴, Samo Ribarič⁵,
Janez Rozman¹**

¹Centre for Implantable Technology and Sensors, Itis, d. o. o. Ljubljana, Lepi pot 11, 1000 Ljubljana, Slovenia

²Department of Materials and Metallurgy, Faculty of Natural Sciences and Engineering, University of Ljubljana, Aškerčeva cesta 12, 1000 Ljubljana, Slovenia

³Marko Pribošek, zasebni raziskovalec, Pot v smrečje 11, 1000 Ljubljana, Slovenia

⁴Institute of Metals and Technology, Lepi pot 11, 1000 Ljubljana, Slovenia

⁵Institute of Pathophysiology, Medical Faculty, University of Ljubljana, Zaloška 4, 1000 Ljubljana, Slovenia
janez.rozman@guest.arnes.si

Prejem rokopisa – received: 2013-09-25; sprejem za objavo – accepted for publication: 2013-10-07

In the past few decades, considerable efforts have been devoted to develop neuroprosthetics that interface selectively with the human nervous system via multi-electrode spiral cuffs, using implantable electronic devices. The objective of this study was to investigate the structural properties of a cold-rolled platinum foil used to manufacture multi-electrode spiral nerve cuffs. To achieve this objective, thick cold-rolled platinum foil strips 0.03 mm with 99.99 % purity were used. For this purpose, the strips were mounted into the sample holder within the furnace of a custom-designed set-up. The resistivity measurements were made using a 4-point probe technique in which the strips were subjected to dynamic annealing in an argon atmosphere within the temperature range between room temperature and 900 °C. Finally, the microstructures of the strips, prepared using standard metallographic techniques, were investigated using light microscopy. In the resistivity measurements, a small change is observed at ≈ 280 °C. This change could be explained as the partial recovery elicited by a decrease of the dislocation density. Above 500 °C, a significant decrease in the resistivity was recorded, and the decrease reached a maximum at ≈ 750 °C. These results provide a deeper insight into the fabrication of platinum foil to be used in the further development of multi-electrode neural stimulating spiral cuffs. The most important finding is that the results of the resistivity measurements provide one criterion for selecting materials, and that the appropriate thermal and mechanical working processes are required to fabricate stimulating electrodes. These results may make cold-rolled platinum ribbon the best material for the long-term application of multi-electrode spiral cuffs in SNS.

Keywords: selective nerve stimulation (SNS), platinum electrodes, annealing, recrystallization, microstructure, resistivity, light microscopy

V zadnjih nekaj desetletjih je bilo pri razvoju elektronskih živčnih protez, ki prihajajo preko večelektrodnih spiralnih objemk selektivno v stik z živčnim sistemom človeka, namenjenih veliko naporov. Cilj raziskave je bil preiskati strukturne lastnosti hladno valjane platinske folije za izdelavo večelektrodnih živčnih spiralnih objemk. Za doseg tega cilja so bili uporabljeni trakci iz 0,03 mm debele hladno valjane platinske folije čistosti 99,99 %. V ta namen so bili trakci montirani v nosilec vzorcev v peči posebej izdelanega merilnega sistema. Meritve upornosti so bile izvedene z uporabo 4-točkovne merilne tehnike, pri kateri so bili trakci dinamično žarjeni v argonu v temperaturnem območju med sobno temperaturo in 900 °C. Na koncu je bila mikrostruktura trakcev, pripravljenih po standardnih metalografskih tehnikah, preiskana z uporabo svetlobne mikroskopije. Pri meritvah upornosti je bilo opaziti majhne spremembe pri temperaturi približno 280 °C. Te spremembe je mogoče pripisati delnemu okrevanju, ki ga povzroči zmanjšanje gostote dislokacij. Pri temperaturah nad 500 °C pa je bilo opaziti znaten padec upornosti, ki je dosegel največjo vrednost pri temperaturi približno 750 °C. Dobljeni rezultati omogočajo poglobljen vpogled v izdelavo platinske folije, uporabne pri nadaljnjem razvoju večelektrodnih stimulacijskih spiralnih objemk. Najpomembnejši sklep je, da rezultati meritev upornosti podajajo enega od meril za izbiro materiala ter primernih procesov mehanske predelave ter toplotne obdelave folije za izdelavo stimulacijskih elektrod. Na osnovi tovrstnih rezultatov lahko preverimo, ali je ustrezno hladno valjana platinska folija najboljši material za dolgotrajno uporabo pri večelektrodnih spiralnih objemkah za selektivno stimulacijo živcev.

Ključne besede: selektivna stimulacija živca, platinske elektrode, žarjenje, rekristalizacija, mikrostruktura, upornost, svetlobna mikroskopija

1 INTRODUCTION

In the past few decades, considerable scientific and technological efforts have been devoted to developing neuroprostheses that interface the human nervous system with implantable electronic devices. Potential applications include limb prostheses, bladder prostheses, cochlear and brain-stem auditory prostheses, retinal and cortical visual prostheses, cortical recording for the cognitive control of assistive devices, vagus nerve stimulation and deep brain stimulation for essential tremor, Parkinson's disease, epilepsy, dystonia, and depression. However, all the applications require electrodes characterized by high spatial and nerve fibre type selectivity and low impedance for recording and safe reversible charge injection for stimulation at the same time. With this in mind, an understanding of the electrochemical mechanisms underlying the behaviour of neural stimulation and recording electrodes is important for the development of chronically implanted devices, particularly those employing large numbers of electrodes.^{1,2}

Since the installation of such a multi-electrode system onto a peripheral nerve also causes mechanical issues, the designer must consider and optimize both the aforementioned issues. To minimize the mechanical issues such as abrasive or compressive injuries and fitness difficulties in the application of multi-electrode systems, flexible substrates and appropriate metal materials have emerged.

In the area of Functional Electrical Stimulation, multi-electrode cuffs have been used in peripheral nerves for stimulation as well as for the recording of an electro-neurogram for more than 35 years.³⁻⁵

In the last two decades, particular attention is being paid to vagus nerve stimulation, techniques that are to be used as a method to treat a number of autonomous nervous-system disorders.

In this regard, selective nerve stimulation (SNS) is usually delivered from a group of three electrodes (triplet) within the spiral cuff installed onto the nerve. The efficacy of SNS is dependent exclusively on localizing charge delivery to specific populations of nerve fibres. Charge delivery, however, is influenced by the electrode-tissue interface, where a transduction of charge carriers from electrons in the metal electrode to ions in the tissue occurs.

Electrodes for SNS face electrochemically harsh working conditions. At the same time, it is imperative that in contact with the nerve tissue, the electrodes must remain non-toxic and non-reactive with the tissue. That means while injecting a required amount of charge, the formation of any harmful reactions should be avoided.⁶⁻⁸

For SNS, different materials that support charge injection by capacitive and faradaic mechanisms are available. These materials have certain advantages and limitations. Among the criteria that must be considered when choosing the material for electrodes that make

electrical contact with a neural tissue are the mechanical characteristics of the material.⁹

The noble metal commonly used as a stimulating electrode material which is capable of supplying adequate electrical charge to activate neural tissue is pure platinum.¹⁰ As with most metals with a face-centred cubic structure, platinum is a very ductile metal.¹¹ High-purity platinum is non-toxic, insoluble in mineral and organic acids and does not corrode or tarnish. However, soluble salts are highly toxic by deposition within the internal organ tissues.

Apart from the chemical inertness, platinum has a number of physical properties of great value for its use in the technology of implantable stimulating electrodes.¹²⁻¹⁸ These include general properties, mechanical properties and physical properties:

General Properties

Density: 21.45 g/cm³

Thermal Conductivity: 0.716 W/(cm K) at 298.2 K

Electrical Resistivity: 105 nΩ m at 293.2 K

Mechanical Properties

Young's modulus: 168000 MPa

Tensile Strength: 125–165 MPa (annealed at 426.8 K)

Elongation: 30–40 % in 50 mm (annealed at 426.8 K)

Tensile Strength: 205–240 MPa (hard drawn, 50 % cold worked)

Elongation: 1–3 % in 50 mm (hard drawn, 50 % cold worked)

Elastic Modulus: 171000 MPa (annealed at 426.8 K) at 293.2 K

Elastic Modulus: 156000 MPa (hard drawn, 50 % cold worked) at 293.2 K

Yield strength: 38-180 MPa

Vickers hardness: 549 MPa

Physical Properties

Absolute electrode potential: 4.44 ± 0.02 V at 298.2 K

Melting temperature: 1495.1 K

Thermal expansion: 8.8 μm·m⁻¹·K⁻¹ at 298.2 K

In the electrical stimulation of nerves, platinum is often used in the form of the pure metal. Namely, impurities and alloying elements may adversely affect both its mechanical characteristics and its stability against corrosion in physiological media. This metal injects charge by both faradaic reactions and double-layer charging. The relative contribution of each process depends on the current density and the pulse width, although the faradaic processes predominate under most neural stimulation conditions.^{10,19} However, in a SNS with a high charge density, pH shifts causing irreversible changes in tissue proteins, metallic dissolution products, gross hydrogen and oxygen gas bubbles, and oxidized organic and inorganic species, could occur.²⁰ It is of a crucial importance that the electrodes in SNS function without facing degradation over a prolonged time period.

Although the charge-injection limits of Pt are based on avoiding the electrolysis of water, Pt dissolution can occur at lower charge densities.²¹

The principal approach to controlling the interface voltage in SNS has been the use of charge-balanced biphasic stimuli, having cathodic and anodic phases that contain equal but opposite charge. However, even with charge-balanced stimulating pulses it is possible that the interface voltage may reach levels where electrochemical reactions can occur.^{22,23}

Mechanical fitness is another important issue in multi-electrode systems design. Low strength, typical of a platinum of high purity (99.93 %), is accepted in stimulating and recording electrodes, despite being a significant disadvantage. To optimise the parameters for the thermal and mechanical processing of platinum a knowledge of its rheological characteristics, including deformation resistance, is required.^{24–26} The deformation resistance, however, is considered in terms of the uniaxial compression or tension of the sample under conditions of plastic deformation, resulting in lattice defects. With this regard, the cold strength depends on the degree to which the object has been deformed: the more lattice defects the harder the metal. Grain boundaries disrupt the motion of dislocations through a material, so reducing crystallite size is a common way to improve the strength. It was assumed that during cold deformation, the deformation resistance depends only on the geometric parameters of the change in shape. When a metal is annealed, however, it loses this strength via the reaction known as recrystallization. The annealing temperature range for 99.93 % platinum is 400–1000 °C, and depends on the degree of cold-working.^{27–29}

Resistivity, sometimes called the Specific Resistance, is one of the fundamental electrical properties of a particular material which gives it electrical resistance.³⁰ Resistance can be calculated by using a knowledge of both the resistivity of the material of a particular object and the shape and geometry of the object. Accordingly, the electric resistance of a square sheet is independent of the size of the square, but depends only on the sheet resistivity and the thickness of the sheet.

Characterizing the resistivity of a material for the SNS electrode could help to determine the long-term charge delivery to the nerve without harmful effects for both the neural tissue and the electrode.

It has been common knowledge that, in general, the resistivity of a metal is higher when cold-worked than in an annealed state.^{31,32} Namely, grain boundaries are defects in the crystal structure and they tend to decrease the electrical conductivity of the material. It was found that platinum of the highest purity almost completely recovers its electrical properties at a temperature as low as 300 °C, although a slight further recovery occurs with an increase of the annealing temperature up to 1450 °C.³³ The result of annealing is the diffusion of dislocations and their cancellation through encounters with disloca-

tions of the opposite sign. In this regard, the increase in hardness and resistivity due to the strain condition obtained during cold-rolling could be reduced to zero by annealing within the temperature range between 400 °C and 800 °C.

Improved, implantable, multi-electrode stimulating systems with greater strength, desirable for an individual electrode, may be achieved through plastic deformation during cold-rolling and partial annealing by carefully choosing the appropriate annealing regimes.

In order to set up the appropriate working cycles, metallographic analysis revealing the microstructure of platinum after each cycle should be used. The most convenient way to reveal the microstructure of cold-rolled and/or thermally treated platinum foil used for stimulating electrodes is by electrolytic etching.^{34,35} Namely, work hardening and thermal treatments cause significant changes to the microstructure of the platinum with respect to the as-cast condition.

The objective of this study was to investigate the temperature-dependent structural properties of a cold-rolled platinum foil used to manufacture stimulating electrodes within the spiral nerve cuffs for SNS using a custom-designed four-point resistivity-measuring device.

2 METHODS

The foil was obtained by means of cold-rolling of the sheet material. In the most labour-intensive method of foil preparation, a small piece of the ingot (chemical composition of the ingot: Pt 99.99 %, Rh 0.01 %) was extracted and, after initial working cycles, the material was annealed and subsequently rolled flat on a mill to obtain a thick foil 0.15 mm. Because platinum has a very high stiffness, work hardening during working cycles made the foil appear excessively hard. In addition, the platinum foil experienced severe local hardening arising from the high strain rates during cold-rolling. We presumed that a gradual increase in the dislocation density

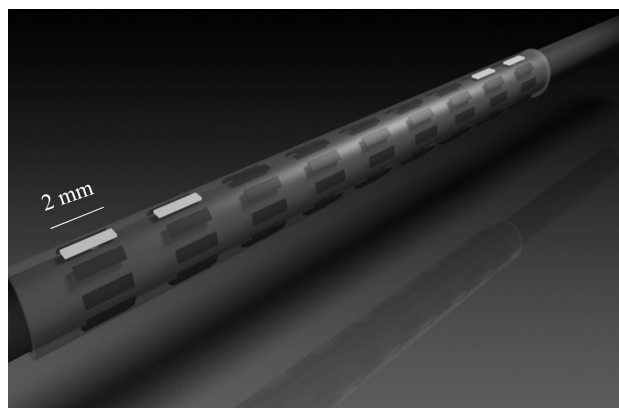


Figure 1: The 99-electrode spiral cuff and an arbitrarily chosen longitudinal row of electrodes

Slika 1: Prikaz 99-elektrodne spiralne manšete in poljubno izbrana vzdolžna vrsta elektrod

occurred, causing increased hardness and a localized loss of ductility. To reduce the dislocation density, renew the softness and ductility, and provide a correct orientation of the metal grains for further cold rolling, recrystallization was promoted by subsequent annealing at 700–800 °C. Finally, the foil was rolled to achieve the final thickness of 0.03 mm on a mill with diameter rollers 300 mm, using varying degrees of cold-working.

The long-term electrochemical stability of platinum stimulating electrodes within the multi-electrode spiral nerve cuff, shown schematically in **Figure 1**, may be connected with the resistivity of the grain boundaries and its change with time.

We measured the electrical resistivity of the platinum strips currently used to manufacture the electrodes used in the 99-electrode spiral nerve cuff. For this purpose, test strips were cut from the foil, with their long axes oriented along the rolling direction. The resistivity measurements were made with a modified 4-probe (also called Kelvin probe) resistance-measurement technique.

For this purpose, a high-temperature resistivity measurement device shown schematically in **Figure 2**, designed by a research team at the Department of Materials and Metallurgy, Faculty of Natural Sciences

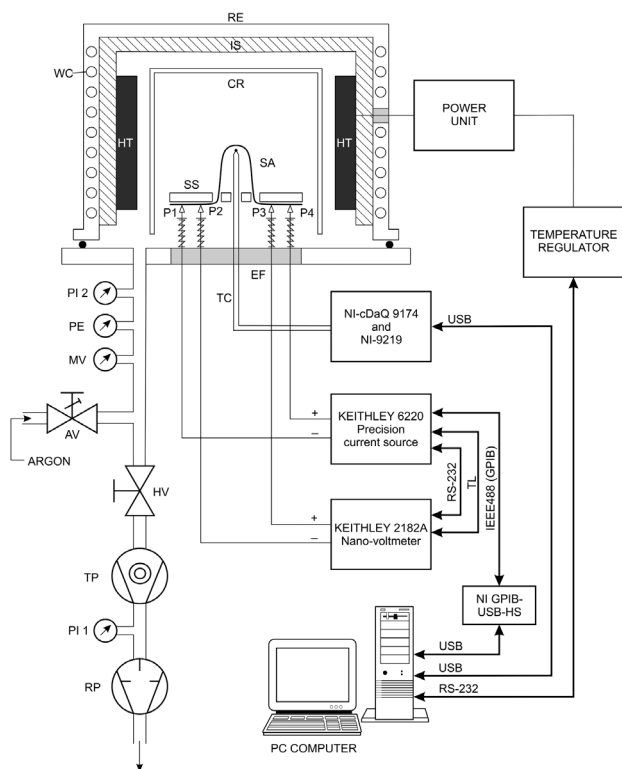


Figure 2: Schematic diagram of the complete measuring device
Slika 2: Shematski prikaz kompleta merilne opreme

Legend to the figure: RE- Recipient, IS- Isolation, CR- Ceramic retort, WC- Water cooling, HT- Heater, SA- Sample, SS- Sample support, P1, P2, P3, P4- Spring-loaded measuring points or contacts, EF- Electric (cable) feed through, TC- Thermocouple, RP- Rotary pump, TP- Turbomolecular pump, HV- High-vacuum valve, AV- Argon dosing valve, PI 1- Pirani vacuum gauge, PI 2- Pirani vacuum gauge, PE- Penning vacuum gauge, MV- Membrane vacuum gauge

and Engineering, University of Ljubljana and Marko Pribošek, an individual investigator, was used.

The main parts of the measurement device are a custom-designed furnace that could withstand a temperature up to 900 °C and the sample holder. To maintain a reliable contact at the sample holder during the measurement, the strips were contacted by four spring-loaded platinum probes.

Direct current was supplied via two probes (source and sink) that were connected to the current source (Model: 6220, Keithley Instruments, Inc., Cleveland, Ohio, USA), and the voltage was measured between the other two probes, connected to the nanovoltmeter (Model: 2182A, Keithley, Keithley Instruments, Inc., Cleveland, Ohio, USA³⁶; Model 6220 DC Current Source and Model 6221 AC and DC Current Source³⁷; Model 2182 and 2182A Nanovoltmeter³⁸).

The complete measuring device and the sample holder housing four spring-loaded platinum probes are shown in **Figure 3**.

To maintain a linear pattern of heating, the system included a digital proportional-integral-derivative (PID) controller, which uses the principle of a “continuous” furnace controller. The PID controller was interfaced with a computer via an RS232 port. A thermocouple (K-type) was used to measure the furnace temperature, while a Pt-100 sensor was used to measure the sample temperature. The data on temperature were retrieved using a USB data-acquisition module (Model: NI-9219, National Instruments, Corporation, Austin, Texas, U.S.A.) and a USB data-acquisition chassis (Model: NI cDAQ-9174, National Instruments Corporation, Austin, Texas, U.S.A.). With this configuration, the test current was forced through the strip resistance using one set of test leads, while the voltage across the sample was measured using a second set of leads, called the sense leads. Although some small current may flow through

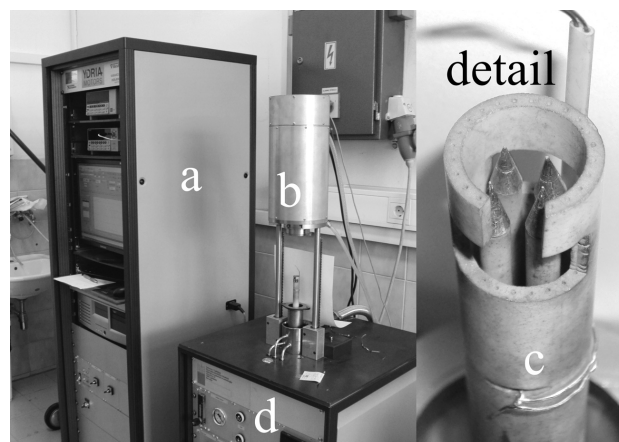


Figure 3: Complete measuring device: a) measuring and computer unit, b) furnace, c) four spring-loaded platinum probes (detail), d) vacuum unit

Slika 3: Celotna merilna naprava: a) merilna in računalniška enota, b) peč, c) platinasta sonda s štirimi vzmetmi (detajl), d) vakuumska enota

the sense leads, it is usually negligible (typically pA or less) and can generally be ignored for all practical purposes. Because the voltage drop across the sense leads was negligible, the voltage measured by the nanovoltmeter was considered to be essentially the same as the voltage across the resistance. Both instruments worked in tandem; the intercommunication was realized via a Trigger Link (TL) and an RS232 serial port interfaced with the computer using a data bus IEEE488 (GPIB), an interface (Model: NI-GPIB-USB-HS, National Instruments Corporation, Austin, Texas, USA), and Lab-view software (Version 10.0, National Instruments, National Instruments Corporation, Austin, Texas, USA).

Platinum strips were subjected to annealing and, at the same time, the electrical resistance of the grain boundaries was measured using a direct method.³⁰ For the measuring conditions, the strips underwent annealing in an argon atmosphere using a linearly increasing temperature range from room temperature to approximately 900 °C, so as to achieve recrystallization. The heating rate was 5 K/min. This temperature range was initially estimated to be high enough to ensure complete recrystallization.²⁴ Under these conditions the temperature distribution during annealing was uniform along the strip in the argon atmosphere. In the measurements, the strips were so placed that the grain boundaries were oriented predominantly parallel to the length of the strip. Afterwards, at arbitrarily chosen points on the strip, platinum probes connected to the potential leads were mechanically pressed to the strip. An electrical measuring current of approximately 2–3 A/mm² was then passed through the strip and a potential difference of approximately 10 μ V was measured using the aforementioned nanovoltmeter, having an input resistance of 50 M Ω .

To reveal the changes in the microstructure that occurred after the cold-roll hardening and the recrystalli-

zation thermal treatments of the strips, optical metallography was employed. To obtain this goal, the most convenient way, namely electrolytic etching, was used.^{34,35} The preparation of the metallographic specimens consisted of the following four steps: sectioning the platinum foil into the strips, embedding the strips into the epoxy resin, mechanical grinding and polishing of the specimens, electro-polishing of the exposed metallographic section in a controlled-atmosphere glove box, and electrochemical etching for microstructure detection.

For the electrolytic etching, the polished specimens were immersed into the most widely used electrolytic solution, i.e., a saturated solution of sodium chloride in concentrated hydrochloric acid (100 cm³ HCl (37 %) + 10 g NaCl electrolytic). Afterwards, the samples were exposed to electrolytic etching with an AC power supply (3–6 V). Because of the "forced corrosion", brought on by the etching, the specimen surface showed inhomogeneous corrosion, and different microstructural features, which varied from area to area, were revealed.

3 RESULTS

The results of the resistivity measurements are plotted in **Figure 4**. Because the plot was difficult to interpret, a transformation of the plot was performed, in which the first derivative of the resistance-change plot was used to identify the points where the resistance change was most apparent.

It can be seen in **Figure 4** that immediately upon heating from room temperature, the electrical resistance of the strips linearly increased with increasing temperature. The starting conditions were as follows: temperature 27 °C and resistivity $20.846 \times 10^{-3} \Omega$. At approximately 280 °C, a small decrease in the resistivity was observed, which could have been the result of a decrease in the dislocation density as part of the recovery. Nevertheless, above 500 °C, a larger decrease in resistivity was recorded, and a maximum decrease was attained at approximately 750 °C. This is consistent with the recrystallization trend (dislocation-free grains), in which the corresponding maximum peak was determined by differential scanning calorimetry (not shown in this paper).

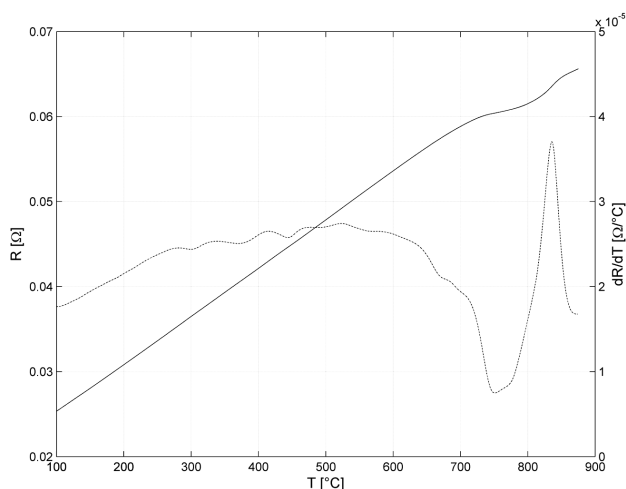


Figure 4: A plot of the resistivity changes during the recrystallization versus the temperature

Slika 4: Diagram spreminjanja upornosti med rekristalizacijo v odvisnosti od temperature

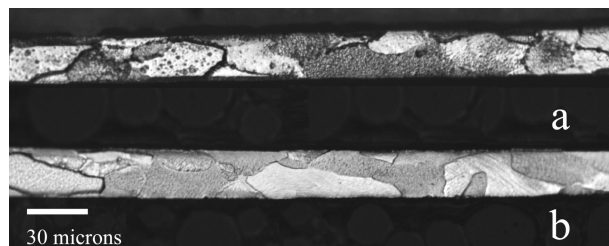


Figure 5: Microstructure: a) deformed and b) recrystallized

Slika 5: Mikrostruktura: a) deformirano, b) rekristalizirano

The recrystallization is shown to depend on the stored energy of the cold-worked foil, the nature of the nucleation sites, and the pinning of the boundaries. Furthermore, knowing that the hardness of platinum and platinum alloys decreases with the increasing temperature and time of annealing, a rapid decrease in the hardness is expected in the temperature range where the recrystallization takes place.³⁹ According to Loginov et al.,²⁴ with a decrease in the initial deformation, the annealing point shifts towards higher temperatures.

According to a comprehensive study about the work-hardening, recovery, and recrystallization of three grades of platinum, reported by Raub (1964),⁴⁰ pure platinum was recovered after heavy cold-working at approximately 200 °C. The temperature ranges for the recovery and recrystallization for platinum of different grades, however, were found to increase with increasing impurity content.

An optical micrograph of cold-rolled and recrystallized strips is shown in **Figures 5a** and **b**, respectively. The etched specimens showed a selectively corroded surface as a consequence of different grain orientations, crystal defects such as dislocations and grain boundaries, and cold-worked regions. The grains appear as elongated particles when the differential interference-contrast technique was used. A finer structure is observed in the cold-rolled sample (**Figure 5a**). After a short period of recrystallization, slightly larger grains are observed (**Figure 5b**). The size of the grains depends not only on the temperature used but also on the annealing time. In this study, the relatively small increase of grain size after annealing confirms the benefit of using a low annealing temperature and a short annealing time.

4 DISCUSSION

The present work aims at giving some explanations about the microstructure of platinum foil to be used in the fabrication of electrodes for SNS, in both the cold-rolled hardened and annealed conditions. More specifically, this paper discusses an analysis, the design criteria, and the structural properties of the platinum ribbon to be used for the fabrication of capacitive as well as faradaic recording and stimulating electrodes within the multi-electrode spiral nerve cuff for SNS.⁹ Namely, it is important to understand all the problems that may occur when using an electrode for SNS and the situations in which a stimulating electrode poses the greatest risk to the nerve.⁶ Only by combining the knowledge about appropriate stimulation parameters and the thermal treatments of cold-worked platinum foil, could result in the optimized fabrication of SNS electrodes used in clinical studies. Namely, it is well known from the literature that significant chemical reactions may occur during stimulation that can destroy a platinum stimulating electrode.⁴¹ Decomposition of the stimulating electrode is a far more significant problem than just the loss of the

electrode itself. It can result in the deposition of metal ions in the body of the patient.

5 CONCLUSION

To address some of the key issues currently inhibiting the widespread adoption of implanted stimulation technologies, research in the design and characterization of metallic materials for implantable multi-electrode systems should be intensified. To achieve suitable final properties of the platinum foil for the fabrication of stimulating electrodes, it is crucial to establish the right combination of plastic deformation and annealing treatment. From these experiments, we concluded that the deployed measurement technique is adequately sensitive to the resistivity changes due to the cold-rolling so that the temperature of recrystallization could be determined. Besides the aforementioned techniques used, however, a wide variety of analytical techniques such as Auger and SEM, could be used alongside it to provide a far more complete knowledge of the microstructure. In this regard, the direction of our further work would involve quantitative and qualitative information about the physical and chemical changes during the cold deformation of a platinum foil that would be obtained using the thermo-analytical technique of differential scanning calorimetry. Furthermore, the recrystallization kinetics of cold-rolled platinum foil containing an oriented grain structure will be studied.

In summary, this study utilized electrical resistivity measurements to characterize a material with the potential for use in the production of neural stimulation electrodes.

Acknowledgements

This work was supported by the Ministry of Higher Education and Science, Republic of Slovenia, research programme P3-0171. Additional support was provided by the ITIS d. o. o. Ljubljana, Centre for Implantable Technology and Sensors. The research was also performed as partial fulfilment of the requirements for the Doctor of Philosophy Degree (Polona Pečlin, MD).

6 REFERENCES

- ¹ P. F. Johnson, L. L. Hench, An in vitro model for evaluating neural stimulating electrodes, *J Biomed Mater Res.*, 10 (1976) 6, 907–28
- ² D. R. Merrill, The Electrochemistry of Charge Injection at the Electrode/Tissue Interface, *Implantable Neural Prostheses 2, Biological and Medical Physics, Biomedical Engineering*, Springer Verlag, New York 2010, 85–138
- ³ R. B. Stein, D. Charles, L. Davis, J. Jhamandas, A. Mannard, T. R. Nichols, Principles underlying new methods for chronic neural recording, *Can J Neurol Sci*, 2 (1975), 235–244
- ⁴ G. G. Naples, J. D. Sweeny, J. T. Mortimer, Inventors, Implantable cuff, Method and manufacture, and Method of installation, U. S. Patent #4, 1986, 602–624

- ⁵ J. D. Sweeney, D. A. Ksienski, J. T. Mortimer, A nerve cuff technique for selective excitation of peripheral nerve trunk regions, *IEEE Trans. Biomed. Eng.*, BME, 37 (1990) 7, 706–715
- ⁶ L. S. Robblee, T. L. Rose, Electrochemical guidelines for selection of protocols and electrode materials for neural stimulation Neural Prostheses: Fundamental Studies, In: W. F. Agnew, D. B. McCreery (ed.), Englewood Cliffs, NJ, Prentice-Hall, 1990
- ⁷ A. M. Dymond, Characteristics of the metal–tissue interface of stimulation electrodes, *IEEE Trans. Biomed. Eng.*, 23 (1976), 274–80
- ⁸ E. Gileadi, E. Kirowa-Eisner, J. Penciner, *Interfacial Electrochemistry: An Experimental Approach*, Reading, MA: Addison-Wesley, 1975
- ⁹ L. A. Geddes, R. Roeder, Criteria for the selection of materials for implanted electrodes, *Ann Biomed Eng.*, 31 (2003) 7, 879–90
- ¹⁰ S. B. Brummer, M. J. Turner, Electrochemical considerations for safe electrical stimulation of the nervous system with platinum electrodes, *IEEE Trans. Biomed. Eng.*, 24 (1977), 59–63
- ¹¹ J. M. Ziman, *Principles of the Theory of Solids*, 2nd ed., Cambridge University Press, 1972
- ¹² R. Tudor, M. Ashley, *Platinum Metals Rev.*, 51 (2007) 3, 116
- ¹³ C. F. J. Barnard, *Platinum Metals Rev.*, 34 (1990) 4, 207
- ¹⁴ S. A. French, *Platinum Metals Rev.*, 51 (2007) 2, 54
- ¹⁵ D. J. Ager, A. H. M. de Vries, J. G. de Vries, *Platinum Metals Rev.*, 50 (2006) 2, 54
- ¹⁶ J. F. Roth, *Platinum Metals Rev.*, 19 (1975) 1, 12
- ¹⁷ J. H. Jones, *Platinum Metals Rev.*, 44 (2000) 3, 94
- ¹⁸ Official Journal of the European Union, Commission Directive 2004/96/EC, 27. September 2004, EU, 28. 9. 2004, L 301/51–L 302/52
- ¹⁹ L. S. Robblee, T. L. Rose, The electrochemistry of electrical stimulation, Proc. 12th Ann. Conf. IEEE Eng. in Med. & Biol. Soc., Philadelphia, PA, 1990, 1479–1480
- ²⁰ B. Onaral, H. H. Sun, H. P. Schwan, Electrical properties of bioelectrodes, *IEEE Trans Biomed Eng.*, 31 (1984) 12, 827–832
- ²¹ L. S. Robblee, J. McHardy, W. F. Agnew, L. A. Bullara, Electrical stimulation with Pt electrodes, VII. Dissolution of Pt electrodes during electrical stimulation of the cat cerebral cortex, *J. Neurosci. Methods*, 9 (1983) 301, 8
- ²² D. B. McCreery, W. F. Agnew, T. G. H. Yuen, L. A. Bullara, Relationship between stimulus amplitude, stimulus frequency and neural damage during electrical stimulation of sciatic nerve of cat, *Med. Biol. Eng. Comput.*, 33 (1995) 3, 426–429
- ²³ T. G. H. Yuen, W. F. Agnew, L. A. Bullara, S. Jacques, D. B. McCreery, Histological evaluation of neural damage from electrical stimulation, considerations for the selection of parameters for clinical application, *Neurosurgery*, 9 (1981) 3, 292–299
- ²⁴ Y. N. Loginov, A. V. Yermakov, L. G. Grohovskaya, G. I. Studenok, Annealing Characteristics and Strain Resistance of 99.93 % Platinum, Implications for the manufacture of platinum artefacts, *Platinum Metals Rev.*, 51 (2007) 4, 178–184
- ²⁵ M. Savitsky (ed.), *Precious Metals Handbook*, Metallurgiya, Moscow 1984 (in Russian)
- ²⁶ *Properties of Platinum Group Metals: Platinum Today*, Johnson Matthey (<http://www.platinum.matthey.com/applications/properties.html>)
- ²⁷ J. C. Wright, Jewellery-Related Properties of Platinum. Low thermal diffusivity permits use of laser welding for jewellery manufacture, *Platinum Metals Rev.*, 46 (2002) 2, 66–72
- ²⁸ K. Toyoda, T. Miyamoto, T. Tanihira, H. Sato, Pilot Pen Co Ltd, High Purity Platinum and Its Production, Japanese Patent 7/150, 271, 1995
- ²⁹ Russian State Standard GOST 13498-79, *Platinum and Platinum Alloys, Trade Marks*, Moscow, 1979 (http://www.eastview.com/xq/ASP/sku=G2010120f_locale=/Moskva/Russia/English/Russian/qx/russian/standards/product.asp)
- ³⁰ W. Hiebsch, Electrical resistance of grain boundaries in platinum, *Czechoslovak Journal of Physics*, 29 (1979) 8, 928–932
- ³¹ E. P. Unskov, W. Johnson, V. L. Kolmogorov, E. A. Popov, Y. S. Safarov, R. D. Venter, H. Kudo, K. Osakada, H. L. D. Pugh, R. S. Sowerby, *Theory of Plastic Deformations of Metals*, Mashinostroenie, Moscow 1983 (in Russian)
- ³² T. Biggs, S. S. Taylor, E. van der Lingen, The Hardening of Platinum Alloys for Potential Jewellery Application, *Platinum Metals Rev.*, 49 (2005) 1, 2–15
- ³³ J. R. Corruccini, Annealing of Platinum for Thermometry, *Journal of Research of the National Bureau of Standards*, 47 (1951) 2, 94–103
- ³⁴ P. Battaini, Electrolytic Etching for Microstructure Detection in Platinum Alloys, *Platinum Metals Rev.*, 55 (2011) 1, 71–72
- ³⁵ P. Battaini, Microstructure Analysis of Selected Platinum Alloys, *Platinum Metals Rev.*, 55 (2011) 2, 74–83
- ³⁶ *Low Level Measurements Handbook*, Keithley www.keithley.com
- ³⁷ User's Manual, ©2004, Keithley Instruments, Inc., Cleveland, Ohio, U.S.A., Second Printing, June 2005, Document Number: 622x-900-01 Rev. B
- ³⁸ User's Manual, ©2004, Keithley Instruments, Inc., Cleveland, Ohio, U.S.A., First Printing, June 2004, Document Number: 2182A-900-01 Rev. A
- ³⁹ Q. Zhang, D. Zhang, S. Jia, W. Shong, Microstructure and Properties of Some Dispersion Strengthened Platinum Alloys, The influence of Yttrium and Zirconium additions, *Platinum Metals Rev.*, 39 (1995) 4, 167–171
- ⁴⁰ E. Raub, Einfluss des Reinheitsgrades von Platin auf Versfestigung, Erholung und Rekristallisation, *Zeitschrift für Metallkunde*, 55 (1964) 9, 512
- ⁴¹ D. B. Hibbert, K. Weitzner, B. Tabor, P. Carter, Mass changes and dissolution of platinum during electrical stimulation in artificial perilymph solution, *Biomaterials*, 21 (2000), 2177–2182

VARIATION IN MAGNETIC PROPERTIES OF SOL-GEL-SYNTHESIZED COBALT FERRITES

SPREMINJANJE MAGNETNIH LASTNOSTI KOBALTOVIH FERITOV, SINTETIZIRANIH PO SOL-GEL POSTOPKU

Anuchit Hunyek, Chitnarong Sirisathitkul

Molecular Technology Research Unit, School of Science, Walailak University, 80161 Nakon Si Thammarat, Thailand
schitnar@wu.ac.th

Prejem rokopisa – received: 2012-11-28; sprejem za objavo – accepted for publication: 2013-04-10

Single-phase cobalt ferrite (CoFe_2O_4) was synthesized with a sol-gel reaction between 10.59 g of cobalt nitrate and 29.40 g of iron nitrate using 480 mL of 10 % polyvinyl alcohol (PVA) in water. Their magnetic squareness and coercive field were slightly reduced with the increase in the annealing at 800 °C from 2 h to 6 h. To examine the reproducibility of ferrite products of the PVA sol-gel method, the synthetic condition was repeated 28 times. After annealing for 4 h, CoFe_2O_4 samples from different batches exhibit variations in the magnetic properties. The coercive field has a large distribution because of its sensitivity to the particle agglomeration, whereas the squareness fluctuates in a narrower range from 0.22 to 0.29. Since the squareness is the ratio of the remanence to the saturation magnetization, the particle agglomeration tends to increase both values while keeping this ratio rather unchanged.

Keywords: cobalt ferrites, PVA sol-gel, annealing time, magnetic squareness, coercive field

Enofazni kobaltov ferit (CoFe_2O_4) je bil sintetiziran s sol-gel reakcijo med 10,59 g kobaltovega nitrata in 29,40 g železovega nitrata z uporabo 480 mL 10-odstotne raztopine polivinil alkohola (PVA) v vodi. Njihova četverkotna magnetna oblika in koercitivno polje sta se rahlo zmanjšala s podaljšanjem žarjenja na 800 °C iz 2 h na 6 h. Da bi preiskali ponovljivost feritnih proizvodov iz PVA sol-gel metode, je bila sinteza ponovljena 28-krat. Po žarjenju 4 h so kazali vzorci CoFe_2O_4 iz različnih serij razliko v magnetnih lastnostih. Koercitivno polje kaže velik raztros zaradi občutljivosti za aglomeracijo delcev, medtem ko se četverkotnost oblike spreminja v ožjem področju od 0,22 do 0,29. Ker je četverkotnost razmerje med remanenco in nasičeno magnetizacijo, aglomeracija delcev povečuje obe vrednosti, medtem ko razmerje ostaja skoraj nespremenjeno.

Gljučne besede: kobaltov ferit, PVA sol-gel, čas žarjenja, magnetna četverkotna oblika, koercitivno polje

1 INTRODUCTION

Cobalt ferrite (CoFe_2O_4) is under research and development for its applications in magneto-optical recording media, magnetic refrigerants, microwave absorbers and stress sensors.^{1,2} Bulk CoFe_2O_4 has an inverse spinel structure consisting of a cubic close-packed (fcc) arrangement of oxide anions, O^{2-} . The tetrahedral and octahedral interstitial sites in the lattice are partially occupied by the Co^{2+} and Fe^{3+} cations, respectively.^{1,2} Like the other spinel ferrites (e.g., NiFe_2O_4 , MnFe_2O_4 , ZnFe_2O_4 , CuFe_2O_4) and barium ferrites, CoFe_2O_4 nanoparticles can be synthesized with the sol-gel method.³⁻¹⁷ In a sol-gel reaction, homogeneous CoFe_2O_4 nanoparticles are produced in-situ with a controlled decomposition of precursors, while the chelating gel is dried during the heat treatment at a relatively low temperature. Gately et al.⁷ demonstrated that the characteristics of CoFe_2O_4 , NiFe_2O_4 , ZnFe_2O_4 , YFeO_3 and $\text{Y}_3\text{Fe}_5\text{O}_{12}$ produced with aqueous sol-gel reactions under the same synthesis condition were comparable.

According to our previous sol-gel synthesis using polyvinyl alcohol (PVA) as the chelating agent,⁸ the magnetic properties of CoFe_2O_4 are influenced by PVA contents for two reasons. Firstly, the single-phase CoFe_2O_4 obtained in the case of sufficient PVA gives rise

to a relatively high coercive field because of its strong magnetic anisotropy. In the case of a diluted PVA solution, the second phase (e.g., $\alpha\text{-Fe}_2\text{O}_3$) may also be present, reducing the overall coercive field. The other reason is the dependence of the cluster size on the PVA contents used in the sol-gel reaction. The cluster size, on the other hand, dictates the coercive field and magnetization of CoFe_2O_4 .^{9,15} The role of the PVA gel is to cleave atoms during the reaction. An increase in PVA improves the crystallinity of CoFe_2O_4 without an excessive particle agglomeration.

The temperature of the heat treatment of the as-synthesized products also affects the magnetic properties of CoFe_2O_4 . Our previous result agrees with the other experimental works indicating that both the coercive field and the magnetic squareness (the ratio of the remanence to the saturation magnetization) of CoFe_2O_4 are initially increased with an increase in the annealing temperature up to 700–800 °C and then reduced with further increases in the temperature.^{8,15-19} The growth and agglomeration of CoFe_2O_4 particles at high temperatures result in a decrease in the coercive field and an increase in the saturation magnetization. The squareness is, therefore, reduced due to this high-temperature regime. In addition, Toksha et al.¹⁵ reported a decrease in the coercive field and an increase in the saturation magne-

tization due to an increased particle size after prolonged annealing. Recently, Sajjia et al.¹⁴ employed the response surface methodology to simulate the optimum heat treatment to obtain single-phase CoFe_2O_4 and minimize the cost of electricity.

To implement a sol-gel synthesis of ferrites on a commercial scale, another aspect of concern is the reproducibility of the products from different batches. Although this issue is hardly addressed in research papers, it is particularly important since ferrites of the order of a hundred grams or less are usually obtained with a laboratory-scale sol-gel synthesis. In this research, the condition for preparing the single-phase CoFe_2O_4 from the previous work⁸ is reproduced in order to study the variation in magnetic properties observed after a repeated synthesis. The effect of the annealing time is also investigated.

2 EXPERIMENTAL WORK

The PVA solution was prepared by dissolving PVA powders in distilled water (10 %). It was heated at 70–80 °C until the solution became clear (5–7 h). Then, 10.59 g of cobalt nitrate, $\text{Co}(\text{NO}_3)_2 \cdot 6\text{H}_2\text{O}$, and 29.40 g of iron nitrate, $\text{Fe}(\text{NO}_3)_3 \cdot 9\text{H}_2\text{O}$ powders were mixed with the 480 mL PVA solution. The reaction mixture was stirred for a further 3 h. After that, it was heated at 80 °C for 10–12 h or until the gel was dry.

The morphology of the ferrite product was shown with scanning electron microscopy (SEM) and its structure was characterized with powder X-ray diffractometry (XRD). A copper target was used as an X-ray source (K_{α} , $\lambda = 0.154058$ nm) with 40 kV between the cathode and the copper target. The measurement was performed in the range of 2θ angles from 10° to 80° with each rotating step accounting for 0.02°. The crystallite size

was calculated from the peak width using the Scherrer's formula:

$$d = \frac{0.9\lambda}{\beta \cos \theta} \quad (1)$$

where β is the broadening of the diffraction line measured at half the maximum intensity and λ is the wavelength of K_{α} .

To investigate the effect of the annealing time and reproducibility of sol-gel products, the time of annealing at 800 °C varied between (2, 4, 6) h and the same synthesis condition was repeated for 28 batches with the same, annealing 4 h. The magnetic properties of all the samples were characterized with vibrating sample magnetometry (VSM).

3 RESULTS AND DISCUSSION

The XRD pattern in **Figure 1** shows the cubic spinel CoFe_2O_4 phase [JCPDS 22-1086] with the peaks at 30.0°, 35.4°, 43.0°, 56.9°, 62.6° corresponding to the (220), (311), (400), (511) and (440) planes, respectively. Other oxides or impurity phases are not detected and the CoFe_2O_4 peaks are particularly sharp. The crystallite size, calculated from the line broadening of the (311) diffraction peak is approximately 45 nm. These crystallites tend to agglomerate into microscale clusters that are quite common for sol-gel-synthesized ferrites.²⁰ As seen in the SEM micrograph in the inset, these aggregates have flat surfaces and sharp edges. Compared to the ferrite products from the previous work,⁸ the cluster size tends to increase with a reduction of PVA in the sol-gel reaction.

According to VSM hysteresis loops in **Figure 2** all the CoFe_2O_4 samples after varying annealing times exhibit ferrimagnetic properties. The absence of superparamagnetic behaviors is due to the particle agglomeration.

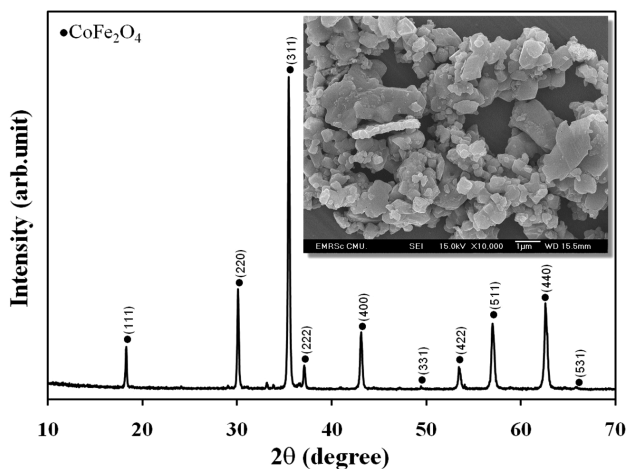


Figure 1: XRD pattern of sol-gel-synthesized ferrite products. Its SEM micrograph is shown in the inset.

Slika 1: XRD-posnetek feritnega proizvoda, sintetiziranega po sol-gel postopku. SEM-posnetek je vloženo.

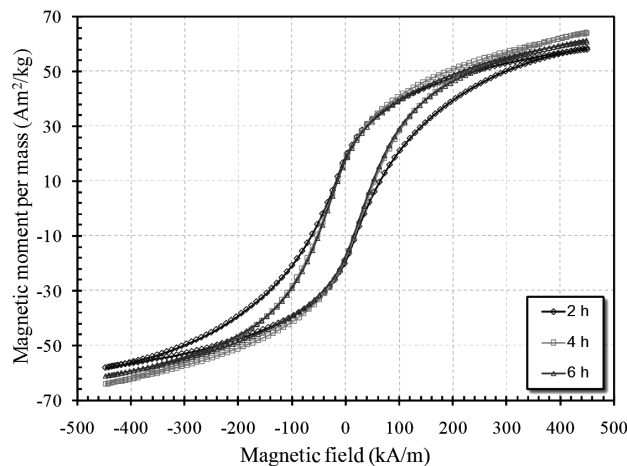


Figure 2: Hysteresis loops of CoFe_2O_4 from the sol-gel reaction after annealing at 800 °C for (2, 4 and 6) h

Slika 2: Histerezna zanka CoFe_2O_4 , izdelanega po sol-gel reakciji, po žarjenju (2, 4 in 6) h na 800 °C

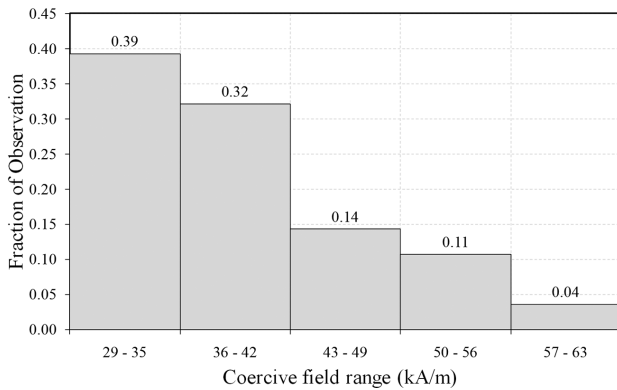


Figure 3: Distribution of the coercive field of CoFe_2O_4 synthesized in 28 batches

Slika 3: Razporeditev koercitivnega polja CoFe_2O_4 , sintetiziranega v 28 ponovitvah

ration. In the applied magnetic field of 440 kA/m, the magnetization does not reach the complete saturation. The highest magnetic moment per mass is around 60 A m²/kg, a value comparable to that of sol-gel-synthesized CoFe_2O_4 nanoparticles.^{9–11,15} Both the coercive field and the squareness are slightly decreased with the increase in the annealing time from 2 h to 6 h. Longer annealing times apparently have a similar effect on the increase in the annealing temperature beyond 800 °C and the cluster size is, consequently, enhanced. It follows that the coercive field and the squareness are reduced.

The variation in the coercive field of CoFe_2O_4 is shown in the form of a histogram in **Figure 3**. Ranging from 31.2 kA/m to 63.2 kA/m, the distribution is approximately exponential with the coercive field of less than 40 kA/m in the majority of the samples. This implies that most particles are unevenly agglomerated, like those in **Figure 1**. The average coercive field of 28 batches is (39.8 ± 8.7) kA/m (compared to 34.4 kA/m in **Figure 2**). If an enhanced coercive field is aimed for, either an increase in the PVA contents or a decrease in the annealing temperature and time is recommended. In **Figure 4**, the squareness exhibits a narrower distribution, from

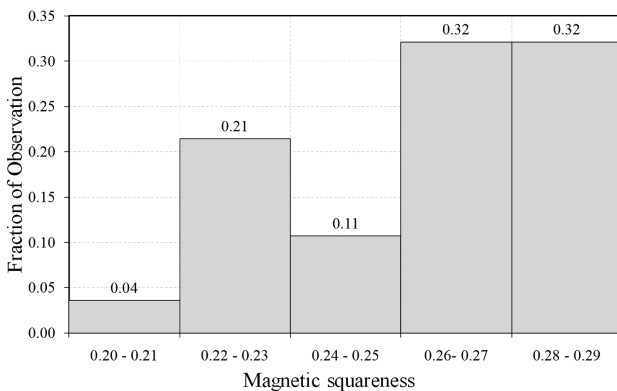


Figure 4: Distribution of the magnetic squareness of CoFe_2O_4 synthesized in 28 batches

Slika 4: Razporeditev magnetne četverkotne oblike CoFe_2O_4 , sintetiziranega v 28 ponovitvah

0.22 to 0.29. In addition to its effect on the coercive field, the particle agglomeration also results in an increase in the magnetization. However, the squareness does not exhibit a large variation, because it is the ratio between the magnetizations. With the average value of 0.26 ± 0.03 , a large fraction of the samples have a squareness beyond 0.25. Interestingly, the minimum squareness of 0.22 is obtained from the batch with the smallest cluster size, signified by the maximum coercive field.

4 CONCLUSION

The magnetic squareness and coercive field of the single-phase CoFe_2O_4 synthesized with a sol-gel reaction between $\text{Co}(\text{NO}_3)_2 \cdot 6\text{H}_2\text{O}$ and $\text{Fe}(\text{NO}_3)_3 \cdot 9\text{H}_2\text{O}$ exhibit a slight decrease with the increase in the annealing time from 2 h to 6 h at 800 °C. However, repeated syntheses show that the magnetic properties of CoFe_2O_4 obtained under the same synthetic and annealing conditions may vary due to non-uniform particle agglomerations. This must be taken into the account before implementing the sol-gel-synthesized ferrites on a large scale.

Acknowledgements

This work was funded by the Industry/University Cooperative Research Center (I/UCRC) in HDD Component, the Faculty of Engineering, the Khon Kaen University and the National Electronics and Computer Technology Center, the National Science and Technology Development Agency. The characterizations using XRD, SEM and VSM were carried out at the National Metal and Materials Technology Center (MTEC), the Chiang Mai University and the Kasetsart University, respectively.

5 REFERENCES

- D. S. Mathew, R. S. Juang, An overview of the structure and magnetism of spinel ferrite nanoparticles and their synthesis in micro-emulsions, *Chemical Engineering Journal*, 129 (2007) 1–3, 51–65
- P. C. Fannin, C. N. Marin, I. Malaescu, N. Stefu, P. Vlazan, S. Novaconi, P. Sfirloaga, S. Popescu, C. Couper, Microwave absorbent properties of nanosized cobalt ferrite powders prepared by coprecipitation and subjected to different thermal treatments, *Materials & Design*, 32 (2011) 3, 1600–1604
- A. Gurbuz, N. Onar, I. Ozdemir, A. C. Karaoglanli, E. Celik, Structural, thermal and magnetic properties of barium-ferrite powders substituted with Mn, Cu or Co and X (X = Sr and Ni) prepared by the sol-gel method, *Mater. Tehnol.*, 46 (2012) 3, 305–310
- M. Sivakumar, S. Kanagesan, R. S. Babu, S. Jesurani, R. Velmurugan, C. Thirupathi, T. Kalaivani, Synthesis of CoFe_2O_4 powder via PVA assisted sol-gel process, *Journal of Materials Science-Materials in Electronics*, 23 (2012) 5, 1045–1049
- Z. Y. Wang, W. J. Fei, H. C. Qian, M. Jin, H. Shen, M. L. Jin, J. Y. Xu, W. R. Zhang, Q. Bai, Structure and magnetic properties of CoFe_2O_4 ferrites synthesized by sol-gel and microwave calcination, *Journal of Sol-Gel Science and Technology*, 61 (2012) 2, 289–295

- ⁶ I. Zalite, G. Heidemane, M. Kodols, J. Grabis, M. Maiorov, The synthesis, characterization and sintering of nickel and cobalt ferrite nanopowders, *Materials Science Medziagotyra*, 18 (2012) 1, 3–7
- ⁷ A. Gatelyte, D. Jasaitis, A. Beganskiene, A. Kareiva, Sol-gel synthesis and characterization of selected transition metal nano-ferrites, *Materials Science Medziagotyra*, 17 (2011) 3, 302–307
- ⁸ A. Hunyek, C. Sirisathitkul, P. Harding, Formation of cobalt ferrites from aqueous solutions of metal nitrates containing PVA: effects of the amount of PVA and annealing temperature, *Journal of the Ceramics Society of Japan*, 119 (2011) 1390, 541–543
- ⁹ W. P. Wang, H. Yang, T. Xian, Z. Q. Wei, R. S. Li, W. J. Feng, Polyacrylamide gel synthesis, characterization and magnetic properties of CoFe_2O_4 nanopowders, *Chinese Journal of Inorganic Chemistry*, 27 (2011) 6, 1071–1076
- ¹⁰ I. H. Gul, A. Maqsood, Structural, magnetic and electrical properties of cobalt ferrites prepared by the sol-gel route, *Journal of Alloys and Compounds*, 465 (2008) 1–2, 227–231
- ¹¹ E. V. Gopalan, P. A. Joy, I. A. Al-Omari, D. S. Kumar, Y. Yoshida, M. R. Anantharaman, On the structural, magnetic and electrical properties of sol-gel derived nanosized cobalt ferrite, *Journal of Alloys and Compounds*, 485 (2009) 1–2, 711–717
- ¹² H. Cui, Y. Jia, W. Ren, W. Wang, Facile and ultra large scale synthesis of nearly monodispersed CoFe_2O_4 nanoparticles by a low temperature sol-gel route, *Journal of Sol-Gel Science and Technology*, 55 (2010) 1, 36–40
- ¹³ R. Qin, F. Li, L. Liu, W. Jiang, Synthesis of well-dispersed CoFe_2O_4 nanoparticles via PVA-assisted low-temperature solid state process, *Journal of Alloys and Compounds*, 482 (2009) 1–2, 508–511
- ¹⁴ M. Sajjia, K. Y. Benyounis, A. G. Olabi, The simulation and optimization of heat treatment of cobalt ferrite nanoparticles prepared by the sol-gel technique, *Powder Technology*, 222 (2012), 143–151
- ¹⁵ B. G. Toksha, S. E. Shirsath, S. M. Patange, K. M. Jadhav, Structural investigations and magnetic properties of cobalt ferrite nanoparticles prepared by sol-gel auto combustion method, *Solid State Communications*, 147 (2008) 11–12, 479–483
- ¹⁶ L. Ai, J. Jiang, Influence of annealing temperature on the formation, microstructure and magnetic properties of spinel nanocrystalline cobalt ferrites, *Current Applied Physics*, 10 (2010) 1, 284–288
- ¹⁷ K. Parekh, Effect of preparative conditions on magnetic properties of CoFe_2O_4 nanoparticles, *Indian Journal of Pure & Applied Physics*, 48 (2010) 8, 581–585
- ¹⁸ W. S. Chiu, S. Radiman, R. Abd-Shukor, M. H. Abdullah, P. S. Khiew, Tunable coercivity of CoFe_2O_4 nanoparticles via thermal annealing treatment, *Journal of Alloys and Compounds*, 459 (2008) 1–2, 291–297
- ¹⁹ S. I. El-Dek, Effect of annealing temperature on the magnetic properties of CoFe_2O_4 nanoparticles, *Philosophical Magazine Letters*, 90 (2010) 4, 233–240
- ²⁰ M. Chand, A. Kumar, S. Kumar, A. Shankar, R. P. Pant, Investigations on $\text{Mn}_x\text{Zn}_{1-x}\text{Fe}_2\text{O}_4$ ($x = 0.1, 0.3$ and 0.5) nanoparticles synthesized by sol-gel and co-precipitation methods, *Indian Journal of Engineering and Materials Sciences*, 18 (2011) 5, 385–389

ASSESSING THE QUALITY OF CORROSION EDUCATION IN THE UNITED ARAB EMIRATES

PRESOJA KVALITETE IZOBRAŽEVANJA NA PODROČJU KOROZIJE V ZDRUŽENIH ARABSKIH EMIRATIH

Hwee Ling Lim, Lyas Al Tayeb Ait Tayeb, Mohamed Abdulrahman Othman

The Petroleum Institute, P.O. Box 2533, Sas Al Nakheel Campus, Abu Dhabi, United Arab Emirates
hlim@pi.ac.ae

Prejem rokopisa – received: 2012-08-27; sprejem za objavo – accepted for publication: 2013-03-27

The economic consequences of corrosion failure can be minimized by an engineering workforce well trained in corrosion fundamentals and management. The United Arab Emirates (UAE) incurs the second highest annual cost of corrosion after Saudi Arabia, given its large petroleum industry. Hence, this study examined the quality of corrosion education in engineering programs of the universities in the UAE. Using a single-embedded case-study design, academia and industry respondents were surveyed on the competence of engineering undergraduates/graduates in corrosion. The findings showed that the dedicated corrosion courses and engineering courses integrating corrosion into the curricula are available in the UAE universities. Regarding the competence of engineering students/graduates, the consensus view was that there was an insufficient fundamental knowledge of corrosion engineering. The industry respondents were highly critical, believing that graduate engineers had a superficial understanding of corrosion in real-life design contexts. The effectiveness of engineering curricula in corrosion is determined by both the competence in corrosion knowledge/skills and the availability of resources (qualified staff and new knowledge from research) to support corrosion education. The findings showed that most departments would not hire new corrosion specialists. However, the aspect of research was more encouraging with the universities reporting availability of departmental research and industry partnerships in corrosion research. This paper gives recommendations for improving the knowledge and skills of future engineers in corrosion management and for enhancing corrosion training to better meet the industry needs.

Keywords: corrosion, engineering education, case study, United Arab Emirates

Ekonomske posledice korozijskih poškodb je mogoče zmanjšati z inženirji, ki so dobro izobraženi na področju osnov korozije in upravljanja s korozijo. Združeni arabski emirati (ZAE) imajo za Savdsko Arabijo drugi največji letni strošek zaradi korozije v svoji veliki naftni industriji. Zato ta študija posega na področje kvalitete poučevanja korozije pri inženirskih programih na univerzah v ZAE. Z enotno obliko študija primera v obliki ankete so bile pregledane akademije in industrija o pristojnosti inženirjev in diplomiranih inženirjev glede korozije. Ugotovitve kažejo, da so namenski tečaji o koroziji in inženirski predmeti, ki vključujejo korozijo, vključeni v programih univerz v ZAE. Glede pristojnosti študentov tehnike in inženirjev je bilo soglasno potrjeno, da ni dovolj temeljnega znanja s področja obvladovanja korozije. Anketiranci iz industrije so bili kritični, da imajo inženirji pomanjkljivo razumevanje korozije pri projektih v realnem okolju. Učinkovitost inženirskih programov glede korozije je določena tako s kompetenčnim znanjem in izkušnjami s korozijo ter z razpoložljivimi viri (usposobljenimi delavci in novim znanjem iz raziskav), ki naj bi podpirale izobraževanje o koroziji. Rezultati so pokazali, da večina podjetij ne bi zaposlila novih strokovnjakov za korozijo. Vendar pa je vidik raziskav bolj spodbuden na univerzah, ki poročajo o možnosti raziskav in partnerstvu z industrijo na področju raziskav korozije. Članek se konča s priporočilom po izboljšanju znanja in izkušenj bodočih inženirjev pri upravljanju s korozijo, kot tudi spodbujanje korozijskega svetovanja za boljše zadovoljevanje potreb industrije.

Ključne besede: korozija, izobraževanje inženirjev, študij primera, Združeni arabski emirati

1 INTRODUCTION

The United Arab Emirates (UAE) incurs a high annual cost of corrosion of US\$ 14.26 billion (2011), which is about 5.2 % of the country's GDP over three years (2009–2011), due to its large petroleum industry¹. Corrosion is a deterioration of metals or materials due to chemical, biological or environmental agents^{2,3} resulting in serious health, safety and environmental (HSE) risks. When poorly managed, corrosion affects the equipment integrity and serviceability, raises the risk of discharge of flammable fluids and gases that companies can be held liable for⁴. Since it is impossible to eliminate corrosion, engineers in the petroleum industry need to be competent in corrosion fundamentals and management to minimize the economic, environmental and social consequences of a corrosion failure. Much of this competence is gained

through higher education. Yet, 54 % of the corrosion-protection practitioners have not taken a corrosion course in their formal education. Also, 45 % of the currently active and experienced corrosion technologists are likely to retire in the next 10 years⁴. Furthermore, there is little research on the quality of corrosion education in the UAE. Hence, this study aims to assess the quality of corrosion education in engineering programs of the universities in the UAE. The research questions are:

RQ 1a: What is the level of corrosion training available at the universities in the UAE?

RQ 1b: Why is this level of corrosion training characteristic of the UAE universities?

RQ 2a: How competent are the engineering undergraduates/graduates from the UAE universities in corrosion knowledge and skills?

RQ 2b: What resources are available to the UAE universities to support effective corrosion education?

2 CASE STUDY RESEARCH DESIGN

A single-embedded case design was used where, within a single case, attention is also given to subunits.^{5,6} This design enabled in-depth analyses of the subunits providing an insight into the main case. The main case is the engineering education program of the UAE universities, while four universities were the subunits in the primary case. Through purposive sampling, four institutions were identified that met the following criteria: location in the UAE; availability of engineering programs, for which corrosion is relevant; at least one cohort of graduates; reliable accessibility to the participants. Due to ethical considerations, the universities were pseudonymised.

The primary data sources were the academics (*n* = 58) from the four institutions and the engineers from the oil/gas industry (*n* = 8). The latter were interviewed to understand the employers’ perspective on the competence of engineering graduates in corrosion. The total sample consisted of 66 respondents. Surveys and interviews (individuals, focus groups) were used to gather quantitative and qualitative data that were statistically and interpretively analyzed, respectively. The questionnaires provided information on the respondent demographics, the level of the existing engineering curricula in corrosion, the effectiveness of engineering curricula in corrosion, and recommendations for enhancing the corrosion knowledge and skills. **Table 1** summarizes the

constructs and questions that constitute the operational measures.

The first construct, *the level of the existing engineering curricula in corrosion*, is defined as the extent of the corrosion training available. The construct is operationalized by Q.10 measuring the availability of corrosion training on the scale from having a dedicated corrosion course, teaching corrosion as part of other courses (integrated) to not teaching corrosion at all. The second construct, *the effectiveness of the existing engineering curricula in corrosion*, is defined as the degree, to which a course produces the desired educational outcomes measured as (a) the level of competence in corrosion knowledge and skills of engineering undergraduates/graduates (Q.34-35); (b) the availability of the resources to achieve the desired outcomes (Q.29, 32-33).

3 RESULTS

Regarding *the level of corrosion training*, this study found that the dedicated corrosion courses and the engineering courses integrating corrosion into the curricula were available at the UAE universities. Detailed findings on the structure of the dedicated and integrated corrosion courses are reported in the author’s expanded publication⁷. For *the competence* in corrosion knowledge and skills, the consensus was that there is *insufficient fundamental knowledge* of corrosion engineering due to the limited scope of corrosion in the curricula. Another dimension of the competence is the ability to *apply theoretical knowledge in practice*. Interestingly, while academia respondents held a positive

Table 1: Questions relating to constructs and measures

Tabela 1: Vprašanja glede načrtovanja in ukrepov

Construct – Level of the existing engineering curricula in corrosion	
	<p>Q10. Does your department offer a course or courses specifically in corrosion? Yes, my department offers course(s) specifically in corrosion No, my department teaches corrosion as part of other courses No, corrosion is NOT taught at all in my department</p>
Construct – Effectiveness of the existing engineering curricula in corrosion	
<i>Level of competence in corrosion knowledge and skills</i>	<p>Q34. Do you think engineering undergraduates/graduates (from your university) have a sufficient fundamental knowledge of corrosion engineering? Please explain.* Q35. Do you think engineering undergraduates/graduates (from your university) have a sufficient understanding of the importance of corrosion in engineering design? Please explain.*</p>
<i>Availability of resources (manpower, knowledge)</i>	<p>Q29. Would your department consider hiring a faculty member whose technical focus is corrosion? Yes No Q32. Is your department doing any corrosion-specific research? If so, who is funding it? No Yes, funding organization(s): _____ Q33. Do you have any actual or potential partnerships with the industry to study corrosion or develop continuing education for practicing engineers? No Yes If so, please describe your partnerships with the industry to study corrosion.</p>

*Industry respondents answered the variation of Q34/35 that excluded the phrase "from your university"

Table 2: Availability of resources to support corrosion training: faculty and research
Tabela 2: Razpoložljivost virov za podporo poučevanja korozije: fakultete in raziskave

	University A	University B	University C	University D
Recruitment of corrosion specialists*				
Hiring corrosion specialists	0 %	8 %	6 %	55 %
Not hiring corrosion specialists	100 %	92 %	94 %	45 %
Research efforts in corrosion*				
Corrosion research carried out by department	10 %	0 %	25 %	55 %
Industry research partnership available	0 %	0 %	13 %	25 %

*Based on 58 academic respondents who are instructors in mechanical, civil and chemical-engineering departments of the universities

view that the students had *a sufficient understanding* of the importance of corrosion in engineering design, the industry respondents were more critical, believing that the graduates had *a superficial understanding* of the corrosion in real-life design contexts.

The effectiveness of engineering curricula in corrosion is determined by both *the competence in corrosion knowledge/skills* and *the availability of resources* (qualified staff, new knowledge from research) to support corrosion education. Unfortunately, the engineering departments in three out of the four universities *would not hire* corrosion specialists as other topics have more priority. However, the aspect of research is more encouraging, as two universities reported the availability of both departmental research and industry partnerships in corrosion research (Table 2).

In terms of the overall quality of corrosion education, this study concluded that while corrosion is part of most engineering programs of the UAE universities, there are inadequate resources to support corrosion education with respect to hiring corrosion specialists or gaining new knowledge from department research and industry partnerships in corrosion research.

4 RECOMMENDATIONS AND FUTURE RESEARCH

Respondents were asked to propose the strategies for enhancing the corrosion knowledge and skills of engineering undergraduates. Three main themes were identified and the following recommendations are offered for improving the corrosion training to better meet industry expectations:

Set corrosion courses as mandatory courses in the curriculum framework of engineering fields, where corrosion is particularly relevant so that a common level of knowledge and skills can be established.

Integrate the corrosion theory with practical experience in engineering courses and senior design projects so that the undergraduates can be actively involved in applying the corrosion theory to actual design processes.

Promote the awareness of the corrosion impact through campus-wide activities to raise the appreciation of the need for corrosion mitigation and management.

Future research in this area could include comparative studies examining the differences in quality of corrosion education in other Middle-East countries. The major oil/gas producing countries such as Qatar, Saudi Arabia and Kuwait have established universities offering extensive engineering programs, for instance: Texas A&M University in Qatar, Qatar University, King Fahd University of Petroleum and Minerals, and Kuwait University. Hence, such studies could capture a more complete picture of the quality of corrosion education in the region, where corrosion prevention and management are crucial for its petroleum-based economies.

5 REFERENCES

- ¹ A. Al Hashem, Corrosion in the Gulf Cooperation Council (GCC) states: Statistics and figures, presented at the Corrosion UAE, Abu Dhabi, UAE, 2011
- ² Z. Ahmad, Principles of Corrosion Engineering and Corrosion Control, Butterworth-Heinemann, Oxford 2006
- ³ P. Roberge, Corrosion Engineering: Principles and Practice, McGraw-Hill Professional, New York 2008
- ⁴ D. Rose, Current practice: The teaching of corrosion in colleges and universities in Materials Forum 2007: Corrosion Education for the 21st Century, Washington, DC 2007, 8–12
- ⁵ R. Yin, Case Study Research: Design and Methods, 2nd ed., Sage Publishing, Beverly Hills, CA 1994
- ⁶ R. Yin, Case Study Research: Design and Methods, 3rd ed., Sage Publications, Inc., Thousand Oaks, CA 2003
- ⁷ H. L. Lim, Assessing level and effectiveness of corrosion education in the United Arab Emirates, International Journal of Corrosion, (2012), 1–10

ŠOLSKI CENTER RAVNE NA KOROŠKEM KONČAL PROJEKTA ENERGETSKE SANACIJE IN GRADNJE SODOBNEGA IZOBRAŽEVALNEGA CENTRA V SKUPNI VREDNOSTI PRIBLIŽNO TRI MILIJONE EVROV

Dne 25. oktobra 2013 je na Srednji šoli Ravne potekalo uradno odprtje Medpodjetniškega izobraževalnega centra Ravne (MIC ŠC Ravne) za področje obdelave in predelave kovin in slovesnost ob energetske sanaciji objektov Šolskega centra Ravne na Koroškem, ki naj bi za 63 % zmanjšala porabo toplotne energije in za 20 % električne energije. Skupna vrednost projektov je bila približno tri milijone evrov. Odprtja se je udeležil tudi minister za izobraževanje, znanost in šport dr. Jernej Pikalo, ki je poudaril pomen medpodjetniških izobraževalnih centrov in njihovo povezovalno vlogo med izobraževanjem in industrijo. Povedal je, da »mora sedaj industrija jasno izraziti svoje potrebe« in tako omogočiti MIC-em, da bodo »dajali tisto, kar potrebuje slovensko gospodarstvo«. Po končanem uradnem delu z nastopom Eve Boto so si udeleženci ogledali naj-sodobnejšo tehnološko opremo v skupni vrednosti približno 1 800 000 evrov in del objekta Srednje šole Ravne, ki je bil energetske saniran.

Šolski center Ravne na Koroškem je septembra končal energetske sanacije stavb Gimnazije in Srednje šole Ravne, sofinancirano iz Kohezijskega sklada, oktobra pa končal gradnjo sodobnega in tehnološko naprednega MIC ŠC Ravne, ki je bil sofinanciran iz Evropskega sklada za regionalni razvoj. Dne 25. oktobra 2013 je na Srednji šoli Ravne potekala slovesnost ob končanju obeh projektov. Direktor Šolskega centra in ravnatelj Gimnazije Ravne na Koroškem **Dragomir Benko** je ob tem povedal, da »so s projektoma, vrednima nekaj več kot tri milijone evrov, opravili odlično delo,

vzpostavili boljše razmere in zmanjšali negativne vplive na okolje«.

Energetska sanacija Gimnazije in Srednje šole Ravne je potekala na 6000 m² ogrevanih površin in bo predvidoma zmanjšala porabo toplotne energije za 63 % ter električne energije za 20 %. Skupna vrednost projekta je bila približno 940 000 EUR.

Starejši del fasade Gimnazije je bil izoliran in zaključen z novim ometom teranova, novejši del pa izoliran in zaključen s fasadnimi ploščami. Dodatno je bila izolirana podstreha, zamenjane so bile zunanje okenske police in dotrajana vrata. Vgrajene so bile nove svetilke, zamenjani radiatorski termostatski ventili na zaklep ter vgrajeni toplotna črpalka (zrak-voda), prezračevalne naprave in razvod za prezračevanje. Na Srednji šoli Ravne je potekala energetska sanacija na vzhodnem traktu objekta. Sanirana je bila fasada, zamenjana so bila okna. Vgrajene so varčne svetilke in senzorji gibanja. Na vsa grelna telesa so nameščeni termostatski ventili. V okviru sanacije je bila vgrajena prezračevalna naprava.



Na obeh objektih je vzpostavljen sistem digitalnega obratovalnega nadzora (DOM:EU), ki omogoča spremljanje porabe toplotne in električne energije ter vode in stanja klimatskih razmer.

»Za vzpostavitev MIC-a je bil zgrajen prizidek in dobavljena najsodobnejša oprema, ki bo izboljšala kakovost praktičnega dela izobraževanja in usposabljanja dijakov, študentov ter odraslih udeležencev.« je na odprtju povedala ravnateljica Srednje šole Ravne **Ivanka Stopar**. V okviru projekta so bili dobavljeni merilna, strojna, didaktično-tehnološka, računalniška in varilna oprema, stroj za centriranje, mala fotovoltaična elektrarna (MFE), laserski stroj, mini robot, testna steza itd. Med najpomembnejše pridobitve spadajo 5-osni CNC vertikalni rezkalni obdelovalni center – DOOSAN VC630/5AX, CNC-stružnica z gnanim orodjem in Y-osjo – DOOSAN PUMA 2100LY ter CNC brusilni stroj za okroglo zunanje in notranje brušenje – OKAMOTO OGM-NCIII 390.

Vir: EUTRIP

MIC tako ustvarja razmere za inovativne načine izobraževanja in raziskovanja v sklopu naslednjih poklicev: oblikovalec kovin, mehatronik operater, avtoserviser, metalurg, strojni tehnik, elektrotehnik, računalniški in strojni tehnik, pomočnik pri tehnoloških procesih. Obenem je MIC podporno okolje za osvajanje praktičnih znanj, spretnosti in sposobnosti za takojšnjo vključitev v delovne procese pri delodajalcih, delodajalcem pa omogoča prenos znanja in sodobnih tehnologij v delovne procese. MIC bo opravljal tudi praktično izpopolnjevanje za zaposlene v obrti in gospodarstvu, za učitelje praktičnega usposabljanja in strokovno-teoretičnih predmetov v strokovnih in poklicnih šolah ter za nezaposlene, ki jih bo v MIC napotil zavod za zaposlovanje. MIC se bo povezoval tudi z osnovnimi šolami v regiji.

Skupna vrednost investicije v gradnjo MIC-a Ravne na področju obdelave in predelave kovin je bila 2 136 000 evrov in je bila v vrednosti 1 740 000 evrov sofinancirana iz Evropskega sklada za regionalni razvoj.